

Advanced Nanomaterials for Biological Applications

Lead Guest Editor: Faheem Ahmed

Guest Editors: Ameer Azam, Mohammad Mansoob Khan,
and Samuel M. Mugo





Advanced Nanomaterials for Biological Applications

Journal of Nanomaterials

Advanced Nanomaterials for Biological Applications

Lead Guest Editor: Faheem Ahmed

Guest Editors: Ameer Azam, Mohammad Mansoob Khan,
and Samuel M. Mugo



Copyright © 2018 Hindawi. All rights reserved.

This is a special issue published in "Journal of Nanomaterials." All articles are open access articles distributed under the Creative Commons Attribution License, which permits unrestricted use, distribution, and reproduction in any medium, provided the original work is properly cited.

Editorial Board

- Domenico Acierno, Italy
Katerina Aifantis, USA
Nageh K. Allam, USA
Margarida Amaral, Portugal
Martin Andersson, Sweden
Raul Arenal, Spain
Ilaria Armentano, Italy
Vincenzo Baglio, Italy
Lavinia Balan, France
Thierry Baron, France
Andrew R. Barron, USA
Hongbin Bei, USA
Stefano Bellucci, Italy
Enrico Bergamaschi, Italy
D. Bhattacharyya, New Zealand
Sergio Bietti, Italy
Giovanni Bongiovanni, Italy
Mohamed Bououdina, Bahrain
Victor M. Castaño, Mexico
Albano Cavaleiro, Portugal
Bhanu P. S. Chauhan, USA
Shafiq Chowdhury, USA
Yu-Lun Chueh, Taiwan
Elisabetta Comini, Italy
Giuseppe Compagnini, Italy
David Cornu, France
Miguel A. Correa-Duarte, Spain
P. Davide Cozzoli, Italy
Anuja Datta, USA
Loretta L. Del Mercato, Italy
Yong Ding, USA
Yu Dong, Australia
Zehra Durmus, Turkey
Joydeep Dutta, Oman
Ovidiu Ersen, France
Ana Espinosa, France
Claude Estournès, France
Andrea Falqui, Saudi Arabia
Matteo Ferroni, Italy
Ilaria Fratoddi, Italy
Siddhartha Ghosh, Singapore
Filippo Giubileo, Italy
Fabien Gasset, France
Jean M. Greneche, France
- Kimberly Hamad-Schifferli, USA
Simo-Pekka Hannula, Finland
Michael Harris, USA
Yasuhiko Hayashi, Japan
Michael Z. Hu, USA
Nay Ming Huang, Malaysia
Zafar Iqbal, USA
Balachandran Jeyadevan, Japan
J.-w. Kang, Republic of Korea
Hassan Karimi-Maleh, Iran
Antonios Kelarakis, UK
Alireza Khataee, Iran
Ali Khorsand Zak, Iran
Philippe Knauth, France
Prashant Kumar, UK
Eric Le Bourhis, France
Jun Li, Singapore
Meiyong Liao, Japan
Shijun Liao, China
Silvia Licoccia, Italy
Nathan C. Lindquist, USA
Zainovia Lockman, Malaysia
Jim Low, Australia
Gaurav Mago, USA
Muhamamd A. Malik, UK
Francesco Marotti de Sciarra, Italy
Ivan Marri, Italy
Laura Martinez Maestro, UK
Sanjay R. Mathur, Germany
Tony McNally, UK
Yogendra Mishra, Germany
Paulo Cesar Morais, Brazil
Paul Munroe, Australia
Jae-Min Myoung, Republic of Korea
Rajesh R. Naik, USA
Albert Nasibulin, Russia
Toshiaki Natsuki, Japan
Hiromasa Nishikiori, Japan
Natalia Noginova, USA
Sherine Obare, USA
Won-Chun Oh, Republic of Korea
Abdelwahab Omri, Canada
Ungyu Paik, Republic of Korea
Piersandro Pallavicini, Italy
- Edward A. Payzant, USA
Alessandro Pegoretti, Italy
Oscar Perales-Pérez, Puerto Rico
Jorge Pérez-Juste, Spain
Alexey P. Popov, Finland
Thathan Premkumar, Republic of Korea
Helena Prima-García, Spain
Alexander Pyatenko, Japan
Haisheng Qian, China
You Qiang, USA
Philip D. Rack, USA
Peter Reiss, France
Ilker S. Bayer, Italy
Lucien Saviot, France
Sudipta Seal, USA
Shu Seki, Japan
Donglu Shi, USA
Bhanu P. Singh, India
Surinder Singh, USA
Vladimir Sivakov, Germany
Adolfo Speghini, Italy
Marinella Striccoli, Italy
Fengqiang Sun, China
Xuping Sun, Saudi Arabia
Ashok K. Sundramoorthy, India
Angelo Taglietti, Italy
Bo Tan, Canada
Leander Tapfer, Italy
Valeri P. Tolstoy, Russia
Muhammet S. Toprak, Sweden
R. Torrecillas, Spain
Achim Trampert, Germany
Takuya Tsuzuki, Australia
Tamer Uyar, Turkey
Luca Valentini, Italy
Antonio Vassallo, Italy
Ester Vazquez, Spain
Ajayan Vinu, Australia
Ruibing Wang, Macau
Shiren Wang, USA
Yong Wang, USA
Magnus Willander, Sweden
Ping Xiao, UK
Zhi Li Xiao, USA



Yingchao Yang, USA
Yoke K. Yap, USA
Dong Kee Yi, Republic of Korea

Jianbo Yin, China
William Yu, USA
Michele Zappalorto, Italy

Renyun Zhang, Sweden

Contents

Advanced Nanomaterials for Biological Applications

Faheem Ahmed , Ameer Azam , Mohammad Mansoob Khan , and Samuel M. Mugo
Editorial (2 pages), Article ID 3692420, Volume 2018 (2018)

Evaluation of the Coating with TiO₂ Nanoparticles as an Option for the Improvement of the Characteristics of NiTi Archwires: Histopathological, Cytotoxic, and Genotoxic Evidence

Javier Morán-Martínez , Roberto Beltrán del Río-Parra, Nadia Denys Betancourt-Martínez, Rubén García-Garza, Joel Jiménez-Villarreal, María Soñadora Niño-Castañeda, Lydia Enith Nava-Rivera, José Alfredo Facio Umaña, Pilar Carranza-Rosales , and Rubén Daniel Arellano Pérez-Vertti
Research Article (11 pages), Article ID 2585918, Volume 2018 (2018)

Exosomes: A Paradigm in Drug Development against Cancer and Infectious Diseases

Mohammad Oves , Huda A. Qari, Nadeem M. Felemban, Aftab Aslam Parwaz Khan , Mohd Rehan, Shams Tabrez, Faheem Ahmed, Ashanul Haque, Mohd Shahnawaz Khan, Javed M. Khan, Fohad M. Husain , Afzal Hussain, Mohiuddin Khan Warsi, and Iqbal I. M. Ismail
Review Article (17 pages), Article ID 6895464, Volume 2018 (2018)

Detection of HER2 through Antibody Immobilization Is Influenced by the Properties of the Magnetite Nanoparticle Coating

Enrique Villegas-Serralta, Oscar Zavala, Israel Alejandro Flores-Urquizo, Perla E. García-Casillas , and Christian Chapa González 
Research Article (9 pages), Article ID 7571613, Volume 2018 (2018)

Gold Nanoparticles as X-Ray, CT, and Multimodal Imaging Contrast Agents: Formulation, Targeting, and Methodology

Matthew M. Mahan and Amber L. Doiron 
Review Article (15 pages), Article ID 5837276, Volume 2018 (2018)

Electrochemical Biosensor Based on Optimized Biocomposite for Organophosphorus and Carbamates Pesticides Detection

R. Montes, F. Céspedes, D. Gabriel, and M. Baeza 
Research Article (13 pages), Article ID 7093606, Volume 2018 (2018)

Rapid Adsorption of Proinflammatory Cytokines by Graphene Nanoplatelets and Their Composites for Extracorporeal Detoxification

Yishan Zheng, Nicholas Pescatore, Yury Gogotsi, Boris Dyatkin, Ganesh Ingavle, Vadym Mochalin , Tochukwu Ozulumba, Sergey Mikhailovsky, and Susan Sandeman 
Research Article (8 pages), Article ID 6274072, Volume 2018 (2018)

Biofabrication of Zinc Oxide Nanoparticle from *Ochradenus baccatus* Leaves: Broad-Spectrum Antibiofilm Activity, Protein Binding Studies, and *In Vivo* Toxicity and Stress Studies

Nasser A. Al-Shabib , Fohad Mabood Husain , Iftekhar Hassan, Mohd Shahnawaz Khan, Faheem Ahmed , Faizan Abul Qais, Mohammad Oves , Mashihur Rahman, Rais Ahmad Khan , Altaf Khan, Afzal Hussain, Ibrahim M. Alhazza, Shazia Aman, Saba Noor, Hossam Ebaid, Jameel Al-Tamimi, Javed Masood Khan, Abdul Rehman M. Al-Ghadeer, Md Khurshid Alam Khan, and Iqbal Ahmad
Research Article (14 pages), Article ID 8612158, Volume 2018 (2018)

Embedding of Bacterial Cellulose Nanofibers within PHEMA Hydrogel Matrices: Tunable Stiffness Composites with Potential for Biomedical Applications

Radka Hobzova , Jakub Hrib, Jakub Sirc, Evgeny Karpushkin, Jiri Michalek, Olga Janouskova, and Paul Gatenholm

Research Article (11 pages), Article ID 5217095, Volume 2018 (2018)

Heparin-Based Nanoparticles: An Overview of Their Applications

Maria del Pilar Rodriguez-Torres , Laura Susana Acosta-Torres , and Luis Armando Diaz-Torres 

Review Article (8 pages), Article ID 9780489, Volume 2018 (2018)

Practical Solution for Effective Whole-Body Magnetic Fluid Hyperthermia Treatment

Hiroaki Mamiya, Yoshihiko Takeda, Takashi Naka, Naoki Kawazoe, Guoping Chen, and Balachandran Jeyadevan

Research Article (7 pages), Article ID 1047697, Volume 2017 (2018)

Evaluation of the Osteoblast Behavior to PGA Textile Functionalized with RGD as a Scaffold for Bone Regeneration

Mariné Ortiz, Diana María Escobar-García, Marco Antonio Álvarez-Pérez, Amaury Pozos-Guillén, Christian Grandfils, and Héctor Flores

Research Article (8 pages), Article ID 4852190, Volume 2017 (2018)

Studies of the Influence of Gold Nanoparticles on Characteristics of Mesenchymal Stem Cells

Nataliia Volkova, Olena Pavlovich, Olena Fesenko, Oksana Budnyk, Serhii Kovalchuk, and Anatoliy Goltsev

Research Article (9 pages), Article ID 6934757, Volume 2017 (2018)

Bacterial Stress and Osteoblast Responses on Graphene Oxide-Hydroxyapatite Electrodeposited on Titanium Dioxide Nanotube Arrays

Yardnapar Parcharoen, Preecha Termsuksawad, and Sirinrath Sirivisoot

Research Article (12 pages), Article ID 2194614, Volume 2017 (2018)

Editorial

Advanced Nanomaterials for Biological Applications

Faheem Ahmed ¹, Ameer Azam ², Mohammad Mansoob Khan ³, and Samuel M. Mugo⁴

¹College of Science, Alfaisal University, Riyadh, Saudi Arabia

²Department of Applied Physics, Faculty of Engineering & Technology, Aligarh Muslim University, Aligarh, India

³Faculty of Science, Chemical Sciences, Universiti Brunei Darussalam, Gadong BE1410, Brunei Darussalam

⁴Physical Sciences Department, 10700 104 Avenue, MacEwan University, Edmonton, AB, Canada T5J 4S2

Correspondence should be addressed to Faheem Ahmed; faheem030@gmail.com and Ameer Azam; aazam.ap@amu.ac.in

Received 13 June 2018; Accepted 14 June 2018; Published 29 August 2018

Copyright © 2018 Faheem Ahmed et al. This is an open access article distributed under the Creative Commons Attribution License, which permits unrestricted use, distribution, and reproduction in any medium, provided the original work is properly cited.

Nanomaterials have been widely studied for many years and they have also generated an intense scientific interest due to a wide variety of potential applications in biomedical, optical, and electronic fields. Nanomaterials have drawn attention based on the few properties they exhibit like their surface to mass ratio and the reactivity of their surface. Also, the control of composition, size, shape, and morphology of nanomaterials is an essential cornerstone for the development and application of nanomaterials and nanoscale devices. The selection of material depends on factors such as (i) required size of nanoparticles, (ii) aqueous solubility and stability, (iii) surface characteristics as charge and permeability, or (iv) degree of biodegradability, biocompatibility, and toxicity.

This special issue holds 3 reviews and 10 original research articles. Various nanomaterials including gold nanoparticles, TiO₂, ZnO, magnetic nanomaterials, graphene, heparin-based nanoparticles, and polymer nanocomposites were used to show their potential applications in multimodal imaging contrast agents, cancer detection, drug delivery, cytotoxicity and genotoxicity, biosensing, antibiofilm, protein binding, and tumor destruction via heating (hyperthermia).

J. Morán-Martínez and coworkers reported the utilization of coating with TiO₂ nanoparticles for the improvement of the characteristics of NiTi archwires and discussed their effect on histopathological, cytotoxic, and genotoxic properties. They have used male rats in four groups with different treatments, and the amount of TiO₂ nanoparticles was changed gradually. Their results showed that cell viability in lymphocytes treated with TiO₂ NPs did not cause genotoxicity.

In addition, the histopathological studies of hepatic and renal tissue indicated the nuclear alterations and necrosis.

M. Oves and coworkers contributed with a review on the exosomes for drug development against cancer and other infectious diseases. They have focused on the studies reported in the literature on the application of exosomes in tumor therapy and infectious disease control. In particular, they have highlighted the importance of exosomes in cancer biology and infectious disease diagnoses and therapy and provide a comprehensive account of exosome biogenesis, extraction, molecular profiling, and application in drug delivery.

For the detection of human epidermal growth factor receptor 2 (HER2) protein, E. Villegas-Serralta and coworkers contributed a research article on the magnetic nanoparticles coated by aminosilane and dextran various species and their conjugation with the single-chain variable fragment antibodies (scFVs). Their analyses concluded that aminosilane surface coating enhanced the scFv conjugation efficiency over twofold compared to that of the dextran-coated magnetite NPs for the detection of HER2 proteins. The utilization of magnetic fluid in hyperthermia was presented by H. Mamiya and coworkers in their research article. Magnetic fluid hyperthermia therapy is considered as a promising treatment for cancers including unidentifiable metastatic cancers that are scattered across the whole body. They mentioned that the indicated allowable upper limit of field amplitude for constant irradiation over the entire human body corresponded to approximately 100 Oe at a frequency of 25 kHz. The limit corresponds to the value of 2.5×10^6 Oe·s⁻¹ and is

significantly lower than the conventionally accepted criteria of $6 \times 10^7 \text{ Oe}\cdot\text{s}^{-1}$. In their research, they focused on the evaluating maximum performance of conventional magnetic fluid hyperthermia cancer therapy below the aforementioned limit using magnetic fluid. Their results showed that the whole-body magnetic fluid hyperthermia treatment is still a possible candidate for future cancer therapy.

M. M. Mahan and A. L. Doiron highlighted the role of gold nanoparticles as X-ray, CT, and multimodal imaging contrast agents in their review. Gold nanoparticles (AuNP) have attracted interest recently for their use as CT CA due to their high X-ray attenuation, simple surface chemistry, and biocompatibility. They have summarized the current state-of-the-art knowledge in the field of AuNP used as X-ray and multimodal contrast agents based on their design specification of particles that includes size, shape, surface functionalization, composition, circulation time, and component synergy. N. Volkova and coworkers also used gold nanoparticles to study the effect of concentrations of gold nanoparticles on the immunophenotype, synthesis collagen type I, ability to direct differentiation, and spectroscopic characteristics of bone marrow mesenchymal stem cells (MSCs). They observed that lower concentration (1.5–9 $\mu\text{g}/\text{ml}$) did not lead to changes in the level of expression of CD 45, CD 90, and CD 73, thus safe for MSCs. However, at particular concentrations of 6 and 9 $\mu\text{g}/\text{ml}$ of AuNPs, a decrease in CD 44 cells by 6% and 9%, respectively, was observed.

Y. Zheng and coworkers contributed a research article on the graphene nanoplatelets and their nanocomposites for extracorporeal detoxification. They showed that the graphene nanoplatelets (GNP) can be used as a low-cost alternative hemosorbents for rapid removal of a broad spectrum of proinflammatory cytokine markers, with low cytotoxicity towards the hepatic cell line HepG2. Y. Parcharoen and coworkers also used the family of graphene especially graphene oxide and hydroxyapatite composites electrodeposited on TiO_2 nanotube arrays, and their bacterial stress and osteoblast responses were presented.

N. A. Al-Shabib and coworkers reported in their research article the biosynthesis of zinc oxide nanoparticle using *Ochradenus baccatus* leaves and their antibiofilm activity, protein binding studies, and in vivo toxicity and stress studies. Their studies confirmed that ZnO nanoparticles demonstrated significant biofilm inhibition in human and food-borne pathogens at subinhibitory concentrations. In addition, these nanoparticles demonstrated efficient binding with HSA protein with no change in their structure. Interestingly, in vivo toxicity evaluation confirmed that OB-ZnNPs possessed no serious toxic effect even at higher doses. Moreover, they were found to have excellent antioxidant properties that can be employed in the fields of food safety and medicine.

In summary, this special issue will provide a detailed account of the present status of nanomaterials and highlights the recent developments which cover the novel and important aspects of these materials and their biological applications.

Authors' Contributions

Faheem Ahmed and Ameer Azam are shared first authors.

Acknowledgments

The editors would like to thank all authors who submitted their research to this special issue as well as all reviewers for their valuable contribution.

Faheem Ahmed
Ameer Azam
Mohammad Mansoob Khan
Samuel M. Mugo

Research Article

Evaluation of the Coating with TiO₂ Nanoparticles as an Option for the Improvement of the Characteristics of NiTi Archwires: Histopathological, Cytotoxic, and Genotoxic Evidence

Javier Morán-Martínez ¹, Roberto Beltrán del Río-Parra,^{1,2}
Nadia Denys Betancourt-Martínez,¹ Rubén García-Garza,³ Joel Jiménez-Villarreal,⁴
María Soñadora Niño-Castañeda,¹ Lydia Enith Nava-Rivera,¹ José Alfredo Facio Umaña,^{1,2}
Pilar Carranza-Rosales ⁵, and Rubén Daniel Arellano Pérez-Vertti¹

¹Departamento de Biología Celular y Ultraestructura, Centro de Investigación Biomédica, Facultad de Medicina, Universidad Autónoma de Coahuila, Torreón, COAH, Mexico

²Clínica de Ortodoncia, Facultad de Odontología, Universidad Autónoma de Coahuila, Torreón, COAH, Mexico

³Departamento de Histología, Facultad de Medicina, Universidad Autónoma de Coahuila, Torreón, COAH, Mexico

⁴Escuela de Medicina, Universidad Autónoma de Coahuila, Unidad Norte, Piedras Negras, COAH, Mexico

⁵Instituto Mexicano del Seguro Social, Centro de Investigación Biomédica del Noreste, Departamento de Biología Celular y Molecular, Monterrey, NL, Mexico

Correspondence should be addressed to Javier Morán-Martínez; javmoran@yahoo.com

Received 25 July 2017; Revised 29 December 2017; Accepted 18 March 2018; Published 6 May 2018

Academic Editor: Zafar Iqbal

Copyright © 2018 Javier Morán-Martínez et al. This is an open access article distributed under the Creative Commons Attribution License, which permits unrestricted use, distribution, and reproduction in any medium, provided the original work is properly cited.

For the EPD, different voltages and different times were used. Male rats were used in four groups ($n = 3$) with different treatments. The blood sample was obtained for genotoxic analysis and liver and kidney organs were removed for histopathological analysis. The amount of NPs TiO₂ deposited on the samples of the arches increases gradually in the times of 15 and 30 s. At all voltages, however, at 45, 60, 75, and 90 s, there is an increase up to 25 V. Cell viability in lymphocytes treated with TiO₂ NPs did not cause genotoxicity. In the histopathological findings of hepatic and renal tissue, nuclear alterations and necrosis were observed. The objective of the study was to improve the physical and biocompatibility characteristics of the NiTi arches for which the EPD is used. The technique for the deposition of TiO₂ NPs was used, where this technique could be used as an economical and versatile way to perform homogeneous depositions even on surfaces with the complexity of the NiTi alloy. As for genotoxicity and cytotoxicity, we continue to have controversial results.

1. Introduction

In the recent practice of orthodontics, the use of Nickel-Titanium (NiTi), Nickel-Titanium-Copper (NiTiCu), or Titanium-Molybdenum (TiMo) alloys predominates due to its elastic characteristics that facilitate the alignment and leveling of the arches, improving the elasticity and flexibility [1]. The use of NiTi arches is widely accepted by the orthodontic

community and offers biomechanical benefits difficult to match by some other materials on the market; however, a negative aspect of these arches is the roughness which has the ability to retain a greater amount of dental plaque because it favors its adhesion [2]; principally constituted by aerobic bacteria such as *Streptococcus sanguinis* and *Streptococcus mutans*, this plaque propitiates the corrosion of metals and alloys through the formation of organic acids during the

glycolysis of sugars, reducing the pH [3]. Currently, the search for improvement of existing materials in the field of orthodontics has been a subject of study; for example, the organically modified antibacterial silicates (ORMOSIL) such as quaternary ammonium methacryloxy silicate (QAMS) is added to the orthodontic acrylic resins in order to improve antimicrobial activity and toughness [4], resin-based adhesion materials contain Portland-type cement to provide adequate shear bond strength (SBS) and a caries-preventive effect [5], the incorporation of bioactive glass (BAG) into composite resins (BAG-Bonds) showed the capacity for buffering acidic oral conditions through the liberation of calcium in the environment [6], and also the modification of the arches with the application of nanomaterials, for example, nanoparticles (NPs), is an interesting topic due to popularity carried in recent times, and the advantages above the other modification techniques are low cost through the use of simple devices and easy handling. Between the diverse types of nanomaterials used in order to improve the arches' characteristics, the nanoparticles of TiO₂ have been shown to be cost-effective [7] and they possess a unique photocatalytic property that results in enhanced microbicide activity, principally against bacterial strains of the plaque [8–10] besides their apparently low toxicity and excellent biocompatibility [11, 12]; regardless, there is still controversy about it being harmless [13, 14], since TiO₂ NPs have been related to the induction of cytotoxicity and genotoxicity due to the production of reactive oxygen species (ROS) in different cell types [15–17]; in addition, *in vivo* studies have shown apparently nanoscale and microscale toxicological effects associated with the size of the nanoparticles of TiO₂ [18, 19].

The efficacy of electrochemical methods such as electrophoretic deposition (EPD) is an alternative, versatile, and inexpensive procedure for depositing of these nanomaterials [20] and is a very useful tool for the manufacture of films of nanostructures, where thickness can be controlled varying parameters such as voltage and time, principally with the use of TiO₂ NPs which have been already proven in the literature; moreover, compared with other wet, dry, or plasma deposition methods, attachment could be oriented more effectively due its nondestructive depositing method that does not affect the particle [21]. The efficiency of EPD in the production of homogeneous and reliable films depends to a great extent on the surface chemistry of the particles, the behavior of surface-liquid interfaces under an electric field, and the development of the particle-particle network and particle-substrate network [22]; because of this, the good quality of TiO₂ NPs deposition on stainless steel bars [23] found in the literature does not necessarily correspond to a good deposition quality on other materials including NiTi arches. In our research, we propose an adequate technique for the correct deposition of TiO₂ NPs on the surface of NiTi arches, since the current bibliographic data in this type of material is virtually nonexistent and the methodology is poor described; for this reason, the objective of this study was to evaluate the electrophoretic deposition (EPD) of TiO₂ NPs in arches as well as their histopathological, genotoxic, and cytotoxic effects in Long-Evans rats.

2. Materials and Methods

2.1. Preparation of the NiTi Archwires. Conventional NiTi archwires (0.017 × 0.025 inches) (Ah-Kim-Pech®, México) were sandblasted with aluminum oxide (Zogear Blaster, CHN) and subsequently etched with 10% oxalic acid at 80°C for 60 min followed by immersion in an ultrasonic bath in acetone for 3 min and rinsed with distilled water, according to Paoli et al. [22]. To optimize the adhesion of NPs, later the archwires were cut into pieces of 16 mm.

2.2. Suspension Design. A suspension was made for the nanoparticle dispersion with a mixture of H₂O and C₂H₅OH (1:4) with a concentration of TiO₂ NPs (CAS: 13463-67-7; purity ≥ 99.5%; molecular weight: 79.87; particle size: 21 nm), 1% mass, and poly(diallyl dimethyl ammonium chloride) (PDADMAC) 2% mass [24] (all chemicals were obtained from Sigma-Aldrich Co., Ltd., St. Luis, MO, USA). The stability of the suspension was obtained by magnetic stirring (hotplate stirrer LMS-1003 Daihan Labtech Co., Ltd., Korea) during 12 h before the EPD process. This was carried out with two electrodes in a 500 mL glass vessel; the NiTi archwires were used as deposition substrates and a stainless steel sheet was used as a counter electrode, separated by a distance of 20 mm; both the working electrode and the counter electrode were connected to direct current power supply (Enduro 300V, Labnet International Inc., Woodbridge, NJ, USA). The NiTi archwire samples were weighed on an analytical balance with a sensitivity in µg (Denver Instruments apx-200) and then divided into 6 groups which used a constant voltage (V) of 5, 10, 15, 20, 25, and 30 V, respectively, at different times (15, 30, 45, 60, 75, and 90 s); this was carried out in triplicate. After the EPD the samples were allowed to dry for 24 h at room temperature; the samples were observed under a 10x optical microscope (Labomed S1100, Germany) with an AmScope MD700 digital microscope to determine the degree of TiO₂ NPs deposition. A new weighing of the samples was performed to measure the amount (µg) of TiO₂ deposited. The amount of TiO₂ NPs deposited per area in the NiTi arcs was calculated (µg/mm²); the samples were left in a sterile container with 2 mL of PBS solution for 30 days to administer them later to the experimental group (G3).

2.3. Determination of the Genotoxicity of TiO₂ NPs

2.3.1. Animals. Our work was developed under the Official Mexican Standard for use and handling of animals in experimentation (SAGARPA in Mexico, NOM-062-ZOO, 1999). The study was approved by the Bioethics Committee and by the Internal Committee for the Care and Use of Laboratory Animals (CICUAL) of the Faculty of Medicine of the Autonomous University of Coahuila (number CONBIOET-ICA07CEI00320131015). All procedures with experimental animals were supervised by a veterinarian certified by the Secretary of Agriculture, Cattle Raising, Rural Development, Fishing and Food (SAGARPA, key code: MR-0716-33-001-1).

Twelve adult male Long-Evans rats ranging in age from 10 to 12 weeks, with an average weight between 240 and 280 grams, were provided by the Bioterium of the Faculty

of Medicine of the Autonomous University of Coahuila. All animals were maintained under controlled conditions of temperature at 25–26°C in a 12:12 h light/dark cycle housed in individual cages with water and food ad libitum.

2.3.2. Experimental Groups and Treatments. The rats were divided into 4 groups; ($n = 3$) the control group (CG) were given 1 mL of xylocaine®: 2% injectable solution of lidocaine without epinephrine intraperitoneally for 3 days, 1 dose daily; the sacrifice was 24 h after last dose. Group 1 (G1) is given 5 mg/kg body weight of TiO₂ dissolved in 1 mL xylocaine: 2% injectable solution of lidocaine without epinephrine intraperitoneally for 3 days, 1 dose daily. The sacrifice was at 48 h after last dose. Group 2 (G2) is given 5 mg/kg body weight of TiO₂ dissolved in 1 mL xylocaine: 2% injectable solution of lidocaine without epinephrine intraperitoneally for 3 days, 1 dose daily. The sacrifice was at 72 h after last dose. Group 3 (G3) received a solution composed of PBS (2 mL) NPs of TiO₂ plus the arcs NiTi (25 V 90 s). This solution remained at rest for 30 days prior to its administration in the rats; this solution was administered by nasogastric tube for 3 days, and the sacrifice was 72 h after last dose. After the exposure time, the rats were sacrificed by the veterinarian in charge through cervical dislocation; blood samples were extracted by cardiac puncture; the organs (liver and kidney) were removed and fixed in 10% neutral formalin for subsequent histopathological analysis.

2.3.3. Comet Assay in Lymphocytes. DNA fragmentation analysis of individual cells for peripheral blood lymphocytes was performed based on the methodology of Singh et al. [25] with some minor modifications. This allows the differentiation and analysis of cells with fragmented DNA to determine the percentage of fragmentation using specialized software. From each treatment, 10 µL of peripheral blood suspended in 0.5% low melting point agarose was used on slides pretreated with 0.5% normal melting point agarose and then covered with coverslips and the agarose was allowed to solidify at 4°C per 5 min; the slides were placed in a Köpplín with lysis solution (2.5 M NaCl, 0.1 M EDTA, 10% DMSO, and 1% Triton X-100). At the end of the lysis, the samples were taken to horizontal electrophoresis chamber and incubated in electrophoresis buffer (NaOH 0.3 M, 200 mM EDTA) at pH = 13.0 to 20 min at 4°C for the unwinding of DNA in a dark room. The electrophoresis was completed with the following specifications: 25 V (1 V/cm), 300 mA for 20 min. After switching off the electrophoresis power source, the electrophoresis chamber slides were carefully removed and rinsed with a neutralization buffer (0.4 mol/L Tris-HCl, pH 7.5) for 5 min. The excess of neutralization buffer was drained off and placed in ethanol and then allowed to dry; once dried, the slides were stored for later reading.

2.3.4. DNA Fragmentation Analysis. The DNA was stained in phosphate-buffered saline (PBS) with fluorescent solution of GelGreen™ (Nucleic Acid Gel Stains, Biotium®, Fremont, CA, USA). Comets lymphocytes were evaluated under fluorescence microscope, 40x and 100x (Labomed LX 400,

Germany). The images were taken with a fluorescence, 16-megapixel digital camera (AmScope, Digital Camera Microscope # MD700) and were converted into Bitmaps format (*.bmp) and analyzed in TriTek's CometScore Freeware v1.5 software. ImageJ software V.1.8.0 was first used to remove background noise from the DNA images obtained. Automatic image processing software was used for analysis of the comet assay. The software was able to calculate the amount of DNA at specified location based on pixel intensity of images. DNA in the tail was computed as follows:

$$\text{DNA} = \frac{\text{total comet tail intensity}}{\text{total comet intensity}} \times 100. \quad (1)$$

2.4. Histopathological Analysis. At the end of the experimental period, the rats were sacrificed by cervical dislocation; blood samples were collected by cardiac puncture and dissection of the abdominal organs was performed and fixed in 10% neutral formalin for subsequent histological analysis. Representative samples of hepatic and renal tissue previously fixed to be included in paraffin blocks were taken by conventional histological technique, which were cut in a microtome (Leitz 1512, Austria) at a thickness of 5 µm and mounted on slides stained with hematoxylin and eosin (H&E). The stained sections were examined under light microscopy to make the respective observations and to evaluate the morphological changes comparing them with the control tissues.

2.5. Statistical Analysis. We performed Kruskal-Wallis test as a nonparametric test and Dunn test as a post hoc test and unidirectional ANOVA as a parametric test using Tukey as a post hoc test. Measures of central tendency and standard deviation were done. Statistical analysis was performed using the Minitab 17 software for Windows.

3. Results

3.1. Deposition of Arches with TiO₂. The EPD gives us the possibility of generating different rate of amount of TiO₂ NPs deposited per area of NiTi arch (Figure 2) by the modulation of applied voltage and the time of deposition. In our experiment, the amount of TiO₂ NPs deposited on the samples of the arches increases gradually at the times of 15 and 30 s at all voltages (Figures 1(a) and 1(b)); however, at 45, 60, 75, and 90 s, there is an increase up to 25 V (Figures 1(c), 1(d), 1(e), and 1(f)). It was observed that the samples with higher deposition of TiO₂ NPs were 25 V90 s and 30 V90 s (Figures 4(f) and 4(g)). However, in these samples, a large number of fractures were observed in the continuity of the coating; the best ratio between quantity and quality of the coatings obtained by the deposition of TiO₂ NPs in the treated samples, finding the most homogeneous and fracture free coating, was in the sample of 10 V75 s (Figure 4(c)). In the results, a constant increase in the amount of deposited TiO₂ from 15 V to 25 V in all the treated arches could be observed; a variable behavior was found in voltages under 15 V and greater than 25 V. The correlation of the DEF of the TiO₂ NPs at times of 15 and 30 s, 45 and 60 s, 75 and 90 s was highly significant as observed in the correlation

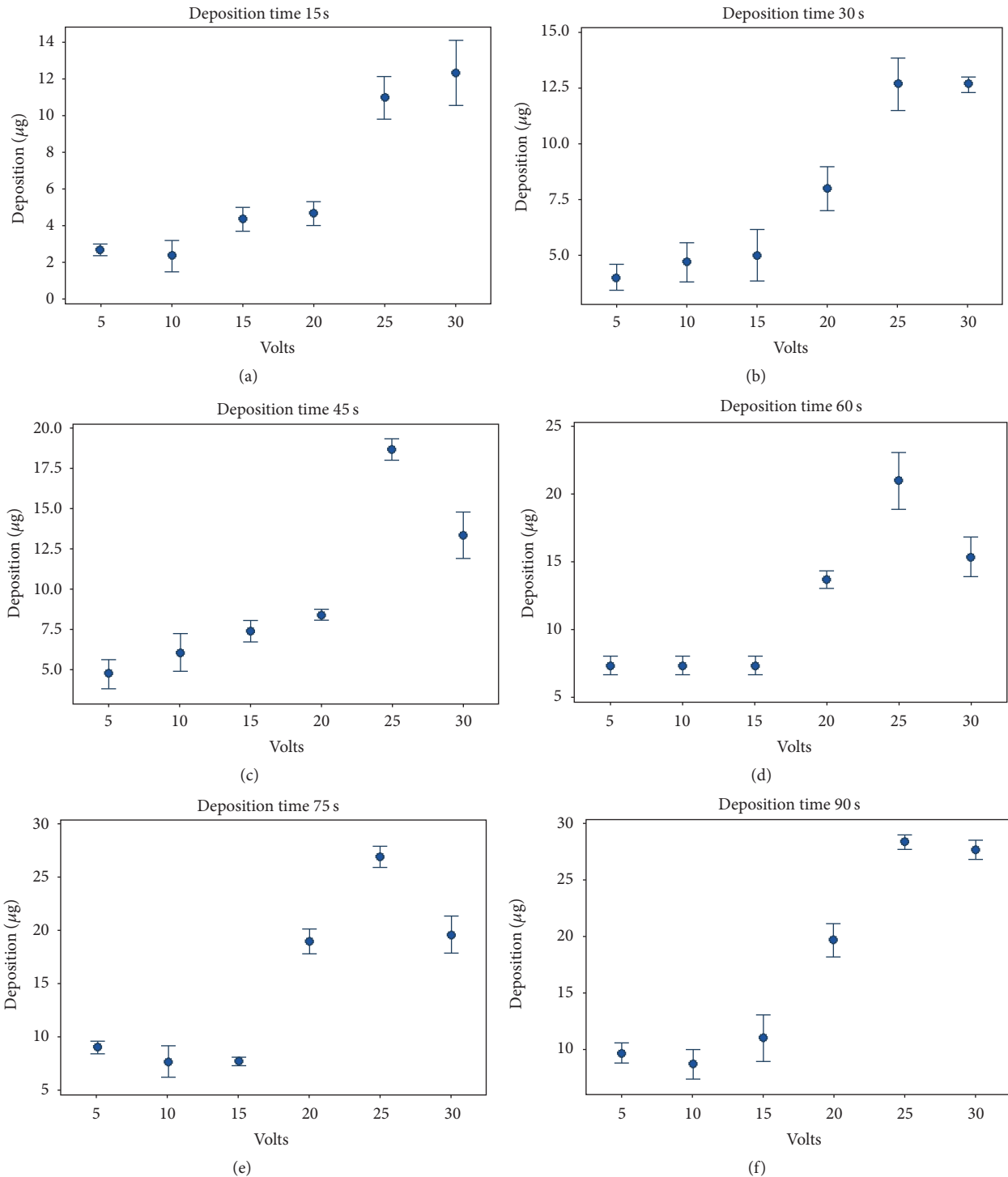


FIGURE 1: Deposition of TiO_2 NPs (μg) voltage (V)/time (s). (a) 15, (b) 30, (c) 45, (d) 60, (e) 75, and (f) 90 seconds versus 10, 15, 20, 25, and 30 V for each deposition. Results are shown in mean and standard error.

graphs (Figures 3(a)–3(c)). This indicates and corroborates what was mentioned above, where, according to the voltage intensity and elapsed time of the DEF, we observed this trend of dependent association because of the voltage with the time of application of voltage to which the arch was submitted.

In the microphotographs, we can see the different groups of arcs with their voltages and their effects (Figure 4). In the group of 5 volts (Figure 4(a)), it was observed that the deposition is minimal; increasing the voltage shows a larger deposition, considering the uniformity of the EPD at 10 V 75 s

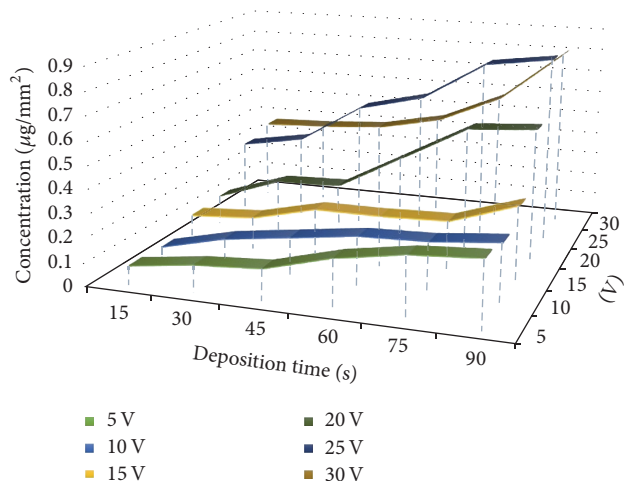


FIGURE 2: Amount of deposition of TiO_2 NPs (μg) per area of NiTi arch ($\mu\text{g}/\text{mm}^2$) (voltage (V)/time (s)). 15, 30, 45, 60, 75, and 90 s versus 5, 10, 15, 20, 25, and 30 V for each deposition.

(Figure 4(c)), the greater amount of deposition is obtained at 25 V to 90 s (Figure 4(f)). The general behavior is that from 15 V there is a sustained increase of NPs deposited up to 30 V where there is a decrease because it exceeds the value of the critical cracking thickness (EAC).

3.2. Analysis of DNA Fragmentation by Exposure to NPs of TiO_2

3.2.1. DNA Fragmentation in Lymphocytes. When the alkaline comet test was performed, a stability was observed in the DNA chain, since there was no significant migration on this (Figure 5); treatment with TiO_2 NPs did not cause cytotoxicity at the concentration of 5 mg/kg for 3 days, 1 daily dose, with the sacrifice being conducted after the last dose at 48 h (G1). There was also no cytotoxicity at the concentration of 5 mg/kg for 3 days, 1 daily dose, with the sacrifice being conducted after the last dose at 72 h (G2) or in the PBS solution (2 mL) in which previously treated arches were submerged (25 V 90 s) and left to rest for 30 days and administered by nasogastric tube for 3 days and with a sacrifice conducted after the last dose of 72 h (G3), suggesting that there were no DNA breaks (see Figure 5(c)). Another parameter delivered by the comet test is the percentage of DNA contained in the comet tail. This parameter is the subtraction of 100% of DNA minus the percentage of DNA contained in the head of the comet. This parameter is the percentage of fragmentation that the evaluated cell has; the group with greater fragmentation was group 1 (G1) which had an average of 6.06 ± 1.49 percent.

3.3. Histopathological Findings. Figure 6 shows the microphotographs with the observations found in liver tissue samples. In the analysis of the samples corresponding to the control group, which was administered only with 2% lidocaine for 3 days, no pathological data were found

(Figure 6(a)). In those corresponding to group 1, which received 5 mg/kg TiO_2 for 3 days, being sacrificed 48 h after the last dose, the presence of vacuoles included within the hepatocyte cytoplasm was observed (Figure 6(b)). In the case of group 2 samples, they received 5 mg/kg of TiO_2 for three days and were sacrificed 72 h after the last dose; it is observed that the hepatocytes present a foamy cytoplasm and nucleus with granular chromatin (Figure 6(c)). Group 3, which was given PBS solution for 3 days in which the TiO_2 treated arches rested and were sacrificed 72 h after the last dose, extensive areas of cell necrosis were observed with destruction of hepatocytes (Figure 6(d)). Figure 7 shows the representative microphotographs, corresponding to the findings in renal tissue samples. In the analysis of the samples from the control group, no pathological data were found. In the samples corresponding to groups 1, 2, and 3, a slight glomerular retraction and moderate vascular congestion were observed.

4. Discussion

4.1. Electrophoretic Deposition. In the course of achieving the final suspension design, 3 mixtures were used, a mixture of H_2O and NaCl without charging agent (data not shown), a mixture of H_2O and $\text{C}_2\text{H}_5\text{OH}$ (1:4) and the polyethylenimine (PEI) charging agent (data not shown), and a mixture of H_2O and $\text{C}_2\text{H}_5\text{OH}$ (1:4) and the poly(diallyl dimethyl ammonium chloride) (PDADMAC) charging agent, which proved to be the best combination to enhance the adhesion effect of TiO_2 NPs layers. It was observed that the mixture of H_2O and NaCl because of being a water-based solution produces electrolysis even at low voltages and this causes bubbles to be trapped causing “gaps” in the deposition of the TiO_2 NPs, coinciding with what was commented on in [26–28]. Therefore, it was decided to use an ethanol-based suspension instead of water in order to avoid harmful hydrogen penetration at the working electrode and a charging agent was added to provide an additional surface charge for the stabilization of suspended particles and electrophoretic mobility during the deposition process [29, 30]. To the mixtures based on H_2O and $\text{C}_2\text{H}_5\text{OH}$ (1:4) a charging agent of PEI and PDADMAC were added, respectively, having the best adhesion results with the PDADMAC charging agent, coinciding with the results of Lau and Sorrell [29]. In the researches conducted by González-Luna et al. and Wu et al. [12, 31], they suggest a deposition in the range of 20–50 V, and Boccaccini et al. [32] suggest ranges from 10 to 50 V; in our study the voltage range was handled between 5 and 30 V with the largest amount of deposition in the 25 V regardless of time, unlike Paoli et al. [22] who suggest 20 V as the most optimal voltage and Hasegawa et al. [33] who suggest 40 V. This study confirms what other authors observed when the amount of deposited layers was modulated with the deposition time and the voltage, although not necessarily more time and voltage mean a better deposition. In our study, with the combination of the voltage/time deposition, the most homogeneous layers obtained without fractures were with the samples of 10 V/75 s. Samples under this voltage show very little deposition and those superior to it show

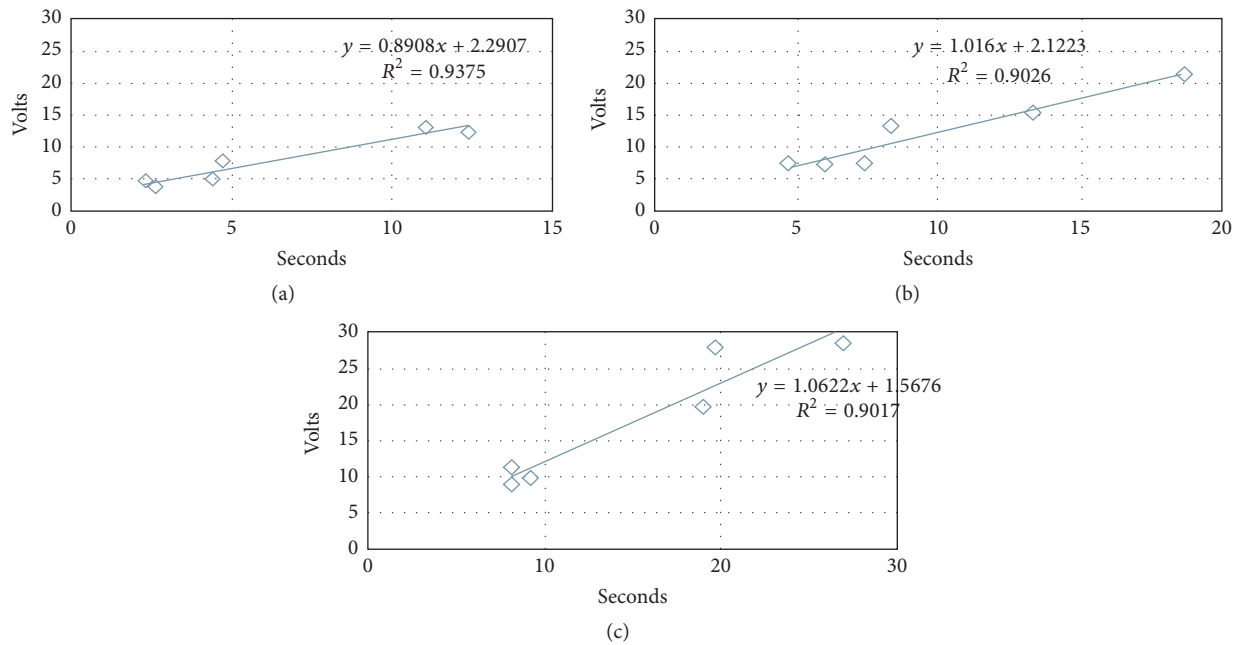


FIGURE 3: Time/voltage correlation. A voltage-dependent association tendency was observed with the time of voltage application. Notes: (a) deposition, 15 and 30 s, (b) deposition, 45 and 60 s, and (c) deposition, 75 and 90 s.

greater deposition but with fractures, which increases the time of deposition/voltage. After having a constant increase, the samples treated at 30 V have a decrease in the deposited TiO_2 NPs, as can be seen in the deposition's interval graphs; the possible explanation for this is that it exceeds the value of the critical cracking thickness (CCT) as explained by Sadeghi et al. [30]. When the layer becomes thicker during the deposition process, there is an increase in the resistance because the previously deposited layer is nonconductive, weakening the electric force field and causing weak connections between the particles along the final layer. Therefore, the accumulated NPs on that layer tend to have fractures that cause the detachment of the NPs due to the accumulated excess. It was decided not to perform any sintering technique after EPD because it has been proven that the exposure of the NiTi archwires at temperatures above 500°C alters their mechanical properties [34–36].

4.2. Comet Assay. Although administration of TiO_2 NPs to the experiment animals was intraperitoneally (G1 and G2) and through nasogastric probe (G3), there was no significant induction of DNA breaks in peripheral blood lymphocytes in the results delivered by the comet assay; our negative results were similar to those found in keratinocytes, irradiated with TiO_2 at 20, 40, and 60 min, where there was no evidence of type IV comet damage and the number of comets II and III was approximately 30% [37] also in human diploid fibroblasts and human bronchial epithelial cells that were exposed at concentrations up to $50 \mu\text{g}/\text{cm}^2$ where the tail moment does not exceed [15]. But, as mentioned above, there are studies where positive results were found in the comet assays, for example, in lymphocytes, which were treated with TiO_2 at concentrations up to $59.7 \mu\text{g}/\text{mL}$ having a mean of olive

moment of 7.30 ± 0.81 [38], human bronchial cell cultures that were treated with $1.77 \text{ g}/\text{cm}^2$ TiO_2 NPs causing olive moments up to 90 [17], Rtg cells exposed for 4 h to TiO_2 NPs ($50 \mu\text{g}/\text{mL}$) in MEM cultures PBS, and H_2O solution where there was a percentage of DNA in tail of 32, 45, and 32, respectively [39]. These inconsistent results may be due to the different sizes and structures of the TiO_2 NPs used in the studies as suggested [40], making it difficult to compare the results between the studies.

4.3. Pathophysiological Findings. The results of the present study show the existence of cytotoxic potential of TiO_2 NPs after acute exposure by intraperitoneal injection (G2 and G3) at a high dose as presented in our methodology and coinciding with Singh et al. [25] with progressive damage even after cessation of exposure, supporting the distribution and accumulation data in liver and kidney [41]. In the case of G3, the liver damage was a lot greater, represented by the extensive areas of cellular necrosis. There was not enough time to find fibrous septa (cirrhosis) in the liver parenchyma as in the findings reported by Umbreit et al. [42] where central fibrous septa were found after 7 days of exposure. In the case of renal damage analysis, the findings were more discrete and there was no significant difference in the cases exposed to a controlled concentration compared to those that received the PBS solution in which the deposited archwires rested. In this case, contrary to the findings of Chen et al. [43], what was observed in our study was a glomerular contraction and not a glomerular inflammation. Our observations seem to indicate that, after deposition of TiO_2 NP, NiTi arcs that exceed the CCT, for example, samples of 25 V/90 s, are susceptible to degradation of the coating in an aqueous medium (PBS solution), when ingests are absorbed and TiO_2

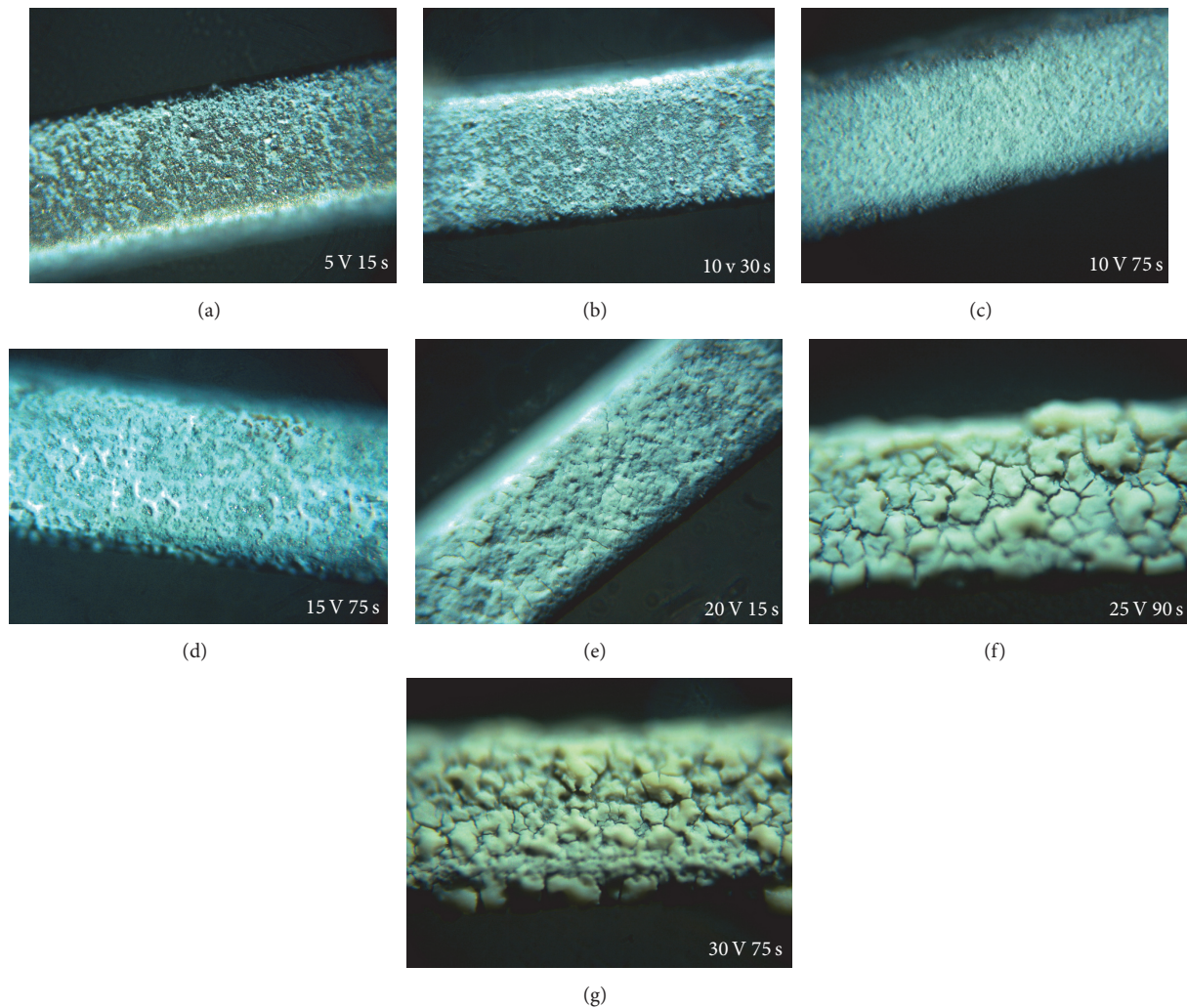


FIGURE 4: Deposited arches. It is observed that, at higher voltage/deposition time, there are more deposited TiO_2 NPs, but there is also an increase in surface fractures ((f) and (g)) (10x).

NPs enter the bloodstream producing a toxic effect on the organs, with the first step being the liver parenchyma, which results in extensive lesions such as those found in our study. Other studies describe the ability of TiO_2 NPs to produce an inflammatory response and induce the production of ROS (reactive oxygen species) inducing apoptosis, as observed in our results [44], in addition to mentioning the relationship between the size of the NPs and their toxicity, suggesting that the smaller the size, the greater the metabolic activity and toxicity. Regarding the intracellular mechanisms of damage [45], when describing the importance of the internalization of NPs of TiO_2 , when they accumulate in lysosomes, this leads to their rupture and releases their content, such as cathepsin B with the subsequent activation of caspases to apoptosis.

5. Conclusion

The aim in this study was to improve the physical and biocompatibility characteristics of the NiTi arches; therefore

the EPD technique was conducted to deposit TiO_2 NPs, thus proving the success of the method as a low-cost and versatile way of performing homogenous depositions even on complex surfaces such as NiTi alloys; the quality of the deposition was controlled with an adequate voltage, a precise time, and an ideal charging agent. With regard to genotoxicity and cytotoxicity, controversial results were still found, in agreement with other authors of the related literature; for example, our results in the comet assays suggest that there is no genotoxicity in any of the experimental groups under the conditions conducted. Nevertheless, in the cytotoxic findings, cytotoxic potential in the TiO_2 NPs was found, representing progressive damage even after the cessation of exposition and in some cases it was the G3 cellular necrosis. At the end, the use of NiTi arches coated with TiO_2 is not recommended to be placed in the mouth until more experimental research is done about friction resistance and degradation in the oral environment, as well as testing of TiO_2 NPs with long term exposition *in vivo*.

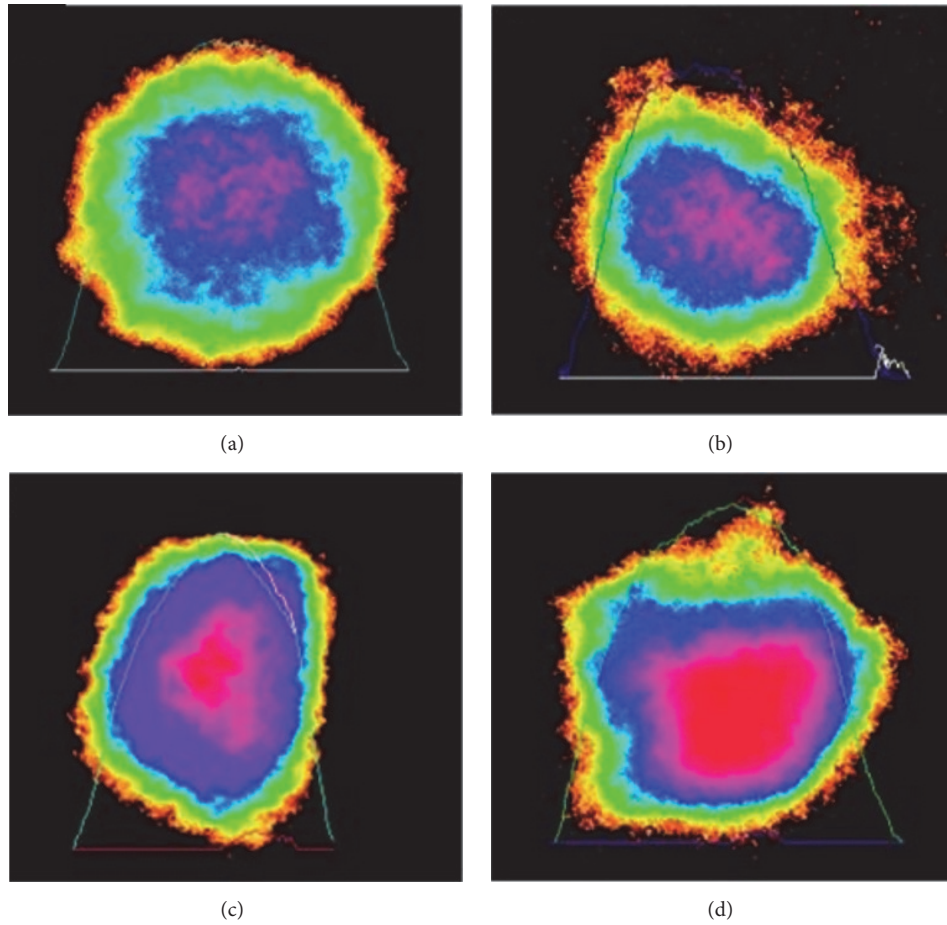


FIGURE 5: Analysis of the cells with the CometScoreTM program for DNA measurement at the comet head, where GC, G1, G2, and G3 ((a), (b), (c), and (d)) showed no significant migration ($P > 0.05$).

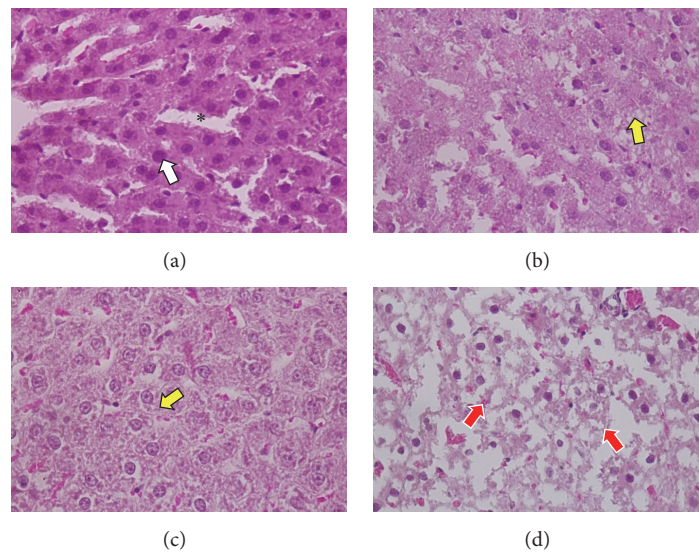


FIGURE 6: Microphotograph of liver dyed with H&E at 40x. (a) Control group, showing sinusoids (*) and hepatocyte cords (white arrow) with nucleus and cytoplasm of typical morphological characteristics. (b) In rats of group 1, few vacuoles in the hepatocytes cytoplasm are observed (yellow arrow). (c) In group 2, abundant intracytoplasmic vacuoles are observed (yellow arrow). (d) In group 3, tissue necrosis areas with hepatocytes destruction are observed (red arrow).

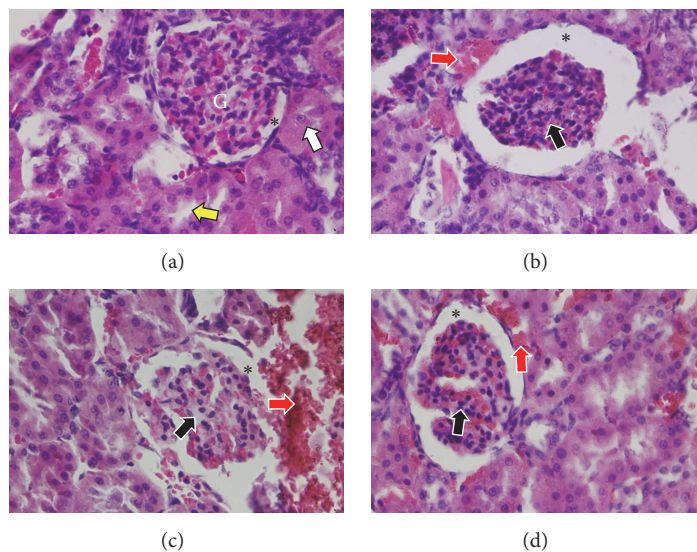


FIGURE 7: Microphotomicrograph of kidney dyed with H&E at 40x. (a) Control group with normal histopathological characteristics, glomerulus (G), urinary space (*), proximal convoluted tubule (white arrow), and distal tubules (yellow arrow) are observed. In 1, 2, and 3 experimental groups (microphotographs b, c, and d, resp.) glomerular retraction (black arrows), an increase of urinary space (*), and mild vascular congestion (red arrow) are observed.

Conflicts of Interest

The authors declare that they have no conflicts of interest.

Acknowledgments

Roberto Beltrán del Río-Parra and José Alfredo Facio Umaña were supported by CONACyT scholarships (#285474 and #285473, resp.). The authors wish to acknowledge Programa Integral de Fortalecimiento Institucional (PIFI, Secretaría de Educación Pública, México) for partial support for Roberto Beltrán del Río-Parra and José Alfredo Facio Umaña for the stay at the Laboratory of the Dental Materials Department of the Faculty of Dentistry of Niigata University (Niigata, Japan). They acknowledge Coordinación General de Estudios de Posgrado e Investigación de Universidad Autónoma de Coahuila and Consejo Estatal de Ciencia y Tecnología del Estado de Coahuila (Grant no. COAH-2016-C11-A02) for partial support of the study.

References

- [1] W. A. Brantley, "Orthodontic materials," *Scientific and Clinical Aspects*, pp. 78–100, 2000.
- [2] C. Ábalos, "Adhesión bacteriana a biomateriales," *Avances en Odontostomatología*, vol. 21, no. 1, pp. 347–353, 2005.
- [3] T. P. Chaturvedi, *Corrosion behaviour of orthodontic alloys-a review [PhD Thesis]*, Banaras Hindu University Varanasi, 2008.
- [4] S.-Q. Gong, J. Epasinghe, F. A. Rueggeberg et al., "An ORMOSIL-containing orthodontic acrylic resin with concomitant improvements in antimicrobial and fracture toughness properties," *PLoS ONE*, vol. 7, no. 8, Article ID e42355, 2012.
- [5] M. Iijima, M. Hashimoto, S. Nakagaki et al., "Bracket bond strength and cariostatic potential of an experimental resin adhesive system containing Portland cement," *The Angle Orthodontist*, vol. 82, no. 5, pp. 900–906, 2012.
- [6] M. L. Brown, H. B. Davis, E. Tufekci, J. J. Crowe, D. A. Covell, and J. C. Mitchell, "Ion release from a novel orthodontic resin bonding agent for the reduction and/or prevention of white spot lesions An in vitro study," *The Angle Orthodontist*, vol. 81, no. 6, pp. 1014–1020, 2011.
- [7] C. Nagelreiter, H. Kotisch, T. Heuser, and C. Valenta, "Size analysis of nanoparticles extracted from W/O emulsions," *International Journal of Pharmaceutics*, vol. 488, no. 1-2, pp. 29–32, 2015.
- [8] F. Ahrari, N. Eslami, O. Rajabi, K. Ghazvini, and S. Barati, "The antimicrobial sensitivity of *Streptococcus mutans* and *Streptococcus sanguis* to colloidal solutions of different nanoparticles applied as mouthwashes," *Dental Research Journal*, vol. 12, no. 1, pp. 44–49, 2015.
- [9] A. Sodagar, M. S. A. Akhouni, A. Bahador et al., "Effect of TiO₂ nanoparticles incorporation on antibacterial properties and shear bond strength of dental composite used in orthodontics," *Dental Press Journal of Orthodontics*, vol. 22, no. 5, pp. 67–74, 2017.
- [10] Y. Xing, X. Li, L. Zhang et al., "Effect of TiO₂ nanoparticles on the antibacterial and physical properties of polyethylene-based film," *Progress in Organic Coatings*, vol. 73, no. 2-3, pp. 219–224, 2012.
- [11] Z. Fei Yin, L. Wu, H. Gui Yang, and Y. Hua Su, "Recent progress in biomedical applications of titanium dioxide," *Physical Chemistry Chemical Physics*, vol. 15, no. 14, pp. 4844–4858, 2013.
- [12] P.-I. González-Luna, G.-A. Martínez-Castanon, N.-V. Zavala-Alonso et al., "Bactericide effect of silver nanoparticles as a final irrigation agent in endodontics on *enterococcus faecalis*:

- an ex vivo study," *Journal of Nanomaterials*, vol. 2016, Article ID 7597295, 7 pages, 2016.
- [13] M. Hamzeh and G. I. Sunahara, "In vitro cytotoxicity and genotoxicity studies of titanium dioxide (TiO₂) nanoparticles in Chinese hamster lung fibroblast cells," *Toxicology in Vitro*, vol. 27, no. 2, pp. 864–873, 2013.
- [14] H. Shi, R. Magaye, V. Castranova, and J. Zhao, "Titanium dioxide nanoparticles: a review of current toxicological data," *Particle and Fibre Toxicology*, vol. 10, no. 1, article 15, 2013.
- [15] K. Bhattacharya, M. Davoren, J. Boertz, R. P. F. Schins, E. Hoffmann, and E. Dopp, "Titanium dioxide nanoparticles induce oxidative stress and DNA-adduct formation but not DNA-breakage in human lung cells," *Particle and Fibre Toxicology*, vol. 6, article 17, 2009.
- [16] G. C. M. Falck, H. K. Lindberg, S. Suhonen et al., "Genotoxic effects of nanosized and fine TiO₂," *Human & Experimental Toxicology*, vol. 28, no. 6-7, pp. 339–352, 2009.
- [17] J. R. Gurr, A. S. S. Wang, C. H. Chen, and K. Y. Jan, "Ultrafine titanium dioxide particles in the absence of photoactivation can induce oxidative damage to human bronchial epithelial cells," *Toxicology*, vol. 213, no. 1-2, pp. 66–73, 2005.
- [18] G. Oberdörster, J. Ferin, G. Finkelstein, P. Wade, and N. Corson, "Increased pulmonary toxicity of ultrafine particles? II. Lung lavage studies," *Journal of Aerosol Science*, vol. 21, no. 3, pp. 384–387, 1990.
- [19] G. Oberdörster, J. Ferin, R. Gelein, S. C. Soderholm, and J. Finkelstein, "Role of the alveolar macrophage in lung injury: Studies with ultrafine particles," *Environmental Health Perspectives*, vol. 97, pp. 193–199, 1992.
- [20] A. R. Boccaccini, S. Keim, R. Ma, Y. Li, and I. Zhitomirsky, "Electrophoretic deposition of biomaterials," *Journal of the Royal Society Interface*, vol. 7, no. 5, pp. S581–S613, 2010.
- [21] R. Kawakami, K. Ito, Y. Sato, Y. Mori, M. Adachi, and S. Yoshikado, "Preparation and evaluation of TiO₂ nanoparticle thin films using electrophoresis deposition method," *IOP Conference Series Materials Science and Engineering*, vol. 18, no. 6, p. 62011, 2011.
- [22] E. Paoli, G. Cappelletti, and L. Falciola, "Electrochemistry as a tool for nano-TiO₂ deposition and for photoremediation pollutant monitoring," *Electrochemistry Communications*, vol. 12, no. 8, pp. 1013–1016, 2010.
- [23] L. E. Vieira, K. C. Kleinjohann, J. B. R. Neto, A. N. Klein, D. Hotza, and R. Moreno, "Dip coating of a carbon steel sheet with Ni reinforced TiO₂ nanoparticles," *Materials Research*, vol. 19, no. 3, pp. 648–653, 2016.
- [24] Y. Sun and I. Zhitomirsky, "Electrophoretic deposition of titanium dioxide using organic acids as charging additives," *Materials Letters*, vol. 73, pp. 190–193, 2012.
- [25] N. P. Singh, M. T. McCoy, R. R. Tice, and E. L. Schneider, "A simple technique for quantitation of low levels of DNA damage in individual cells," *Experimental Cell Research*, vol. 175, no. 1, pp. 184–191, 1988.
- [26] L. Besra and M. Liu, "A review on fundamentals and applications of electrophoretic deposition (EPD)," *Progress in Materials Science*, vol. 52, no. 1, pp. 1–61, 2007.
- [27] O. O. Van Der Biest and L. J. Vandeperre, "Electrophoretic deposition of materials," *Annual Review of Materials Research*, vol. 29, pp. 327–352, 1999.
- [28] T. Uchikoshi, K. Ozawa, B. D. Hatton, and Y. Sakka, "Dense, bubble-free ceramic deposits from aqueous suspensions by electrophoretic deposition," *Journal of Materials Research*, vol. 16, no. 2, pp. 321–324, 2001.
- [29] K. T. Lau and C. C. Sorrell, "Effect of charging agents on electrophoretic deposition of coarse titanium particles," *Journal of The Australian Ceramic Society*, vol. 49, no. 2, pp. 108–115, 2013.
- [30] A. A. Sadeghi, T. Ebadzadeh, B. Raissi, S. Ghashghaie, and S. M. A. Fatemina, "Application of the multi-step EPD technique to fabricate thick TiO₂ layers: effect of organic medium viscosity on the layer microstructure," *The Journal of Physical Chemistry B*, vol. 117, no. 6, pp. 1731–1737, 2013.
- [31] K. Wu, Y. Wang, and I. Zhitomirsky, "Electrophoretic deposition of TiO₂ and composite TiO₂-MnO₂ films using benzoic acid and phenolic molecules as charging additives," *Journal of Colloid and Interface Science*, vol. 352, no. 2, pp. 371–378, 2010.
- [32] A. R. Boccaccini, P. Karapappas, J. M. Marijuan, and C. Kaya, "TiO₂ coatings on silicon carbide and carbon fibre substrates by electrophoretic deposition," *Journal of Materials Science*, vol. 39, no. 3, pp. 851–859, 2004.
- [33] K. Hasegawa, M. Tatsumisago, and T. Minami, "Preparation of thick silica films by the electrophoretic sol-gel deposition using a cationic polymer surfactant," *Journal of the Ceramic Society of Japan*, vol. 105, no. 7, pp. 569–572, 1997.
- [34] S. E. Khier, W. A. Brantley, and R. A. Fournelle, "Bending properties of superelastic and nonsuperelastic nickel-titanium orthodontic wires," *American Journal of Orthodontics and Dentofacial Orthopedics*, vol. 99, no. 4, pp. 310–318, 1991.
- [35] T. Yoneyama, H. Doi, E. Kobayashi, and H. Hamanaka, "Superelastic property of Ti-Ni alloy for use in dentistry," *Frontiers of Medical and Biological Engineering*, vol. 10, no. 2, pp. 97–103, 2000.
- [36] J. Berger and T. Waram, "Force levels of nickel titanium initial archwires," *Journal of Clinical Orthodontics*, vol. 41, no. 5, pp. 286–292, 2007.
- [37] N. Serpone, A. Salinaro, S. Horikoshi, and H. Hidaka, "Beneficial effects of photo-inactive titanium dioxide specimens on plasmid DNA, human cells and yeast cells exposed to UVA/UVB simulated sunlight," *Journal of Photochemistry and Photobiology A: Chemistry*, vol. 179, no. 1-2, pp. 200–212, 2006.
- [38] R. C. Gopalan, I. F. Osman, A. Amani, M. De Matas, and D. Anderson, "The effect of zinc oxide and titanium dioxide nanoparticles in the Comet assay with UVA photoactivation of human sperm and lymphocytes," *Nanotoxicology*, vol. 3, no. 1, pp. 33–39, 2009.
- [39] W. F. Vevers and A. N. Jha, "Genotoxic and cytotoxic potential of titanium dioxide (TiO₂) nanoparticles on fish cells in vitro," *Ecotoxicology*, vol. 17, no. 5, pp. 410–420, 2008.
- [40] R. S. Woodruff, Y. Li, J. Yan et al., "Genotoxicity evaluation of titanium dioxide nanoparticles using the Ames test and Comet assay," *Journal of Applied Toxicology*, vol. 32, no. 11, pp. 934–943, 2012.
- [41] M. A. Smith, R. Michael, R. G. Aravindan et al., "Anatase titanium dioxide nanoparticles in mice: Evidence for induced structural and functional sperm defects after short-, but not long-, term exposure," *Asian Journal of Andrology*, vol. 17, no. 2, pp. 261–268, 2015.
- [42] T. H. Umbreit, S. Francke-Carroll, J. L. Weaver et al., "Tissue distribution and histopathological effects of titanium dioxide nanoparticles after intravenous or subcutaneous injection in mice," *Journal of Applied Toxicology*, vol. 32, no. 5, pp. 350–357, 2012.
- [43] J. Chen, X. Dong, J. Zhao, and G. Tang, "In vivo acute toxicity of titanium dioxide nanoparticles to mice after intraperitoneal

injection,” *Journal of Applied Toxicology*, vol. 29, no. 4, pp. 330–337, 2009.

- [44] A. M. Schrand, M. F. Rahman, S. M. Hussain, J. J. Schlager, D. A. Smith, and A. F. Syed, “Metal-based nanoparticles and their toxicity assessment,” *Wiley Interdisciplinary Reviews: Nanomedicine and Nanobiotechnology*, vol. 2, no. 5, pp. 544–568, 2010.
- [45] S. Boland, S. Hussain, and A. Baeza-Squiban, “Carbon black and titanium dioxide nanoparticles induce distinct molecular mechanisms of toxicity,” *Wiley Interdisciplinary Reviews: Nanomedicine and Nanobiotechnology*, vol. 6, no. 6, pp. 641–652, 2014.

Review Article

Exosomes: A Paradigm in Drug Development against Cancer and Infectious Diseases

Mohammad Oves ¹, Huda A. Qari,^{1,2} Nadeen M. Felemban,¹
Aftab Aslam Parwaz Khan ³, Mohd Rehan,⁴ Shams Tabrez,⁴ Faheem Ahmed,⁵
Ashanul Haque,⁶ Mohd Shahnawaz Khan,⁷ Javed M. Khan,⁸ Fohad M. Husain ⁸,
Afzal Hussain,⁹ Mohiuddin Khan Warsi,¹⁰ and Iqbal I. M. Ismail^{1,11}

¹ Center of Excellence in Environmental Studies, King Abdulaziz University, P.O. Box 21589, Jeddah, Saudi Arabia

² Department of Biological Science, King Abdulaziz University, P.O. Box 21589, Jeddah, Saudi Arabia

³ Center of Excellence for Advanced Materials Research and Chemistry Department, King Abdulaziz University, P.O. Box 21589, Jeddah, Saudi Arabia

⁴ King Fahd Medical Research Center, King Abdulaziz University, Jeddah 21589, Saudi Arabia

⁵ College of Science & General Studies, Alfaisal University, Riyadh, Saudi Arabia

⁶ Department of Chemistry, College of Science, Sultan Qaboos University, P.O. Box 36, 123 Muscat, Oman

⁷ Protein Research Chair, Department of Biochemistry, College of Sciences, King Saud University, Riyadh, Saudi Arabia

⁸ Department of Food Science and Nutrition, Faculty of Food and Agricultural Sciences, King Saud University, P.O. Box 2460, Riyadh 11451, Saudi Arabia

⁹ Department of Pharmacognosy, King Saud University, P.O. Box 2460, Riyadh 11451, Saudi Arabia

¹⁰ Department of Biochemistry, Faculty of Science, University of Jeddah, Jeddah, Saudi Arabia

¹¹ Department of Chemistry, Faculty of Science, King Abdulaziz University, Jeddah, Saudi Arabia

Correspondence should be addressed to Mohammad Oves; owais.micro@gmail.com

Received 27 July 2017; Revised 14 November 2017; Accepted 25 December 2017; Published 26 April 2018

Academic Editor: Stefano Bellucci

Copyright © 2018 Mohammad Oves et al. This is an open access article distributed under the Creative Commons Attribution License, which permits unrestricted use, distribution, and reproduction in any medium, provided the original work is properly cited.

Extracellular vesicles are small single lipid membrane entity secreted by eukaryotic and prokaryotic cells and play an important role in intercellular signaling and nutrient transport. The last few decades have witnessed a plethora of research on these vesicles owing to their ability to answer many hidden facts at the supramolecular level. These extracellular vesicles have attracted the researchers because they act as shuttle agents to transfer biomolecules/drugs between cells. Recently, studies have shown the application of exosomes in tumor therapy and infectious disease control. The present review article shows the importance of exosomes in cancer biology and infectious disease diagnoses and therapy and provides comprehensive account of exosomes biogenesis, extraction, molecular profiling, and application in drug delivery.

1. Introduction

Extracellular vesicles are cell membrane-derived small entity. In general, these are ubiquitously found in all organisms and scattered in all types of biofluids. These are multifunctional units that act as a carrier of cellular communication as well as help in removing cellular garbage. Extracellular vesicle cargo protein, lipid, nucleic acids, or RNA from mother cells to

distant tissue cells through the support of biofluids and transfer the information [1]. Earlier, extracellular vesicles were considered as an insignificant bioentity generated by the cell during its lifetime. However, in the last few decades, extracellular vesicles have generated significant interest among the scientific community as they have been found to be associated with many diseases. Recent research works demonstrate that the extracellular vesicles have potential to act as naturally

occurring drug-delivery vehicles and can find application in several diseases including cancers. This is due to their innate biocompatibility, unique capability for targeted delivery, and ability to reach remotely located recipient cells. Number of the findings demonstrated that membrane-derived vesicles are important for diagnostic and therapeutic purposes for different diseases, including cancer, infectious diseases, cardiovascular diseases, neurodegenerative diseases, and pregnancy [2]. Its application depends on the biogenesis and size of the entities; it could be classified into exosomes, microvesicles, apoptotic bodies, and oncosomes (Figure 1). Most of the exosomes are small size extracellular vesicles, ranging between 40 and 120 nm and are created by the fusion of an intracellular multivesicular body with the cell membrane. However, less than 40 nm vesicles were also detected by subdiffraction imaging and fluorescent probe during a real-time study of exosomes trafficking in living cells [3, 4]. Microvesicles are generated by normal cell and its size ranges from 100 to 1000 nm and apoptotic bodies' sizes up to 5 μm are generated by apoptotic cell. Similarly, oncosomes are the largest vesicles, their size ranges from 1 to 5 μm , and they are secreted by cancer cells [1, 5].

Among all above-mentioned vesicles, exosomes have attracted more interest among the researchers, owing to their intriguing capabilities like mediating cell-to-cell communication. Intercellular communication is an important process to maintain homeostasis in multicellular systems. The dysregulation of communication pathways have been associated with the cancer development and progression [48]. Therefore, the development of novel anticancer treatments will strongly depend on improving our understanding of the cellular interactions between cancer cells and other cells. Cellular communication takes place between cells through gap junctions, adhesion molecules, and nanotubes; also, it can be via soluble communication signals like growth factors, cytokines, tumor, and non-tumor-derived hormones. To date, several researches have showed a positive correlation between carcinogenesis/metastasis/drug resistance/bacterial infection and the concentration of exosomes [49, 50]. Logozzi et al. have also quantified the exosomes of plasma of melanoma patient and healthy donors by housekeeping proteins and caveolin-1 marker and found significant higher exosome in plasma of melanoma patient and concluded that exosomes have direct relation in malignant progression [51]. Recently, VanDeun et al. have developed a knowledge base EV-TRACK for enhancement of transparency and reproducibility of vesicles research road map [52]. Based on these notions, we herein present a brief review on the importance of exosomes in drug delivery in both cancerous and noncancerous ailments. Additionally, we have also discussed the basic function of exosomes in the human body, molecular profiling, and its characteristics.

2. Exosomes Uniqueness and Natural Existence

Initially, researchers observed human plasma fraction has coagulant properties as "platelet dust," and, later on, the fraction was characterized as microparticles [53]. Trams et al. made the first description of exosomes in 1981 [54]. Johnstone

and coauthors have also termed the extracellular vesicles as exosomes. They had isolated exosomes from sheep reticulocytes during reticulocytes maturation into erythrocytes [55]. Whenever cells enter apoptosis, irregular shaped apoptotic vesicles are generated with size 50–5000 nm [56]. These vesicles may contain histones, DNA, and RNA molecules and are immediately cleared by the immune system (macrophages) in response to their apoptotic signaling [57]. In contrast, microvesicles originate by budding and fission of the cellular plasma membrane into extracellular space. These vesicles are more homogeneously shaped, smaller than the apoptotic bodies in size ranging from 50 to 1000 nm and rich in specific proteins and lipids [58]. The major population of extracellular vesicles is identified as exosome by size less than 100 nm in diameter. Most of the mammalian cells like neurons and immune cells secrete exosomes and cancer cells also secrete greater amounts of exosomes. Interestingly, Gram-negative bacteria also produce outer membrane vesicles during normal growth, which contain bioactive proteins and it has diverse biological functions. The bacterial outer membrane vesicles are small ball-shaped structures with a size range from 20 to 250 nm in diameter. Mayrand and Grenier have described the formation, growth conditions, isolation, composition, and biological activities of bacterial outer membrane vesicles [59]. Similarly, Kulp and Kuehn investigated the natural sources, characteristics, biological functions, and biogenesis of vesicles from bacteria and revealed the vesicle secretion through the distal effect of membrane molecules during environmental interaction [60]. Moreover, it has been reported that bacteria can also secrete outer membrane vesicles during their normal activities. Gram-negative bacteria that are able to secrete outer membrane vesicles during normal growth include *E. coli*, *N. meningitis*, *Sh. flexneri*, *P. aeruginosa*, and *H. pylori* [61–64]. In addition, it has been reported that fungi and eukaryotic parasite can also secrete extracellular vesicles [65].

Exosomes are membrane-derived vesicles actively secreted by mammalian cell particularly immune cells, such as macrophages [66], dendritic cells, T cells [67, 68], and B cells [69]. Exosomes are also secreted by mesenchymal stem cells [70], epithelial [71] and endothelial cells [72], and cancer cells [42]. Li et al. have reported the secretion of exosomes from intestinal epithelial cells, fibroblasts, mastocytes, antigen presenting cells, platelets, hepatocytes, and lymphocyte [73]. In addition, exosomes have also been identified in different body fluids, including human saliva, serum, breast milk [74], CSF [75], urine [76], and semen [77].

3. Structure and Contents

In 2014, the International Society for Extracellular Vesicles (ISEV) has reported the presence of exosomes-associated surface markers and the absence of nonexosomal proteins for the characterization of exosomes. The exosomes-associated surface markers include Alix, TSG101, tetraspanins (CD9, CD63, and CD81), flotillin 1, cell adhesion molecules (CAM), and integrins [79]. Exosomes consist of a lipid bilayer membrane and are characterized by a size of 50–100 nm in diameter, and they have "cup" or "dish" shaped morphology when

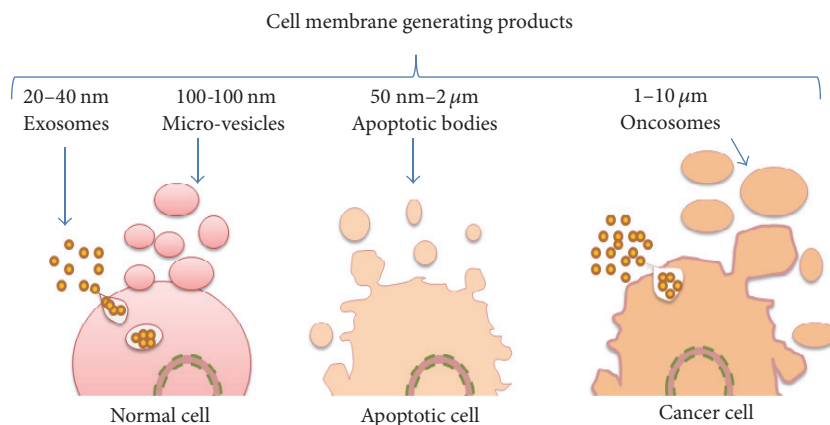


FIGURE 1: Different types of extracellular vesicles (EVs) produced by normal and diseased cells.

analyzed by electron microscopy and are enriched with certain protein markers such as tetraspanins [42]. Moreover, its presence is also determined by density gradient, it has density $\sim 1.13\text{--}1.19\text{ g/ml}$ and membrane rich in lipids like ceramide, cholesterol, and sphingolipids [80]. ExoCarta is an exosomes database, which was created in 2008 to collect and classify the identified exosomal proteins and RNA molecules. The resource is web-based (<http://www.exocarta.org>) and freely available to the scientific community [81]. To this date, they have identified 9769 proteins, 3408 mRNAs, and 2838 miRNAs by independent examinations in exosomes from different species and tissues. In addition, the membrane structure of Gram-negative envelope consists of two membranous structures: the inner one (IM) and the outer membrane (OM) and these two membranes are separated by the periplasm. The outer layer of the OM is composed of lipopolysaccharide (LPS), whereas the inner layer and both layers of the IM are composed of phospholipids. The periplasm is a gel-like layer that contains a thin layer of peptidoglycan (4 nm thick) [60]. Therefore, the secreted vesicles are composed of lipopolysaccharide, periplasm, and phospholipids [82].

4. Biogenesis, Release, and Uptake

Membrane vesicles play diverse roles in cellular communications in both prokaryotic and eukaryotic cells, while Gram-negative bacteria secrete outer membrane vesicles and eukaryotic cells secrete microvesicles for cellular contact. Mechanisms of bacterial vesicle biogenesis and the pathological roles are still not defined clearly. However, vesicles secreted by different types of cells may have several similarities in the biogenesis and functions in different biological systems. Zhou et al. [83] have suggested that the biogenesis of Gram-negative bacteria derived vesicles could be because of cell wall turnover during growth, which causes a turgor on the outer membrane, eventually causing the outer membrane to bulge and then bleb. It is excised and removed from the peptidoglycan layer of the cell wall. Independent experimental studies also demonstrated that membrane vesicles are generated as a result of cell wall turnover in Gram-negative bacteria [83, 84]. However, Wensink and Witholt

[85] have described a hypothesis for the biogenesis of Gram-negative bacteria derived vesicles. They suggested that the blebbing of outer membrane might occur in response to a high rate outer membrane synthesis in comparison to peptidoglycan.

On the other hand, the process of exosome biogenesis in human samples has been clearly defined in several studies, which includes four sequential stages: (1) initiation, (2) endocytosis, (3) multivesicular bodies, and (4) exosomes secretion [86]. Previous studies have suggested that exosomes are derived from the multivesicular bodies sorting pathway. Exosomes originate by inward budding into large multivesicular bodies in the cell cytoplasm, and then these bodies fuse with the plasma membrane leading to exosome secretion into the extracellular space. Moreover, either the endosomal-sorting complex is required for transport signaling or the sphingolipid ceramide pathway [87] regulates this process. In response to vesicular accumulation, the multivesicular bodies will be either sorted to be degraded by lysosome or released into the extracellular space for exosome secretion through the process of exocytosis. The exosomal cargo, including proteins, lipids, and RNA/DNA molecules, is all packed into the exosomes during this process; the exosomal contents may vary according to the parent cell type. Previous studies have reported that a number of proteins play a role in regulating exosomes secretion pathway. Ostrowski et al. have shown that Rab GTPase machinery can regulate exosome secretion, in which Rab27a and Rab27b proteins can affect the size and localization of multivesicular bodies [88]. Other studies have demonstrated that the exosome secretion can be affected by different factors. For instance, the secretion will be increased in response to intracellular Ca^{+2} accumulation [89]. Another factor that would affect the exosome release is the cellular pH. When the pH of the microenvironment is low, exosomes secretion and uptake by target cells increase as well. In a recent study, it was observed that low pH conditions have significant effect on the exosomes expression of the cancerous cells. When prostate cancer cell lines were cultured at both low pH and 7.4 pH, then exosomes were more predominant at low pH cultured condition. Similarly, tumor-released exosomes are able to transfer their content to target cells by

membrane-to-membrane fusion and this is much favored by microenvironmental conditions such as low pH. The delivery of exosomal cargo for uptake of their target cells can occur by one of the following ways: (1) receptor-ligand interaction; (2) direct fusion of exosomes with the plasma membrane of the recipient cell, which leads to releasing the exosomal content into the cellular cytoplasm; (3) endocytosis by phagocytosis.

5. Extraction of Exosomes

The abnormality in proteins/enzymes or nucleic acid function is an indication of cellular dysregulation or diseases. Identification of such dysfunctions could significantly change the outcome and condition of a patient. The biophysical characterization/screening of exosomes in biofluids are an emerging area of research, as they contain information from the mother cells. It has been demonstrated that the concentration of exosomes is directly related to the health condition of a person [90]. In such situations, the development of novel methods for isolation, molecular profiling, and concentration determination of exosomes would not only enhance the knowledge at supramolecular level but also help in delineating many hidden questions related to deadly diseases like cancer. For this purpose, several classical and modern methods for extraction, isolation, and characterization from different biomatrices are available. It must be noted that exosomes isolation methods to date only enable enrichment but not distinct separation of these extracellular vesicles subpopulations [1]. Table 1 depicts some general approaches and mechanisms used for the isolation of exosomes [6–13].

Recently, ultracentrifugation was used for exosomes isolation in combination with the sucrose gradient and immune-dependent isolation such as Magnetic Activated Cell Sorting (MACS) [91]. Deun et al. have suggested a comparative evaluation of exosome isolation protocols: (i) OptiPrep™ density gradient centrifugation which outperforms ultracentrifugation and (ii) ExoQuick and total exosomes isolation and precipitation in terms of purity, quantity, and purity and their impact on downstream omics approach for biomarker development [91].

Differential ultracentrifugation involves applying different levels of centrifugal force on a solution containing exosomes such as biological fluids or conditioned cell culture media [92]. Starting from low speed centrifugation, which is necessary initially to remove cells and large cellular debris, then, the resulting supernatant is centrifuged at 10,000–20,000 ×g in order to remove large debris and intact organelles. Lastly, the supernatant is again subjected to a high-speed centrifugation (100,000–150,000 ×g) in order to achieve a pellet exosomes. Therefore, this method precipitates not only the exosomes but also other membrane vesicles, proteins, and/or protein-RNA aggregates. In general, the density of exosomes is different from the contaminants; it can be separated by using sucrose density gradient with centrifugation. This technology is more efficient than ultracentrifugation while it is requiring more centrifugation time up to 62 to 90 h [52]. In addition to this, immune-affinity chromatography and size exclusion chromatography are also normally used for the extraction of exosomes. In the antibody-dependent

method, it is covalently attached to exosomal surface markers like TSG 101 or tetraspanins and nontarget particles remain unbound. When the unbounded particles are removed then washing the stationary phase with a low pH buffer may collect the bounded particles. This process is efficient and provides pure exosomes compared to other size/density-dependent methods. Likewise, Kalra et al. have confirmed OptiPrep density gradient method was more efficient to isolate exosomes without plasma proteins [94].

Size exclusion chromatography contains different size components which separate solutions according to their size. In addition, the SEC is using a gravity flow for separation, to maintain the vesicle structure, integrity, and biological activity of exosomes [12]. This technology has high sensitivity and excellent reproducibility, because it is using gravity flow for separation which makes it time-consuming if it could be combined with ultracentrifugation; then high isolation rate can be achieved in less time [94]. Moreover, commercial kits are also available for exosomal extraction process. Besides these two techniques, polymer precipitation and microfluidic technologies, are also effective methods to be used for exosomal isolation as an alternative to ultracentrifugation; these methods were described in detail by Batrakova et al. [93]. ExoQuick-TC kit is the most common commercial polymer precipitation-based method for exosomes extraction. This method is employed to isolate viruses and other macromolecules by using polyethylene glycol (PEG). On the other hand, microfluidic-based techniques use smaller volumes of starting solution and provide more pure exosomal isolate within a short time [95]. Moreover, these technologies have been used for diagnostic purposes because of their low yield and high sensitivity. This method depended on one of the following techniques: (a) immunoaffinity, (b) sieving, and (c) trapping exosomes, which was described by Batrakova et al. [93].

6. Molecular Profiling of Exosomes

Molecular profiling of exosomes obtained from different sources is an important step. Exosomes are characterized according to their biochemical properties (size, protein, and lipid content) using different methods [96] like Western Blotting, transmission electron microscope (TEM), nanoparticle tracking analysis (NTA) [9], dynamic light scattering (DLS), mass spectrometry (MS), flow cytometry [95, 96], tunable elastomeric pore sensing, [97] and microfluidics [98] but these are not limited. The detection and profiling are often hindered by the requirements of high purity and large sample amount. To circumvent these issues, several new, sensitive, and selective methodologies based on surface plasmon resonance (SPR), fluorescence fluctuation spectroscopy (FFS), and so forth have been applied in several reports in Table 2 [14–19]. Among these, SPR is the most popular label-free, real-time sensing technique [99]. Vogel and coworkers have developed a label-free SPR based methodology for the detection of exosomes derived from breast cancer cell lines (MCF-7, BT-474, and MDA-MB-231) [15]. They reported immunosensor surface has the ability to identify various exosomes as well as exosomal biomarkers [98, 100]. The molecular profiling results of exosomes have indicated the selective and

TABLE 1: Exosomes isolation methods and mechanisms with specificity and demerits.

| Methods | Steps | Mechanism | Specificity | Demerit | Ref. |
|-------------------------------|---|---|---|---|----------|
| Differential centrifugation | (i) 300 ×g (10 min) (ii) 1000 ×g to 20000 ×g (30 min) (iii) 100,000 ×g (60 min) | Based on centrifugal force | Common method to isolate exosomes from biological fluids | Yield lower when sample is viscous | [6] |
| Density gradient | (i) 30% sucrose gradient (ii) Differential centrifugation | Based on centrifugal force and density gradient | Separate low-density exosomes from high density contaminants and vesicles | Sensitivity high with centrifugation time | [7] |
| Size exclusion chromatography | (i) Sample applied on column packed with specific designed porous beads that allow elation only exosomes, without centrifugal force | Based on porosity of materials | Centrifugal force sensitive vesicles isolate this method and specific beads used for specific size. multiple biological samples can run together in this method | Long time taking procedure | [8] |
| Filtration | (i) Exosomes separate from the high molecular weight proteins and fatty acids | Based on membrane materials and porosity | Easily separate the soluble molecules and small particles from exosomes | Exosomes attached with membranes and lost the yield and original size | [9] |
| Polymer-based precipitation | (i) Biological fluid mixing with polymer (ii) Incubation till precipitation (iii) Centrifugation at low speed. (vi) Resuspend in PBS | Based on polymer materials and precipitation | The advantages of precipitation include the mild effect on isolated exosomes and usage of neutral pH | Polymer-based precipitation and co-isolation of contaminants, like lipoproteins. In the presence of polymer material, not compatible with downstream analysis | [10, 11] |
| Immunological separation | (i) Magnetic beads bound to the specific antibodies Example: ELISA-based separation method | Based on antibody receptor interaction | Methods for characterization and quantification of protein involve in selective subtypes of exosomes | Method is not applicable for large volumes | [7] |
| Isolation by sieving | (i) Sample sieving via a membrane (ii) Perform filtration with pressure (iii) electrophoresis | Based on sieving size and pressure | Short separation time with high purity of exosomes | Low recovery rate | [12] |
| Cell sorting | (i) Sample incubation 4 h with magnetic beads (ii) centrifugation 100,000 ×g (60 min) | Based on centrifugal and magnetic force | Short separation time with high purity of exosomes | Expensive and hectic | [13] |

effective discrimination between the antigen generated by three different types of cell lines. In previous studies, the same research team has reported the molecular and dimensional profiling of exosomes by using the FFS method [100, 101]. Another SPR based method has been reported recently to determine the concentration of exosomes in solution [98]. Using surface functioned sensor with anti-CD63 antibodies, the authors detected exosomes selectively obtained from human mast cells. By this method, total mass (lipids, proteins, and nucleotides) could also be determined using a small

sample volume. Despite the fact that exosome deformation hindered the study, the authors reported high accuracy ($\pm 50\%$) in concentration determination. An easy, efficient, and novel label-free SPR imaging (SPRi) technique in combination with antibody microarrays was reported for the quantitative determination of exosomes in cell culture supernatant (CCS) [102]. The study also showed a positive association between exosome secretion and metastatic potential in hepatocellular carcinoma cells (highly metastatic cell line secreted more exosomes than poorly metastatic ones).

TABLE 2: Recent reported methods for molecular profiling of exosomes.

| Method | Source | Application | Explanations | Ref. |
|--|--------------------|--|--|------|
| Combined colloidal gold nanoplasmonics and SPR | Serum | Oncology | Detection at molar level, Showed presence of 4-fold exosomes in MM patients than normal | [14] |
| Microfluidic | Plasma | Cancer as well as non-cancerous diseases | Enhanced and minimal invasive detection, | [15] |
| SPR | Serum | Oncology | Quantification of the proportion of CREs within the bulk exosome population | [16] |
| NTA | Whole blood sample | Oncology | Enriched level of MDR-1, MDR-3, endophilin-A2, and PABP4 in resistance prostate cancer cells (DU145) | [17] |
| Metal Nanoparticle | Serum | Oncology | Microsome and exosome detection, detection of two surface markers on exosome | [18] |
| Dual-wavelength SPR | Synthetic | Drug development | Vesicles carrying marker CD63 link to not greater than 10% of the vesicles in sample. | [19] |

Zhu et al. developed a label-free nanoplasmonic exosome (nPlex) assay for quantitative analysis of exosomes [105]. The method, which was based on transmission mode SPR through functionalized nanohole arrays (Figure 2(a)), has the ability to detect proteins present on the surface as well as in the lysate of exosomes. They found that a large amount of exosomes with an average diameter of 100 nm was secreted by the ovarian carcinoma cell lines. The selective identification of ovarian carcinoma exosomes (detection of 12 potential exosomal markers within 30 mins) dictates the potential of the method for diagnostic purposes (Figure 2(b)).

Proteomic analyses have been used to identify and decode the proteins associated with outer membrane vesicles. Although bacterial outer membrane vesicles are more abundant and easier to obtain than human vesicles, only few proteomic profiling instances of native outer membrane vesicles derived from bacterial strains have been reported [78, 104–107]. Previous studies described the process of Sodium dodecyl sulphate-polyacrylamide gel electrophoresis (SDS-PAGE) of outer membranes and vesicle polypeptides to identify their protein profiles [108]. In addition, exosomal RNA and proteins were also identified using RT-PCR, nucleic acid sequencing, Western Blot, or ELISA [42]. Sambrook et al. have also described the conventional agarose electrophoresis in the presence of ethidium bromide in order to detect nucleic acids in samples of vesicles derived from bacterial strain [111].

7. Exosomes Role in Normal and Cancer Cells

A number of studies have demonstrated the tumor-derived exosomes, which serve as biologic messengers for immune suppression and other pro-cancer activities [64, 110, 111]. Cancer-derived exosomes play diverse roles in the tumorigenesis, tumor growth, angiogenesis, metastasis, and drug resistance [42]. During the process of tumorigenesis, normal cells are transformed into cancerous cells and subsequently secrete exosomes, which have the potential to transform the healthy cells to cancerous cells. As an example, neoplastic transformation of adipose-derived stem cells (ASCs) could be induced in response to prostate cancer cell-associated exosomes, which

deliver the oncogenic proteins and mRNA molecules to recipient cells and subsequently induce tumor formation [112]. Sometimes tumor-released exosomes, expressing a reporter-gene, travel through the blood of xenografts ending within the germ line that in turn expressed the exosomes-delivered gene, thus supporting the idea of a key role of extracellular vesicles in somato-to-germ-line transmission of nucleic acids. In addition, it has been widely reported that tumor-derived exosomes show promoting effect on tumor growth. During tumor formation, exosome containing cell survive because it has the ability to inhibit apoptosis and promote proliferation and metastasis [113]. Similarly, in human tumor cell line derived exosomes may induce tumor-like transformation of human mesenchymal stem cells, supporting a key role of exosomes in tumor metastasis [114]. Consequently, angiogenic factors are usually present in tumor-derived exosomes, which is necessary for angiogenesis and tumor proliferation [115]. Exosomes also contain factors required for metastasis, thus enhancing migration and invasiveness of cancerous cells [116–118]. Moreover, exosomes also play a role in the development of drug resistance via different mechanisms. For example, cancer cell-derived exosomes transmit multidrug resistance (MDR) associated proteins and miRNAs to recipient cells leading to the development of resistance [119]. Another mechanism by which exosomes induce resistance is an exosomal drug efflux, in which drugs can be affixed from the cancerous cells by exosomes [120]. During cancer therapy development of intrinsic resistance against drugs happens due to acidic microenvironment and chemo resistance impairment in drug delivery. In addition to these, several studies have shown the relationship between exosome and immune system function [121]. They suggested that exosomes can interact through signaling and the exosome comes from immune cells. While melanoma cell releases extracellular vesicles expressing FasL that efficiently induces Fas-mediated apoptosis in target T cells, suggesting the role of tumor exosomes in tumor immune escape. Extracellular vesicles released by human colon cancer cells express that both FasL and Trail are able to induce cell death of target T cells through the specific pathways and that exosomes expressing these

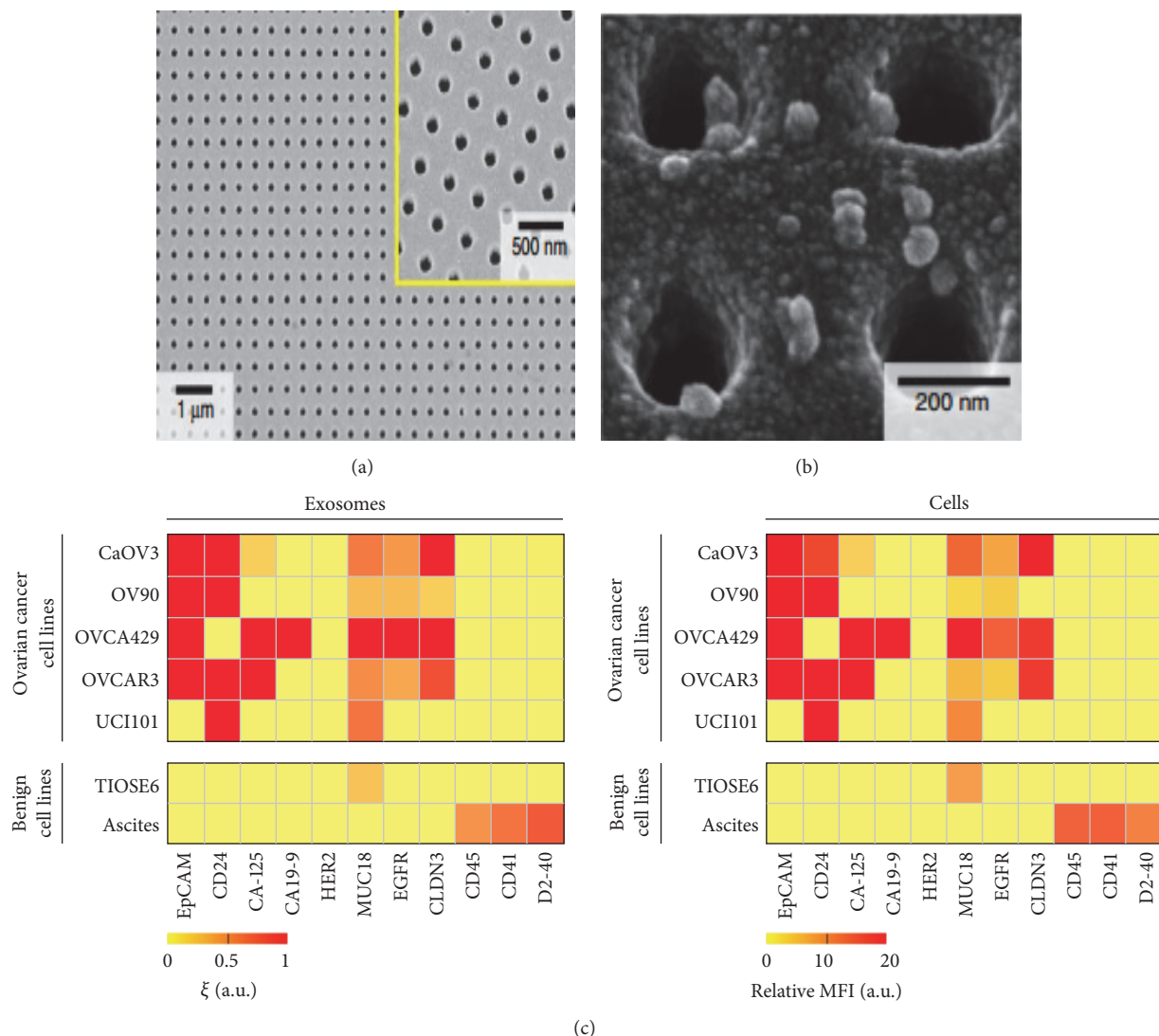


FIGURE 2: Scanning electron microscopy image of (a) nPLEX sensor with periodic nanoholes in the range from 200 to 450 nm in diameter, and here (2b) exosome captured by functionalized nPLEX. (2c) EpCAM, CD24, CA19-9, CLDN3, CA-125, MUC18, EGFR, and HER2, a list of putative ovarian cancer markers; CD41 and CD45 for immune host cell markers and D2-40 a mesothelial marker for exosomes profiled left in nPLEX sensor and their parental ovarian cell lines filled in right for flow cytometer, according to Im et al. [78].

two molecules are detectable in the plasma of colon cancer patients and entirely functional in inducing T cell death [122]. In mammalian cells, exosomes have pro- and anti-inflammatory properties depending on the type of cell origin [80]. For example, NK cells release exosomes expressing functional molecules associated with NK-cell function and the same exosomes are detectable in the plasma of healthy humans, suggesting a key role of NK-released exosomes in the control of our body homeostasis [114, 123]. However, similar findings have been reported with single cell eukaryotic-derived vesicles. Zhang et al. have demonstrated that exosomes are involved in cell-to-cell contact during immune responses for tumorigenesis, infectious diseases, allergies, and autoimmune diseases [42], for example, during myocardial infarctions in the presence of clusterin in exosomes obtained from pericardial fluids of patients [124]. Currently,

there are two main groups of exosomes that are involved in infectious biological: (1) single-celled eukaryotic exosomes and (2) exosomes derived from infected cells. The eukaryotic single-celled pathogens such as the pathogenic fungus *Cryptococcus neoformans* and the protozoan parasites *Leishmania major* and *donovani* [125] secrete exosomes, which may influence the host immune system. The second group is exosomes released by mammalian cells infected with pathogenic bacteria, prion protein, and viruses [126, 127]. Previous studies have reported that bacteria can secrete outer membrane vesicles; fungi and eukaryotic parasite can also secrete extracellular vesicles [128]. Pathogen-derived exosomes carry specific virulence factors like proteins or RNA molecules, which can either spread or limit the infection depending on the pathogen and its target cells, Table 3 [20–27]. Furthermore, the potential roles of pathogen-derived vesicles

TABLE 3: Examples of infectious disease where pathogen-derived exosomes play a role in pathogenesis.

| Disease causing agents | Name of disease | Exosomes role | Ref. |
|---|---|--|------|
| <i>Leishmania</i> spp. | Leishmaniasis | Spread virulence factors | [20] |
| HIV | AIDS | CD4+ T cells transinfection and delivery of Nef to by stander cells | [21] |
| Prion protein | Transmissible spongiform encephalopathies | Virulent factors delivery to normal cells | [22] |
| <i>Cryptococcus neoformans</i> | Cryptococcosis | Virulence factors spread and polysaccharide capsule formation | [23] |
| <i>Histoplasma capsulatum</i> | Ascomycota opportunistic fungal pathogens | Spread virulence factor in intracellular and extracellular space and promote virulence and provide stress response and fungal growth | [24] |
| <i>C. Albicans</i> , <i>C. parapsilosis</i> <i>S. schenckii</i> <i>S. cerevisiae</i> | Oral, vaginal, and systemic infections Candidiasis RTI Rarely pathogenic | Help in growth, Spread virulence and enhance pathogenicity | [25] |
| <i>Trypanosoma cruzi</i> | | Surface antigens spread during pathogenicity with membrane vesicles | [26] |
| HCV | Chronic HCV | v RNA transfer in normal cells | [27] |

in infection biology are illustrated in Table 3 [20]. However, during infection pathogen derived vesicles formation is much less recognized about the molecules involved in exosomes biogenesis and secretion. In mammalian cells, the molecules that are involved in exosomes biogenesis and secretion include ESCRT protein [27], ceramide [87], Rab27 [88], Rab11 [89], and Rab35 [129]. Although a similar subset of these proteins (ESCRTs, Rab11, and Rab27) has been identified in and *Leishmania* exosomes [125], their role in single-celled eukaryotic exosome biogenesis and release is not clear yet. In another experimental study, Silverman et al. have suggested that HSP100 plays an important role in packaging of proteins into *Leishmania* exosomes [135]. Interestingly, exosome has been associated with prion related disease. Berrone et al. observed pathological prion protein from the blood of animals with a prion related disease only associated with exosomes and this was in turn associated with plasma infectivity as well [136].

8. Exosomes from Bacteria and Its Function

The outer membrane vesicles associated proteins have significant biological activities as mentioned in previous studies [132, 133]. In addition, the outer membrane vesicles can mediate the secretion of both soluble and insoluble compounds (such as bacterial lipids and membrane proteins). For instance, then it allows the secretion of adhesion molecules of pathogenic bacteria. Adhesins are insoluble proteins that mediate coaggregation and these proteins are important for host tissues colonization. Another type of insoluble molecule like quinolone was secreted in outer membrane vesicles by *Pseudomonas* as a signal molecule, which is important for cellular communication [134]. Moreover, the bacterial exosomes are also mediating the secretion of soluble proteins in a protective complex, in which soluble molecules are part of

the lumen or attached to their surface. The surface-associated soluble proteins and the periplasmic molecules within the vesicle lumen are resistant against extracellular degradations by proteases. This complexity provides the ability of membrane vesicles to protect the secreted proteins and to allow less stable molecules, to reach further destinations during their transport [135]. Kadurugamuwa and Beveridge [137] have proposed two mechanisms for delivering the soluble content of membrane vesicles to its target site. The content could be delivered either through spontaneous lysis of outer membrane vesicles and consequently content diffuses or attachment of vesicles to their target followed by proximal lysis, internalization, or fusion to deliver the content.

The outer membrane vesicles secreted by bacterial strain might contribute significantly to bacterial survival and virulence factor existence. For instance, membrane vesicles could act as a defense and resistance mechanism against both internal or external damaging agents, and thus the vesicles can eliminate these toxicants instantly [136]. In addition, vesicles are loaded with lytic enzymes and receptors, which are important for bacterial nutrient acquisition [137]. Moreover, these vesicles are also important for nucleation and mediating the interactions of biofilm [138]. All the above-mentioned survival-related functions are important to enable the pathogenic organism to survive inside the host and eventually cause diseases. In addition, it also contains virulence factors such as an active toxin, which can be delivered into host cells by different mechanisms [139, 140].

9. Exosomes-Mediated Drug Delivery

Recently, evidences of natural exosomes-mediated drug delivery are increasing for cancer and infectious disease treatment [70, 141, 142]. In current opinion, two approaches are

considered to develop drug carriers for in vivo drug-delivery system based on cell-derived membrane vesicles which include the following: (1) modification and engineering of natural cell membrane vesicles primed with therapeutic compounds to target certain cell types and (2) using the essential characteristics of membrane vesicles in order to design nanoscaled drug vehicles [141]. Lately, exosomes have gained considerable interests for being used as a vehicle for either cell-derived materials or therapeutic drug-delivery systems. Exosomes are ideal candidates for drug delivery because they are bioavailable vehicles, which are known to be well tolerated, bioactive, specific to their target cells, and resistant to metabolic processes and have the ability to easily penetrate through impermeable biological barriers like blood-brain barrier (BBB). Increased evidence suggested that the natural membrane vesicles have more advantages than the synthetic nanoscaled drug systems due to their natural specificity to their target cells [143], their natural stability in blood, and their ability to tolerate the patient's immune response. However, exosomal purification is difficult because mammalian cells usually release small quantities of exosomes; thus exosome-mimetic nanoscaled vesicles were developed when overproduction is needed [38].

10. Exosomes as Carrier for Therapeutic Agents

There are so many approaches that can be used in order to load exosomal carriers with therapeutic agents and all were described in detail by Batrakova et al. [93]. There are advantages and disadvantages for each approach, and also this may be restricted to the type of drug, the targeted disease, and the conditions required for a specific type of exosomal cargo. The first one is ex vitro loading of naïve exosomes that are purified from parental donor cells and then incorporated with a therapeutic agent. The other approach is by loading parental cells with a drug, which is subsequently released in the exosomes. The final approach is by transfecting or infecting donor cells with drug-encoding DNA, which is eventually released in exosomes.

Therefore, exosomes serve as effective vehicles for many molecules that would be otherwise rapidly degraded before approaching their target like drugs, proteins, and microRNA/silent interfering RNA (siRNA). Alvarez-Erviti et al. have provided the first demonstration of biotechnological exploitation of cell membrane vesicles [29]. The authors showed a successful in vivo delivery with low or no toxicity or immunogenicity of exosomes-mediated siRNA to the mouse brain through injection of targeted exosomes. In order to ensure a successful delivery of the injected exosomes to their target cells in vivo and to avoid the exosomal removal of tissues of drug clearance, a novel targeting strategy was suggested. Therefore, exosomal surface protein lamp2b was used to display a targeting peptide to bind (AChR) receptor present on neurons and the vascular endothelium of the blood-brain barrier (BBB). The BBB was the major obstacle in the macromolecular drug delivery to the CNS [144]. On the other hand, artificial cell membrane vesicles mimic is also an alternative approach to obtain membrane vesicles and subsequently provides a controlled and clean drug-delivery system.

Currently, specific lipid and protein compositions are used in liposomal drug formulations to create CMV mimics that have similar properties of the natural ones [145]. Gao et al. have presented a novel strategy to generate neutrophil cell membrane-derived nanovesicles to target inflamed vasculature and significantly reduce acute lung inflammation by using nitrogen cavitation. Nitrogen cavitation was described in this study [148], which is a novel approach to fracture cells with no chemicals or long-term physical stress that could disrupt the biological functions of cellular membrane antigens.

11. Therapeutic Application

11.1. As Anticancer Drug Delivery. Recently, in vitro and in vivo experimental findings have shown that extracellular vesicles can be used as vehicles for several therapeutic agents for cancer treatment [147]. Previous clinical studies have been conducted in order to assess the efficacy of dendritic cell-derived exosomes (dexosomes) as cancer vaccines. The authors obtained promising results in phase I clinical trial following vaccination of metastatic melanoma patients [28] and in patients with advanced non-small cell lung cancer [29]. In a recent study, the effect of exosome-delivered siRNA on target cancer cells was observed. These experimental findings have shown that exosome-mediated siRNA can induce posttranscriptional gene silencing and apoptotic cell death of targeted cancer cells [30]. Smyth et al. have found that tumor-derived exosomes have been used as an effective vehicle for drug delivery [31]. Moreover, experimental studies have shown that exosomes can be used as carriers for therapeutic agents with low molecular weight [35, 149]. Other studies have demonstrated that when exosomes or exosome-mimetic nanovesicles loaded with various chemotherapeutic agents, Dox or PTX, they were able to target tumor cells in mice and significantly inhibit tumor growth without observing any side effects [38, 150, 151]. Jang et al. [28] have found that both Dox-loaded exosomes and Dox-loaded nanovesicles demonstrated similar antitumor activity, but Dox-loaded liposomes were not efficient in diminishing tumor growth. Similarly, mesenchymal stromal cells (MSCs) are an efficient mass producer of exosomes, which makes them ideal for drug delivery [61]. Pascucci et al. [33] have shown that MSCs have the ability to pack and then release drug such as Paclitaxel through their microvesicles, suggesting that MSCs can be used for drug-delivery system development with high specificity and more detail is provided in Table 4 [28–38]. Moreover, there are recently published papers showing and commenting on the ability of exosomes in delivering photodynamic drugs, possibly useful in the therapeutics of tumors.

11.2. Exosome Removal as Cancer Therapy. Cancer cells ubiquitously secrete exosomes, which transport oncoproteins and other immune suppressive molecules in order to promote tumorigenesis as well as metastasis. Therefore, several attractive therapeutic strategies have been suggested for targeting their cancer activities. Previous studies have suggested the removal of exosomes from the circulation as a strategy to attenuate the exosomal metastatic effect. Researchers have

TABLE 4: Exosomes used for cancer therapy.

| Exosomal cargo | Secreting cell | Recipient cell/patient | Activity | Ref. |
|--|---|-------------------------------------|---|------|
| DC-exosomes pulsed with functional MHC/peptide molecules | Dendritic cell | Metastatic melanoma patients | Cancer immunotherapy strategy (cancer vaccine) | [28] |
| DC-derived exosomes loaded with MAGE tumor antigens | Dendritic cell | Advanced non-small cell lung cancer | Cancer immunotherapy strategy (cancer vaccine) | [29] |
| exosome-delivered siRNA | Deliver tumor suppressors to their target sites by exosomes | Cancer cells | Posttranscriptional gene silencing and apoptotic cell death of targeted cancer cells | [30] |
| CMV-delivered miRNA-128 | | Glioblastoma | Can affect cancer cell behavior Inhibits Glioma proliferation and self-renewal | [31] |
| CMV-delivered miRNA-7 | | Glioblastoma | Inhibits the epidermal growth factor receptor and down-regulate the Akt-pathway | [32] |
| Aex in combination with GM-CSF | Ascites | Advanced colorectal cancer | Used as immunotherapy –tumor specific antitumor cytotoxic T lymphocyte | [33] |
| mmnResistant anticancer drug-treated HepG2 cells -derived exosomes | Resistant anticancer drug-treated HepG2 cells | Hepatocellular carcinoma | Elicit effective NK-cell antitumor responses in vitro; Vaccine for Hepatocellular carcinoma immunotherapy | [34] |
| Brain endothelial cell-derived exosomes | Brain endothelial cell | Brain cancer | Can deliver anticancer drugs across the BBB | [35] |
| List of various types | Refer to the reference | Various | Nanoscale cancer vaccine | [36] |
| List of tumor suppressive miRNA | Refer to the reference | Various | Tumor suppressive | [37] |
| Dox-loaded exosomes and Dox-loaded nanovesicles | Cell-derived exosomes (monocytes/macrophages) | Malignant cells | Antitumor | [38] |

TABLE 5: Novel strategies/devices of exosomal removal for cancer and infectious disease therapy.

| Mechanism of exosomal removal | Disease | Effect | Ref. |
|--|-----------------------------------|--|------|
| Extracorporeal hemofiltration of exosomes | Hepatitis C | Minimize viral titers in patients | [39] |
| Exosome enervation by Dimethyl amiloride (DMA) in mice | Colorectal cancer | Restore the cyclophosphamide (CTX) anti-tumor effect through the inhibition of MDSC functions | [40] |
| Extracorporeal filtration of exosomes (The Hemopurifier) | Advanced stage of cancer patients | To remove exosomes from the blood | [41] |
| Adjunct therapeutic method HER2osome | Breast cancer | Decrease the tumor secreted HER2 containing exosomes in circulation and afterward impede HER2 positive breast cancer progression | [42] |

TABLE 6: Exosomes used for infectious diseases treatment.

| Exosomal cargo | Secreting cell | Biological activity | Ref. |
|--|--|--|----------|
| Exosomes pulsed with <i>Toxoplasma gondii</i> antigens | Dendritic cells | A defensive immune response against <i>Toxoplasma gondii</i> infection | [43, 44] |
| Exosomes pulsed with <i>Leishmania major</i> antigens | Dendritic cells | A defensive immune response against <i>L. major</i> infection | [45] |
| Exosomes containing M. tuberculosis antigens | Macrophage infected with M. Tuberculosis | Tuberculosis vaccine, activate innate/acquired immune responses | [46] |
| shRNA against HCV replication-loaded exosomes | Transfected into several cell types | Decrease in HCV infection of liver cells | [47] |

suggested a wide range of methods to inhibit exosome production, which involve targeting microtubules assembly and stability and endosomal-sorting pathway and by using inhibitors of the proton pump [67, 88]. Marleau et al. have suggested a novel mechanism involving the use of extracorporeal hemofiltration of exosomes from circulation in order to minimize viral titers in patients [157]. Further, more information regarding exosomes removal from cancer and infected cells is listed in Table 5 [39–42].

11.3. Exosomes as Cancer Diagnostic Biomarkers. Depending on the type of tumor and location, exosomes can be isolated from almost all body fluids, including human saliva, serum, breast milk, CSF, urine, and semen [74–77]. Exosomes are novel sources of biomarkers because they contain bioactive molecules, which can help to assess the pathological state of the originated cells [40]. In addition, exosomes can be used to predict or monitor a patient's response to the given treatment. More importantly, exosomes provide noninvasive and continuous access to the required information to be used for tumor progression assessment [40]. It has been documented that the level of exosomes increased in some cancer patients in comparison to healthy individuals and has been correlated with poor prognosis [41]. Recent studies have shown that most of the circulating microRNAs detectable serum and saliva are concentrated in tumor-derived exosomes [152]. Extensive studies have shown that tumor-derived exosomes from either tumor cells or extracellular fluids of cancer patients can be used as biomarkers because they have a unique molecular signature on their biocontents (proteins, DNA/RNA molecules) [153–155]. A list of exosomes isolated

from biofluids of cancer patients used as biomarkers were prepared with details in previous studies [33, 40].

12. Exosomes Used for Infectious Disease Treatment

Bukong et al. have provided a novel mechanistic strategy for HCV transmission that can compromise immune-based therapies for HCV infection and thus suggested potential therapeutic strategies in order to block exosome-mediated transmission of HCV infection [132]. The clinical application of extracellular vesicles is discussed in detail: (i) therapeutic application and both (ii) diagnosis and therapy together [156]. Exosomes are recognized as a novel therapeutic tool for anti-tumor therapy, immune-modulation regenerative therapy, pathogen vaccination, and drug delivery but there is still a need for high level cooperation between researchers and expert clinicians for approval from recognized authorities [157]. Table 6 illustrates a number of studies that provided evidence for exosomes used for infectious disease treatment [43–47].

13. Benefits and Future Prospects

Exosomes are cell-derived membrane vesicles secreted by different cell types and present in body fluids. Proteomic profiling of EVs demonstrated that these vesicles play a valuable role in cellular communications and they act as natural vehicles for cell signaling proteins and genetic molecules. These findings indicated that it is possible to explore the vesicles as novel drug-delivery systems for many therapeutic agents that targeted different diseases such as cancers, infectious

diseases, and cardiovascular disease. European Cooperation in Science and Technology and International Society for Extracellular Vesicles (ISEV) are also constructing a network on Microvesicles and Exosomes in Health and Disease (ME-HaD) for ensuring the safety aspect and future application of exosomes in drugs.

In some cases exosomes not only are an ideal vehicle for therapeutic agents but also have been used as diagnostic and prognostic indicators for various cancers. Further studies of exosomes in the pathogenesis of cancer will open new avenues to explore novel diagnostic and therapeutic strategies. Isolation of vesicles of specific size and properties from the bacterial cells and application in drug delivery will be most fascinating research area in future because they will be cheaper and safe from cancers cell exosomes. Yield optimization and purification still require a single technique which is not available, and hopefully in future research will help in developing a single step device for development, purification, and characterization. Furthermore, the findings discussed in this review demonstrated that membrane-derived vesicles play a valuable role in infection biology. This applies to all organisms with different range of complexity from prions to eukaryotic pathogens. Further studies are needed to investigate more pathogens-derived exosomes that play a role in infection transmission and pathogenesis and to explore other novel therapeutic strategies to block exosome-mediated infection transmission. Further studies are also needed to explore novel bacterial species that are able to secrete outer membrane vesicles during their normal growth. More investigations are also needed to study the biogenesis of membrane vesicles in Gram-negative bacteria, which will help to generate more ideal outer membrane vesicles and improve human health. It is also important to study the mechanism of outer membrane vesiculation and to identify the essential envelop compositions that may play a role in vesicles generation. Therefore, a novel antibiotic could be designed to target these virulence components, which will help to inhibit bacterial growth and pathogens.

Novel insights for exosome-mediated drug-delivery systems were illustrated, which is important for the development of novel therapeutics and vaccines. In addition, there is an urgent need to develop advanced technologies to generate more controllable and homogenous membrane vesicles to be used for drug development. Finally, the findings discussed in this article showed the therapeutic effects of exosomes when loaded with drugs for the targeted diseases. The newly discovered drug-loaded exosomes should go for further animal testing and clinical trials to make the formulations ready in the market for clinical applications and to improve the therapeutic index of established drugs.

14. Conclusion

Taken together, these findings have shown that there is a relation between exosomes and cancer or infection biology, which is important for the development of novel therapeutics and vaccines. Exosomes are ideal candidates for drug delivery and further studies are needed to explore novel strategies of exosome-mediated therapies particularly for cancer

and infectious diseases. We have also discussed the major obstacles of exosome-mediated drug development and the most common methods used for exosomes generation and purification. We also confer the need for developing advanced technologies to generate more ideal and controllable exosomes for drug-delivery systems.

Conflicts of Interest

The authors declare that they have no conflicts of interest.

Acknowledgments

This research was financially supported by the Center of Excellence in Environmental Studies (CEES) and Ministry of Higher Education of Saudi Arabia.

References

- [1] M. P. Zaborowski, L. Balaj, X. O. Breakefield, and C. P. Lai, "Extracellular vesicles: composition, biological relevance, and methods of study," *Bioscience*, vol. 65, no. 8, pp. 783–797, 2015.
- [2] J. De Toro, L. Herschlik, C. Waldner, and C. Mongini, "Emerging roles of exosomes in normal and pathological conditions: new insights for diagnosis and therapeutic applications," *Frontiers in Immunology*, vol. 6, article 203, 2015.
- [3] K. I. Willig, S. O. Rizzoli, V. Westphal, R. Jahn, and S. W. Hell, "STED microscopy reveals that synaptotagmin remains clustered after synaptic vesicle exocytosis," *Nature*, vol. 440, no. 7086, pp. 935–939, 2006.
- [4] M. Bates, B. Huang, G. T. Dempsey, and X. Zhuang, "Multicolor super-resolution imaging with photo-switchable fluorescent probes," *Science*, vol. 317, no. 5845, pp. 1749–1753, 2007.
- [5] S. A. Soper and A. Rasooly, "Cancer: A global concern that demands new detection technologies," *Analyst*, vol. 141, no. 2, pp. 367–370, 2016.
- [6] I. Parolini, C. Federici, C. Raggi et al., "Microenvironmental pH is a key factor for exosome traffic in tumor cells," *The Journal of Biological Chemistry*, vol. 284, no. 49, pp. 34211–34222, 2009.
- [7] C. Beyer and D. S. Pisetsky, "The role of microparticles in the pathogenesis of rheumatic diseases," *Nature Reviews Rheumatology*, vol. 6, no. 1, pp. 21–29, 2010.
- [8] M. A. Livshts, E. Khomyakova, E. G. Evtushenko et al., "Isolation of exosomes by differential centrifugation: Theoretical analysis of a commonly used protocol," *Scientific Reports*, vol. 5, Article ID 17319, 2015.
- [9] D. W. Greening, R. Xu, H. Ji, B. J. Tauro, and R. J. Simpson, "A protocol for exosome isolation and characterization: Evaluation of ultracentrifugation, density-gradient separation, and immunoaffinity capture methods," *Methods in Molecular Biology*, vol. 1295, pp. 179–209, 2015.
- [10] A. N. Böing, E. van der Pol, A. E. Grootemaat, F. A. W. Coumans, A. Sturk, and R. Nieuwland, "Single-step isolation of extracellular vesicles by size-exclusion chromatography," *Journal of Extracellular Vesicles (JEV)*, vol. 3, no. 1, Article ID 23430, 2014.
- [11] R. Grant, E. Ansa-Addo, D. Stratton et al., "A filtration-based protocol to isolate human Plasma Membrane-derived Vesicles and exosomes from blood plasma," *Journal of Immunological Methods*, vol. 371, no. 1-2, pp. 143–151, 2011.

- [12] D. D. Taylor and S. Shah, "Methods of isolating extracellular vesicles impact down-stream analyses of their cargoes," *Methods*, vol. 87, pp. 3–10, 2015.
- [13] M. F. Peterson, N. Otoc, J. K. Sethi, A. Gupta, and T. J. Antes, "Integrated systems for exosome investigation," *Methods*, vol. 87, pp. 31–45, 2015.
- [14] E. Van der Pol, F. A. W. Coumans, A. E. Grootemaat et al., "Particle size distribution of exosomes and microvesicles determined by transmission electron microscopy, flow cytometry, nanoparticle tracking analysis, and resistive pulse sensing," *Journal of Thrombosis and Haemostasis*, vol. 12, no. 7, pp. 1182–1192, 2014.
- [15] G. Vogel, A. Strauss, B. Jenni et al., "Development and validation of a protocol for cell line identification by MALDI-TOF MS," *BMC Proceedings*, vol. 5, no. Suppl 8, p. P45, 2011.
- [16] M. A. Obeid, I. Khadra, A. B. Mullen, R. J. Tate, and V. A. Ferro, "The effects of hydration media on the characteristics of non-ionic surfactant vesicles (NISV) prepared by microfluidics," *International Journal of Pharmaceutics*, vol. 516, no. 1–2, pp. 52–60, 2017.
- [17] G. Di Noto, A. Bugatti, A. Zendrini et al., "Merging colloidal nanoplasmonics and surface plasmon resonance spectroscopy for enhanced profiling of multiple myeloma-derived exosomes," *Biosensors and Bioelectronics*, vol. 77, pp. 518–524, 2016.
- [18] M. He, J. Crow, M. Roth, Y. Zeng, and A. K. Godwin, "Integrated immunoisolation and protein analysis of circulating exosomes using microfluidic technology," *Lab on a Chip*, vol. 14, no. 19, pp. 3773–3780, 2014.
- [19] A. A. I. Sina, R. Vaidyanathan, S. Dey, L. G. Carrascosa, M. J. A. Shiddiky, and M. Trau, "Real time and label free profiling of clinically relevant exosomes," *Scientific Reports*, vol. 6, Article ID 30460, 2016.
- [20] E. Foglio, G. Puddighinu, P. Fasanaro et al., "Exosomal clusterin, identified in the pericardial fluid, improves myocardial performance following MI through epicardial activation, enhanced arteriogenesis and reduced apoptosis," *International Journal of Cardiology*, vol. 197, Article ID 20664, pp. 333–347, 2015.
- [21] J. M. Silverman, J. Clos, C. C. DeOliveira et al., "An exosome-based secretion pathway is responsible for protein export from *Leishmania* and communication with macrophages," *Journal of Cell Science*, vol. 123, no. 6, pp. 842–852, 2010.
- [22] D. G. Nguyen, A. Booth, S. J. Gould, and J. E. K. Hildreth, "Evidence that HIV budding in primary macrophages occurs through the exosome release pathway," *The Journal of Biological Chemistry*, vol. 278, no. 52, pp. 52347–52354, 2003.
- [23] S. Bhatnagar and J. S. Schorey, "Exosomes released from infected macrophages contain *Mycobacterium avium* glycopeptidolipids and are proinflammatory," *The Journal of Biological Chemistry*, vol. 282, no. 35, pp. 25779–25789, 2007.
- [24] J. H. Campos, R. P. Soares, K. Ribeiro, A. Cronemberger Andrade, W. L. Batista, and A. C. Torrecilhas, "Extracellular Vesicles: Role in Inflammatory Responses and Potential Uses in Vaccination in Cancer and Infectious Diseases," *Journal of Immunology Research*, vol. 2015, Article ID 832057, 2015.
- [25] J. M. Silverman and N. E. Reiner, "Exosomes and other microvesicles in infection biology: organelles with unanticipated phenotypes," *Cellular Microbiology*, vol. 13, no. 1, pp. 1–9, 2011.
- [26] M. Lenassi, G. Cagney, M. Liao et al., "HIV Nef is secreted in exosomes and triggers apoptosis in bystander CD4⁺ T cells," *Traffic*, vol. 11, no. 1, pp. 110–122, 2010.
- [27] B. Fevrier, D. Vilette, F. Archer et al., "Cells release prions in association with exosomes," *Proceedings of the National Academy of Sciences of the United States of America*, vol. 101, no. 26, pp. 9683–9688, 2004.
- [28] S. C. Jang, O. Y. Kim, C. M. Yoon et al., "Bioinspired exosome-mimetic nanovesicles for targeted delivery of chemotherapeutics to malignant tumors," *ACS Nano*, vol. 7, no. 9, pp. 7698–7710, 2013.
- [29] L. Alvarez-Erviti, Y. Seow, H. Yin, C. Betts, S. Lakhali, and M. J. A. Wood, "Delivery of siRNA to the mouse brain by systemic injection of targeted exosomes," *Nature Biotechnology*, vol. 29, no. 4, pp. 341–345, 2011.
- [30] M. Çağdaş, A. D. Sezer, and S. Bucak, "Liposomes as potential drug carrier systems for drug delivery," *Application of Nanotechnology in Drug Delivery*, 2014.
- [31] T. Smyth, M. Kullberg, N. Malik, P. Smith-Jones, M. W. Graner, and T. J. Anchordoquy, "Biodistribution and delivery efficiency of unmodified tumor-derived exosomes," *Journal of Controlled Release*, vol. 199, pp. 145–155, 2015.
- [32] T. Yang, P. Martin, B. Fogarty et al., "Exosome delivered anti-cancer drugs across the blood-brain barrier for brain cancer therapy in Danio Rerio," *Pharmaceutical Research*, vol. 32, no. 6, pp. 2003–2014, 2015.
- [33] L. Pascucci, V. Coccè, A. Bonomi et al., "Paclitaxel is incorporated by mesenchymal stromal cells and released in exosomes that inhibit in vitro tumor growth: a new approach for drug delivery," *Journal of Controlled Release*, vol. 192, pp. 262–270, 2014.
- [34] Y. Tian, S. Li, J. Song et al., "A doxorubicin delivery platform using engineered natural membrane vesicle exosomes for targeted tumor therapy," *Biomaterials*, vol. 35, no. 7, pp. 2383–2390, 2014.
- [35] K. B. Johnsen, J. M. Gudbergsson, M. N. Skov, L. Pilgaard, T. Moos, and M. Duroux, "A comprehensive overview of exosomes as drug delivery vehicles—endogenous nanocarriers for targeted cancer therapy," *Biochimica et Biophysica Acta (BBA) - Reviews on Cancer*, vol. 1846, no. 1, pp. 75–87, 2014.
- [36] S. Rani, A. E. Ryan, M. D. Griffin, and T. Ritter, "Mesenchymal stem cell-derived extracellular vesicles: toward cell-free therapeutic applications," *Molecular Therapy*, vol. 23, no. 5, pp. 812–823, 2015.
- [37] J. Godlewski, M. O. Nowicki, A. Bronisz et al., "Targeting of the Bmi-1 oncogene/stem cell renewal factor by MicroRNA-128 inhibits glioma proliferation and self-renewal," *Cancer Research*, vol. 68, no. 22, pp. 9125–9130, 2008.
- [38] H. Gankema, J. Wensink, P. A. M. Guinee, W. H. Jansen, and B. Witholt, "Some characteristics of the outer membrane material released by growing enterotoxigenic *Escherichia coli*," *Infection and Immunity*, vol. 29, no. 2, pp. 704–713, 1980.
- [39] B. Kefas, J. Godlewski, L. Comeau et al., "microRNA-7 inhibits the epidermal growth factor receptor and the akt pathway and is down-regulated in glioblastoma," *Cancer Research*, vol. 68, no. 10, pp. 3566–3572, 2008.
- [40] S. Dai, D. Wei, Z. Wu et al., "Phase I clinical trial of autologous ascites-derived exosomes combined with GM-CSF for colorectal cancer," *Molecular Therapy*, vol. 16, no. 4, pp. 782–790, 2008.
- [41] L.-H. Lv, Y.-L. Wan, Y. Lin et al., "Anticancer drugs cause release of exosomes with heat shock proteins from human hepatocellular carcinoma cells that elicit effective natural killer cell antitumor responses in vitro," *The Journal of Biological Chemistry*, vol. 287, no. 19, pp. 15874–15885, 2012.

- [42] X. Zhang, X. Yuan, H. Shi, L. Wu, H. Qian, and W. Xu, "Exosomes in cancer: Small particle, big player," *Journal of Hematology & Oncology*, vol. 8, no. 1, article no. 83, 2015.
- [43] F. Chalmin, S. Ladoire, G. Mignot et al., "Membrane-associated Hsp72 from tumor-derived exosomes mediates STAT3-dependent immunosuppressive function of mouse and human myeloid-derived suppressor cells," *The Journal of Clinical Investigation*, vol. 120, no. 2, pp. 457–471, 2010.
- [44] F. Hochberg and et al., "Second International Meeting of ISEV 2013: Boston, USA, April 17th–20th," *Journal of Extracellular Vesicles*, 2013.
- [45] J. Rak, "Extracellular vesicles—biomarkers and effectors of the cellular interactome in cancer," *Frontiers in Pharmacology*, vol. 4, article 21, 2013.
- [46] H. K. Kim, K. S. Song, Y. S. Park et al., "Elevated levels of circulating platelet microparticles, VEGF, IL-6 and RANTES in patients with gastric cancer: possible role of a metastasis predictor," *European Journal of Cancer*, vol. 39, no. 2, pp. 184–191, 2003.
- [47] A. Gallo, M. Tandon, I. Alevizos, and G. G. Illei, "The majority of microRNAs detectable in serum and saliva is concentrated in exosomes," *PLoS ONE*, vol. 7, no. 3, Article ID e30679, 2012.
- [48] L. A. Emery, A. Tripathi, C. King et al., "Early dysregulation of cell adhesion and extracellular matrix pathways in breast cancer progression," *The American Journal of Pathology*, vol. 175, no. 3, pp. 1292–1302, 2009.
- [49] J. S. Schorey, Y. Cheng, P. P. Singh, and V. L. Smith, "Exosomes and other extracellular vesicles in host-pathogen interactions," *EMBO Reports*, vol. 16, pp. 24–43, 2015.
- [50] A. Shimoda, K. Ueda, S. Nishiumi et al., "Exosomes as nanocarriers for systemic delivery of the *Helicobacter pylori* virulence factor CagA," *Scientific Reports*, vol. 6, Article ID 18346, 2016.
- [51] M. Logozzi, A. de Milito, L. Lugini et al., "High levels of exosomes expressing CD63 and caveolin-1 in plasma of melanoma patients," *PLoS ONE*, vol. 4, no. 4, Article ID e5219, 2009.
- [52] J. VanDeun, A. Hendrix, and On behalf of the EV-TRACK consortium, "Is your article EV-TRACKed?" *Journal of Extracellular Vesicles*, vol. 6, no. 1, Article ID 1379835, 2017.
- [53] P. Wolf, "The nature and significance of platelet products in human plasma," *British Journal of Haematology*, vol. 13, no. 3, pp. 269–288, 1967.
- [54] E. G. Trams, C. J. Lauter, J. Norman Salem, and U. Heine, "Exfoliation of membrane ecto-enzymes in the form of microvesicles," *Biochimica et Biophysica Acta*, vol. 645, no. 1, pp. 63–70, 1981.
- [55] R. M. Johnstone, M. Adam, J. R. Hammond, L. Orr, and C. Turbide, "Vesicle formation during reticulocyte maturation. Association of plasma membrane activities with released vesicles (exosomes)," *The Journal of Biological Chemistry*, vol. 262, no. 19, pp. 9412–9420, 1987.
- [56] F. Doonan and T. G. Cotter, "Morphological assessment of apoptosis," *Methods*, vol. 44, no. 3, pp. 200–204, 2008.
- [57] M. Schiller, I. Bekeredian-Ding, P. Heyder, N. Blank, A. D. Ho, and H.-M. Lorenz, "Autoantigens are translocated into small apoptotic bodies during early stages of apoptosis," *Cell Death & Differentiation*, vol. 15, no. 1, pp. 183–191, 2008.
- [58] S. A. A. Kooijmans, P. Vader, S. M. van Dommelen, W. W. van Solinge, and R. M. Schiffelers, "Exosome mimetics: a novel class of drug delivery systems," *International Journal of Nanomedicine*, vol. 7, pp. 1525–1541, 2012.
- [59] D. Mayrand and D. Grenier, "Biological activities of outer membrane vesicles," *Canadian Journal of Microbiology*, vol. 35, no. 6, pp. 607–613, 1989.
- [60] A. Kulp and M. J. Kuehn, "Biological Functions and biogenesis of secreted bacterial outer membrane vesicles," *Annual Review of Microbiology*, vol. 64, pp. 163–184, 2010.
- [61] D. Hoekstra, J. W. van der Laan, L. de Leij, and B. Witholt, "Release of outer membrane fragments from normally growing *Escherichia coli*," *BBA - Biomembranes*, vol. 455, no. 3, pp. 889–899, 1976.
- [62] I. W. Devoe and J. E. Gilchrist, "Release of endotoxin in the form of cell wall blebs during in vitro growth of *Neisseria meningitidis*," *The Journal of Experimental Medicine*, vol. 138, no. 5, pp. 1156–1167, 1973.
- [63] J. L. Kadurugamuwa and T. J. Beveridge, "Virulence factors are released from *Pseudomonas aeruginosa* in association with membrane vesicles during normal growth and exposure to gentamicin: a novel mechanism of enzyme secretion," *Journal of Bacteriology*, vol. 177, no. 14, pp. 3998–4008, 1995.
- [64] R. Fiocca, V. Necchi, P. Sommi et al., "Release of *Helicobacter pylori* vacuolating cytotoxin by both a specific secretion pathway and budding of outer membrane vesicles. Uptake of released toxin and vesicles by gastric epithelium," *The Journal of Pathology*, vol. 188, no. 2, pp. 220–226, 1999.
- [65] M. L. Rodrigues, E. S. Nakayasu, I. C. Almeida, and L. Nimrichter, "The impact of proteomics on the understanding of functions and biogenesis of fungal extracellular vesicles," *Journal of Proteomics*, vol. 97, pp. 177–186, 2014.
- [66] S. Bhatnagar, K. Shinagawa, F. J. Castellino, and J. S. Schorey, "Exosomes released from macrophages infected with intracellular pathogens stimulate a proinflammatory response in vitro and in vivo," *Blood*, vol. 110, no. 9, pp. 3234–3244, 2007.
- [67] C. Théry, S. Amigorena, G. Raposo, and A. Clayton, "Isolation and characterization of exosomes from cell culture supernatants and biological fluids," *Current Protocols in Cell Biology*, vol. 3, 2006.
- [68] E. N. M. Nolte, S. I. Buschow, S. M. Anderton, W. Stoorvogel, and M. H. M. Wauben, "Activated T cells recruit exosomes secreted by dendritic cells via LFA-1," *Blood*, vol. 113, no. 9, pp. 1977–1981, 2009.
- [69] A. Clayton, A. Turkes, H. Navabi, M. D. Mason, and Z. Tabi, "Induction of heat shock proteins in B-cell exosomes," *Journal of Cell Science*, vol. 118, no. 16, pp. 3631–3638, 2005.
- [70] R. W. Y. Yeo, R. C. Lai, B. Zhang et al., "Mesenchymal stem cell: an efficient mass producer of exosomes for drug delivery," *Advanced Drug Delivery Reviews*, vol. 65, no. 3, pp. 336–341, 2013.
- [71] G. Skogberg, V. Lundberg, M. Berglund et al., "Human thymic epithelial primary cells produce exosomes carrying tissue-restricted antigens," *Immunology & Cell Biology*, vol. 93, no. 8, pp. 727–734, 2015.
- [72] J. Song, X. Chen, M. Wang, Y. Xing, Z. Zheng, and S. Hu, "Cardiac endothelial cell-derived exosomes induce specific regulatory B cells," *Scientific Reports*, vol. 4, article 7583, 2014.
- [73] X. Li, Z. Zhang, T. Beiter, and H. J. Schluessener, "Nanovesicular vaccines: Exosomes," *Archivum Immunologiae et Therapia Experimentalis*, vol. 53, no. 4, pp. 329–335, 2005.
- [74] C. Lässer, V. S. Alikhani, K. Ekström et al., "Human saliva, plasma and breast milk exosomes contain RNA: uptake by macrophages," *Journal of Translational Medicine*, vol. 9, article 9, 2011.

- [75] J. M. Street, P. E. Barran, C. L. Mackay et al., "Identification and proteomic profiling of exosomes in human cerebrospinal fluid," *Journal of Translational Medicine*, vol. 10, no. 1, article 5, 2012.
- [76] J. W. Dear, J. M. Street, and M. A. Bailey, "Urinary exosomes: a reservoir for biomarker discovery and potential mediators of intrarenal signalling," *Proteomics*, vol. 13, no. 10-11, pp. 1572–1580, 2013.
- [77] M. N. Madison, R. J. Roller, and C. M. Okeoma, "Human semen contains exosomes with potent anti-HIV-1 activity," *Retrovirology*, vol. 11, article 102, 2014.
- [78] H. Im, H. Shao, Y. I. Park et al., "Label-free detection and molecular profiling of exosomes with a nano-plasmonic sensor," *Nature Biotechnology*, vol. 32, no. 5, pp. 490–495, 2014.
- [79] J. Lötvall, A. F. Hill, F. Hochberg et al., "Minimal experimental requirements for definition of extracellular vesicles and their functions: a position statement from the International Society for Extracellular Vesicles," *Journal of Extracellular Vesicles (JEV)*, vol. 3, Article ID 26913, 2014.
- [80] C. Théry, M. Ostrowski, and E. Segura, "Membrane vesicles as conveyors of immune responses," *Nature Reviews Immunology*, vol. 9, no. 8, pp. 581–593, 2009.
- [81] S. Mathivanan, J. W. E. Lim, B. J. Tauro, H. Ji, R. L. Moritz, and R. J. Simpson, "Proteomics analysis of A33 immunoaffinity-purified exosomes released from the human colon tumor cell line LIM1215 reveals a tissue-specific protein signature," *Molecular & Cellular Proteomics*, vol. 9, no. 2, pp. 197–208, 2010.
- [82] E. Work, K. W. Knox, and M. Vesik, "The chemistry and electron microscopy of an extracellular lipopolysaccharide from *Escherichia coli*," *Annals of the New York Academy of Sciences*, vol. 133, no. 2, pp. 438–449, 1966.
- [83] L. Zhou, R. Srisatjaluk, D. E. Justus, and R. J. Doyle, "On the origin of membrane vesicles in Gram-negative bacteria," *FEMS Microbiology Letters*, vol. 163, no. 2, pp. 223–228, 1998.
- [84] C. Schwechheimer, C. J. Sullivan, and M. J. Kuehn, "Envelope control of outer membrane vesicle production in Gram-negative bacteria," *Biochemistry*, vol. 52, no. 18, pp. 3031–3040, 2013.
- [85] J. Wensink and B. Witholt, "Outer-Membrane Vesicles Released by Normally Growing *Escherichia coli* Contain Very Little Lipoprotein," *European Journal of Biochemistry*, vol. 116, no. 2, pp. 331–335, 1981.
- [86] C. Théry, L. Zitvogel, and S. Amigorena, "Exosomes: composition, biogenesis and function," *Nature Reviews Immunology*, vol. 2, no. 8, pp. 569–579, 2002.
- [87] K. Trajkovic, C. Hsu, S. Chiantia et al., "Ceramide triggers budding of exosome vesicles into multivesicular endosomes," *Science*, vol. 319, no. 5867, pp. 1244–1247, 2008.
- [88] M. Ostrowski, N. B. Carmo, S. Krumeich et al., "Rab27a and Rab27b control different steps of the exosome secretion pathway," *Nature Cell Biology*, vol. 12, no. 1, pp. 19–30, 2010.
- [89] A. Savina, C. M. Fader, M. T. Damiani, and M. I. Colombo, "Rab11 promotes docking and fusion of multivesicular bodies in a calcium-dependent manner," *Traffic*, vol. 6, no. 2, pp. 131–143, 2005.
- [90] F. Cappello, M. Logozzi, C. Campanella et al., "Exosome levels in human body fluids: A tumor marker by themselves?" *European Journal of Pharmaceutical Sciences*, vol. 96, pp. 93–98, 2017.
- [91] A. Liga, A. D. B. Vliegthart, W. Oosthuyzen, J. W. Dear, and M. Kersaudy-Kerhoas, "Exosome isolation: A microfluidic roadmap," *Lab on a Chip*, vol. 15, no. 11, pp. 2388–2394, 2015.
- [92] B. J. Tauro, D. W. Greening, R. A. Mathias et al., "Comparison of ultracentrifugation, density gradient separation, and immunoaffinity capture methods for isolating human colon cancer cell line LIM1863-derived exosomes," *Methods*, vol. 56, no. 2, pp. 293–304, 2012.
- [93] E. V. Batrakova and M. S. Kim, "Using exosomes, naturally-equipped nanocarriers, for drug delivery," *Journal of Controlled Release*, vol. 219, pp. 396–405, 2015.
- [94] H. Kalra, C. G. Adda, M. Liem et al., "Comparative proteomics evaluation of plasma exosome isolation techniques and assessment of the stability of exosomes in normal human blood plasma," *Proteomics*, vol. 13, no. 22, pp. 3354–3364, 2013.
- [95] L. Muller, C.-S. Hong, D. B. Stolz, S. C. Watkins, and T. L. Whiteside, "Isolation of biologically-active exosomes from human plasma," *Journal of Immunological Methods*, vol. 411, pp. 55–65, 2014.
- [96] J. Van Deun, P. Mestdagh, R. Sormunen et al., "The impact of disparate isolation methods for extracellular vesicles on downstream RNA profiling," *Journal of Extracellular Vesicles (JEV)*, vol. 3, no. 1, Article ID 24858, 2014.
- [97] H. Saari, E. Lázaro-Ibáñez, T. Viitala, E. Vuorimaa-Laukkanen, P. Siljander, and M. Yliperttula, "Microvesicle- and exosome-mediated drug delivery enhances the cytotoxicity of Paclitaxel in autologous prostate cancer cells," *Journal of Controlled Release*, vol. 220, pp. 727–737, 2015.
- [98] R. A. Dragovic, C. Gardiner, A. S. Brooks et al., "Sizing and phenotyping of cellular vesicles using nanoparticle tracking analysis," *Nanomedicine: Nanotechnology, Biology and Medicine*, vol. 7, no. 6, pp. 780–788, 2011.
- [99] G. Cesi, G. Walbrech, C. Margue, and S. Kreis, "Transferring intercellular signals and traits between cancer cells: extracellular vesicles as 'homing pigeons,'" *Cell Communication and Signaling*, vol. 14, no. 1, article 13, 2016.
- [100] Y.-G. Zhou, R. M. Mohamadi, M. Poudineh et al., "Interrogating Circulating Microsomes and Exosomes Using Metal Nanoparticles," *Small*, vol. 12, no. 6, pp. 727–732, 2016.
- [101] E. Helmerhorst, D. J. Chandler, M. Nussio, and C. D. Mamotte, "Real-time and label-free bio-sensing of molecular interactions by surface plasmon resonance: A laboratory medicine perspective," *The Clinical Biochemist Reviews*, vol. 33, no. 4, pp. 161–173, 2012.
- [102] D. L. M. Rupert, G. V. Shelke, G. Emilsson et al., "Dual-Wavelength Surface Plasmon Resonance for Determining the Size and Concentration of Sub-Populations of Extracellular Vesicles," *Analytical Chemistry*, vol. 88, no. 20, pp. 9980–9988, 2016.
- [103] L. Grasso, R. Wyss, L. Weidenauer et al., "Molecular screening of cancer-derived exosomes by surface plasmon resonance spectroscopy," *Analytical and Bioanalytical Chemistry*, vol. 407, no. 18, article no. 8711, pp. 5425–5432, 2015.
- [104] R. Wyss, L. Grasso, C. Wolf, W. Grosse, D. Demurtas, and H. Vogel, "Molecular and dimensional profiling of highly purified extracellular vesicles by fluorescence fluctuation spectroscopy," *Analytical Chemistry*, vol. 86, no. 15, pp. 7229–7233, 2014.
- [105] L. Zhu, K. Wang, J. Cui et al., "Label-free quantitative detection of tumor-derived exosomes through surface plasmon resonance imaging," *Analytical Chemistry*, vol. 86, no. 17, pp. 8857–8864, 2014.
- [106] D. M. B. Post, D. Zhang, J. S. Eastvold, A. Teghanemt, B. W. Gibson, and J. P. Weiss, "Biochemical and functional characterization of membrane blebs purified from *Neisseria meningitidis*

- serogroup B," *The Journal of Biological Chemistry*, vol. 280, no. 46, pp. 38383–38394, 2005.
- [107] S. J. Bauman and M. J. Kuehn, "Purification of outer membrane vesicles from *Pseudomonas aeruginosa* and their activation of an IL-8 response," *Microbes and Infection*, vol. 8, no. 9-10, pp. 2400–2408, 2006.
- [108] M. Nevot, V. Deroncelé, P. Messner, J. Guinea, and E. Mercadé, "Characterization of outer membrane vesicles released by the psychrotolerant bacterium *Pseudoalteromonas antarctica* NF3," *Environmental Microbiology*, vol. 8, no. 9, pp. 1523–1533, 2006.
- [109] E.-Y. Lee, Y. B. Joo, W. P. Gun et al., "Global proteomic profiling of native outer membrane vesicles derived from *Escherichia coli*," *Proteomics*, vol. 7, no. 17, pp. 3143–3153, 2007.
- [110] U. K. Laemmli, "Cleavage of structural proteins during the assembly of the head of bacteriophage T4," *Nature*, vol. 227, no. 5259, pp. 680–685, 1970.
- [111] J. Sambrook, E. F. Fritsch, and T. Maniatis, *Molecular cloning: A laboratory manual*, 2nd edition, 1983.
- [112] J. A. Tickner, A. J. Urquhart, S. A. Stephenson, D. J. Richard, and K. J. O'Byrne, "Functions and therapeutic roles of exosomes in cancer," *Frontiers in Oncology*, vol. 4, article 127, 2014.
- [113] S. Khan, J. R. Aspe, M. G. Asumen et al., "Extracellular, cell-permeable survivin inhibits apoptosis while promoting proliferative and metastatic potential," *British Journal of Cancer*, vol. 100, no. 7, pp. 1073–1086, 2009.
- [114] Z. Y. A. Elmageed, Y. Yang, R. Thomas et al., "Neoplastic reprogramming of patient-derived adipose stem cells by prostate cancer cell-associated exosomes," *Stem Cells*, vol. 32, no. 4, pp. 983–997, 2014.
- [115] C. Cossetti, L. Lugini, L. Astrologo, I. Saggio, S. Fais, and C. Spadafora, "Soma-to-germline transmission of RNA in mice xenografted with human tumour cells: possible transport by exosomes," *PLoS ONE*, vol. 9, no. 7, Article ID e101629, 2014.
- [116] L. Lugini, M. Valtieri, C. Federici et al., "Exosomes from human colorectal cancer induce a tumor-like behavior in colonic mesenchymal stromal cells," *Oncotarget*, vol. 7, no. 31, pp. 50086–50098, 2016.
- [117] J. E. Park, H. S. Tan, A. Datta et al., "Hypoxic tumor cell modulates its microenvironment to enhance angiogenic and metastatic potential by secretion of proteins and exosomes," *Molecular & Cellular Proteomics*, vol. 9, no. 6, pp. 1085–1099, 2010.
- [118] M. Aga, G. L. Bentz, S. Raffa et al., "Exosomal HIF1 α supports invasive potential of nasopharyngeal carcinoma-associated LMP1-positive exosomes," *Oncogene*, vol. 33, no. 37, pp. 4613–4622, 2014.
- [119] H. Peinado, M. Alečković, S. Lavotshkin et al., "Melanoma exosomes educate bone marrow progenitor cells toward a pro-metastatic phenotype through MET," *Nature Medicine*, vol. 18, no. 6, pp. 883–891, 2012.
- [120] A. Zomer, C. Maynard, F. J. Verweij et al., "In vivo imaging reveals extracellular vesicle-mediated phenocopying of metastatic behavior," *Cell*, vol. 161, no. 5, pp. 1046–1057, 2015.
- [121] Y. Wei, X. Lai, S. Yu et al., "Exosomal miR-221/222 enhances tamoxifen resistance in recipient ER-positive breast cancer cells," *Breast Cancer Research and Treatment*, vol. 147, no. 2, pp. 423–431, 2014.
- [122] R. Safaei, B. J. Larson, T. C. Cheng et al., "Abnormal lysosomal trafficking and enhanced exosomal export of cisplatin in drug-resistant human ovarian carcinoma cells," *Molecular Cancer Therapeutics*, vol. 4, no. 10, pp. 1595–1604, 2005.
- [123] C. Federici, F. Petrucci, S. Caimi et al., "Exosome release and low pH belong to a framework of resistance of human melanoma cells to cisplatin," *PLoS ONE*, vol. 9, no. 2, Article ID e88193, 2014.
- [124] C. Gutiérrez-Vázquez, C. Villarroja-Beltri, M. Mittelbrunn, and F. Sánchez-Madrid, "Transfer of extracellular vesicles during immune cell-cell interactions," *Immunological Reviews*, vol. 251, no. 1, pp. 125–142, 2013.
- [125] G. Andreola, L. Rivoltini, C. Castelli et al., "Induction of lymphocyte apoptosis by tumor cell secretion of FasL-bearing microvesicles," *The Journal of Experimental Medicine*, vol. 195, no. 10, pp. 1303–1316, 2002.
- [126] V. G. Y. Nanda, W. Peng, P. Hwu et al., "Melanoma and immunotherapy bridge 2015," *Journal of Translational Medicine*, vol. 14, supplement 1, p. 65, 2015.
- [127] "Scientific Program 2012 ISEV meeting Wednesday 18th April," *Journal of Extracellular Vesicles (JEV)*, vol. 1, no. 1, p. 18182, 2012.
- [128] M. M. Rashid, A. Runci, L. Polletta et al., "Muscle LIM protein/CSRP3: a mechanosensor with a role in autophagy," *Cell Death Discovery*, vol. 1, no. 1, 2015.
- [129] D. L. Oliveira, C. G. Freire-de-Lima, J. D. Nosanchuk, A. Casadevall, M. L. Rodrigues, and L. Nimrichter, "Extracellular vesicles from *Cryptococcus neoformans* modulate macrophage functions," *Infection and Immunity*, vol. 78, no. 4, pp. 1601–1609, 2010.
- [130] P. C. Albuquerque, E. S. Nakayasu, M. L. Rodrigues et al., "Vesicular transport in *Histoplasma capsulatum*: an effective mechanism for trans-cell wall transfer of proteins and lipids in ascomycetes," *Cellular Microbiology*, vol. 10, no. 8, pp. 1695–1710, 2008.
- [131] M. F. Goncalves, E. S. Umezawa, A. M. Katzin et al., "*Trypanosoma cruzi*: shedding of surface antigens as membrane vesicles," *Experimental Parasitology emphasizes*, vol. 72, no. 1, pp. 43–53, 1991.
- [132] T. N. Bukong, F. Momen-Heravi, K. Kodys, S. Bala, and G. Szabo, "Exosomes from hepatitis C infected patients transmit HCV infection and contain replication competent viral RNA in complex with Ago2-miR122-HSP90," *PLoS Pathogens*, vol. 10, no. 10, Article ID e1004424, 2014.
- [133] K. Tamai, N. Tanaka, T. Nakano et al., "Exosome secretion of dendritic cells is regulated by Hrs, an ESCRT-0 protein," *Biochemical and Biophysical Research Communications*, vol. 399, no. 3, pp. 384–390, 2010.
- [134] C. Hsu, Y. Morohashi, S.-I. Yoshimura et al., "Regulation of exosome secretion by Rab35 and its GTPase-activating proteins TBC1D10A-C," *The Journal of Cell Biology*, vol. 189, no. 2, pp. 223–232, 2010.
- [135] J. M. Silverman, J. Clos, E. Horakova et al., "*Leishmania* - modulate innate and adaptive immune responses through effects on monocytes and dendritic cells," *The Journal of Immunology*, vol. 185, no. 9, pp. 5011–5022, 2010.
- [136] E. Berrone, C. Corona, M. Mazza et al., "Detection of cellular prion protein in exosomes derived from ovine plasma," *Journal of General Virology*, vol. 96, no. 12, pp. 3698–3702, 2015.
- [137] J. L. Kadurugamuwa and T. J. Beveridge, "Bacteriolytic effect of membrane vesicles from *Pseudomonas aeruginosa* on other bacteria including pathogens: Conceptually new antibiotics," *Journal of Bacteriology*, vol. 178, no. 10, pp. 2767–2774, 1996.
- [138] Z. Li, A. J. Clarke, and T. J. Beveridge, "A major autolysin of *Pseudomonas aeruginosa*: Subcellular distribution, potential

- role in cell growth and division, and secretion in surface membrane vesicles," *Journal of Bacteriology*, vol. 178, no. 9, pp. 2479–2488, 1996.
- [139] J.-F. Dubern and S. P. Diggle, "Quorum sensing by 2-alkyl-4-quinolones in *Pseudomonas aeruginosa* and other bacterial species," *Molecular BioSystems*, vol. 4, no. 9, pp. 882–888, 2008.
- [140] N. C. Kesty and M. J. Kuehn, "Incorporation of heterologous outer membrane and periplasmic proteins into *Escherichia coli* outer membrane vesicles," *The Journal of Biological Chemistry*, vol. 279, no. 3, pp. 2069–2076, 2004.
- [141] A. J. McBroom and M. J. Kuehn, "Release of outer membrane vesicles by Gram-negative bacteria is a novel envelope stress response," *Molecular Microbiology*, vol. 63, no. 2, pp. 545–558, 2007.
- [142] S. S. Thompson, Y. M. Naidu, and J. J. Pestka, "Ultrastructural localization of an extracellular protease in *Pseudomonas fragi* by using the peroxidase-antiperoxidase reaction," *Applied and Environmental Microbiology*, vol. 50, no. 4, pp. 1038–1042, 1985.
- [143] S. R. Schooling and T. J. Beveridge, "Membrane vesicles: an overlooked component of the matrices of biofilms," *Journal of Bacteriology*, vol. 188, no. 16, pp. 5945–5957, 2006.
- [144] N. C. Kesty, K. M. Mason, M. Reedy, S. E. Miller, and M. J. Kuehn, "Enterotoxigenic *Escherichia coli* vesicles target toxin delivery into mammalian cells," *EMBO Journal*, vol. 23, no. 23, pp. 4538–4549, 2004.
- [145] S. M. van Dommelen, P. Vader, S. Lakhal et al., "Microvesicles and exosomes: opportunities for cell-derived membrane vesicles in drug delivery," *Journal of Controlled Release*, vol. 161, no. 2, pp. 635–644, 2012.
- [146] P. Kharaziha, S. Ceder, Q. Li, and T. Panaretakis, "Tumor cell-derived exosomes: a message in a bottle," *Biochimica et Biophysica Acta (BBA) - Reviews on Cancer*, vol. 1826, no. 1, pp. 103–111, 2012.
- [147] S. El Andaloussi, I. Mäger, X. O. Breakefield, and M. J. A. Wood, "Extracellular vesicles: biology and emerging therapeutic opportunities," *Nature Reviews Drug Discovery*, vol. 12, no. 5, pp. 347–357, 2013.
- [148] J. Gao, D. Chu, and Z. Wang, "Cell membrane-formed nanovesicles for disease-targeted delivery," *Journal of Controlled Release*, vol. 224, pp. 208–216, 2016.
- [149] B. Escudier, T. Dorval, N. Chaput et al., "Vaccination of metastatic melanoma patients with autologous dendritic cell (DC) derived-exosomes: results of the first phase I clinical trial," *Journal of Translational Medicine*, vol. 3, no. 1, article 10, 2005.
- [150] M. A. Morse, J. Garst, T. Osada et al., "A phase I study of dexamethasone immunotherapy in patients with advanced non-small cell lung cancer," *Journal of Translational Medicine*, vol. 3, article 9, 2005.
- [151] Y. Zhang, L. Li, J. Yu et al., "Microvesicle-mediated delivery of transforming growth factor $\beta 1$ siRNA for the suppression of tumor growth in mice," *Biomaterials*, vol. 35, no. 14, pp. 4390–4400, 2014.
- [152] A. Tan, H. de la Peña, and A. M. Seifalian, "The application of exosomes as a nanoscale cancer vaccine," *International Journal of Nanomedicine*, vol. 5, no. 1, pp. 889–900, 2010.
- [153] N. Kosaka, F. Takeshita, Y. Yoshioka et al., "Exosomal tumor-suppressive microRNAs as novel cancer therapy. "Exocure" is another choice for cancer treatment," *Advanced Drug Delivery Reviews*, vol. 65, no. 3, pp. 376–382, 2013.
- [154] E. Iessi, M. Logozzi, L. Lugini et al., "Acridine orange/exosomes increase the delivery and the effectiveness of acridine orange in human melanoma cells: A new prototype for theranostics of tumors," *Journal of Enzyme Inhibition and Medicinal Chemistry*, vol. 32, no. 1, pp. 648–657, 2017.
- [155] K. Kusuzaki, T. Matsubara, H. Murata et al., "Natural extracellular nanovesicles and photodynamic molecules: is there a future for drug delivery?" *Journal of Enzyme Inhibition and Medicinal Chemistry*, vol. 32, no. 1, pp. 908–916, 2017.
- [156] M. Iero, R. Valenti, V. Huber et al., "Tumour-released exosomes and their implications in cancer immunity," *Cell Death & Differentiation*, vol. 15, no. 1, pp. 80–88, 2008.
- [157] A. M. Marleau, C.-S. Chen, J. A. Joyce, and R. H. Tullis, "Exosome removal as a therapeutic adjuvant in cancer," *Journal of Translational Medicine*, vol. 10, no. 1, article 134, 2012.

Research Article

Detection of HER2 through Antibody Immobilization Is Influenced by the Properties of the Magnetite Nanoparticle Coating

Enrique Villegas-Serralta,¹ Oscar Zavala,² Israel Alejandro Flores-Urquizo,³ Perla E. García-Casillas ¹, and Christian Chapa González ¹

¹Instituto de Ingeniería y Tecnología, Universidad Autónoma de Ciudad Juárez, Ciudad Juárez, CHIH, Mexico

²Instituto de Ciencias Biomédicas, Universidad Autónoma de Ciudad Juárez, Ciudad Juárez, CHIH, Mexico

³Facultad de Ciencias Químicas, Universidad Autónoma de Nuevo León, San Nicolás de los Garza, NL, Mexico

Correspondence should be addressed to Christian Chapa González; christian.chapa@uacj.mx

Received 28 July 2017; Revised 27 December 2017; Accepted 12 February 2018; Published 2 April 2018

Academic Editor: Jin-Ho Choy

Copyright © 2018 Enrique Villegas-Serralta et al. This is an open access article distributed under the Creative Commons Attribution License, which permits unrestricted use, distribution, and reproduction in any medium, provided the original work is properly cited.

Considerable effort has been focused on improving the control of size, shape, and surface modifications to detect proteins. The purpose of this study was to compare the efficiencies of aminosilane-coated magnetite (As-M) nanoparticles (NPs), dextran-coated magnetite nanoparticles (Dx-M), and bare nanoparticles for conjugating single-chain variable fragment antibodies (scFvs) with the aim of detecting the human epidermal growth factor receptor 2 (HER2) protein. Dx-M and As-M NPs were characterized using scanning electron microscopy, energy dispersive X-ray spectroscopy, X-ray diffraction, and Raman spectroscopy. Dx-M and As-M were conjugated with a monoclonal scFv for active targeting of the HER2 antigen. Aminosilane surface coating enhanced the scFv conjugation efficiency over twofold compared to that of the dextran-coated magnetite NPs for the detection of HER2 proteins.

1. Introduction

The development of nanomaterials has been widely touted as a revolutionary paradigm shift for biological applications. In recent years, considerable effort has been focused on improving the control of size, shape, and surface modifications to gain better behavior as well as improved functionalization. Magnetic nanoparticles (NPs) have become widely studied due to the rapid increase in the number of applications in the biomedical field, such as magnetic resonance imaging [1], hyperthermia [2], drug delivery [3, 4], gene therapy [5, 6], protein immobilization [7, 8], and immunoassay [9]. Among other applications of magnetic NPs, for the immunoassay, the conjugation of NPs with antibodies is the critical step and severely limited by low efficiency of antibodies grafted on the NP surface.

Although there has been significant work done on the conjugation of chemically synthesized magnetite NPs to antibodies [10–15] there have been relatively few studies

comparing the influence of antibody immobilization method in effectiveness of antigen detection. The conjugation of the proteins with magnetic NPs can be done via physical adsorption using polymer coatings, such as dextran, and by covalent immobilization using amino derivatives, such as aminosilane [3]. Dextran is a natural polysaccharide that confers exceptionally high colloidal stability to NPs [16]. 3-(2-aminoethylamino) propyltrimethoxysilane (APTES) is the most frequently used compound to produce the aminosilane coating to enhance protein adhesion [17–20]. Both dextran and aminosilane have been used for the surface modification of NPs to immobilize antibodies and to improve the dispersion of magnetite NPs. Despite the influence on dispersion stability of the NPs, the type of coating has a remarkable influence on the effectiveness of antibody immobilization.

The effectiveness of conjugation has an impact on the detection of bioanalytes, such as cancer biomarkers. Overexpression of human epidermal growth factor receptor 2 (HER2) is common to several types of human carcinomas [21–23], is

involved in cell growth, and is a recognized biomarker for breast cancer therapy [24–27]. The aim of this study is to compare aminosilane-coated magnetite (As-M) NPs and dextran-coated magnetite (Dx-M) NPs conjugated with recombinant single-chain variable fragment antibodies (scFvs) to Her2 (anti-HER2) through an adapted enzyme-linked immunosorbent assay (ELISA) in order to choose the most efficient scFv immobilizing agent.

2. Materials and Methods

2.1. Synthesis of Magnetite NPs. Magnetite NPs were synthesized by alkaline coprecipitation of two equivalents of ferric chloride ($\text{FeCl}_3 \cdot 6\text{H}_2\text{O}$; Mallinckrodt) and one equivalent of ferrous sulfate ($\text{FeSO}_4 \cdot 7\text{H}_2\text{O}$; J.T.Baker) in 30% ammonium hydroxide solution (NH_4OH ; J.T.Baker) with stirring. The obtained precipitate was centrifuged at 6,000 rpm and washed several times with distilled water until a pH ~ 7 was reached. Finally, the precipitate was dried at 80°C for 24 hours.

2.1.1. scFv Conjugation on Dx-M NPs. For the preparation of Dx-M NPs, dextran (molecular weight 20,000 Da) was dissolved in distilled water. FeCl_3 (0.01 M) and FeSO_4 (0.005 M) were dispersed in 0.05% dextran solution. Synthesis of the NPs was done as previously described. The products were separated with a magnet and washed several times with deionized water. Dx-M was resuspended in phosphate buffer solution (pH 7.4). Then, 500 μL of Dx-M suspension and 500 μL of scFvs were mixed by stirring gently and incubated in a cold room at 4°C for 24 hours. The products were collected with a magnet and washed with buffer.

2.1.2. scFv Conjugation on As-M NPs. The obtained magnetite powder (200 mg) was dispersed in 150 mL of ethanol and sonicated for 15 minutes, before the addition of 3-(2-aminoethylamino) propyltrimethoxysilane (AEPTMS, Sigma-Aldrich). After ultrasonic agitation for 30 min, the suspended NPs were collected by magnetic decantation. The precipitated product (As-M) was washed with ethanol five times and dried at 80°C for 24 hours. The As-M NPs were resuspended in 1.0 mL of 2% glutaraldehyde aqueous solution with stirring for 4 hours at room temperature. Then, a mixture of 500 μL of As-M and 500 μL of scFvs was added and incubated in a cold room at 4°C for 24 hours to allow conjugation to take place. Finally, the solution was dialyzed with phosphate buffered saline (PBS).

2.2. Characterization of NPs. The bare magnetite sample was analyzed in PANalytical X'Pert MRD PRO device with a Cu- α source ($\lambda = 1.5406 \text{ \AA}$) operating at 40 kV and 30 mA and at a scanning rate of $0.1^\circ 2\theta\text{s}^{-1}$ from 10 to $80^\circ 2\theta$. Distances between peaks were compared to the International Centre for Diffraction Data JCDPS, number 5-0664. The average diffracting crystallite size of the prepared NPs was calculated using Scherrer's equation from the most intense peak. Scanning electron microscopy (SEM) was performed using a JEOL JSM6010LV/PLUS SEM to determine the

particle size and morphology of the magnetite nanoparticles. For particle size analysis, the image processing software Scandium was used and 100 particles were analyzed to calculate the mean diameter \pm standard deviation (SD). SEM images were made with an accelerating voltage of 20 kV and a working distance of 410 mm. Energy dispersive X-ray spectroscopy (EDS) using an Inca apparatus (Oxford Instruments, Oxford, UK) was done for elemental analysis or chemical characterization of the samples. TEM data was also provided to confirm the chemically well-defined magnetite nanoparticles. Hydrodynamic diameters and zeta potentials were analyzed using a dynamic light scattering (DLS) (Nanotracer Wave, Microtrac) operating at 25°C in a scattering angle of 180° ; samples were suspended in Triton 2%, pH 7, and sonicated 5 minutes prior to measurement. Fourier transform infrared spectra (FTIR) were recorded using a spectrometer (Nicolet 6700/Thermo Electron) to identify functional groups present in the surface-modified magnetite nanoparticles. Infrared spectra with attenuated total reflection (ATR) were recorded with a resolution of 4 cm^{-1} and the scan range was set from 4000 to 600 cm^{-1} . Raman spectra were recorded in a WiTec system model Alpha 300 RA equipped with a 785 nm laser source. Raman spectroscopy was used to measure bands of -S-S-, -N-C-N-, and -C-S-, which are likely to be found in proteins (scFvs). These groups are rich in π -electron and, thus, have larger polarizability and totally symmetric vibrational modes that are Raman active but may not be infrared (IR) active and show no IR bands [28]. Because of these differences and considering that water, the natural medium for proteins is a weak Raman scatterer; Raman was the method chosen for characterization of antibody-NP conjugate. In addition, for proteins, studies focused on investigating Raman spectra of proteins and the successful design of NP probes has allowed advances in immunoassays [29].

2.3. ELISA. Aliquots (50 μL) of the homogenized suspensions (scFv-Dx-M, scFv-As-M, and Dx-M) were deposited on the bottom of wells in a 96 well microplate. Next, a permanent magnet was used to immobilize the conjugates at the bottom. The plates were blocked with PBS containing 5% bovine serum albumin (BSA). Successively, anti-HA antibody and horseradish peroxidase (HRP; GE Healthcare Life Sciences) were added and incubated at 37°C for 1 hour. Unbound anti-HA was discarded by washing. All washing steps were performed with 200 μL of PBS-0.05% Tween 20. Finally, 50 μL of 2,2'-Azino-bis(3-ethylbenzthiazoline-6-sulfonic acid) (ABTS, Roche) was added and incubated for 15 minutes at room temperature and the absorbance was read at $\lambda = 405 \text{ nm}$ in a Benchmark Plus device (Bio-Rad, Hercules, CA, USA). Each independent experiment was run in triplicate.

2.4. Statistical Analyses. Data are presented as the mean \pm standard deviation (SD). Differences between groups were assessed by one-way analysis of variance (ANOVA) followed by Tukey's Multiple Comparison Analysis test. Values were determined as significant when $P < 0.05$.

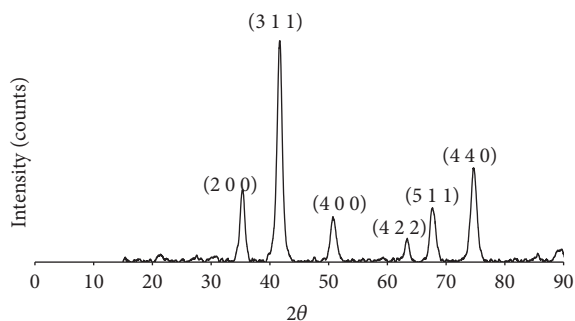


FIGURE 1: XRD pattern for the magnetite (Fe_3O_4) nanoparticles.

3. Results and Discussion

The X-ray diffraction (XRD) pattern of uncoated magnetite is shown in Figure 1, with the peaks corresponding to the planes for (2 2 0), (3 1 1), (4 0 0), (4 2 2), (5 1 1), and (4 4 0); peaks are matched in position and in relative intensity to the inverse spinel structure of magnetite pattern according to JCPDS 5-0664. The average size of the crystallite was calculated by the Scherrer equation [30–33], in which peak width is inversely proportional to crystallite size. The average crystallite size was 10.1 nm, which is consistent with the size of superparamagnetic particles [34].

SEM revealed the morphological properties of the prepared samples (Figure 2). Monodisperse magnetite NPs were successfully synthesized. While a number of suitable methods have been developed for the synthesis of magnetic NPs, the coprecipitation method yielded magnetite NPs with a relatively uniform and spherical morphology with narrow particle size distribution (8 ± 5 nm) according to SEM measurements. The mean diameter of both coated particles was around 20 nm. Furthermore, the EDS spectrum revealed Fe and O in bare magnetite samples; Fe, O, and C in Dx-M samples; and Fe, O, and Si in As-M samples, consistent with the presence of aminosilane-modified NPs. In all the samples, the carbon signal appeared due to the preparation of the sample; however in Dx-M sample the signal was more intense.

Representative TEM image with corresponding size distribution of magnetite nanoparticles is shown in Figure 3. Well-defined nearly spherically shaped nanoparticles were indeed obtained. Their average size, determined from the statistical sample of over one hundred nanoparticles, was found to be 9.0 nm, while standard deviation of 2.3 nm indicated a reasonably narrow size distribution. Moreover, notice the accurate agreement between the average diameter assessed from both XRD and TEM data confirming the presence of monodomain nanoparticles.

Figure 4 shows the hydrodynamic size of M, As-M, and Dx-M samples. The particle size, its distribution, and the surface charge of Fe_3O_4 are very important parameters not only for modifying Fe_3O_4 nanoparticles, but also for biomedical applications. The coating of the nanoparticles can be evaluated by measuring the zeta potential. The results of the mean hydrodynamic diameter, polydispersity index (PDI), and zeta potential of the surface-modified magnetite nanoparticles

TABLE 1: Hydrodynamic diameter, polydispersity index, and zeta potential of M, As-M, and Dx-M.

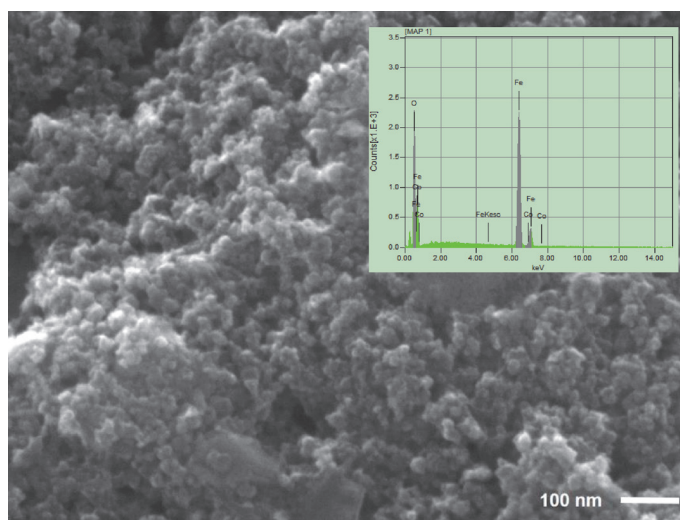
| Sample | HD, nm | SD | ZP, mV |
|--------|--------|------|--------|
| M | 4.97 | 1.64 | -1.10 |
| As-M | 11.48 | 5.68 | -23.10 |
| Dx-M | 7.47 | 2.31 | -8.56 |

Abbreviations. M: magnetite nanoparticles; Dx-M: dextran-modified magnetite nanoparticles; As-M: AEPTMS-modified magnetite nanoparticles; HD: hydrodynamic diameter; SD: standard deviation; ZP: zeta potential.

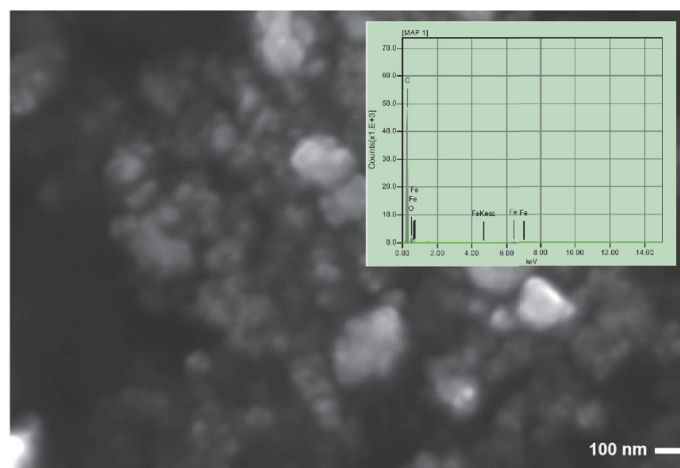
developed in this study are listed in Table 1. The smallest hydrodynamic diameter of about 4.97 ± 1.64 nm was obtained for bare magnetite nanoparticles. The mean particles size of As-M and Dx-M was found to be 11.48 ± 5.68 , and 7.47 ± 2.31 nm, respectively, suggesting that the AEPTMS coating did induce a significant increase of the mean particles size ($P < 0.05$). Contrastingly, the coating with dextran did not induce a significant increase of the particles diameter ($P < 0.05$). The zeta potential value obtained for M was slightly negative (-1.10 mV); this explains why magnetite nanoparticles do not remain suspended for a long period of time. A zeta potential of -23.10 mV was observed for magnetite nanoparticles coated with AEPTMS. Thus, the use of AEPTMS as a coating also contributed to an increase in colloidal stability. The zeta potential of Dx-M nanoparticles was -8.56 mV, which suggested that the nanoparticles were mainly stabilized by steric repulsion.

The FTIR-ATR comparative spectra of bare and coated Fe_3O_4 nanoparticles, as well as the coating molecules, are displayed in Figure 5. The samples that contain magnetite (M, Dx-M, and As-M) clearly reveal the presence of strong IR absorption band between 500 and 600 cm^{-1} characteristic to the Fe-O vibration. IR spectra of pure AEPTMS are shown in Figure 5(b) while the IR spectra of As-M are shown in Figure 5(c). The IR spectrum of AEPTMS exhibits absorptions at 2890 cm^{-1} and 1059 cm^{-1} , which are characteristic peaks of the stretching vibration of C-H and Si-O, respectively. In the spectrum for As-M the peaks for the functional group N-H and silane binding are marked. A displacement of the Si-O peak is observed in the As-M NPs. The peak found at 1383 cm^{-1} attributed to the stretching vibrations of C-N bond, along with the band at 3360 cm^{-1} attributed to the H-N-H bending mode of free amino groups, indicates that the AEPTMS has been grafted onto the nanoparticles' surface. In the same way, Figures 5(d) and 5(e) give the IR absorption spectra of pure dextran and Dx-M, respectively. The very broad band at 3380 cm^{-1} in both Dx and Dx-M can be attributed to the stretching vibration of O-H. The absorption bands at 2924 cm^{-1} can be ascribed to the asymmetrical stretching vibration of C-H and the band at 1008 cm^{-1} belongs to stretching vibrations of C-O-C bond and glycosidic bridge. Regardless of the Fe-O band found in Dx-M, very few differences can be found in the IR spectra of Dx and Dx-M which indicates that dextran coating occurs by physical adsorption.

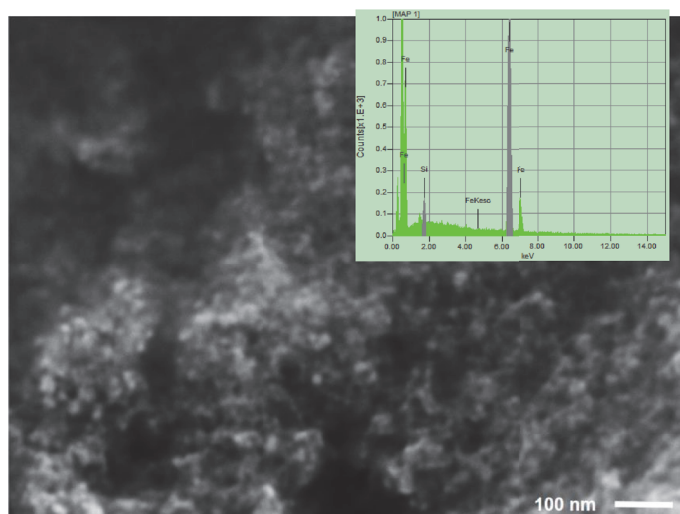
Nevertheless, to further evaluate the antibody Raman spectroscopy was conducted. Raman spectra of the obtained



(a)



(b)



(c)

FIGURE 2: SEM image and EDS analysis of (a) uncoated magnetite nanoparticles, (b) DX-M nanoparticles, and (c) As-M nanoparticles.

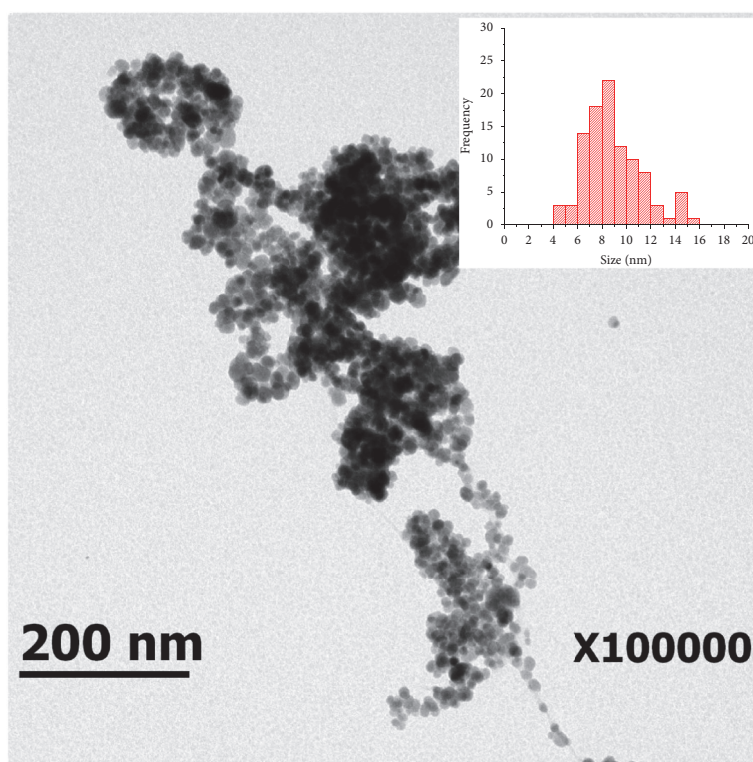


FIGURE 3: TEM image of bare magnetite nanoparticles with image with corresponding size distribution.

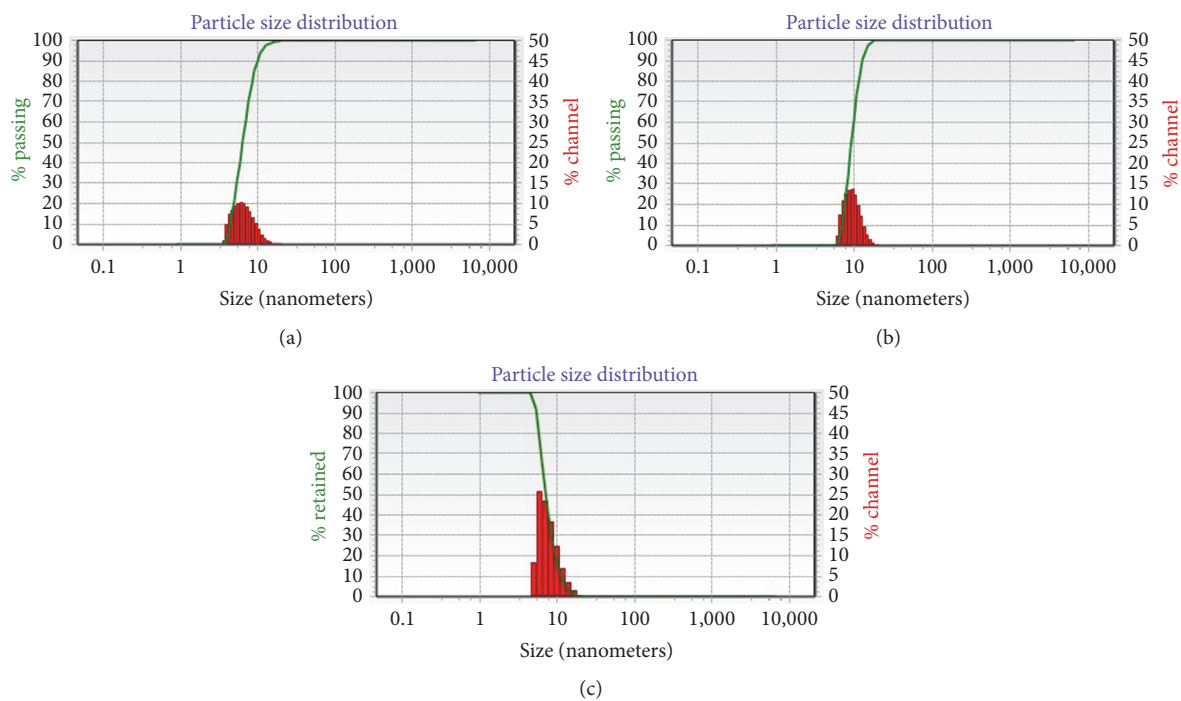


FIGURE 4: Particle size distribution of (a) magnetite, (b) AEPTMS-coated magnetite, and (c) dextran-coated magnetite.

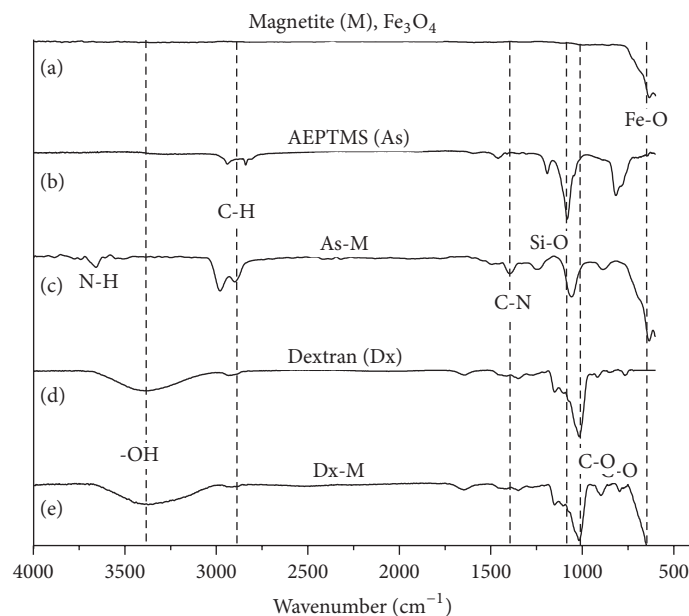


FIGURE 5: FTIR spectra of (a) magnetite, (b) AEPTMS, (c) aminosilane-coated magnetite, (d) dextran, and (e) dextran-coated magnetite.

materials are shown in Figure 6. According to the literature, the modes present at 207, 392, and 470 cm^{-1} (Figure 6(a)) correspond to magnetite [35] and the band at near 1300 cm^{-1} is also attributable at magnetite [36, 37]. In the other samples, the spectral bands seen below 800 cm^{-1} are primarily attributed to presence of magnetite [38] (Figures 6(b), 6(c), 6(e), and 6(f)). The Raman spectrum for the Dx-M included the typical signals for the dextran and weak bands typical of magnetite. For the Raman spectroscopy of the Dx-M, the surface modification of dextran-coated magnetite manifested in the electronic and vibrational properties of the magnetite and resulted in the lowering of the energy (Figure 6(b)). For aminosilane treated surfaces (Figure 6(c)), the characteristic bands at 1117 cm^{-1} corresponded to Si-O-C, 1348 cm^{-1} could be attributed to Csp³ bound with or without heteroatoms, 1575 cm^{-1} was associated with bound Csp², and 3300 cm^{-1} was related to an amine group. The results were consistent with the presence of aminosilane on the surface of the magnetite NPs. Raman spectroscopy of the antibody (Ab) soluble scFv (Figure 6(d)) was obtained. The test solution contained 1 $\mu\text{g}/\text{mL}$ scFv diluted in PBS. The Raman spectra scFv is typical of proteins [38, 39] with bands associated with disulfide bonds (-S-S-, 544 cm^{-1}), polypeptide backbone (C α -C, 940 cm^{-1}), aromatic amino acids (phenylalanine, tryptophan, and tyrosine, bands from 1000 to 1205 cm^{-1}), C-H deformation (1325 and 1452 cm^{-1}), and amide III (1267 cm^{-1}). The immobilization of the antibodies in both conjugates Dx-M and As-M were consistent with the Raman spectra of Dx-M-Ab (Figure 6(e)) and As-M-Ab (Figure 6(f)); both exhibited bands characteristic of the scFvs. The Raman spectrum for the Dx-M-Ab conjugates included the typical signals for the dextran and weak bands

typical of proteins (amide I and phenylalanine aromatic ring near at 1600 cm^{-1}). The Raman band at $\approx 1550 \text{ cm}^{-1}$ arises from an indole ring vibration that is contributed mainly by Trp in Dx-M-Ab and As-M-Ab samples [20].

The conjugated product was verified by ELISA using a magnetic separator (Figure 7). Fifty microliters of the homogenized suspensions (scFv-Dx-M, scFv-As-M, and Dx-M) were used for ELISA using a magnet to immobilize the conjugates (Figure 7) using HRP-conjugated anti-HA. The ABTS assay is a colorimetric assay based on the ABTS cation radical formation. The radical formation is catalyzed by the reduction of HRP in the presence of H₂O₂. Employing this assay, we are able to compare the absorbance generating from the Dx-M-Ab and As-M-Ab conjugates and Dx-M nonconjugate scFv (as the negative control) against a secondary anti-HA antibody. The 2-fold difference in ELISA absorbance between scFv-AsM conjugates and scFv-DxM was indicative of successful conjugation (Figure 8). Based on the results of the evaluation of the ability of anti-HER2 scFv-magnetite conjugate in binding and detecting the studied protein, the chemical modification with aminosilane remarkably improved the protein detection. In addition, the success of binding to HER2 by As-M confirmed the existence of stable chemical bonding between the NPs and antibody. This was not evident in the Dx-M material whose modification occurs primarily by physical adsorption. However, a considerable difference was observed with respect to the first coating. The results allowed us to infer that, despite the washes performed on the aminosilane coating, the continuous antibody coupled to the nanoparticles and was recognized by the secondary anti-HA antibody. The results indicate that this coating is suitable for this type of material bioconjugate.

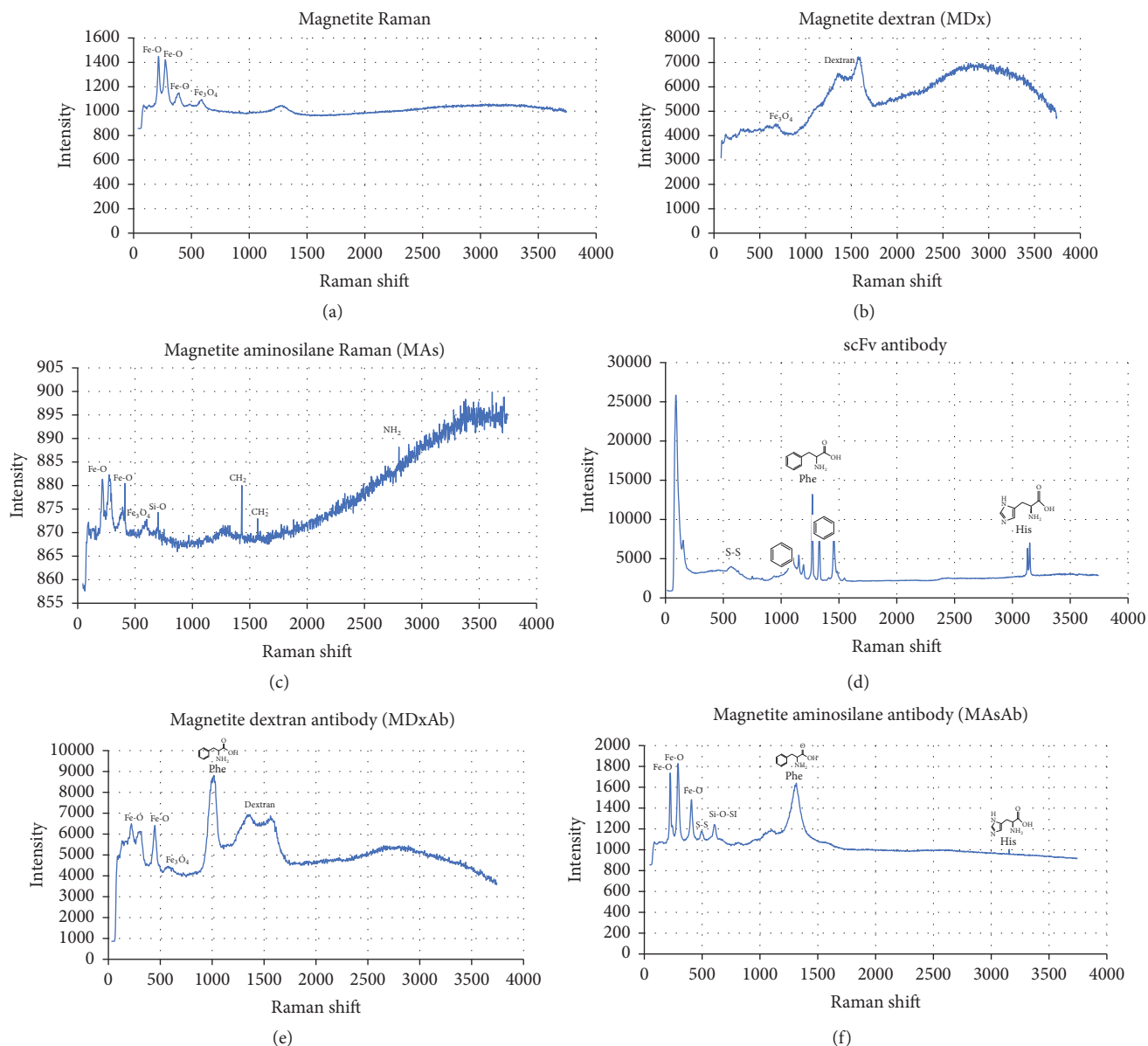


FIGURE 6: Comparative Raman spectra of (a) magnetite, (b) dextran-coated magnetite, (c) aminosilane-coated magnetite, (d) scFv antibody, (e) scFv conjugated with dextran-coated magnetite, and (f) scFv conjugated with aminosilane-coated magnetite.

4. Conclusions

In this study, well-defined magnetite nanoparticles with a narrow size distribution and coated with AEPTMS and dextran were successfully obtained. Furthermore, zeta potential measurements show that the magnetite nanoparticles coated with AEPTMS or dextran are stable in aqueous suspension at pH 7 which makes these nanomaterials suitable for biomedical applications. Surface-modified magnetite nanoparticles containing antibodies were prepared and their antigen recognition ability toward HER2 as a model biomarker was performed. We successfully used this nanomaterial to study how coating changes the efficiency of antibody conjugation and, consequently, how it also affects protein detection in

the magnetic bead ELISA. As-M NPs were more efficient in scFv immobilization than Dx-M NPs conjugated with recombinant scFv anti-Her2. This strategy provides an alternative approach to controlling surface functionalization with a view to preparing high-efficiency receptor for specific proteins. The immunoconjugate was proven to have a biomarker-targeting activity. Such As-M might be very useful for biomagnetically targeted detection in several types of human carcinoma.

Conflicts of Interest

The authors declare that there are no conflicts of interest regarding the publication of this article.

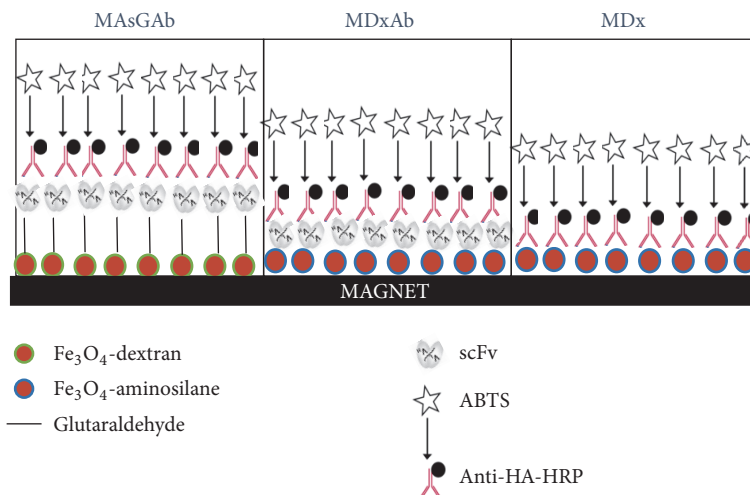


FIGURE 7: Scheme of the adapted ELISA using a permanent magnet to immobilize the conjugates.

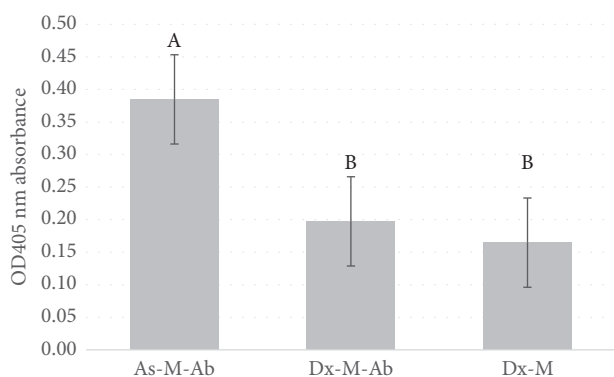


FIGURE 8: ELISA distinguishes specific binding to HER2 protein. All nanomaterial, except the As-M-antibody, has an absorbance value < 0.20. Anti-HER2 scFv conjugated with As-M can detect HER2 protein, with a 1.95-fold difference compared with Dx-M-antibody. Dx-M (nonconjugate scFv) was used as the negative control. The results were obtained from triplicate determinations and are expressed as mean ± SD.

Acknowledgments

The authors thank Karla Jacqueline Licon, for her help in preparing the manuscript, and Professor Carlos Rodriguez from UTCJ, for providing the SEM-EDS facilities.

References

- [1] S. Shabestari Khiabani, M. Farshbaf, A. Akbarzadeh, and S. Davaran, "Magnetic nanoparticles: preparation methods, applications in cancer diagnosis and cancer therapy," *Artificial Cells, Nanomedicine and Biotechnology*, vol. 45, no. 1, pp. 6–17, 2017.
- [2] K. Adhikary and M. Banerjee, "A thermofluid analysis of the magnetic nanoparticles enhanced heating effects in tissues embedded with large blood vessel during magnetic fluid hyperthermia," *Journal of Nanoparticles*, vol. 2016, 18 pages, 2016.
- [3] L. Buzoglu, E. Maltas, M. Ozmen, and S. Yildiz, "Interaction of donepezil with human serum albumin on amine-modified magnetic nanoparticles," *Colloids and Surfaces A: Physicochemical and Engineering Aspects*, vol. 442, pp. 139–145, 2014.
- [4] E. Maltas and M. Ozmen, "Spectrofluorometric and thermal gravimetric study on binding interaction of thiabendazole with hemoglobin on epoxy-functionalized magnetic nanoparticles," *Materials Science and Engineering C: Materials for Biological Applications*, vol. 54, pp. 43–49, 2015.
- [5] J. Roacho-Perez, H. Gallardo-Blanco, M. Sanchez-Dominguez, P. Garcia-Casillas, C. Chapa-Gonzalez, and C. Sanchez-Dominguez, "Nanoparticles for death-induced gene therapy in cancer (Review)," *Molecular Medicine Reports*, 2017.
- [6] E. Maltas, M. Ozmen, and H. Cingilli Vural, "Interaction of L-myc oncogene in breast cancer with irinotecan onto functionalized magnetic nanoparticles," *Materials Letters*, vol. 106, pp. 8–10, 2013.
- [7] M. Bayrakci, O. Gezici, S. Z. Bas, M. Ozmen, and E. Maltas, "Novel humic acid-bonded magnetite nanoparticles for protein immobilization," *Materials Science and Engineering C: Materials for Biological Applications*, vol. 42, pp. 546–552, 2014.
- [8] E. Maltas, M. Ozmen, H. C. Vural, S. Yildiz, and M. Ersoz, "Immobilization of albumin on magnetite nanoparticles," *Materials Letters*, vol. 65, no. 23–24, pp. 3499–3501, 2011.
- [9] A. E. Urusov, A. V. Petrakova, A. V. Zherdev, and B. B. Dzantiev, "Magnetic nanoparticles as carriers for immunoassays," *Nano Hybrids and Composites*, vol. 13, pp. 54–62, 2017.
- [10] M. Suzuki, M. Shinkai, M. Kamihira, and T. Kobayashi, "Preparation and characteristics of magnetite-labelled antibody with the use of poly(ethylene glycol) derivatives," *Biotechnology and Applied Biochemistry*, vol. 21, pp. 335–45, 1995.
- [11] E.-Q. Song, J. Hu, C.-Y. Wen et al., "Fluorescent-magnetic-biotargeting multifunctional nanobioprobes for detecting and isolating multiple types of tumor cells," *ACS Nano*, vol. 5, no. 2, pp. 761–770, 2011.
- [12] S. A. Martel-Estrada, I. Olivas-Armendáriz, E. Santos-Rodriguez et al., "Evaluation of in vitro bioactivity of Chitosan/Mimosa tenuiflora composites," *Materials Letters*, vol. 119, pp. 146–149, 2014.
- [13] C. C. Gonzalez, C. A. M. Pérez, A. M. Martínez et al., "Development of antibody-coated magnetite nanoparticles for biomarker immobilization," *Journal of Nanomaterials*, vol. 2014, Article ID 978284, 7 pages, 2014.

- [14] D. Lago-Cachón, M. Rivas, C. López-Larrea, A. López-Vázquez, G. Martínez-Paredes, and J. A. García, "HeLa cells separation using MICA antibody conjugated to magnetite nanoparticles," *Physica Status Solidi (c)—Current Topics in Solid State Physics*, vol. 11, no. 5-6, pp. 1043–1047, 2014.
- [15] B. A. Otieno, C. E. Krause, and J. F. Rusling, "Bioconjugation of antibodies and enzyme labels onto magnetic beads," *Methods in Enzymology*, vol. 571, pp. 135–150, 2016.
- [16] A. K. Hauser, R. Mathias, K. W. Anderson, and J. Zach Hilt, "The effects of synthesis method on the physical and chemical properties of dextran coated iron oxide nanoparticles," *Materials Chemistry and Physics*, vol. 160, pp. 177–186, 2015.
- [17] X. Liu, J. Xing, Y. Guan, G. Shan, and H. Liu, "Synthesis of amino-silane modified superparamagnetic silica supports and their use for protein immobilization," *Colloids and Surfaces A: Physicochemical and Engineering Aspects*, vol. 238, no. 1-3, pp. 127–131, 2004.
- [18] K. Can, M. Ozmen, and M. Ersoz, "Immobilization of albumin on aminosilane modified superparamagnetic magnetite nanoparticles and its characterization," *Colloids and Surfaces B: Biointerfaces*, vol. 71, no. 1, pp. 154–159, 2009.
- [19] R. T. Reza, C. A. M. Pérez, C. A. R. González, H. M. Romero, and P. E. G. Casillas, "Effect of the polymeric coating over Fe₃O₄ particles used for magnetic separation," *Central European Journal of Chemistry*, vol. 8, no. 5, pp. 1041–1046, 2010.
- [20] I. A. Flores-Urquizo, P. García-Casillas, C. Chapa-González, and P. García-Casillas, "Development of magnetic nanoparticles Fe₂³⁺X²⁺O₄ (X= Fe, Co y Ni) coated by amino silane," *Revista Mexicana de Ingeniería Biomédica*, vol. 38, no. 1, 2017.
- [21] H.-S. Cho, K. Mason, K. X. Ramyar et al., "Structure of the extracellular region of HER2 alone and in complex with the Herceptin Fab," *Nature*, vol. 421, no. 6924, pp. 756–760, 2003.
- [22] R. D. M. C. Filho, P. Kassab, L. C. L. Claro et al., "Evaluation of the expression of the human epithelial receptor 2 (HER2) in gastric carcinoma," *The Scientific World Journal*, vol. 2016, Article ID 7951365, 6 pages, 2016.
- [23] R. J. Morrow, N. Etemadi, B. Yeo, and M. Ernst, "Challenging a misnomer? The role of inflammatory pathways in inflammatory breast cancer," *Mediators of Inflammation*, vol. 2017, Article ID 4754827, 15 pages, 2017.
- [24] S. Loibl and L. Gianni, "HER2-positive breast cancer," *The Lancet*, vol. 389, no. 10087, pp. 2415–2429, 2017.
- [25] J. O. Eloy, R. Petrilli, D. L. Chesca, F. P. Saggiaro, R. J. Lee, and J. M. Marchetti, "Anti-HER2 immunoliposomes for co-delivery of paclitaxel and rapamycin for breast cancer therapy," *European Journal of Pharmaceutics and Biopharmaceutics*, vol. 115, pp. 159–167, 2017.
- [26] S. Parakh, H. K. Gan, A. C. Parslow, I. J. G. Burvenich, A. W. Burgess, and A. M. Scott, "Evolution of anti-HER2 therapies for cancer treatment," *Cancer Treatment Reviews*, vol. 59, pp. 1–21, 2017.
- [27] von Minckwitz G. et al., "Adjuvant pertuzumab and trastuzumab in early HER2-positive breast cancer," *The New England Journal of Medicine*, vol. 377, no. 7, pp. 702–702, 2017.
- [28] X. X. Han, B. Zhao, and Y. Ozaki, "Surface-enhanced Raman scattering for protein detection," *Analytical and Bioanalytical Chemistry*, vol. 394, no. 7, pp. 1719–1727, 2009.
- [29] P. Scherrer, in *Bestimmung der inneren Struktur und der Größe von Kolloidteilchen mittels Röntgenstrahlen*, Kolloidchemie Ein Lehrbuch, pp. 187–409, Springer, Berlin, Germany, 1912.
- [30] S. A. Majetich and Y. Jin, "Magnetization directions of individual nanoparticles," *Science*, vol. 284, no. 5413, pp. 470–473, 1999.
- [31] D. Han, S. C. Hong, J. H. Lee et al., "Subtle cytotoxicity and genotoxicity differences in superparamagnetic iron oxide nanoparticles coated with various functional groups," *International Journal of Nanomedicine*, vol. 6, pp. 3219–3231.
- [32] C. Marcott, M. Padalkar, and N. Pleshko, "Infrared and raman microscopy and imaging of biomaterials at the micro and nano scale," in *Comprehensive Biomaterials II*, pp. 498–518, Elsevier, 2017.
- [33] E. Alp and N. Aydogan, "A comparative study: synthesis of superparamagnetic iron oxide nanoparticles in air and N₂ atmosphere," *Colloids and Surfaces A: Physicochemical and Engineering Aspects*, vol. 510, pp. 205–212, 2016.
- [34] L. V. Gasparov, D. Arenas, K. Choi et al., "Magnetite: Raman study of the high-pressure and low-temperature effects," *Journal of Applied Physics*, vol. 97, no. 10, p. 10A922, 2005.
- [35] P. Panta and C. Bergmann, "Raman spectroscopy of iron oxide of nanoparticles (Fe₃O₄)," *Journal of Material Science & Engineering*, vol. 05, no. 01, pp. 1–3, 2015.
- [36] N. Lee, P. J. Schuck, P. S. Nico, and B. Gilbert, "Surface enhanced Raman spectroscopy of organic molecules on magnetite (Fe₃O₄) nanoparticles," *The Journal of Physical Chemistry Letters*, vol. 6, no. 6, pp. 970–974, 2015.
- [37] M. A. G. Soler and F. Qu, "Raman spectroscopy of iron oxide nanoparticles," in *Raman Spectroscopy for Nanomaterials Characterization*, pp. 379–416, Springer, Berlin, Germany, 2012.
- [38] R. Tuma, "Raman spectroscopy of proteins: from peptides to large assemblies," *Journal of Raman Spectroscopy*, vol. 36, no. 4, pp. 307–319, 2005.
- [39] H. Takeuchi, "Raman structural markers of tryptophan and histidine side chains in proteins," *Biopolymers—Biospectroscopy Section*, vol. 72, no. 5, pp. 305–317, 2003.

Review Article

Gold Nanoparticles as X-Ray, CT, and Multimodal Imaging Contrast Agents: Formulation, Targeting, and Methodology

Matthew M. Mahan and Amber L. Doiron 

Department of Biomedical Engineering, Binghamton University (SUNY), Binghamton, NY 13902, USA

Correspondence should be addressed to Amber L. Doiron; adoiron@binghamton.edu

Received 28 July 2017; Accepted 22 January 2018; Published 7 March 2018

Academic Editor: Faheem Ahmed

Copyright © 2018 Matthew M. Mahan and Amber L. Doiron. This is an open access article distributed under the Creative Commons Attribution License, which permits unrestricted use, distribution, and reproduction in any medium, provided the original work is properly cited.

Computed tomography (CT) is among the most popular medical imaging modalities due to its high resolution images, fast scan time, low cost, and compatibility with all patients. CT scans of soft tissues require the localization of imaging contrast agents (CA) to create contrast, revealing anatomic information. Gold nanoparticles (AuNP) have attracted interest recently for their use as CT CA due to their high X-ray attenuation, simple surface chemistry, and biocompatibility. Targeting molecules may be attached to the particles to allow for the targeting of specific cell types and disease states. AuNP can also be readily designed to incorporate other imaging contrast agents such as rare earth metals and dyes. This review summarizes the current state-of-the-art knowledge in the field of AuNP used as X-ray and multimodal contrast agents. Primary research is analyzed through the lens of structure-property-function to best explain the design of a particle for a given application. Design specification of particles includes size, shape, surface functionalization, composition, circulation time, and component synergy. Key considerations include delivery of a CA payload to the site of interest, nontoxicity of particle components, and contrast enhancement compared to the surrounding tissue. Examples from literature are included to illustrate the strategies used to address design considerations.

1. Introduction

Medical imaging is a critical component in the diagnosis and treatment of disease. X-ray imaging was the first modern imaging technique, but rapid advancement of technology has led to the development of other clinically employed methods including ultrasound (US) [1], magnetic resonance (MR) imaging [2], computed tomography (CT) [3], positron emission tomography (PET) [4], PET/CT [5], and PET-MRI [6]. These modalities differ in image quality metrics and application-specific factors such as depth-related image quality, resolution, signal-to-noise ratio, contrast, and sensitivity, as well as practical considerations such as safety, cost, and availability. In many clinical situations, an imaging contrast agent (CA) may be employed to enhance differentiation between two tissue types or to highlight disease-specific anatomical features or functional processes at the molecular, cellular, or tissue level. Colloidal gold is a unique material investigated as a CA in several medical imaging modalities, as summarized in Table 1 [7, 8].

Historically, gold solutions were used in stained glass windows and as a purple dye [9]. Colloidal gold was first described by Faraday in 1857 [10]. Gold nanoparticles (AuNP) are now at the forefront of developments in chemistry, biology, and medicine. Their high biocompatibility and versatile surface properties allow gold nanoparticles to be a safe platform for many biomedical technologies. Gold nanoparticles have been employed as optical biosensors [11], drug delivery vehicles [12], and imaging contrast agents [13] and laser-based treatments [14]. Their simple formulation and reactive surface allow for a variety of molecules including drugs, targeting peptides or proteins, contrast agents, or other moieties to be attached. The morphology of particles is diverse: spheres [15, 16], hollow shells [17], star-shapes [18], rods [19], clusters [20], and cubes [21] have all been formulated. The size of particles can range from 1 nm to over 100 nm. Both size and shape have important effects on the optical properties of the particle as well as its fate *in vivo*.

Gold nanoparticles were first investigated as an X-ray CA by Hainfeld, who imaged organs and vasculature of mice by

TABLE 1: Imaging modalities achieved using gold nanoparticles by inclusion of various moieties or formulation methods.

| Imaging modality | Formulation method |
|------------------|--|
| X-ray/CT | Gold nanoparticles |
| MRI | Inclusion of heavy metals (gadolinium, iron oxide) |
| Ultrasound | Core-shell structure with high acoustic impedance |
| Fluorescence | Inclusion of fluorescent dyes |
| Photoacoustic | Inclusion of fluorescent dyes |
| Nuclear imaging | Radioisotopes (^{64}Cu , ^{111}In) |

injecting bare AuNP intravenously [22, 23]. The attachment of chemical moieties and targeting molecules allowed for use of these particles as multimodal contrast agents and in active targeting of disease states. A variety of capping agents or formulation methods available can increase the circulation time of AuNP, allowing for wider imaging windows. AuNP are also capable of carrying a drug or nucleic acid load [15] or mediating light-based treatments [14]. Recent reviews of therapeutic uses of AuNP are available elsewhere [24–27].

2. Gold Nanoparticles in X-Ray Imaging

In addition to being effective in scattering visible light, gold has a high X-ray attenuation coefficient at the energy levels utilized for clinical X-ray and CT [28]. Research-use only gold nanoparticle formulations are available commercially as X-ray contrast agent AuroVist™ from nanoprobes at sizes of 1.9 and 15 nm. Additionally, a number of innovative formulations of gold nanoparticles are under development for varied physiological applications to achieve targeted, high contrast X-ray images for diseases diagnosis.

2.1. X-Ray/Computed Tomography. X-ray imaging was invented by Wilhelm Röntgen in 1895. It utilizes high-energy electromagnetic radiation to create images of internal structures. Today it is the most widely used method of medical imaging, accounting for 50–75% of all medical imaging done [29]. X-ray imaging is considered safe and cost-effective if the radiation dose is monitored and limited over the lifetime of the patient. An important breakthrough in 1973 resulted in the development of CT [30], which allows for 3-dimensional (3D) reconstructions of X-ray images by rotating the detector and the X-ray source about the imaged body.

When traveling through the body, X-rays undergo attenuation, the loss of beam intensity, due to photoelectric absorption or scattering. Attenuation is described by the Beer-Lambert law:

$$I = I_0 e^{-\mu x}, \quad (1)$$

where I_0 is initial beam intensity, μ is the material's characteristic absorption coefficient, and x is the thickness of the tissue

through which X-rays travel. The attenuation coefficient μ is described by the following equation:

$$\mu = \frac{\rho Z^4}{AE^3}, \quad (2)$$

where ρ is density, Z is the atomic number, A is the atomic mass, and E is the X-ray energy. Attenuation is often measured in Hounsfield units (HU), normalized to the attenuation of water. The scale assigns an arbitrary value of 0 HU to water and scales linearly. Viewing this equation, it is apparent that the energy of the X-ray scan will have an effect on HU; therefore HU between different experimental groups are not directly comparable.

X-ray beams can have several different interactions with matter, but it is worth highlighting the two that predominate at clinically relevant levels of energy. Photoelectric absorption occurs when an X-ray photon interacts with an inner-shell (K or L) electron of an atom. If the energy of the incident photon is greater than that of the electron, then the electron is ejected and the atom absorbs the photon completely. The inner-shell vacancy causes a cascade of electrons as outer-shell electrons fill inner-shell vacancies, releasing secondary radiation in the process. The ejected electron is absorbed by the surrounding tissue and is a main cause of biological damage in X-ray imaging. The energy threshold required to eject an inner-shell electron is referred to as the absorption edge. A spike in the mass attenuation of the bulk material is observable at these thresholds. The K-edge of several common contrast agents is within clinical CT range, including iodine (33.2 keV), barium (34.7 keV), and gold (80.7). K-edge imaging, the detection of contrast agents using measurements of their characteristic X-ray attenuation profiles, has been used to detect AuNP *in vivo* [31]. Schirra utilized this property to create high contrast particles for CT scanning. 120 nm polysorbate cores with a lipid encapsulation were used to entrap 2–4 nm AuNP. Formulated particles provided high contrast in CT phantoms and *in vivo* studies [32]. This material property can be exploited to increase signal-to-noise ratio. The second type of interaction is Compton scattering. This occurs when a photon strikes a low-energy outer-shell electron, ejecting the electron and scattering the photon. Scattered Compton photons are a radiation hazard and degrade the overall image quality.

2.2. Contrast in X-Ray Imaging. Contrast in X-ray imaging is derived from the difference in mass attenuation between two tissues. Materials with a high atomic number or density such as bone absorb more X-rays. Lowering the energy of the X-ray beam creates a higher contrast between two tissue types because photoelectric events predominate at lower energy (<50 kVp) [33]. Contrast agents play an important role in allowing higher energy, safer scans with high contrast by introducing high atomic number media into the body.

X-ray contrast agents have been widely investigated over the last 20 years [34]. Iodine is the most common radiopaque element used in X-ray imaging owing to its high atomic number compared to biological tissues. For contrast media, iodine is included in compounds as triiodobenzene in either monomer or dimer structures. The agents can be

ionic or nonionic owing to the hydrophilic residues attached to the aromatic ring. Iodinated contrast medium is in an aqueous solution with concentrations of 150 to 400 mg I/mL, equivalent to 0.4 to 1.0 mol/L. Its high osmolarity as well as a high viscosity can lead to poor patient tolerance. Dimeric iodine-based CA show an increase in retention in the kidneys [35] and can cause renal injury [36]. When comparing low-osmolarity CA with ones isotonic to blood plasma, a metastudy found a just-significant difference in contrast-induced nephropathy incidence [37]. The Food and Drug Administration also warns that low thyroid activity has been reported in infants who receive iodinated contrast media [38]. Iodine-based CA have also recently been linked to amplification in DNA damage during CT scans [39]. Currently, several iodinated contrast agent formulations are used clinically, including iohexol (Omnipaque™, GE Healthcare), iopromide (Ultravist™, Bayer Healthcare), ioxaglate (Hexabrix™, Mallinckrodt Imaging), iobitridol (Xenetix™, Guerbet), and iomeprol (Imcron™, Bracco).

2.3. Cancer Targeted Gold Nanoparticles Formulations. Many researchers have used targeted gold nanoparticles to achieve contrast for the diagnostic imaging of cancer *in vitro* and *in vivo* in animal models. These approaches may employ the use of antibodies, proteins or peptides, nucleic acids, or other biomolecules. In an approach based on cancerous cells' increased metabolism and a requirement for glucose at higher rates than surrounding cells, researchers have coated gold nanoparticles with glucose analogues. Aydogan and colleagues targeted human alveolar epithelial cancer cells (A-549) *in vitro* using AuNP conjugated with 2-deoxy-D-glucose (2-DG). Cells were allowed to incubate with targeted AuNP before being imaged. Glucose allowed for an increased uptake of AuNP to cells, resulting in a 4-fold increase in CT attenuation in these targeted cells over nontargeted trials [40]. Li et al. similarly described attachment of 2-DG to AuNP and subsequent uptake into A-549 cells *in vitro*. Transmission electron microscopy images confirmed internalization of AuNP after incubation. A comparison between 1-deoxy-D-glucose and 2-DG showed 4-fold CT attenuation increase, and thereby higher uptake, to A-549 cells by 2-DG-functionalized AuNP [41]. Furthermore, polyethylene glycol- (PEG-) functionalized AuNP coated with 2-[18F]-fluoro-2-deoxy-D-glucose were used to target tumors owing to their higher metabolism compared to normal tissue. A mouse model was used to assess the targeting ability *in vivo*. Tumors continued to display significant contrast over nontargeted connective tissue 7 days after injection before being eliminated [42].

Many studies have successfully attached antibodies to the surface of gold nanoparticles for active targeting of an antigen on cancerous cells. Popovtzer synthesized AuNP conjugated with UM-49 antibodies, which specifically targeted squamous cell carcinomas (SCC). An *in vitro* study was performed using targeted and nontargeted AuNP incubated with a variety of SCC cell types. CT attenuation was 4-fold higher in trials with targeted particles and SCC cells [43]. In a separate approach, Eck et al. used two sizes, 28

and 38 nm, of PEGylated AuNP functionalized with anti-mouse CD4 antibodies to target the lymph nodes of mice. AuNP were injected into the tail vein of mice and imaged at 1 and 48 hours postinjection. The targeted 38 nm AuNP provided a 2-fold increase in contrast of lymph tissue, but interestingly the nontargeted 38 nm particles provided the second highest one. The authors suggested PEGylated particles may be taken up by macrophages and transported to the lymph nodes [44]. Conversely, Hainfeld et al. found that PEGylated AuNP conjugated with anti-Her2 antibody accumulated on the tumor periphery of Her2+ mice in drastically higher quantities than nontargeted particles, based on CT attenuation data. AuNP were injected intravenously into Her2+ and Her2- tumor-bearing mice and imaged using CT, showing a twofold increase in attenuation [45]. Reuveni et al. attached antiepidermal growth factor receptor (EGFR) antibodies to PEGylated AuNP in order to target squamous cell carcinomas. Particles were injected into the tail vein of mice bearing a xenografted tumor and compared to passively targeted AuNP. Contrast in the tumors was measured up to 6 hours later. Similar attenuation was measured for both passively and actively targeted AuNP within 0–3 hours, but within 3–6 hours active targeting had a twofold higher contrast [46]. Kao et al. functionalized PEGylated AuNP with cetuximab, an EGFR-targeting drug to target and image human lung cancer line A-549. Cetuximab is a chimeric monoclonal antibody that inhibits EGFR. A tumor was xenografted into a mouse model and the particles were injected intravenously. CT imaging showed the majority of particles accumulated in the liver and bladder, although the tumor was visible up to 4 hours postinjection [47].

In addition to using antibodies, proteins or peptides can be attached to gold nanoparticles to target cancerous cells. Chanda et al. attached bombesin peptide, which targets gastrin-releasing peptide receptors that are overexpressed in several cancers, to AuNP. Human prostate tumors were xenografted into mice and the AuNP injected intraperitoneally to assess their ability to target a tumor *in vivo*. CT attenuation was found to be 4-fold higher within the tumor up to 6 hours after injection of particles [48]. Additionally, Angiopep-2, another tumor-targeting peptide, was used by Hao et al. Poly(lactic glycolic acid) (PLGA) nanoparticles coated with Angiopep-2-functionalized AuNP were injected into a mouse and compared against untargeted particles. Formulated particles showed a linear attenuation curve with a slope of $0.1 \text{ mg Au ml}^{-1} \text{ HU}^{-1}$. Tumors showed higher attenuation for both particles, although the control group had some signal the authors attributed to the enhanced permeability and retention effect (EPR) [49].

In a separate approach, Tian and colleagues conjugated arginine-glycine-aspartic acid (RGD) peptides to hollow gold nanospheres. The widely used RGD peptides target $\alpha_5\beta_3$ integrin receptors overexpressed by tumor blood vessels. The targeting ability of RGD-AuNP was assessed by injecting the particles into rabbits with a xenografted VX2 liver tumor and imaging after 60 minutes. Particles were injected via several routes and in conjunction with different iodized oils to improve liver accumulation; the highest levels were found with intra-arterial injection and lipiodol. A twofold

CT attenuation increase was observed in the tumor tissue under these conditions [50]. RGD was also employed by Zhu et al., who used generation 5 (G5) poly(amidoamine) (PAMAM) dendrimers as a scaffold to entrap AuNP and RGD peptide. This polymer can be used as a scaffold on which to reduce AuNP as well as PEG using 1-ethyl-3-(3-dimethylaminopropyl)carbodiimide (EDC) chemistry. The so-called generation of the PAMAM dendrimers refers to its size; for example, generation 2 dendrimers have a lower size and molecular weight than generation 5. The particles were assessed for their CT contrast and targeting ability *in vitro*. CT phantoms showed an attenuation similar to Omnipaque. Trials using free RGD and U87MG cells overexpressing $\alpha_5\beta_3$ integrin receptors showed that blocking these receptors prevented attachment of the particles, so targeting was concluded to be specific [51].

Aptamers represent a newer approach to active targeting. Aptamers are typically synthetic, short strands of oligonucleic acids or oligopeptides (15–60 amino acids) that bind to a specific target molecule. Kim et al. attached a prostate-specific membrane antigen ribonucleic acid-aptamers to AuNP with the goal of targeting prostate cancer cells. Targeting efficiency of the AuNP was assessed *in vitro* after incubation with prostate-specific membrane antigen-overexpressing cells. CT attenuation was threefold higher than that of the control cells [52]. ASI411 aptamers attached to AuNP were used in one study to investigate their tumor-targeting ability. These particles had a linear attenuation curve with a slope of $0.027 \text{ mM Au HU}^{-1}$. CL1-5 tumor-bearing mice were used to assess this targeting ability *in vivo*. A high CT attenuation at the tumor site indicated high accumulation of particles at the tumor site [53]. Additionally, Melancon et al. compared the targeting ability of EGFR-targeting aptamers to targeting antibodies on hollow AuNP. Squamous cell carcinomas were created by injection of cells into mice and particles injected intravenously. Higher CT attenuation was observed for aptamer particles at 4 and 24 hours postinjection, showing much promise for this aptamer-based approach to active targeting [54].

Receptor-antigen binding is another biological mechanism that can be taken advantage of for targeting of nanoparticles for imaging purposes. Folic acid receptor, a glycosylphosphatidylinositol anchored cell surface receptor, is overexpressed on the majority of cancer tissues, compared to healthy tissues and organs. Folic acid- (FA-) conjugated G5 PAMAM dendrimers were used as a template to attach AuNP in order to target human lung adenocarcinoma cells (SPC-A1). The particles were used both *in vitro* and *in vivo* in a xenografted tumor mouse model. TEM images of *in vitro* incubations showed internalized AuNP. Tumors continued to display significant X-ray attenuation up to 6 hours postinjection, with up to a fourfold increase when an intratumoral injection route was used [55]. Liu and colleagues used a similar approach in creating silver-gold alloys with amine-terminated generation 5 (G5.NH2) dendrimers as stabilizers. The dendrimers were functionalized with FA for targeting of cancer cells. Human epithelial carcinoma cell lines (KB cells) over- and underexpressing FA receptors were incubated with the particles *in vitro*. However, CT

attenuation of KB cells exposed to targeted particles was not significantly different over nontargeted particles in this study [56]. In another dendrimer-based approach, Cai et al. used poly(γ -glutamic acid) (PGA) dendrimers attached to Fe_3O_4 nanoparticles to entrap AuNP. These particles were further functionalized with FA to target KB cells. *In vivo* studies showed targeted particles created a twofold increase in CT attenuation after 24 hours [57]. Similarly, Chen et al. entrapped AuNP in a G5.NH2 dendrimer functionalized with FA to target KB cells. Entrapped particles showed a linear attenuation curve with a slope of $0.2 \text{ mM Au HU}^{-1}$. *In vitro* and *in vivo* studies were conducted to test the targeting abilities. Contrast was 2-fold higher over control 24 hours postinjection [58]. A follow-up study replaced FA with the RGD peptide. After demonstrating significant cellular uptake *in vitro*, particles were assessed in a mouse tumor. Included were trials where mice were injected with free RGD to block $\alpha_5\beta_3$ receptors. The CT attenuation of tumor tissue was 1.5-fold higher than control between 1 and 20 hours postinjection [59]. Zhou created gold nanoclusters with silica oxide shells conjugated with FA for targeting of MGC803 (gastric cancer) cells in a xenografted mouse model. Despite the shell, a linear attenuation curve with a slope of $0.74 \text{ mM Au HU}^{-1}$ was observed. Particles injected by the tail vein showed high contrast 6 hours postinjection at the tumor site, although attenuation was not quantified [60].

Various other biomolecule-based approaches to targeting exist in the literature as well. Sun et al. investigated the tumor-targeting ability of glycolic chitosan- (GC-) capped AuNP [61] based on previous literature using GC-targeting of tumors [62, 63]. *In vitro* studies demonstrated that the formulated particles had similar CT attenuation to eXIA 160, a commercial CT contrast agent. An *in vivo* study using mice compared heparin-coated AuNP, a nontargeted vehicle, to GC-AuNP. GC-AuNP were found to have a 2-fold CT signal increase over control 2 hours postinjection [61]. Furthermore, gold-coated Fe_2O_3 particles were conjugated with lectin, a glycan-targeting molecule, and used to image colorectal cancer in a mouse model. Several lectins were used, including *Ricinus communis* agglutinin I (RCA), concanavalin A (ConA), and wheat germ agglutinin (WGA). RCA and WGA exhibited similar targeting capability as measured by CT imaging 24 hours postinjection [64]. One study used G5.NH2 dendrimers modified with lactobionic acid (LA), which specifically binds asialoglycoprotein (ASGP), as a scaffold to reduce AuNP. Hepatocellular carcinoma (HCC) was used to test targeting ability owing to the cell line's overexpression of ASGP receptors. This targeting ability was assessed *in vivo* in a mouse model. LA-conjugated scaffolds showed a 1.5-fold higher tumor CT attenuation after 2 hours when injected intravenously [65]. Zeng et al. functionalized AuNP with LA to target HCC cell line HepG2. This targeting ability was assessed by comparing internalization versus an ASGP-cell line (HeLa). Only HepG2 showed internalization after incubation *in vivo*. X-ray images of a phantom were obtained that showed a steep linear attenuation slope of $0.00016 \text{ mM Au HU}^{-1}$ [66].

Li et al. created Fe_3O_4 core gold nanostars with a polyethyleneimine layer to entrap hyaluronic acid (HA).

HA was used to target CD44 receptors overexpressed by cancer cells. This targeting was tested both *in vitro* using CD44+ and CD44- cells and *in vivo* in a mouse model. *In vitro* trials showed 1.5-fold increase in CT attenuation over control at concentrations above 2.50 mM Au. *In vivo* CT scans conducted showed significant contrast at the tumor site 10 minutes postinjection [18]. Bisphosphonate-conjugated AuNP were formulated to target microcalcifications in breast tissue and improve cancer detection *in vivo* using CT imaging. Bisphosphonate specifically binds hydroxyapatite, the mineral component of calcifications. Mammary tumor-bearing mice were used as a model and particles were injected into the mammary tissue. Particles allowed imaging of previously undetectable microcalcification and provided CT contrast for up to 48 hours [67]. One study by Meir has even demonstrated that cancerous tissue may be targeted without the use of small molecules. AuNP were incubated with T cells transformed to express a melanoma-specific T-cell receptor before being injected intravenously into mice bearing human melanoma xenografts. The internalized particles were tracked using CT and cells were found to accumulate in the melanomas, while nontransformed cells did not [68].

Cancer remains an important focus of health science study in general and AuNP research in particular. Many of these studies opted to localize particles by functionalizing them with cancer cell-specific molecules such as antibodies and antigens. While this has been shown to be effective at localizing particles within the tumor bulk, many of these studies are conducted in mice. It remains to be seen whether such targeting methods are viable in human subjects.

2.4. Thrombus Targeted Gold Nanoparticles. Kim et al. investigated the thrombus localization of GC-coated AuNP. Clots were induced in mice before particles were injected. CT imaging was able to visualize plaques 30 minutes after induction of the thrombus and 5 minutes after injection of particles and also 48 hours and 3 weeks later without further injection of AuNP. Application of tissue plasminogen activator, the clinical preference for clot breakdown, led to a decrease in CT signal at the clot areas [69]. A follow-up study added fibrin-targeting peptides to the formulation. Fib-GC-AuNP had superior targeting to GC-AuNP *in vitro*. Cerebral embolisms were induced by injecting fluorescently labeled thrombi into the cerebral artery of mice. Fluorescence imaging was used to colocalize visualization of the particles and found a significant signal at the site of clots [70]. Ghann et al. coated AuNP with Lisinopril, an angiotensin-converting enzyme (ACE) inhibitor, and targeted ACE *in vivo* to track the progression of heart disease. Particles were injected into mice and targeted to the lungs and heart. Thioctic acid attached to Lisinopril was required to stabilize the particles. Particles provided significant contrast and pretreatment with free Lisinopril resulted in low signal scans, confirming direct targeting [71].

2.5. Macrophage Targeted Formulations. Macrophages are important markers of diseases such as heart disease and cancer. Cormode et al. created high-density lipopolysaccharide capsules with AuNP cores to assess macrophage burden and

plaque stability. Atherosclerosis was induced in mice, and the particles were injected 24 hours before sacrifice. Spectral CT scanning of the aorta showed high CT attenuation at areas known to accumulate plaque such as the arch and the bifurcation [72]. From the same group, van Schooneveld et al. formulated a gold core/silica shell with surface lipid molecules and PEG. *In vitro* phagocytic studies and *in vivo* liver visualization studies were conducted. Fluorescence microscopy images of macrophages revealed particle internalization and images taken 24 hours after intravenous injection to mice revealed an increase in CT signal in the liver [73]. De Wilde's group investigated using CT to monitor the stability of arterial plaques. They observed AuNP were phagocytosed by macrophages. Exploiting this, they tracked the macrophages and quantified their accumulation within the plaques [16]. Allijn et al. incorporated AuNP into low-density lipopolysaccharide capsules and tracked their fate *in vivo*. These capsules displayed a linear attenuation curve with a slope of $0.25 \text{ mM Au HU}^{-1}$. Mice bearing B16F10 tumors were injected with LDL-AuNP and imaged using CT. A significant signal was measured at the tumor site and the liver. Fluorescence activated cell sorting revealed that the majority of particles were taken up by macrophages [74]. Qin et al. used G5.NH₂ dendrimers functionalized with fluorescein isothiocyanate as scaffolds to reduce AuNP. Macrophage uptake was assessed *in vivo* using Apolipoprotein-E knockout mice. Atherosclerotic vessels had significantly higher CT signal 6 hours postinjection. Hematoxylin and eosin staining of resected arteries confirmed macrophage uptake of the particles [75].

AuNP coated in heparin were tested for their ability to accumulate in Kupffer cells. These particles were used as contrast agents to image a mouse liver *in vivo*. In a comparison with eXIA160, formulated particles had a higher CT signal intensity within the liver [76]. Zhao et al. reduced AuNP onto Fe₃O₄ particles using mercaptosuccinic acid. The synthesized particles were intended to accumulate in Kupffer cells and were investigated *in vivo* for their diagnostic potential of three stages of liver diseases: fatty liver, cirrhotic liver, and HCC. In the case of HCC, particles acted as a negative contrast by providing contrast to the liver parenchyma but not the tumor location [77].

Furthermore, Chhour et al. used 11-mercaptopundecanoic acid (11-MUDA) as a stabilizer for formulated AuNP in order to track macrophages. These particles were used to label monocytes *ex vivo* before injection into atherosclerotic mice. Over the course of 5 days, CT signal at the aorta increased significantly pointing to an accumulation of AuNP and therefore the macrophages [78].

Many of these macrophage targeting methods rely on encapsulation or cellular uptake. Strategies such as the use of lipopolysaccharides have great potential for targeting by exploiting the physiological mechanisms. These encapsulated particles still display attenuation curves comparable to other CT contrast agents. It remains to be seen whether these targeting strategies provide enough contrast in human subjects.

2.6. Bone Targeted Formulations. Zhang sought to quantify microdamage to bone using AuNP as CA in CT imaging. By

functionalizing AuNP with glutamic acid, particles were able to be targeted towards bone by chelating calcium ions at the surface of bone crystals. Bovine bone resections were used as a model, and particle accumulation was visualized using scanning electron microscopy. Authors note the potential of the particle to be used as an X-ray contrast agent [79]. Another study encapsulated Fe_3O_4 and AuNP within a silica matrix before incorporation into a calcium phosphate-based bone replacement cement. This formulation was tested *in vitro* for its physical properties and *in vivo* for its incorporation into a mouse femoral condyle defect. The cement was able to be visualized up to 8 weeks after implantation [80]. While bone itself does not require a CA, these methods of targeting may allow the imaging of bone defects or tissue implants.

2.7. Kidney Targeted Formulations. Renal imaging is an important factor in the diagnosis of kidney disease and cancer. Wang et al. created small (<2 nm) AuNP clusters coated with bovine serum albumin (BSA) in order to diagnose kidney disease. The formulated particles were compared *in vitro* to iopromide as well as being used for CT imaging *in vivo*. Similar CT attenuation was achieved with lower concentrations of the particles compared to iopromide. A high resolution image of the kidneys was possible using CT scanning 2 hours postinjection [81].

2.8. Blood Pool Imaging Gold Nanoparticle Formulations. AuNP have been utilized as blood pool contrast agents in lieu of localization for a particular disease. Kattumuri et al. utilized gum arabic as a capping agent for AuNP. CT attenuation was measured at 80 and 140 kVp using phantoms; the particles were also injected in a swine model to assess biodistribution. Particles at both CT energies had a linear relationship to CT attenuation and accumulated in the liver, lungs, and spleen [82]. A follow-up study by the same group used the gum arabic-coated particles to image swine organs. CT scans of the liver and spleen revealed an increase in HU after intravenous particle injection [83]. In a different approach, Cai et al. investigated PEGylated 38 nm AuNP as blood pool contrast by injecting the particles into Balb/c mice. Significant CT contrast was measured in the right ventricle, inferior vena cava, liver, spleen, and kidneys at all time points between 0.1 and 24 hours after injection. Histological staining of these organs confirmed the presence of AuNP [84]. AuNP have been shown to be superior to iodine-based CA for imaging of vasculature. PEGylated AuNP injected into mice were compared to iodine injections at a tube voltage of 60 kVp. AuNP persisted in the vasculature for up to 24 hours and had a higher contrast than did iodine, which was eliminated after 6 hours [85].

Polymers are also capable of long circulation times that allow for vascular imaging. Peng et al. reported use of G5.NH₂ dendrimers modified with diatrizoic acid (DA) to entrap AuNP. DA is an iodine containing compound designed to enhance CT contrast. Particles were injected intravenously into mice to evaluate their CT contrast. Particles containing DA showed 2-fold over scaffolds without DA and 10-fold higher contrast over Omnipaque [86]. In another

case, PEGylated generation 4 PAMAM dendrimers with reduced AuNP were formulated to be used as a blood pool contrast agent. Mice were injected with formulated particles or iopamidol in a comparison of contrasting ability and half-life. HU values were similar for both CA, although iopamidol accumulated within the bladder due to renal elimination [87].

Hayashi et al. formulated gold clusters with a silica shell to visualize lymph nodes and lymphatic vessels using CT scanning. The CT attenuation of the particles was first compared to Iopamiron before injection into mice. Formulated particles displayed greater CT attenuation than Iopamiron and lymphatic vessels in phantoms and were used to visualize nodes 18 hours postinjection [88].

Although nontargeted formulations do not have a method of tissue localization, they still require long enough circulation times to be of use in a clinical setting. Particles used in a blood pool setting may be relied upon for perfusion studies, while imaging of organs relies upon natural physiological processes to localize particles.

2.9. Passively Targeted Gold Nanoparticle Formulations. While not targeted in the active sense, AuNP can be formulated such that their accumulation in certain tissues is predictable. A small particle with a long circulation time *in vivo* can lead to the accumulation of particles in tumors owing to their leaky vasculature. This EPR effect allows researchers to accumulate particles within tumors without actively targeting them. Hainfeld et al. injected AuNP into a mouse model with a brain tumor xenograft to assess uptake. A high concentration (4 g Au/kg) was used to achieve a high tumor uptake (1.5% w/w Au). Tumors continued to be visible on CT scans up to 8 days after intravenous injection [89].

Another popular strategy is the coating of AuNP with PEG, which changes their route of clearance from the renal system to the reticuloendothelial system (RES). PEGylation increases circulation time of the particles within the body and can allow particles to be passively targeted to tumor cells. Clearance by the RES also causes particle accumulation in the liver and spleen. Maltzahn et al. compared PEGylated AuNR with a commercial iodine-based CT CA Isovue-370 (iopamidol). AuNR were injected both intratumorally and intravenously into a tumor-bearing mouse. The formulated particles had a nonlinear CT attenuation higher than that of iopamidol, and intravenously injected particles had a 17-hour half-life [90]. Ashton et al. demonstrated tumor accumulation of PEGylated AuNP in an interesting study using dual-energy CT. AuNP were injected and allowed to accumulate in tumors for 2 days before the injection of iodine nanoparticles. The iodine particles acted as blood pool CA, while the AuNP provided contrast within the tumors [91]. PEGylated hollow AuNP are also capable of targeting tumors passively as shown by Park et al. After injection into the tail vein, particle location was assessed using CT imaging and inductively coupled plasma (ICP) mass spectroscopy. Although particles could be detected within the body, authors were unable to image the tumor owing to a low concentration of particles [17]. Naha et al. used PEGylated gold-silver alloy particles to passively target breast cancer tumors and perform dual-energy mammography CT scans. Mice were injected

with the particles via the tail vein and imaged at 30, 60, and 120 minutes postinjection. Contrast was significantly higher in the blood and tumor at all time points. The gold-silver alloy reduced the amount of silver ion leaching over silver nanoparticles alone [92].

Wang targeted tumors using a G5.NH₂ PAMAM dendrimer scaffold with reduced gold particles. The dendrimers were then acetylated to neutralize the positive surface potential. Targeting was assessed *in vivo* using a mouse xenograft tumor. Particles were injected intratumorally and intraperitoneally; both routes showed a high CT attenuation in the tumor indicating targeting by the EPR effect [93]. Li used G5.NH₂ PAMAM dendrimers with gadolinium chelator tetraazacyclododecane tetraacetic acid (DOTA-NHS) as scaffolds to attach gadolinium, AuNP, and PEG. The particles were assessed for their ability to accumulate in tumors using CT imaging. CT attenuation was highest in the tumor 100 minutes postinjection, although significance was not shown. The particles also had a much higher accumulation in the liver, lungs, and spleen [94]. Another study utilizing G5.NH₂ dendrimers modified with AuNP and PEG imaged the blood pool of mice using CT as well as a xenograft tumor targeted via the EPR effect. The particles showed higher CT attenuation than Omnipaque in phantoms and displayed 1.5-fold contrast over control up to 6 hours after injection [95]. Generation 2 PAMAM dendrimers have also been utilized by Liu in a similar study using the scaffold as a platform to attach AuNP and PEG. These low generation dendrimers were injected both intravenously and interperitoneally to assess their tumor accumulation and body clearance. The particles were found to accumulate in tumor and the bladder, although much higher CT attenuation was observed in the latter. In a comparison to Omnipaque, formulated particles remained in the bladder for longer time periods [96].

Polymers are a popular tool to allow the attachment of several functionalizing molecules. Zhou et al. used PEGylated branched polyethylenimine as a scaffold to synthesize AuNP. Subcutaneous injection into healthy rats allowed the particles to be used as blood pool CA, while intravenous injection into a tumor model showed accumulation at the cancer site owing to the EPR effect [97]. AuNP loaded into 1,2-distearoyl-*sn*-glycero-3-phosphoethanolamine-*N*-[methoxy(polyethylene glycol)-2000] (DPSE-PEG2000) micelles were used to target tumors *in vivo*. Particles were injected intravenously into CT26 tumor-bearing mice and imaged using CT. The highest CT signal was observable at the liver, although the tumor site also exhibited high signal [98]. Wang et al. encapsulated Fe₃O₄ nanoparticles in dipalmitoylphosphatidylcholine (DPPC)/cholesterol/DSPE-PEG₂₀₀₀ liposomes coated in AuNP and PEG. These particles were injected intravenously to assess their accumulation in tumors. Particles did enhance CT contrast, although the majority of particles accumulated in the organs [99]. Li reported a gold nanocluster assembly encapsulated by polyacrylic acid (PAA)/calcium phosphate. Particles were injected intravenously into mice to assess their fate *in vivo*. Tumor tissue had the highest CT signal and gold concentration as assessed by ICP atomic emission spectroscopy [20].

PEG has been shown to play a major role in determining the location and accumulation of nanoparticles *in vivo*, and a wide variety of PEGylated particles have been investigated for tumor accumulation. Fullerenes have been used as a template to reduce AuNP and were functionalized using PEG attached via a pH-sensitive hydrazine bond. This allowed particles to be targeted to tumors owing to the EPR effect, but upon reaching the tumor site PEG would be cleaved allowing uptake directly into cells. This process was evaluated *in vivo* using a tumor-bearing mouse. CT signal was observable 8 hours postinjection. Histological staining of resected tumor cells revealed internalization of particles [100]. Hayashi designed large (<100 nm) gold core cluster/silica shell particles with surface PEG for passive targeting of tumors in an animal model. Particles were injected intravenously, and CT imaging was performed at 3 and 24 hours. Tumor tissue had a 2.5-fold difference in attenuation 24 hours postinjection. Histological staining of tumor tissue confirmed the presence of formulated particles [88]. Ke coated perfluorooctylbromide capsules with gold to create a dual ultrasound/CT CA agent (discussed below). Particles were also PEGylated to enhance accumulation in a mouse tumor *in vivo*. CT imaging after intravenous administration of the particles showed highest accumulation in the liver and kidneys [101].

Various other surface molecules and capping agents are capable of increasing circulation time enough to allow tumor accumulation of particles. Chanda et al. performed a green synthesis of AuNP using cinnamon phytochemicals as reducing agents. TEM images showed internalization to cancer cell lines PC-3 and MCF-7 after *in vitro* incubation. CT imaging phantoms showed a linear attenuation curve of 54.1 $\mu\text{M HU}^{-1}$. They concluded the cinnamon-capped particles could circulate for long enough to accumulate in the lungs [102]. Luo et al. attached Cyanine5.5 (a near-infrared fluorescent dye) and a black hole quencher to a GC-capped AuNP and assessed its ability to target tumors *in vivo*. Particles were injected intravenously into a tumor-bearing mouse and assessed after 24 hours. Tumors were targeted by the EPR effect and showed a fivefold CT attenuation increase over control [103]. Prussian blue-coated AuNP were used in a study assessing their use as CT/photoacoustic CA. Particles were injected into a tumor-bearing mouse and CT imaging was performed over a 24-hour period. Despite the lack of surface functionalization, CT signal continued to increase over the time course. Biodistribution studies revealed the highest accumulation was in the spleen [104].

Sousa et al. designed human serum albumin-coated AuNP as a potential treatment for prion disease. The particles were investigated for their ability to cross the blood brain barrier by intravenous injection into mice. Ex vivo CT scans of the brain showed the highest CT signal was located at the thalamus and hypothalamus [105].

Clark et al. undertook a study to establish a CT imaging protocol to quantify angiogenesis and tumor blood volume. AuroVist AuNP were injected into mice 4 days before liposomal iodine. Scans were conducted using microCT daily up to 6 days postinjection. The difference in CT attenuation between iodine and gold as well as the uptake of particles due to the EPR allowed tumor vasculature to be imaged.

AuNP initially created an attenuation of up to 800 HU in the vasculature but decreased to 10 HU in the tumor tissue. After injection of the iodine, an attenuation of 25 HU was observed in the vasculature, which allowed for the differentiation of vasculature from tumor tissue [106].

As with nontargeting, these passive targeting methods rely on both the EPR effect or the RES system to localize particles within the organs of interest. The liver and spleen, which are responsible for dealing with matter picked up by the RES, thus may be naturally targeted by AuNP. Given long enough circulation time, the EPR effect can also be relied upon to localize particles to tumors.

3. Multimodal Particles

Gold particles can be designed to be used with multiple imaging modalities. A given modality may not be appropriate for all tissue types; for example, X-ray imaging is generally not appropriate for soft tissue due to poor X-ray attenuation. The ability to utilize multiple imaging modalities with one contrast agent allows clinicians to gather varied information with one contrast agent and increase clinical acceptance. Particles can be made multimodal by changing the design to include molecules with the desired properties. Potential modalities include magnetic resonance (MR) imaging, fluorescence imaging, ultrasound, photoacoustic imaging, and nuclear imaging.

3.1. Gold Nanoparticle-Based Contrast Agents for Magnetic Resonance Imaging. Discussion of the mechanisms of MRI are beyond the scope of this paper, but an excellent summary can be found in MRI basic principles and applications [107]. Gadolinium-based contrast agents (GBCA) are the current standard for MRI contrast agents owing to their high paramagnetism. There are 9 GBCA that are clinically approved; however, there are multiple reports of toxicity [108–110]. Superparamagnetic iron oxide (Fe_3O_4) nanoparticles (SPIOs) have been investigated as liver-specific contrast agents [111, 112]. There are reports of increases in reactive oxygen species caused by SPIOs [113], so additional modifications to formulations may be required for complete biocompatibility.

Several formulation methods exist for including paramagnetic components. Two compounds may be combined together to create a heterogenous structure or in a core-shell fashion. One study used gold nanorods, rather than spherical particles, coated with a polypyrrole shell and seeded with reduced Fe_3O_4 crystals. The particles were tested *in vitro* for their contrasting properties; both T_1 and T_2 relaxation was investigated as well as CT contrast. T_2 relaxivity was much higher than T_1 ($128.57 \text{ mM}^{-1}\text{s}^{-1}$ and $7.99 \text{ mM}^{-1}\text{s}^{-1}$, resp.) pointing to effectiveness as a T_2 contrast agent. CT values varied linearly with concentration. Authors note that further *in vivo* studies to assess imaging efficacy and biodistribution are underway [114]. An Fe_3O_4 core/Au nanostar shell coated with polyethyleneimine (PEI) was designed in a study by Li et al. Testing was performed *in vitro* as well as *in vivo* in tumor-bearing mice. The particles had a high CT attenuation and were used as a T_2 contrast agent *in vivo* although scans were only compared after 10 minutes [18]. Amendola et al. created

Au/ Fe_3O_4 alloy nanoparticles by laser ablation of a gold/iron bulk material. These particles were PEGylated and assessed in imaging phantom for their CT and MR contrast ability. The particles were also investigated for toxicity towards cells and their biodistribution in mice [115]. Kim et al. coated a AuNP/ Fe_3O_4 heteroparticle with the amphiphilic polymer poly(DMA-*r*-mPEGMA-*r*-MA), which contains a PEG moiety. An animal model bearing a liver tumor was selected to ascertain whether the tumor could be distinguished from the liver parenchyma. CT images were unclear, but authors noted a 1.5-fold signal enhancement detectable 24 hours postinjection. MR contrast was larger than that of commercial CA Resovist® at similar concentrations [116]. The aforementioned study by Zhao et al. first synthesized Fe_3O_4 particles by coprecipitation, capped with mercaptosuccinic acid (DMSA) before AuNP were reduced onto their surface. Both MR and CT contrast in the liver parenchyma was at a peak 30 minutes postinjection and was still enhanced after 6 hours, although significance was not assessed [77].

Entrapment has been utilized as a particle creation strategy for MR/CT particles. One such method first formulated thiolated Fe_3O_4 /silica composites by self-assembly of amphiphilic block PAA copolymers and Fe_3O_4 cross-linked by 3-mercaptopropyltrimethoxysilane. These were then used as scaffolds to reduce AuNP and used to image mouse tumors *in vivo*. CT and MR images taken at 5 and 30 minutes postinjection did show an increase in contrast, although significance was not determined [117]. Cai et al. used an Fe_3O_4 core with a dendrimer trilayer (PGA/poly(L-lysine) (PLL)/PGA) to entrap gold particles. These AuNP were utilized in seed-mediated growth, and the effect of Au/ Fe_3O_4 molar ratio on MR and CT signal was assessed. At a ratio of 2 : 1 they achieved a T_2 relaxivity of $92.67 \text{ s}^{-1} \text{ mM}^{-1}$. Their particle was assessed *in vivo* in a mouse model and showed a 1.5-fold increase in CT attenuation over control. A biodistribution study showed significant accumulation in the liver and spleen [57]. One study used PEGylated PEI as a scaffold to reduce AuNP. These polymers were then attached to an Fe_3O_4 particle and assessed for their contrast ability in a mouse model. Significant MR contrast was measured up to 4 hours, while CT attenuation was measured to be 1.5-fold higher than baseline after 20 minutes [118]. Sun et al. created an Au/ Fe_3O_4 heteroparticle by entrapment in a PEG/polycaprolactone micelle. They injected it intravenously into mouse models with human glioblastoma multiforme tumors implanted in the flank or brain and measured passive accumulation of their particle by CT and MR scans. The heteroparticle possessed a 3 : 1 gold : iron oxide ratio by mass while still possessing a high T_2 relaxivity ($221.92 \text{ s}^{-1} \text{ mM}^{-1}$). This gave it excellent contrast in MR scans of both areas of interest, but the CT scans showed negligible differences [119]. Wang et al. designed a large PEG micelle with encapsulated Fe_3O_4 particles and a gold shell. Formulated particles possessed a low attenuation slope of $6.7 \mu\text{M HU}^{-1}$. These were injected intravenously into the tail vein of tumor-bearing mice to test the particles' contrast properties. Relatively high concentrations of the particle were required to create appropriate contrast levels *in vivo*, and a high accumulation of particles in the liver, lungs, and spleen was found [99]. Tian et al. studied attachment of gold

nanoparticles to a gadolinium-organometallic framework, rather than a gold particle with gadolinium chelates. PAA acted as the active site to entrap gold particles. The composite particle displayed better MR contrast than clinically available Magnevist at lower concentrations with a similar relaxivity and similar CT attenuation to Omnipaque [120]. G5 PAMAM dendrimers can also be used to entrap other metals for the creation of multimodal particles. Wen et al. created such dendrimers with reduced gold clusters, gadolinium ions, and PEG. The particles were injected into the tail vein of mice and imaged at time points up to 45 minutes postinjection. CT and MR contrast saw a 1.5-fold increase in the liver and kidneys and a 2-fold increase in the bladder [121]. Chen created PEGylated G5 PAMAM dendrimers with reduced 4 nm gold clusters and gadolinium ions. The particles were injected subcutaneously into tumor-bearing mice and used as contrast agents in CT and MR imaging up to 24 hours postinjection. Contrast in both modalities continued to increase up to 24 hours, showing up to 1.5-fold increase in CT attenuation and MRI signal [58].

Encapsulation within biocompatible materials can also be utilized to create multimodal particles. Graphene is one possible encapsulator. One group used an aerosol encapsulation process to create large (>100 nm) graphene particles encapsulating AuNP and Fe₃O₄ particles. The particles were assessed for their material property, including porosity, pore volume, and ability to encapsulate effectively versus associating with metallic particles. CT phantom imaging revealed an attenuation curve consistent with the mass fraction of free AuNP. MR imaging showed a linear relationship between concentration and T₂ signal [122]. Another study reduced Fe₃O₄NP and AuNP onto graphene oxide (GO) sheets as well as PEG. *In vivo* imaging was performed by injecting particles into the tumor of mice. Imaging performed over a 5-minute period postinjection shows an increase in contrast [123]. Wu et al. encapsulated gadolinium-gold clusters in silica to create 80 nm nanoparticles. After injection into a mouse tumor, the particles were used as a contrast agent in MR and CT imaging. CT attenuation was increased 9-fold over preinjection values using 200 μ L of 40 mM particle solution [124]. Zhang's group designed a complex particle with a large gold particle coated by a silica shell with embedded manganese oxide and gold particles. Their idea was to design a particle with components that would amplify the properties each harbors. The T₁ relaxivity of the particle (1.5 mM⁻¹ s⁻¹) was lower than commercial gadolinium-based CA (i.e., Magnevist: 4.6 mM⁻¹ s⁻¹), but it did display 1.5-fold signal over control *in vivo* [125]. Liu et al. encapsulated gold nanostars in silica to allow attachment of gadolinium ions. The particles were evaluated for their CT and MR contrasting ability using phantoms. Both modalities showed a linear relationship between contrast and particle concentration [126].

Gold itself has been shown to be a viable platform for creation of a multimodal particle. Coughlin used 120 nm silica particles with a gold shell as platforms to attach gadolinium and PEG. These particles were injected intratumorally into mice. High contrast was observable in the tumor, although it was not quantified [127]. Zeng et al. used lipid-coated AuNP as a platform to attach gadolinium. Imaging phantoms

were used to evaluate the particles properties as contrast agents. The T₁ relaxivity of the particle was higher than that of commercially available dimeglumine gadopentetate [66]. Alric attached gadolinium particles to 1.9 and 31 nm gold nanoparticles. These particles were injected into mice and imaged at 10 and 30 minutes. CT imaging showed the highest gold accumulation in the renal system, while the highest MR signal was observed in the bladder [128].

Many innovative methods of combining magnetic materials with AuNP have been utilized, including heteroparticles, entrapment, encapsulation, and reduction of one onto the other. These methods have varying effects on both imaging metrics and biocompatibility and thus must be investigated further for their viability in human subjects. The marriage of these materials represents the possible synergy of the two most used clinical imaging methods and thus a step forward in their capability in diagnosis.

3.2. Gold Nanoparticle-Based Contrast Agents for Ultrasound.

Ultrasound is an imaging modality utilizing soundwaves above the human range of hearing, usually taken as above 20 kiloHertz (kHz). Current state of the art in ultrasound contrast agents lies in the use of microbubbles. Their use comes from a desire to image blood flow and perfusion of organ tissues and has expanded into treatment methods [129]. Schutt et al. provide an excellent review of microbubble design as well as signal and mechanical properties [130].

Researchers designing CT/US contrast agents utilize the characteristics of microbubbles combined with gold particles. Ke et al. designed a perfluorooctyl bromide- (PFOB-) gold core-shell complex. PFOB has a much higher acoustic impedance than air, enabling it to be used as US CA. The particles were used to successfully image the kidney and liver of mice [101]. Jin created a microcapsule of poly(lactic acid) containing gold and graphene oxide nanoparticles [131]. Interestingly, the amount of GO increased contrast in pulse inversion harmonic mode which creates contrast by nonlinear scattering. This suggests that the GO itself was resonating with ultrasound pulses. These capsules can also deliver a payload, as with the study by Arifin et al. that utilized alginate microcapsules to protect pancreatic islet cells in mice. The capsule allowed the pancreatic cells to maintain normal glucose levels for 6-7 weeks when injected into diabetic mice. Particles were tracked using CT and US [132]. The previously mentioned study by Zhang used a silica shell rather than a carbon-based one but it was still able to achieve an acceptable signal due to the nonlinear scattering caused by the embedded gold and manganese oxide particles [125]. Teraphongphom et al. encapsulated AuNP within a PLA microbubble. Although the payload was effectively loaded, a significant decrease in US signal at 50.0 wt% AuNP-microbubble was observed [8]. The encapsulation method utilized by many of these methods can have a detrimental effect on CT signal. Further work is required to maximize both CT and US contrast simultaneously.

3.3. *Fluorescence*. Emitted light from fluorescence can originate from a variety of sources including fluorescent dyes, quantum dots, or gold nanoparticles. It is not a commonly

utilized clinical modality but is real-time and noninvasive. Drawbacks include photobleaching, tissue autofluorescence increasing noise, and the low penetration depth of light. However, fluorescence is widely used in research and has some clinical applications. Fluorescence can also be useful when combined with another, high resolution modality to grant colocalization information.

Gold particles may be functionalized with a dye to confer well-studied optical properties. Mesoporous silica-coated gold nanorods were loaded with indocyanine green (ICG) to increase their fluorescence signal when used *in vivo*. The particles were loaded into tumor-bearing mice and used as fluorescence and CT CA. Fluorescence imaging revealed a strong signal 12 hours postinjection owing to the gradual release of ICG from the mesoporous silica [103]. Zhang loaded PEG micelles with AuNP and bis(4-(*N*-(2-naphthyl)phenylamino)phenyl)-fumaronitrile (NPAPF), an aggregation induced emission dye. The fluorescence of this dye is able to overcome the quenching effect of the AuNP when in a high water fraction liquid. These properties made it an appropriate candidate for *in vivo* imaging. The fluorescent signal was still highly detectable in a mouse model after 24 hours [98].

Aggregated or clustered AuNP have been shown to enhance luminescence signal over single particles alone. The above study by Li also utilized fluorescence imaging to track particles *in vivo*. The aggregated nature of the gold particles enhanced fluorescence signal compared to discrete nanoclusters, resulting in a 5-fold higher fluorescence intensity. The particles also created significant contrast *in vivo* after injection into tumor-bearing mice [20]. The above multimodal particle designed by Wu et al. also utilized gold clusters. This allowed the particles to be used as fluorescence contrast agents *in vivo* in a tumor-bearing mouse. Interestingly, these aggregated particles underwent a blue-shift in fluorescence peak compared to discrete AuNP, from 612 to 595 nm [124]. Zhou et al. encapsulated gold clusters in silica for fluorescence imaging in mice. Particles were injected into three separate sites on the back of tumor-bearing mice. Fluorescence imaging revealed a strong signal 6 hours postinjection, while CT imaging showed a 3-fold increase in CT attenuation [60]. Hayashi designed gold aggregates encapsulated with silica to enhance the overall fluorescent property of the particles. Authors noted the strong fluorescence enhancement of particles caused by their surface plasmon resonance. Particles still created a strong fluorescence signal 18 hours after injection into a mouse model [133]. Although fluorescence imaging is not common clinically, its simple image capture technique may point to its use in surgical settings.

3.4. Photoacoustic Imaging. Photoacoustic imaging is a relatively new method that takes advantage of the same optical properties as fluorescence imaging. Tissues are irradiated by visible or near-infrared light resulting in adiabatic expansion. This creates pressure waves, which are in turn measured and used to reconstruct an image. The modality depends upon the optical and thermal properties of the tissues. Contrast agents are utilized in cases where depth of penetration is low or there

is a lack of natural contrast between tissues [134]. Chanda et al. investigated the use of cinnamon phytochemicals as an AuNP capping agent to enhance particle uptake to cancer cells. Particles were added to cells *in vitro* and irradiated using a tunable laser. Untreated cells showed a linear photoacoustic response, while treated cells displayed a time variant signal, indicating particle uptake and particle contrast ability [102]. The fluorescent dye Prussian blue has also been utilized as a coating to enhance photoacoustic signal. Particles were tested in agar gels as well as mice using a 765 nm laser. In the agar gel, increasingly thick layers of tissue were placed in the laser path to investigate signal penetration depth. High resolution was achieved in the absence of tissue, while an increasing loss of clarity was evident up to ~ 4.3 cm [104]. Cheheltani et al. encapsulated AuNP into polydi(carboxylatophenoxy)phosphazene (PCPP) nanospheres. Formulated particles exhibited high CT contrast, while the absorbable wavelengths could be tuned by changing the size or amount of included AuNP [7]. Photoacoustic imaging is still a new modality, and further work is required to fully understand the parameters required for AuNP as a photoacoustic contrast agent.

3.5. Nuclear Imaging: Single Photon Emission Computed Tomography and Positron Emission Tomography. Nuclear imaging comprises two separate 3D modalities, single photon emission computed tomography (SPECT) and positron emission tomography (PET), which both operate on the same principles while utilizing different contrast agents. Both rely on patient internalization of a radiotracer comprised of an isotope and a biological targeting element. Images arise through the detection of gamma rays. The targeting component of the radiotracer gives biologically relevant information such as the metabolism of a compound. Thus while most modalities originate their signal externally, nuclear imaging signal arises internally and depends entirely on the radiotracers used.

The same isotopes traditionally utilized as nuclear imaging radiotracers can be added to AuNP to achieve multimodal imaging. One study used PEGylated, hollow gold nanospheres as platforms to attach ^{64}Cu to achieve PET imaging. Particles were injected into tumor-bearing mice either intra-arterially or intravenously along with iodinated oil to enhance tumor uptake. PET/CT scans 1 hour after injection show high contrast in the tumor area [50]. Li et al. undertook a study using both ^{111}In - or ^{64}Cu -labeled AuNP for SPECT and PET imaging, respectively. The particles were loaded into T cells using electroporation; these cells were subsequently injected into mice for imaging. ^{111}In -labeled cells were injected directly into the lung of mice and successfully imaged using PET/CT. ^{64}Cu -labeled cells were injected into the tail vein and tracked using SPECT/CT imaging over the course of 18 hours [135]. Targeted hollow gold nanospheres carrying ^{111}In were used to image tumors on the tongue of mice. Particles were targeted using EGFR-targeting aptamers and injected intravenously. SPECT/CT imaging showed a much higher signal intensity using targeted particles, even after 24 hours [54]. Although this combination

of imaging techniques is relatively unexplored, the targeting ability and long circulation time of gold nanoparticles may offer a platform for further nuclear imaging studies.

4. Conclusion

Gold nanoparticles have great potential as contrast agents in a variety of imaging modalities. On their own, their high X-ray attenuation and nontoxicity may be combined with surface molecules to enhance tissue-targeting and improve circulation time. AuNP size and reactivity also allow their accumulation in certain organ systems and tissues, especially cancerous tumors. When combined with other materials such as rare earth metals or fluorescent dyes, their use expands to include imaging modalities such as magnetic resonance imaging or ultrasound. These additional materials may add or subtract from image contrast and may create toxicity or circulation concerns. A diverse array of formulation methods including entrapment and encapsulation have been developed to overcome these design hurdles. This multimodal possibility represents a step forward in clinical diagnosis. Long circulating, nontoxic contrast agents that can reveal anatomical and disease information across multiple imaging types could ease clinical imaging burdens and simplify scanning procedures.

AuNP for use as X-ray contrast agents are currently available commercially, although they are for research use only. In order to gain clinical acceptance, further *in vivo* human research must be conducted. Questions still exist as to their biodistribution, circulation times, and targeting ability. Still, AuNP remain an excellent platform for X-ray contrast agents. Improvements in their ability to effectively circulate and localize at a desired area of interest will allow for their use in clinical settings.

Conflicts of Interest

The authors declare that they have no conflicts of interest.

References

- [1] T. L. Szabo, *Diagnostic Ultrasound Imaging: Inside Out*, Academic Press, Cambridge, Mass, USA, 2004.
- [2] D. W. McRobbie, *MRI from Picture to Proton*, Cambridge University Press, Cambridge, UK, 2007.
- [3] J. Hsieh, *Computed Tomography: Principles, Design, Artifacts, and Recent Advances*, SPIE Press, 3rd edition, 2015.
- [4] R. Nutt, "The history of positron emission tomography," *Molecular Imaging and Biology*, vol. 4, no. 1, pp. 11–26, 2002.
- [5] M. Nahrendorf, H. Zhang, S. Hembrador et al., "Nanoparticle PET-CT imaging of macrophages in inflammatory atherosclerosis," *Circulation*, vol. 117, no. 3, pp. 379–387, 2008.
- [6] P. S. Chandra, N. Salamon, J. Huang et al., "FDG-PET/MRI coregistration and diffusion-tensor imaging distinguish epileptogenic tubers and cortex in patients with tuberous sclerosis complex: a preliminary report," *Epilepsia*, vol. 47, no. 9, pp. 1543–1549, 2006.
- [7] R. Cheheltani, R. M. Ezzibdeh, P. Chhour et al., "Tunable, biodegradable gold nanoparticles as contrast agents for computed tomography and photoacoustic imaging," *Biomaterials*, vol. 102, pp. 87–97, 2016.
- [8] N. Teraphongphom, P. Chhour, J. R. Eisenbrey et al., "Nanoparticle loaded polymeric microbubbles as contrast agents for multimodal imaging," *Langmuir*, vol. 31, no. 43, pp. 11858–11867, 2015.
- [9] L. B. Hunt, "The true story of Purple of Cassius - The birth of gold-based glass and enamel colours," *Gold Bulletin*, vol. 9, no. 4, pp. 134–139, 1976.
- [10] M. Faraday, "The Bakerian lecture: experimental relations of gold (and other metals) to light," *Philosophical Transactions of the Royal Society A: Mathematical, Physical & Engineering Sciences*, vol. 147, pp. 145–181, 1857.
- [11] L. Nie, F. Liu, P. Ma, and X. Xiao, "Applications of gold nanoparticles in optical biosensors," *Journal of Biomedical Nanotechnology*, vol. 10, no. 10, pp. 2700–2721, 2014.
- [12] H. Daraee, A. Eatemadi, E. Abbasi, S. F. Aval, M. Kouhi, and A. Akbarzadeh, "Application of gold nanoparticles in biomedical and drug delivery," *Artificial Cells, Nanomedicine and Biotechnology*, vol. 44, no. 1, pp. 410–422, 2016.
- [13] L. E. Cole, R. D. Ross, J. M. Tilley, T. Vargo-Gogola, and R. K. Roeder, "Gold nanoparticles as contrast agents in X-ray imaging and computed tomography," *Nanomedicine*, vol. 10, no. 2, pp. 321–341, 2015.
- [14] S. Hwang, J. Nam, S. Jung, J. Song, H. Doh, and S. Kim, "Gold nanoparticle-mediated photothermal therapy: current status and future perspective," *Nanomedicine*, vol. 9, no. 13, pp. 2003–2022, 2014.
- [15] A. Ahangari, S. Mojtaba, and F. Saghatchi, "Gentamicin-gold nanoparticles conjugate: a contrast agent for X-ray imaging of infectious foci due to staphylococcus aureus," *IET Nanobiotechnology*, vol. 10, no. 4, pp. 190–194, 2016.
- [16] D. De Wilde, B. Trachet, C. Van der Donckt et al., "Vulnerable plaque detection and quantification with gold particle-enhanced computed tomography in atherosclerotic mouse models," *Molecular Imaging*, vol. 14, no. 6, 2015.
- [17] J. Park, J. Park, E. J. Ju et al., "Multifunctional hollow gold nanoparticles designed for triple combination therapy and CT imaging," *Journal of Controlled Release*, vol. 207, pp. 77–85, 2015.
- [18] J. Li, Y. Hu, J. Yang et al., "Hyaluronic acid-modified Fe₃O₄ at Au core/shell nanostars for multimodal imaging and photothermal therapy of tumors," *Biomaterials*, vol. 38, pp. 10–21, 2015.
- [19] P. Jackson, S. Periasamy, V. Bansal, and M. Geso, "Evaluation of the effects of gold nanoparticle shape and size on contrast enhancement in radiological imaging," *Australasian Physical & Engineering Sciences in Medicine*, vol. 34, no. 2, pp. 243–249, 2011.
- [20] L. Li, L. Zhang, T. Wang et al., "Facile and scalable synthesis of novel spherical Au nanocluster assemblies@polyacrylic acid/calcium phosphate nanoparticles for dual-modal imaging-guided cancer chemotherapy," *Small*, vol. 11, no. 26, pp. 3162–3173, 2015.
- [21] Q.-Y. Lin, Z. Li, K. A. Brown et al., "Strong coupling between plasmonic gap modes and photonic lattice modes in DNA-assembled gold nanocube arrays," *Nano Letters*, vol. 15, no. 7, pp. 4699–4703, 2015.
- [22] J. F. Hainfeld, D. N. Slatkin, and H. M. Smilowitz, "The use of gold nanoparticles to enhance radiotherapy in mice," *Physics in Medicine and Biology*, vol. 49, no. 18, pp. N309–N315, 2004.

- [23] J. F. Hainfeld, D. N. Slatkin, T. M. Focella, and H. M. Smilowitz, "Gold nanoparticles: a new X-ray contrast agent," *British Journal of Radiology*, vol. 79, no. 939, pp. 248–253, 2006.
- [24] L. Vigderman and E. R. Zubarev, "Therapeutic platforms based on gold nanoparticles and their covalent conjugates with drug molecules," *Advanced Drug Delivery Reviews*, vol. 65, no. 5, pp. 663–676, 2013.
- [25] J. P. Almeida, E. R. Figueroa, and R. A. Drezek, "Gold nanoparticle mediated cancer immunotherapy," *Nanomedicine: Nanotechnology, Biology and Medicine*, vol. 10, no. 3, pp. 503–514, 2014.
- [26] C. Zhao and Z. Liu, "Application of gold nanoparticles in cancer therapy," *Zhongguo Yi Xue Ke Xue Yuan Xue Bao*, vol. 36, no. 3, pp. 324–329, 2014.
- [27] Y. Ding, Z. Jiang, K. Saha et al., "Gold nanoparticles for nucleic acid delivery," *Molecular Therapy*, vol. 22, no. 6, pp. 1075–1083, 2014.
- [28] C. Suplee, "X-ray mass attenuation coefficients," NIST, 2009, <https://www.nist.gov/pml/x-ray-mass-attenuation-coefficients>.
- [29] S. Yu and A. D. Watson, "Metal-based X-ray contrast media," *Chemical Reviews*, vol. 99, no. 9, pp. 2353–2378, 1999.
- [30] R. E. Alexander and R. B. Gunderman, "EMI and the first CT scanner," *Journal of the American College of Radiology*, vol. 7, no. 10, pp. 778–781, 2010.
- [31] S. Si-Mohamed, D. P. Cormode, D. Bar-Ness et al., "Evaluation of spectral photon counting computed tomography K-edge imaging for determination of gold nanoparticle biodistribution in vivo," *Nanoscale*, vol. 9, no. 46, pp. 18246–18257, 2017.
- [32] C. O. Schirra, A. Senpan, E. Roessel et al., "Second generation gold nanobeacons for robust K-edge imaging with multi-energy CT," *Journal of Materials Chemistry*, vol. 22, no. 43, pp. 23071–23077, 2012.
- [33] R. R. Carlton and A. M. Adler, *Principles of Radiographic Imaging: An Art and A Science*, Delmar/Cengage Learning, Clifton Park, NY, USA, 2013.
- [34] H. Katayama, K. Yamaguchi, T. Kozuka, T. Takashima, P. Seez, and K. Matsuura, "Adverse reactions to ionic and nonionic contrast media. A report from the Japanese Committee on the Safety of Contrast Media," *Radiology*, vol. 175, no. 3, pp. 621–628, 1990.
- [35] G. Jost, H. Pietsch, P. Lengsfeld, J. Hütter, and M. A. Sieber, "The impact of the viscosity and osmolality of iodine contrast agents on renal elimination," *Investigative Radiology*, vol. 45, no. 5, pp. 255–261, 2010.
- [36] D. C. Lenhard, H. Pietsch, M. A. Sieber et al., "The osmolality of nonionic, iodinated contrast agents as an important factor for renal safety," *Investigative Radiology*, vol. 47, no. 9, pp. 503–510, 2012.
- [37] J. Eng, R. F. Wilson, R. M. Subramaniam et al., "Comparative effect of contrast media type on the incidence of contrast-induced nephropathy: a systematic review and meta-analysis," *Annals of Internal Medicine*, vol. 164, no. 6, pp. 417–424, 2016.
- [38] Research C for DE and Drug Safety and Availability, "FDA Drug Safety Communication: FDA advises of rare cases of underactive thyroid in infants given iodine-containing contrast agents for medical imaging," 2017, <http://www.fda.gov/Drugs/DrugSafety/ucm472782.htm>.
- [39] E. I. Piechowiak, J.-F. W. Peter, B. Kleb, K. J. Klose, and J. T. Heverhagen, "Intravenous iodinated contrast agents amplify DNA radiation damage at CT," *Radiology*, vol. 275, no. 3, pp. 692–697, 2015.
- [40] B. Aydogan, J. Li, T. Rajh et al., "AuNP-DG: Deoxyglucose-labeled gold nanoparticles as X-ray computed tomography contrast agents for cancer imaging," *Molecular Imaging and Biology*, vol. 12, no. 5, pp. 463–467, 2010.
- [41] J. Li, A. Chaudhary, S. J. Chmura et al., "A novel functional CT contrast agent for molecular imaging of cancer," *Physics in Medicine and Biology*, vol. 55, no. 15, pp. 4389–4397, 2010.
- [42] G. Feng, B. Kong, J. Xing, and J. Chen, "Enhancing multimodality functional and molecular imaging using glucose-coated gold nanoparticles," *Clinical Radiology*, vol. 69, no. 11, pp. 1105–1111, 2014.
- [43] R. Popovtzer, A. Agrawal, N. A. Kotov et al., "Targeted gold nanoparticles enable molecular CT imaging of cancer," *Nano Letters*, vol. 8, no. 12, pp. 4593–4596, 2008.
- [44] W. Eck, A. I. Nicholson, H. Zentgraf, W. Semmler, and S. Bartling, "Anti-CD4-targeted gold nanoparticles induce specific contrast enhancement of peripheral lymph nodes in X-ray computed tomography of live mice," *Nano Letters*, vol. 10, no. 7, pp. 2318–2322, 2010.
- [45] J. F. Hainfeld, M. J. O'Connor, F. A. Dilmanian, D. N. Slatkin, D. J. Adams, and H. M. Smilowitz, "Micro-CT enables microlocalisation and quantification of Her2-targeted gold nanoparticles within tumour regions," *British Journal of Radiology*, vol. 84, no. 1002, pp. 526–533, 2011.
- [46] T. Reuveni, M. Motiei, Z. Romman, A. Popovtzer, and R. Popovtzer, "Targeted gold nanoparticles enable molecular CT imaging of cancer: an in vivo study," *International Journal of Nanomedicine*, vol. 6, pp. 2859–2864, 2011.
- [47] H.-W. Kao, Y.-Y. Lin, C.-C. Chen et al., "Evaluation of EGFR-targeted radioimmuno-gold-nanoparticles as a theranostic agent in a tumor animal model," *Bioorganic & Medicinal Chemistry Letters*, vol. 23, no. 11, pp. 3180–3185, 2013.
- [48] N. Chanda, V. Kattumuri, R. Shukla et al., "Bombesin functionalized gold nanoparticles show in vitro and in vivo cancer receptor specificity," *Proceedings of the National Academy of Sciences of the United States of America*, vol. 107, no. 19, pp. 8760–8765, 2010.
- [49] Y. Hao, B. Zhang, C. Zheng et al., "The tumor-targeting core-shell structured DTX-loaded PLGA@Au nanoparticles for chemo-photothermal therapy and X-ray imaging," *Journal of Controlled Release*, vol. 220, pp. 545–555, 2015.
- [50] M. Tian, W. Lu, R. Zhang et al., "Tumor uptake of hollow gold nanospheres after intravenous and intra-arterial injection: PET/CT study in a rabbit VX2 liver cancer model," *Molecular Imaging and Biology*, vol. 15, no. 5, pp. 614–624, 2013.
- [51] J. Zhu, F. Fu, Z. Xiong, M. Shen, and X. Shi, "Dendrimer-entrapped gold nanoparticles modified with RGD peptide and alpha-tocopheryl succinate enable targeted theranostics of cancer cells," *Colloids and Surfaces B: Biointerfaces*, vol. 133, pp. 36–42, 2015.
- [52] D. Kim, Y. Y. Jeong, and S. Jon, "A drug-loaded aptamer—gold nanoparticle bioconjugate for combined CT imaging and therapy of prostate cancer," *ACS Nano*, vol. 4, no. 7, pp. 3689–3696, 2010.
- [53] C. Li, T. Kuo, H. Su et al., "Fluorescence-guided probes of aptamer-targeted gold nanoparticles with computed tomography imaging accesses for in vivo tumor resection," *Scientific Reports*, vol. 5, no. 1, 2015.
- [54] M. P. Melancon, M. Zhou, R. Zhang et al., "Selective uptake and imaging of aptamer- and antibody-conjugated hollow nanospheres targeted to epidermal growth factor receptors

- overexpressed in head and neck cancer,” *ACS Nano*, vol. 8, no. 5, pp. 4530–4538, 2014.
- [55] H. Wang, L. Zheng, C. Peng, M. Shen, X. Shi, and G. Zhang, “Folic acid-modified dendrimer-entrapped gold nanoparticles as nanoprobes for targeted CT imaging of human lung adenocarcinoma,” *Biomaterials*, vol. 34, no. 2, pp. 470–480, 2013.
- [56] H. Liu, M. Shen, J. Zhao et al., “Facile formation of folic acid-modified dendrimer-stabilized gold-silver alloy nanoparticles for potential cellular computed tomography imaging applications,” *Analyst*, vol. 138, no. 7, pp. 1979–1987, 2013.
- [57] H. Cai, K. Li, J. Li et al., “Dendrimer-Assisted Formation of $\text{Fe}_3\text{O}_4/\text{Au}$ Nanocomposite Particles for Targeted Dual Mode CT/MR Imaging of Tumors,” *Small*, vol. 11, no. 35, pp. 4584–4593, 2015.
- [58] Q. Chen, K. Li, S. Wen et al., “Targeted CT/MR dual mode imaging of tumors using multifunctional dendrimer-entrapped gold nanoparticles,” *Biomaterials*, vol. 34, no. 21, pp. 5200–5209, 2013.
- [59] Q. Chen, H. Wang, H. Liu et al., “Multifunctional dendrimer-entrapped gold nanoparticles modified with RGD peptide for targeted computed tomography/magnetic resonance dual-modal imaging of tumors,” *Analytical Chemistry*, vol. 87, no. 7, pp. 3949–3956, 2015.
- [60] Z. Zhou, C. Zhang, Q. Qian et al., “Folic acid-conjugated silica capped gold nanoclusters for targeted fluorescence/X-ray computed tomography imaging,” *Journal of Nanobiotechnology*, vol. 11, article 17, 2013.
- [61] I.-C. Sun, J. H. Na, S. Y. Jeong et al., “Biocompatible glycol chitosan-coated gold nanoparticles for tumor-targeting CT imaging,” *Pharmaceutical Research*, vol. 31, no. 6, pp. 1418–1425, 2014.
- [62] J. H. Na, S.-Y. Lee, S. Lee et al., “Effect of the stability and deformability of self-assembled glycol chitosan nanoparticles on tumor-targeting efficiency,” *Journal of Controlled Release*, vol. 163, no. 1, pp. 2–9, 2012.
- [63] Y. Zhang and M. Zhang, “Calcium phosphate/chitosan composite scaffolds for controlled in vitro antibiotic drug release,” *Journal of Biomedical Materials Research Part B: Applied Biomaterials*, vol. 62, no. 3, pp. 378–386, 2002.
- [64] X. He, F. Liu, L. Liu, T. Duan, H. Zhang, and Z. Wang, “Lectin-conjugated $\text{Fe}_2\text{O}_3@ \text{Au}$ core@ shell nanoparticles as dual mode contrast agents for in vivo detection of tumor,” *Molecular Pharmaceutics*, vol. 11, no. 3, pp. 738–745, 2014.
- [65] H. Liu, H. Wang, Y. Xu et al., “Lactobionic acid-modified dendrimer-entrapped gold nanoparticles for targeted computed tomography imaging of human hepatocellular carcinoma,” *ACS Applied Materials & Interfaces*, vol. 6, no. 9, pp. 6944–6953, 2014.
- [66] Y. Zeng, D. Zhang, M. Wu et al., “Lipid-AuNPs@PDA nanohybrid for MRI/CT imaging and photothermal therapy of hepatocellular carcinoma,” *ACS Applied Materials & Interfaces*, vol. 6, no. 16, pp. 14266–14277, 2014.
- [67] L. E. Cole, T. Vargo-Gogola, and R. K. Roeder, “Contrast-enhanced X-ray detection of microcalcifications in radiographically dense mammary tissue using targeted gold nanoparticles,” *ACS Nano*, vol. 9, no. 9, pp. 8923–8932, 2015.
- [68] R. Meir, K. Shamalov, and O. Betzer, “Nanomedicine for cancer immunotherapy: tracking cancer-specific T-cells in vivo with gold nanoparticles and CT imaging,” *ACS Nano*, vol. 9, no. 6, pp. 6363–6372, 2015.
- [69] D.-E. Kim, J.-Y. Kim, I.-C. Sun et al., “Hyperacute direct thrombus imaging using computed tomography and gold nanoparticles,” *Annals of Neurology*, vol. 73, no. 5, pp. 617–625, 2013.
- [70] J.-Y. Kim, J. H. Ryu, D. Schellingerhout et al., “Direct imaging of cerebral thromboemboli using computed tomography and fibrin-targeted gold nanoparticles,” *Theranostics*, vol. 5, no. 10, pp. 1098–1114, 2015.
- [71] W. E. Ghann, O. Aras, T. Fleiter, and M.-C. Daniel, “Syntheses and characterization of lisinopril-coated gold nanoparticles as highly stable targeted CT contrast agents in cardiovascular diseases,” *Langmuir*, vol. 28, no. 28, pp. 10398–10408, 2012.
- [72] D. P. Cormode, E. Roessl, A. Thran et al., “Atherosclerotic plaque composition: Analysis with multicolor CT and targeted gold nanoparticles,” *Radiology*, vol. 256, no. 3, pp. 774–782, 2010.
- [73] M. M. Van Schooneveld, D. P. Cormode, R. Koole et al., “A fluorescent, paramagnetic and PEGylated gold/silica nanoparticle for MRI, CT and fluorescence imaging,” *Contrast Media & Molecular Imaging*, vol. 5, no. 4, pp. 231–236, 2010.
- [74] I. E. Allijn, W. Leong, J. Tang et al., “Gold nanocrystal labeling allows low-density lipoprotein imaging from the subcellular to macroscopic level,” *ACS Nano*, vol. 7, no. 11, pp. 9761–9770, 2013.
- [75] J. Qin, C. Peng, B. Zhao et al., “Noninvasive detection of macrophages in atherosclerotic lesions by computed tomography enhanced with PEGylated gold nanoparticles,” *International Journal of Nanomedicine*, vol. 9, no. 1, pp. 5575–5590, 2014.
- [76] I.-C. Sun, D.-K. Eun, J. H. Na et al., “Heparin-coated gold nanoparticles for liver-specific CT imaging,” *Chemistry*, vol. 15, no. 48, pp. 13276–13347, 2009.
- [77] H. Y. Zhao, S. Liu, J. He et al., “Synthesis and application of strawberry-like Fe_3O_4 -Au nanoparticles as CT-MR dual-modality contrast agents in accurate detection of the progressive liver disease,” *Biomaterials*, vol. 51, pp. 194–207, 2015.
- [78] P. Chhour, P. C. Naha, S. M. O’Neill et al., “Labeling monocytes with gold nanoparticles to track their recruitment in atherosclerosis with computed tomography,” *Biomaterials*, vol. 87, pp. 93–103, 2016.
- [79] Z. Zhang, R. D. Ross, and R. K. Roeder, “Preparation of functionalized gold nanoparticles as a targeted X-ray contrast agent for damaged bone tissue,” *Nanoscale*, vol. 2, no. 4, pp. 582–586, 2010.
- [80] M. Ventura, Y. Sun, V. Rusu et al., “Dual contrast agent for computed tomography and magnetic resonance hard tissue imaging,” *Tissue Engineering - Part C: Methods*, vol. 19, no. 6, pp. 405–416, 2013.
- [81] Y. Wang, C. Xu, J. Zhai et al., “Label-free Au cluster used for in vivo 2D and 3D computed tomography of murine kidneys,” *Analytical Chemistry*, vol. 87, no. 1, pp. 343–345, 2015.
- [82] V. Kattumuri, K. Katti, and S. Bhaskaran, “Gum arabic as a phytochemical construct for the stabilization of gold nanoparticles: in vivo pharmacokinetics and X-ray-contrast-imaging studies,” *Small*, vol. 3, no. 2, pp. 333–341, 2007.
- [83] E. Boote, G. Fent, V. Kattumuri et al., “Gold nanoparticle contrast in a phantom and juvenile swine. Models for molecular imaging of human organs using X-ray computed tomography,” *Academic Radiology*, vol. 17, no. 4, pp. 410–417, 2010.
- [84] Q.-Y. Cai, S. H. Kim, K. S. Choi et al., “Colloidal gold nanoparticles as a blood-pool contrast agent for X-ray computed tomography in mice,” *Investigative Radiology*, vol. 42, no. 12, pp. 797–806, 2007.
- [85] J. T. Au, G. Craig, V. Longo et al., “Gold nanoparticles provide bright long-lasting vascular contrast for CT imaging,” *American Journal of Roentgenology*, vol. 200, no. 6, pp. 1347–1351, 2013.

- [86] C. Peng, K. Li, X. Cao et al., "Facile formation of dendrimer-stabilized gold nanoparticles modified with diatrizoic acid for enhanced computed tomography imaging applications," *Nanoscale*, vol. 4, no. 21, pp. 6768–6778, 2012.
- [87] C. Kojima, Y. Umeda, M. Ogawa, A. Harada, Y. Magata, and K. Kono, "X-ray computed tomography contrast agents prepared by seeded growth of gold nanoparticles in PEGylated dendrimer," *Nanotechnology*, vol. 21, no. 24, p. 245104, 2010.
- [88] K. Hayashi, M. Nakamura, and K. Ishimura, "Near-Infrared Fluorescent Silica-Coated Gold Nanoparticle Clusters for X-Ray Computed Tomography/Optical Dual Modal Imaging of the Lymphatic System," *Advanced Healthcare Materials*, vol. 2, no. 5, pp. 756–763, 2013.
- [89] J. F. Hainfeld, H. M. Smilowitz, M. J. O'connor, F. A. Dilmajian, and D. N. Slatkin, "Gold nanoparticle imaging and radiotherapy of brain tumors in mice," *Nanomedicine*, vol. 8, no. 10, pp. 1601–1609, 2013.
- [90] G. von Maltzahn, J. Park, A. Agrawal et al., "Computationally guided photothermal tumor therapy using long-circulating gold nanorod antennas," *Cancer Research*, vol. 69, no. 9, pp. 3892–3900, 2009.
- [91] J. R. Ashton, D. P. Clark, E. J. Moding et al., "Dual-energy micro-CT functional imaging of primary lung cancer in mice using gold and iodine nanoparticle contrast agents: a validation study," *PLoS ONE*, vol. 9, no. 2, Article ID e88129, 2014.
- [92] P. C. Naha, K. C. Lau, J. C. Hsu et al., "Gold silver alloy nanoparticles (GSAN): An imaging probe for breast cancer screening with dual-energy mammography or computed tomography," *Nanoscale*, vol. 8, no. 28, pp. 13740–13754, 2016.
- [93] H. Wang, L. Zheng, C. Peng et al., "Computed tomography imaging of cancer cells using acetylated dendrimer-entrapped gold nanoparticles," *Biomaterials*, vol. 32, no. 11, pp. 2979–2988, 2011.
- [94] K. Li, S. Wen, A. C. Larson et al., "Multifunctional dendrimer-based nanoparticles for in vivo MR/CT dual-modal molecular imaging of breast cancer," *International Journal of Nanomedicine*, vol. 8, pp. 2589–2600, 2013.
- [95] C. Peng, L. Zheng, Q. Chen et al., "PEGylated dendrimer-entrapped gold nanoparticles for in vivo blood pool and tumor imaging by computed tomography," *Biomaterials*, vol. 33, no. 4, pp. 1107–1119, 2012.
- [96] H. Liu, H. Wang, Y. Xu et al., "Synthesis of PEGylated low generation dendrimer-entrapped gold nanoparticles for CT imaging applications," *Nanoscale*, vol. 6, no. 9, pp. 4521–4526, 2014.
- [97] B. Zhou, L. Zheng, C. Peng et al., "Synthesis and characterization of PEGylated polyethylenimine-entrapped gold nanoparticles for blood pool and tumor CT imaging," *ACS Applied Materials & Interfaces*, vol. 6, no. 19, pp. 17190–17199, 2014.
- [98] J. Zhang, C. Li, X. Zhang et al., "In vivo tumor-targeted dual-modal fluorescence/CT imaging using a nanoprobe co-loaded with an aggregation-induced emission dye and gold nanoparticles," *Biomaterials*, vol. 42, pp. 103–111, 2015.
- [99] L. Wang, P. Zhang, J. Shi et al., "Radiofrequency-triggered tumor-targeting delivery system for theranostics application," *ACS Applied Materials & Interfaces*, vol. 7, no. 10, pp. 5736–5747, 2015.
- [100] J. Shi, Z. Chen, L. Wang et al., "A tumor-specific cleavable nanosystem of PEG-modified C60@Au hybrid aggregates for radio frequency-controlled release, hyperthermia, photodynamic therapy and X-ray imaging," *Acta Biomaterialia*, vol. 29, pp. 282–287, 2016.
- [101] H. Ke, X. Yue, J. Wang et al., "Gold nanoshelled liquid perfluorocarbon nanocapsules for combined dual modal ultrasound/CT imaging and photothermal therapy of cancer," *Small*, vol. 10, no. 6, pp. 1220–1227, 2014.
- [102] N. Chanda, R. Shukla, A. Zambre et al., "An effective strategy for the synthesis of biocompatible gold nanoparticles using cinnamon phytochemicals for phantom CT imaging and photoacoustic detection of cancerous cells," *Pharmaceutical Research*, vol. 28, no. 2, pp. 279–291, 2011.
- [103] T. Luo, P. Huang, G. Gao et al., "Mesoporous silica-coated gold nanorods with embedded indocyanine green for dual mode X-ray CT and NIR fluorescence imaging," *Optics Express*, vol. 19, no. 18, pp. 17030–17039, 2011.
- [104] L. Jing, X. Liang, Z. Deng et al., "Prussian blue coated gold nanoparticles for simultaneous photoacoustic/CT bimodal imaging and photothermal ablation of cancer," *Biomaterials*, vol. 35, no. 22, pp. 5814–5821, 2014.
- [105] F. Sousa, S. Mandal, C. Garrovo et al., "Functionalized gold nanoparticles: A detailed in vivo multimodal microscopic brain distribution study," *Nanoscale*, vol. 2, no. 12, pp. 2826–2834, 2010.
- [106] D. P. Clark, K. Ghaghada, E. J. Moding, D. G. Kirsch, and C. T. Badea, "In vivo characterization of tumor vasculature using iodine and gold nanoparticles and dual energy micro-CT," *Physics in Medicine and Biology*, vol. 58, no. 6, pp. 1683–1704, 2013.
- [107] B. M. Dale, A. Mark, and R. C. Semelka, *MRI: Basic Principles and Applications*, Wiley-Blackwell, 5th edition, 2015.
- [108] M. A. Kirchin, G. P. Pirovano, and A. Spinazzi, "Gadobenate dimeglumine (Gd-BOPTA): An overview," *Investigative Radiology*, vol. 33, no. 11, pp. 798–809, 1998.
- [109] G. Schuhmann-Giampieri, M. Mahler, G. Röhl, R. Maibauer, and S. Schmitz, "Pharmacokinetics of the liver-specific contrast agent Gd-EOB-DTPA in relation to contrast-enhanced liver imaging in humans," *Clinical Pharmacology and Therapeutics*, vol. 37, no. 7, pp. 587–596, 1997.
- [110] P. Marckmann, L. Skov, K. Rossen et al., "Nephrogenic systemic fibrosis: Suspected causative role of gadodiamide used for contrast-enhanced magnetic resonance imaging," *Journal of the American Society of Nephrology*, vol. 17, no. 9, pp. 2359–2362, 2006.
- [111] R. Weissleder, D. D. Stark, B. L. Engelstad et al., "Superparamagnetic iron oxide: pharmacokinetics and toxicity," *American Journal of Roentgenology*, vol. 152, no. 1, pp. 167–173, 1989.
- [112] R. Lawaczeck, H. Bauer, T. Frenzel et al., "Magnetic Iron Oxide Particles Coated with Carboxydextran for Parenteral Administration and Liver Contrast," *Acta Radiologica*, vol. 38, no. 4, pp. 584–597, 2016.
- [113] C. Luo, Y. Li, L. Yang, X. Wang, J. Long, and J. Liu, "Superparamagnetic iron oxide nanoparticles exacerbate the risks of reactive oxygen species-mediated external stresses," *Archives of Toxicology*, vol. 89, no. 3, pp. 357–369, 2015.
- [114] W. Feng, X. Zhou, W. Nie et al., "Au/polypyrrole@Fe₃O₄ nanocomposites for MR/CT dual-modal imaging guided-photothermal therapy: An in vitro study," *ACS Applied Materials & Interfaces*, vol. 7, no. 7, pp. 4354–4367, 2015.
- [115] V. Amendola, S. Scaramuzza, L. Litti et al., "Magneto-plasmonic Au-Fe alloy nanoparticles designed for multimodal SERS-MRI-CT imaging," *Small*, vol. 10, no. 12, pp. 2476–2486, 2014.
- [116] D. Kim, M. K. Yu, T. S. Lee, J. J. Park, Y. Y. Jeong, and S. Jon, "Amphiphilic polymer-coated hybrid nanoparticles as CT/MRI

- dual contrast agents,” *Nanotechnology*, vol. 22, no. 15, Article ID 155101, 2011.
- [117] W. Dong, Y. Li, D. Niu et al., “A simple route to prepare monodisperse Au NP-decorated, dye-doped, superparamagnetic nanocomposites for optical, MR, and CT trimodal imaging,” *Small*, vol. 9, no. 15, pp. 2500–2508, 2013.
- [118] J. Li, L. Zheng, H. Cai et al., “Facile one-pot synthesis of Fe₃O₄@Au composite nanoparticles for dual-mode MR/CT imaging applications,” *ACS Applied Materials & Interfaces*, vol. 5, no. 20, pp. 10357–10366, 2013.
- [119] L. Sun, D. Y. Joh, A. Al-Zaki et al., “Theranostic application of mixed gold and superparamagnetic iron oxide nanoparticle micelles in glioblastoma multiforme,” *Journal of Biomedical Nanotechnology*, vol. 12, no. 2, pp. 347–356, 2016.
- [120] C. Tian, L. Zhu, F. Lin, and S. G. Boyes, “Poly(acrylic acid) Bridged Gadolinium Metal-Organic Framework-Gold Nanoparticle Composites as Contrast Agents for Computed Tomography and Magnetic Resonance Bimodal Imaging,” *ACS Applied Materials & Interfaces*, vol. 7, no. 32, pp. 17765–17775, 2015.
- [121] S. Wen, K. Li, H. Cai et al., “Multifunctional dendrimer-entrapped gold nanoparticles for dual mode CT/MR imaging applications,” *Biomaterials*, vol. 34, no. 5, pp. 1570–1580, 2013.
- [122] Y. Chen, F. Guo, Y. Qiu et al., “Encapsulation of particle ensembles in graphene nanosacks as a new route to multifunctional materials,” *ACS Nano*, vol. 7, no. 5, pp. 3744–3753, 2013.
- [123] X. Shi, H. Gong, Y. Li, C. Wang, L. Cheng, and Z. Liu, “Graphene-based magnetic plasmonic nanocomposite for dual bioimaging and photothermal therapy,” *Biomaterials*, vol. 34, no. 20, pp. 4786–4793, 2013.
- [124] X. Wu, C. Li, S. Liao et al., “Silica-encapsulated Gd³⁺-aggregated gold nanoclusters for in vitro and in vivo multimodal cancer imaging,” *Chemistry*, vol. 20, no. 29, pp. 8876–8882, 2014.
- [125] K. Zhang, H. Chen, P. Li et al., “Marriage strategy of structure and composition designs for intensifying ultrasound MR & CT trimodal contrast imaging,” *ACS Applied Materials & Interfaces*, vol. 7, no. 33, pp. 18590–18599, 2015.
- [126] Y. Liu, Z. Chang, H. Yuan, A. M. Fales, and T. Vo-Dinh, “Quintuple-modality (SERS-MRI-CT-TPL-PTT) plasmonic nanoprobe for theranostics,” *Nanoscale*, vol. 5, no. 24, pp. 12126–12131, 2013.
- [127] A. J. Coughlin, J. S. Ananta, N. Deng, I. V. Larina, P. Decuzzi, and J. L. West, “Gadolinium-conjugated gold nanoshells for multimodal diagnostic imaging and photothermal cancer therapy,” *Small*, vol. 10, no. 3, pp. 556–565, 2014.
- [128] C. Alric, J. Taleb, G. Le Duc et al., “Gadolinium chelate coated gold nanoparticles as contrast agents for both X-ray computed tomography and magnetic resonance imaging,” *Journal of the American Chemical Society*, vol. 130, no. 18, pp. 5908–5915, 2008.
- [129] I. Lentacker, S. C. De Smedt, and N. N. Sanders, “Drug loaded microbubble design for ultrasound triggered delivery,” *Soft Matter*, vol. 5, no. 11, pp. 2161–2170, 2009.
- [130] E. G. Schutt, D. H. Klein, R. M. Mattrey, and J. G. Riess, “Injectable microbubbles as contrast agents for diagnostic ultrasound imaging: the key role of perfluorochemicals,” *Angewandte Chemie*, vol. 42, no. 28, pp. 3218–3235, 2003.
- [131] Y. Jin, J. Wang, H. Ke, S. Wang, and Z. Dai, “Graphene oxide modified PLA microcapsules containing gold nanoparticles for ultrasonic/CT bimodal imaging guided photothermal tumor therapy,” *Biomaterials*, vol. 34, no. 20, pp. 4794–4802, 2013.
- [132] D. R. Arifin, C. M. Long, A. A. Gilad et al., “Trimodal gadolinium-gold microcapsules containing pancreatic islet cells restore normoglycemia in diabetic mice and can be tracked by using US, CT, and positive-contrast MR imaging,” *Radiology*, vol. 260, no. 3, pp. 790–798, 2011.
- [133] K. Hayashi, M. Nakamura, H. Miki et al., “Gold nanoparticle cluster-plasmon-enhanced fluorescent silica core-shell nanoparticles for X-ray computed tomography-fluorescence dual-mode imaging of tumors,” *Chemical Communications*, vol. 49, no. 46, pp. 5334–5336, 2013.
- [134] D. Wu, L. Huang, M. S. Jiang, and H. Jiang, “Contrast agents for photoacoustic and thermoacoustic imaging: A review,” *International Journal of Molecular Sciences*, vol. 15, no. 12, pp. 23616–23639, 2014.
- [135] H. Li, L. Diaz, D. Lee, L. Cui, X. Liang, and Y. Cheng, “In vivo imaging of T cells loaded with gold nanoparticles: A pilot study,” *La Radiologia Medica*, vol. 119, no. 4, pp. 269–276, 2014.

Research Article

Electrochemical Biosensor Based on Optimized Biocomposite for Organophosphorus and Carbamates Pesticides Detection

R. Montes,¹ F. Céspedes,² D. Gabriel,¹ and M. Baeza ³

¹GENOCOV Research Group, Department of Chemical, Biological and Environmental Engineering, School of Engineering, Universitat Autònoma de Barcelona, Carrer de les Sitges, Bellaterra (Cerdanyola del Vallès), 08193 Barcelona, Spain

²Department of Chemistry, Faculty of Science, Edifici C-Nord, Universitat Autònoma de Barcelona, Carrer dels Til·lers, Bellaterra (Cerdanyola del Vallès), 08193 Barcelona, Spain

³GENOCOV Research Group, Department of Chemistry, Faculty of Science, Edifici C-Nord, Universitat Autònoma de Barcelona, Carrer dels Til·lers, Bellaterra (Cerdanyola del Vallès), 08193 Barcelona, Spain

Correspondence should be addressed to M. Baeza; mariadelmar.baeza@uab.cat

Received 21 July 2017; Revised 22 December 2017; Accepted 25 December 2017; Published 1 March 2018

Academic Editor: Mohammad Mansoob Khan

Copyright © 2018 R. Montes et al. This is an open access article distributed under the Creative Commons Attribution License, which permits unrestricted use, distribution, and reproduction in any medium, provided the original work is properly cited.

This paper presents the characterization and optimization of biosensors based on graphite-epoxy which incorporates the enzyme acetylcholinesterase (AChE). By means of advanced electrochemical techniques, such as electrochemical impedance spectroscopy (EIS) and cyclic voltammetry (CV), the characterization and optimization of graphite-epoxy-AChE biosensors have been performed. In order to obtain sensitive electrodes, the optimal composition of the transducer material (graphite-epoxy-enzyme ratio) was studied. The optimization of the conductive particles distribution inside the biomaterial has allowed an improvement of the electrochemical properties. Optimal composition guarantees improving electrochemical properties required, such as high electron-transfer rate, high signal-to-noise ratio, and suitable sensitivity. The optimal biocomposite composition range was obtained between 16% and 17% of graphite and 0.12% of AChE. The biosensors were applied to the analysis of different pesticides, organophosphorus and carbamates, using indirect measurements based on enzymatic inhibition process. These optimized biosensors present detection limit one order of magnitude lower compared to the standard composition (nonoptimized) and allow achieving concentrations lower than the established ones by the pesticides regulation. Finally, spiked tap water samples with pesticides were analyzed with the optimized biosensors.

1. Introduction

The use of (bio)sensors applied to different fields of the analytical chemistry has been done for decades. It can be applied to clinical or medical diagnosis and food control or for environmental monitoring. Regarding the medical applications, biosensors can be used for detecting diabetes mellitus, uremia, heart failure, respiratory insufficiency, metabolic disorders, or muscle damage [1]. Biosensors have been used in environmental applications for the detection of heavy metals or other pollutants [2]. Specifically, in the literature, different biosensors applied to pesticide detection have been described [3]. Pesticides are effective against several types of pests; their long-term toxicity on human health and the ecosystem is becoming an issue at higher levels of authorities worldwide [4]. Since the first biosensor is based on acetylcholinesterase

or butyrylcholinesterase in 1980s, it has been a continuous improvement of cholinesterase based biosensors due to the gradual improvement of transducer devices and the availability of pure enzymes [5–7]. Standard procedures, based on liquid chromatography (LC) or gas chromatography (GC), are currently used for detection of wide range of pollutants with high sensitivity, reliability and precision [8, 9]. Despite their advantages, they are expensive, requiring laboratory facilities and specialized personnel and, moreover, time-consuming and not easily adapted to field analysis [10]. Biosensors based on the inhibition of the enzyme acetylcholinesterase have been an alternative to the use of these techniques [8, 10]. It is well known that organophosphorus and carbamate pesticides quantitatively inhibit cholinesterase. For this reason, amperometric biosensors based on inhibition of AChE have been

extensively applied to rapid, simple, and selective analysis of pesticides (organophosphorous and carbamates) [11, 12].

A biosensor based on a biocomposite is defined as a rigid material made by combining two or more materials of different nature (phases) where at least one of them has a biological origin [20]. The overall analytical performance of the (bio)composite electrodes is strongly influenced by the carbon loading within polymeric matrix. It is due to the fact that carbon loading influences directly the electrochemical surface and inner structure (bulk resistance) of the (bio)composite electrode, which strongly affected the overall electroanalytical performance of such composite electrodes. The incorporation of a biological element inside the composite matrix produces a modification in the internal distribution of the carbon particles on both parameters (electrochemical surface and bulk resistance). Therefore, an important feature for the development of more sensitive amperometric biosensors for pesticide detection is the optimization of the biocomposite composition in order to guarantee the best final electroanalytical properties of response.

Up to now, the characterization and optimization of biosensors based on biocomposites have been done under the criteria of maximum carbon loading and maximum biological charge which provide the maximum conductivity without losing the physical and mechanical stability and the best electroanalytical signal according to the requirements, respectively [21]. However, recently, alternative strategies of characterization have been established, based on advanced electrochemical techniques, which allow improving the electroanalytical properties of the sensor electrode by means of the optimization of the biocomposite composition based on carbon materials (as conductive phase) [22, 23].

These characterization techniques are electrochemical impedance spectroscopy (EIS) and cyclic voltammetry (CV). Moreover, the viability of these techniques has been demonstrated in the characterization of composites based on different carbon allotropic forms [24, 25]. EIS measurements provide, in an easy way, information about the electron-transfer rate, double-layer capacitance, contact resistance, and resistance of the solution (ohmic resistance) [26, 27]. The electroanalytical properties required by an electrode are high electron-transfer rate, the lowest double-layer capacitance, and ohmic resistance in order to guarantee a high signal/noise ratio, high sensitivity, and low detection limits.

The main goal of this study is the application of systematic strategies of characterization in order to optimize the biocomposite composition based on graphite-epoxy that incorporates acetylcholinesterase (AChE) on the matrix. These characterization techniques pretend to optimize the conducting particle distribution on the electrode surface as function of the carbon and biological loading. Optimized biosensors guarantee more sensitive pesticides biosensors regarding detection limits. We have constructed a series of graphite-epoxy-AChE with different graphite loadings and fixed amount of AChE. In a first stage of characterization, EIS has been used to determine the biocomposite composition which provides the best electrochemical properties. Later, these results are compared with CV measurements. Before the determination of pesticides, the electroanalytical response of

the optimized biocomposites has been evaluated using acetylthiocholine (ATCh) as a substrate by direct amperometric measurements. Then, the optimized biosensors have been evaluated using different inhibitors, both organophosphorus and carbamates. Finally, real samples of pesticides (spiked tap water samples) have been analyzed with the optimized biosensors based on an enzymatic inhibition process of AChE.

2. Experimental

2.1. Chemical Reagents. Graphite powder (particle size 50 μm) was supplied by Merck (Merck Millipore, Darmstadt, Germany). Epoxy resin Epotek H77A and hardener Epotek H77B were obtained from Epoxy Technology (Epoxy Technology, Billerica, MA, USA). Potassium ferricyanide/ferrocyanide (99.8%), potassium chloride (99.5%) ACS grade, potassium phosphate monobasic (99.5%), potassium dibasic-anhydrous (98%), nitric acid (65%), methanol for HPLC ($\geq 99.9\%$), acetylcholinesterase from *Electrophorus electricus* (electric eel, type VI-S, EC. 3.1.1.7, 518 units/mg solid), acetylthiocholine chloride ($>99\%$), Carbofuran PESTANAL, Carbaryl PESTANAL, Paraoxon-ethyl PESTANAL, Malathion PESTANAL, and Dichlorvos PESTANAL were supplied from Sigma-Aldrich (St. Louis, MO, USA) and used without further purification. All the dissolutions were prepared using deionised water from Milli-Q system (Millipore, Billerica, MA, USA).

2.2. Fabrication of the Working Electrodes. Handmade biocomposites were prepared following the conventional methodology previously established in our research group [28]. A resin Epotek H77 and their corresponding hardener compound were mixed in a ratio of 20 : 3 (w/w). The graphite composite was prepared by loading different amounts of graphite (14%, 15%, 16%, 17%, and 20% (w/w)) into the epoxy resin before hardening. The composite was homogenized for 30 min. After the homogenization time, the acetylcholinesterase amount (0.12% (w/w) and 0.24% (w/w)) was introduced to the composite paste and homogenized for 15 min more. The final biocomposite paste electrode was introduced in a PVC tube (6 mm i.d.) which has a cavity of 3 mm long. The electrode was allowed to harden during 5 days at 40°C. Finally, the surface was polished with different sandpapers of decreasing grain size (800 and 1200 grits) and with alumina paper (polishing strips 948201, Orion). The final electrode dimensions were 28 mm². When the electrodes were not in use, they were stored at 4°C.

2.3. Apparatus. Electrochemical impedance spectroscopy and voltammetric measurements were performed using a computer controlled Autolab PGSTAT12 potentiostat/galvanostat (Eco Chemie, Utrecht, The Netherlands) with a three-electrode configuration. A platinum-based electrode 53-671 (Crison Instruments, Alella, Barcelona, Spain), an AgCl covered silver wire, and the constructed graphite biocomposite electrodes were used as a counter, reference, and working electrodes, respectively.

Amperometry measurements were done using an amperimeter LC-4C (Bioanalytical Systems Inc., West Lafayette,

IN, USA), connected to a personal computer by data acquisition card ADC-42 Pico Technology (St. Neots, Cambridgeshire, UK) for data registering and visualization. Three-electrode configuration was used: a single junction reference electrode Ag/AgCl Orion 900100 (Thermo Electron Corporation, Beverly, MA, USA) and platinum-based electrode were used as reference and auxiliary, respectively, and graphite biocomposites electrodes were used as working electrode. A magnetic stirrer provided the convective transport during the amperometric measurements.

2.4. Procedure

2.4.1. Electrochemical Characterization. EIS measurements were made in a 0.1 M potassium chloride solution containing 0.01 M potassium ferricyanide/ferrocyanide ($\text{Fe}(\text{CN})_6^{3-}/\text{Fe}(\text{CN})_6^{4-}$) under quiescent condition. The impedance spectra were recorded in the frequency range 0.1 Hz to 100 kHz at the redox equilibrium potential. The signal amplitude to perturb the system was 10 mV. Voltammetric measurements were taken using a 0.1 M potassium chloride solution containing 0.01 M potassium ferricyanide/ferrocyanide ($\text{Fe}(\text{CN})_6^{3-}/\text{Fe}(\text{CN})_6^{4-}$) under quiescent condition and scan rate of $10 \text{ mV}\cdot\text{s}^{-1}$.

2.4.2. Working Potential Selection. The working potential used to perform the electroanalytical characterization was previously determined by linear-voltammetry using acetylthiocholine as a substrate and the optimized biocomposite graphite-epoxy-AChE (16% of graphite loading). The measurements were made in 20 mL glass cell, at room temperature (25°C) using 0.1 M phosphate solution at $\text{pH} = 7.0$ as background electrolyte (prepared using K_2HPO_4 and KH_2PO_4 under quiescent condition), and three-electrode configuration as it was described before (see Apparatus Section 2.3). The spectra were recorded in the potential range -1.0 V to 1.5 V and scan rate of $10 \text{ mV}\cdot\text{s}^{-1}$. Firstly, an initial sweep is made without substrate and then, on the same record, different substrate concentration reaching a final concentration of 10 mM is added.

2.4.3. Amperometric Measurements. Amperometric detection of acetylthiocholine was made under force convection by constant stirring 10 mL of the buffer solution (0.1 M phosphate solution at $\text{pH} = 7.0$) with magnetic stirring and by adding consecutive addition of the substrate solution. The working potential used was fixed at 700 mV (versus Ag/AgCl).

2.4.4. Inhibition Tests. In order to obtain the inhibition plots of the different pesticides, the percentage inhibition method was followed. The procedure used was based on three steps. (a) The biosensor is placed in 10 mL cell glass of stirred buffered solution (0.1 M phosphate buffer at $\text{pH} = 7.0$). When the current of the biosensor becomes constant, a volume of acetylthiocholine solution ($5.5 \cdot 10^{-4} \text{ M}$) was added. The current increases rapidly and reaches a steady state (I_{ss}). (b) After this experiment the same biosensor is incubated for

15 min in 10 mL of a stirred buffer solution (0.1 M PBS at $\text{pH} = 7.0$) where is added a fixed volume of pesticide (in order to achieve the desired concentration of pesticide in the solution). (c) The incubated biosensor is washed well with the working buffer solution and then the step (a) is repeated obtaining lower steady currents (I_p) after the addition of the substrate because of the inhibition (see Figure 3(b)). From these points, the percentage of inhibition, which corresponds to a fix concentration of pesticide, is calculated in the following way:

$$I (\%) = \frac{(I_{ss} - I_p)}{I_{ss}} \times 100. \quad (1)$$

There are numerous relationships between the inhibition percentage and the inhibitory concentration and/or inhibition time reported on the literature. These relationships are usually characterized by linear [19], nonlinear, logarithmic [29, 30], or other type of equations. After these calculations, the inhibition plots, $I (\%)$ versus [pesticide] or $\log[\text{pesticide}]$, are constructed for the different pesticides evaluated (carbofuran, carbaryl, malathion, paraoxon, and dichlorvos).

Pesticide stock solutions were prepared daily in a mixture 50 : 50 of methanol : water (v/v) due to the low solubility of some pesticides in water at room temperature (carbofuran: 320 mg/L, paraoxon: 24 mg/L, carbaryl: 40 mg/L, dichlorvos: 16000 mg/L, and malathion: 145 mg/L) [31].

3. Results

3.1. Electrochemical Impedance Measurements. The electrochemical parameters for each biocomposite electrode composition, such as ohmic resistance (R_Ω), charge-transfer resistance (R_{ct}), and double-layer capacitance (C_{dl}), with different graphite loading and constant amount of AChE, were evaluated by electrochemical impedance spectroscopy. These parameters were obtained by fitting the impedance spectra to a Randles circuit: $R_\Omega \cdot [C_{dl} \cdot (R_{ct} \cdot Z_w)]$ showed in inset Figure 1(a), which is sufficiently suitable to interpret R_Ω , R_{ct} , and C_{dl} values.

Four compositions with variable graphite loading and fixed amount of AChE were evaluated. The interval selected for this study was 14%, 15%, 16%, and 17% of graphite loading and were compared to the conventional composition of 20% of graphite loading which was used as a standard composition in previous works [32]. The amount of AChE immobilized on the matrix of the biocomposite is crucial for the pesticide determination [8]. Moreover, the quality and quantity of the enzyme immobilization will ultimately affect the performance of the biosensor in terms of sensitivity, stability, response time, and reproducibility [33]. According to the enzyme activity, the amount of AChE was initially fixed in 0.12% (w/w) for each composition. Thus, for each biocomposite electrode, the amount of AChE is 746 units which is sufficient for guaranteeing high enough analytical signals in the pesticides determination [31]. In early studies, we have reported that, biosensors with compositions below 14% of graphite loading in spite of having low double-layer capacitance values, it presented high ohmic resistance and

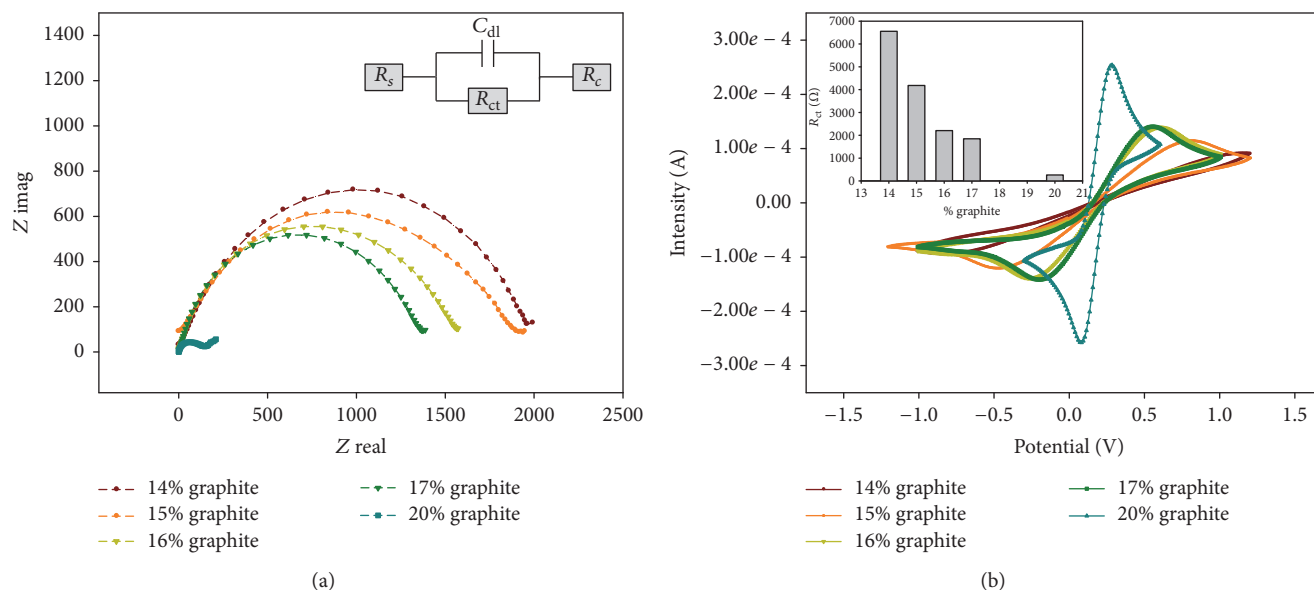


FIGURE 1: (a) Nyquist plots for different graphite loading electrodes with acetylcholinesterase (AChE) in presence of 0.01 M $\text{Fe}(\text{CN})_6^{3-}/\text{Fe}(\text{CN})_6^{4-}$ under quiescent condition in 0.1M KCl. The insets figure shows the equivalent circuit used for the impedance spectra fitting ($R_{\Omega} = R_s + R_c$) (b) Cyclic voltammogram for biocomposites with acetylcholinesterase (AChE) using 0.01 M $\text{Fe}(\text{CN})_6^{3-}/\text{Fe}(\text{CN})_6^{4-}$ and 0.1M KCl. Scan rate $10 \text{ mV}\cdot\text{s}^{-1}$. The inset shows the trend of charge-transfer resistance for different composite composition.

charge-transfer resistance values. However, for biosensors with more than 17% of graphite loading, despite having low ohmic resistance and charge-transfer resistance values, the double-layer capacitance values increased remarkably [23]. Consequently, in the present study, this range of compositions has been not considered.

The impedance spectra recorded for each graphite composition and fixed percentage AChE evaluated are depicted in Figure 1(a). Nyquist plots obtained showed that compositions from 14% to 17% of graphite loading are represented by semicircle with big diameter where the impedance behaviour is dominated by kinetic process. However, for high proportions of graphite loading, 20% of graphite loading, the semicircle diameter decreases and the diffusion control start to be discerned at low frequencies (linear zone). At high carbon proportions, there is no mass transfer charge limitation on the biocomposites electrodes but the electroactive specie diffusion is limited, presenting a diffusion control (similar to macroelectrode behaviour).

The variation of the ohmic resistance as function of the graphite loading with constant amount of AChE is depicted in Figure 2(a). As it can be observed, there is a decrease on the ohmic resistance value when the graphite loading increases. This decrease on the R_{Ω} value can be associated with the increase of the conductive material present on the surface which, at the same time, increases the current conducting zones. Low values of R_{Ω} are required in order to assure good sensitivity and low response time. So, compositions between 16% and 20% of graphite loading presented the lowest ohmic resistance values.

The quantitative values of the charge-transfer resistance are shown in Figure 2(b). In general trends, a decrease on the R_{ct} values with the increase of the graphite loading which

is proportional to the increase of the biosensor active area can be observed. In terms of charge-transfer resistance, the optimal values are presented in biocomposites compositions which presented low R_{ct} values. So, biocomposites between 16% and 20% of graphite loading are the ones which guarantee high electron-transfer rate and will guarantee an optimal electroanalytical response.

Finally, it is important to consider the double-layer capacitance value which is directly related to the charging or background current and inversely proportional to the signal/noise ratio. Figure 2(c) depicts the variation of this parameter as function of the graphite loading. C_{dl} value remains low at low graphite loading. An increase of the C_{dl} value is observed when the graphite loading increases to 20% of graphite loading. Based on these results and taking into the account that biocomposites with low C_{dl} values are the optimal in order to guarantee the minimum background current and, therefore, high signal-to-noise ratio; the biocomposites compositions between 14% and 17% of graphite loading are the ones which present low C_{dl} values.

According to the results obtained in the EIS characterization and taking into the account the electroanalytical properties required by a biosensor such as low response time, low limit of detection, and high sensitivity, the biocomposites between 16% and 17% of graphite loading present these requirements and, therefore, the optimal composition for their use as a transducers in analytical applications has been considered (see Supplementary Materials, Section S1). Moreover, the biocomposites composition included in this interval present similar electrochemical behaviour, so small variations in the composition inside this interval do not produce significance differences in the electrochemical properties.

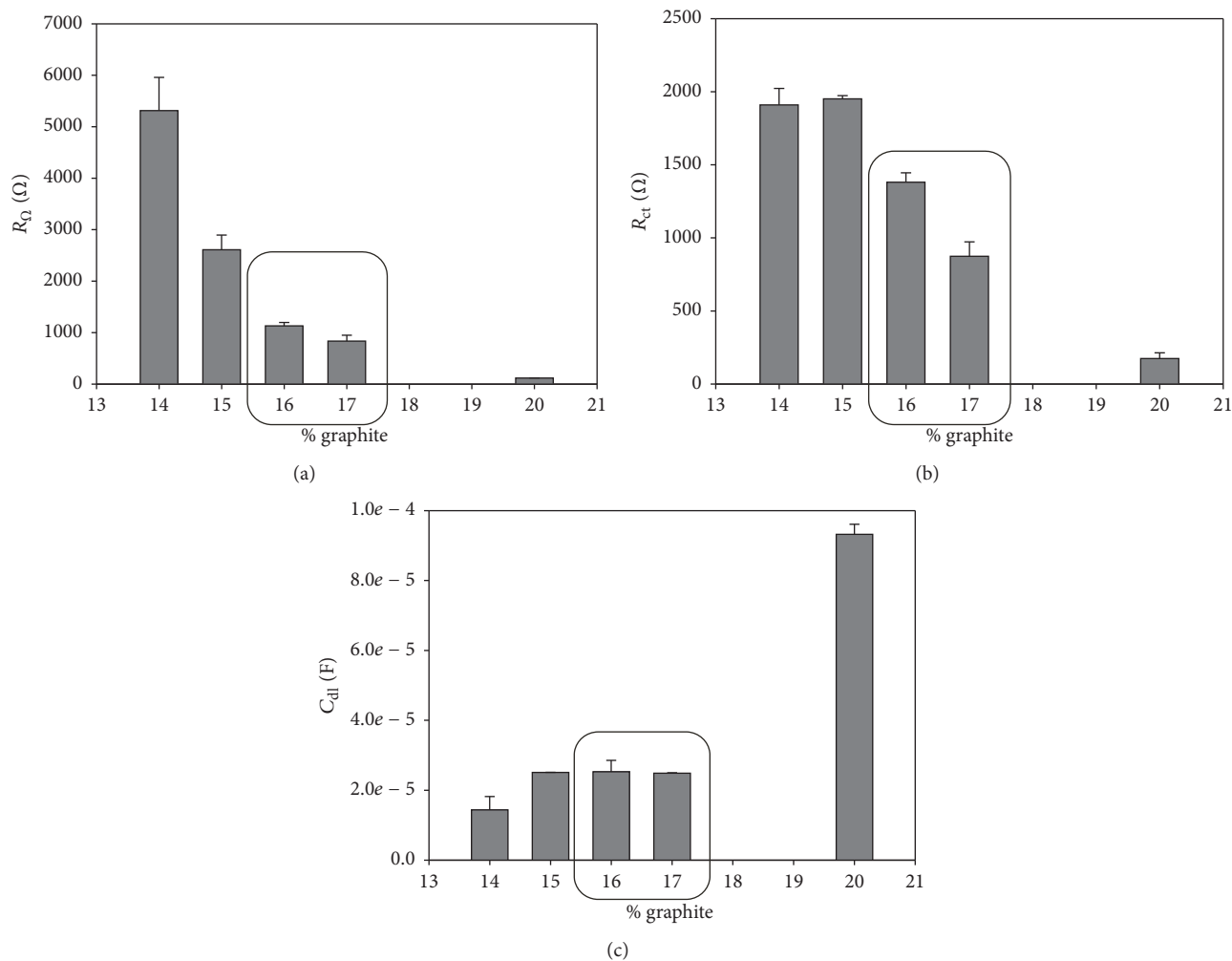


FIGURE 2: Values of (a) ohmic resistance, (b) charge-transfer resistance, and (c) double-layer capacitances, with their corresponding standard deviation ($n = 3$) for the different graphite loading electrodes with acetylcholinesterase (AChE), using the redox probe 0.01 M $\text{Fe}(\text{CN})_6^{3-/4-}$ and 0.1 M KCl.

The results obtained showed that the incorporation of a third biological compound inside the composite matrix produces a displacement in the optimal range composition when it is compared to the graphite-epoxy composite electrodes due to the separation of the conducting particles by the presence of the enzyme charge.

3.2. Cyclic Voltammetry Characterization. Cyclic voltammetry measurements were performed in order to complement EIS measurements. The different voltammograms obtained for each biocomposite composition electrodes evaluated are depicted in Figure 1(b). As it can be observed, for the biocomposite composition with 20% of graphite loading, oxidation and reduction peaks are closer to each other, and the voltammogram presents the typical macroelectrode shape where linear diffusion controls the mass transport. However, composites between 14% and 17% of graphite loading the oxidation and reduction peaks are far to each other. The cyclic voltammograms present behaviour as array

of microelectrodes where the radial diffusion dominates the transport mass [34].

Different parameters can be extracted from the cyclic voltammograms such as the peak separation potential (ΔE) and peak current (I_p) as is shown in Table 1. Furthermore, from the current intensity (I_p) value, the electroactive area using modified Randles-Sevcik equation (see (2)) [26] can be calculated, which is appropriate for electron-transfer controlled process:

$$I_p = 3.01 \times 10^5 n^{3/2} (\alpha D_{\text{red}} \nu)^{1/2} A C_{\text{red}}^* \quad (2)$$

In this equation, α corresponds to the transfer coefficient which was considered to be approximately 0.5; $D_{\text{red}} = 6.32 \cdot 10^{-6} \text{ cm}^2 \text{ s}^{-1}$ [26] corresponds to the diffusion coefficient of the reduced species; $\nu = 0.01 \text{ V s}^{-1}$ represents the scan rate; A is the electroactive area; and $C_{\text{red}}^* = 0.01 \text{ M}$ is the bulk concentration of the electroactive species. As we can see in Table 1, there is an increase of the peak current with the graphite

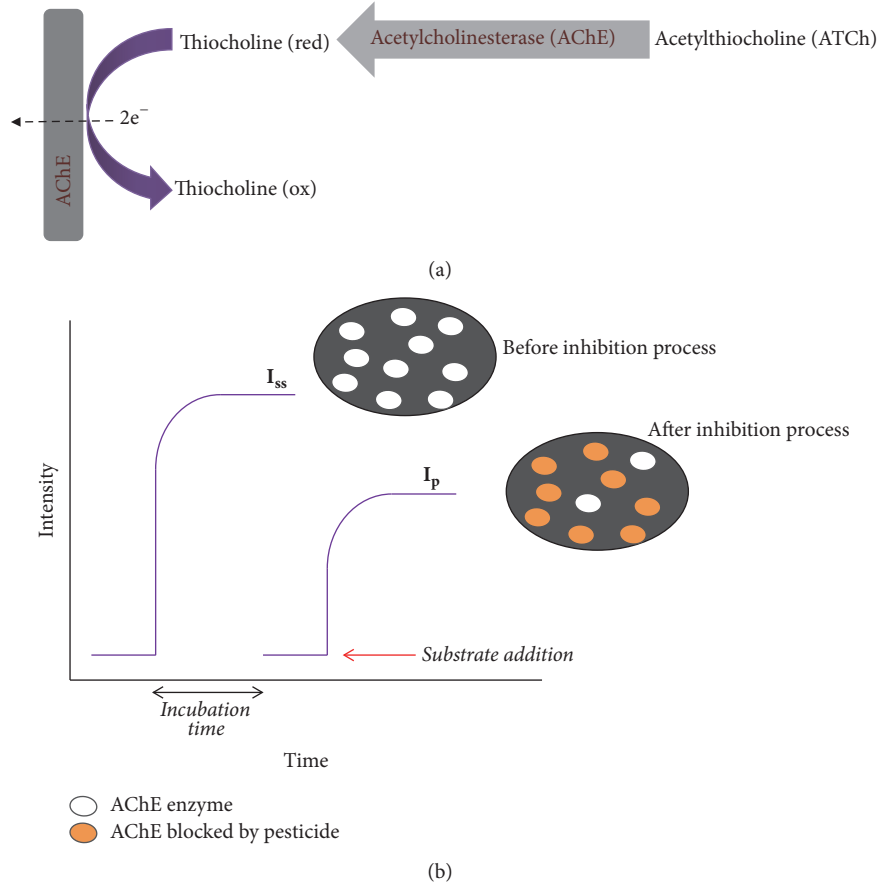


FIGURE 3: (a) Schematic representation of the enzymatic and electrochemical reactions which takes place in the biosensor surface based on biocomposite graphite-epoxy-AChE. (b) Schematic representation of the pesticides indirect determination by enzymatic inhibition. I_{ss} corresponds to the maximum analytical signal of the biosensor in absence of inhibitor and I_p corresponds to the achieved analytical signal after the previous incubation with the inhibitor.

TABLE 1: Cyclic voltammetry parameters for the different biocomposite electrode compositions of graphite/epoxy with 0.12% of AChE. I_o corresponds to the exchange current, R_{ct} to the charge-transfer resistance, I_p to peak current, A to active area, and ΔE to the peak separation potential. $R_{ct} \cdot A$ and $R_{ct}^{EIS} \cdot A$ correspond to R_{ct} obtained by voltammetric and EIS measurements, respectively, and are normalized with respect to the active area.

| Electrodes (% graphite) | i_o (A) | R_{ct} (Ω) | I_p (A) | A (cm^2) | ΔE (V) | $R_{ct} \cdot A$ (Ωcm^2) | $R_{ct}^{EIS} \cdot A$ (Ωcm^2) |
|----------------------------|----------------------|--------------------------|----------------------|-------------------|-------------------|---------------------------------------|---|
| 14% | $3.85 \cdot 10^{-6}$ | 6557 | $9.95 \cdot 10^{-5}$ | 0.19 | 1.5678 | 1219 | 355 |
| 15% | $6.03 \cdot 10^{-6}$ | 4183 | $1.17 \cdot 10^{-4}$ | 0.22 | 1.2195 | 912 | 425 |
| 16% | $1.14 \cdot 10^{-5}$ | 2205 | $1.29 \cdot 10^{-4}$ | 0.24 | 0.7841 | 532 | 333 |
| 17% | $1.36 \cdot 10^{-5}$ | 1849 | $1.44 \cdot 10^{-4}$ | 0.27 | 0.7290 | 497 | 235 |
| 20% | $9.74 \cdot 10^{-5}$ | 259 | $2.59 \cdot 10^{-4}$ | 0.48 | 0.2078 | 126 | 85 |

loading associated with an increase of the electroactive area, together with a decrease of the peak separation related to an enhancement of the electron-transfer rate. We also evaluate the exchange current from the Tafel plots (log current versus potential). Using the exchange current value (i_o), we also can evaluate the charge-transfer resistance through the relation $i_o = RT/nFR_{ct}$. R_{ct} values obtained by EIS are following the same trend like the results obtained by CV technique (see

Figure 2(b) and inset figure in Figure 1(b)). We have normalized R_{ct} value obtained by both electrochemical techniques (EIS and CV) with respect to the electroactive area (A) (see Table 1) and it is observed that there is a decrease on the ($R_{ct} \cdot A$) and ($R_{ct}^{EIS} \cdot A$) values when the graphite loading increases showing the evident influence of the electrochemical anisotropy of the graphite, as a carbon material, which can be more noticeable as the graphite loading is increased.

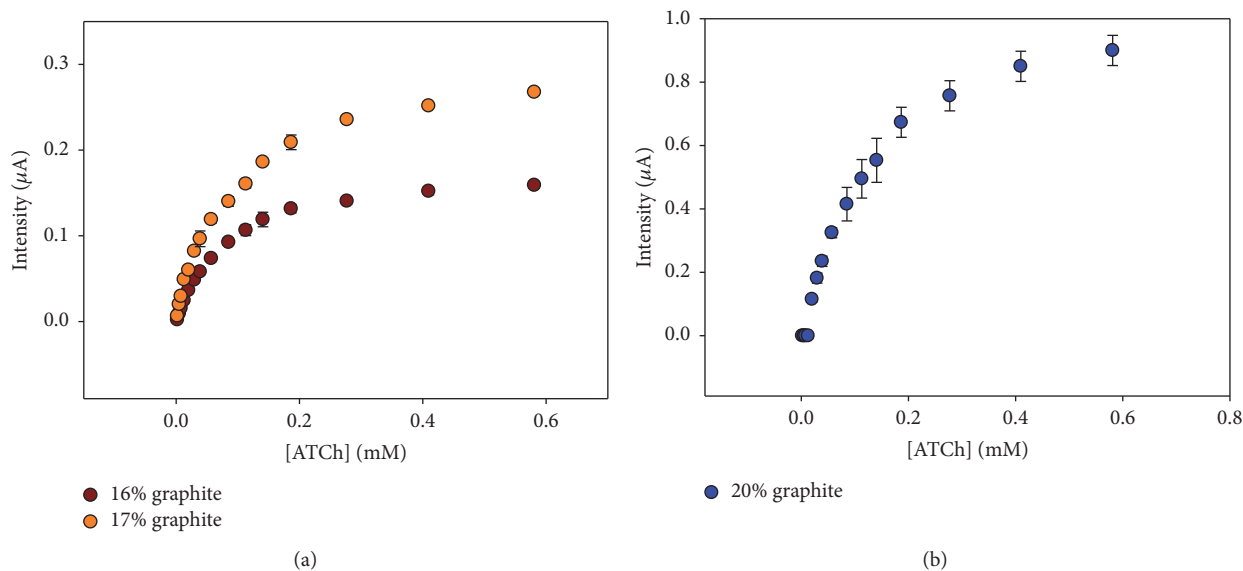


FIGURE 4: Acetylthiocholine calibration plots for biosensors with (a) 16% and 17% of graphite and (b) 20% graphite loading. Measurements were carried out in 0.1 M phosphate solution at pH = 7.0 and 0.1 M KCl. EAPP = 700 mV.

3.3. Electroanalytical Characterization

3.3.1. Inhibition Measurements: Indirect Pesticide Determination. Acetylthiocholine (ATCh) was used as a substrate for evaluating the electroanalytical response of the biocomposite electrodes versus pesticides inhibition. The response mechanism of the biosensor graphite-epoxy-AChE is based on two different steps. In a first step, the acetylthiocholine is biocatalytically hydrolyzed by the acetylcholinesterase enzyme producing acetic acid and thiocholine. In a second step, thiocholine is electrochemically oxidized in the electrode surface using a fixed potential (see Figure 3(a)). The current intensity generated by this oxidation is directly proportional to the ATCh concentration in solution.

Firstly, linear sweep voltammograms were performed on the graphite-epoxy-AChE biocomposites for acetylthiocholine (ATCh) in order to determine the optimum polarization potential used in the amperometric measurements (see Supplementary Materials, Section S2). The result obtained in this study shows that the plateau was obtained at 700 mV (versus Ag/AgCl). So, this potential was chosen for the amperometric measurements.

In order to use the biosensors in the determination of pesticides, it is important to determine the substrate concentration range from which the enzyme begins to saturate. Under saturate conditions, the generated intensity by the biosensor is constant and independent of the substrate concentration present. In the pesticide determination by enzymatic inhibition, it is recommended to work under saturation conditions with a higher initial analytical signal in order to assure the maximum applicability of the biosensor due to the irreversible enzymatic inhibition that the AChE enzyme suffers from. In Supplementary Materials (see Section S3), the electroanalytical parameters of response of the biosensors are described regarding limit of detection, sensibility, and linear range for acetylthiocholine.

As it can be observed in Figure 4(a), for the biocomposites compositions with 16%-17% of graphite loading, concentrations higher than 0.4 mM of ATCh, the analytical signal starts to be independent of the substrate concentration. For biocomposites with 20% of graphite loading (see Figure 4(b)), the saturation zone appears for concentrations of substrate higher than 0.6 mM. An increase of the electrode electrochemical active area produces an increase on the signal current intensity generated on the surface. Therefore, according to the results obtained, pesticide inhibition determination was performed using a constant concentration of ATCh of $5.5 \cdot 10^{-4}$ M.

Two procedures can be followed for the detection of pesticides, the direct method, and the indirect method [35]. By means of the direct determination method, it was only possible to detect pesticide concentrations higher than 10^{-3} M. For this reason, the indirect method was followed in the present study (see Section 2.4.4). Thus, a comparative study for the biocomposite electrodes with 16%, 17% and 20% of graphite loading was performed.

The inhibition effect of carbofuran, carbaryl, dichlorvos, malathion, and paraoxon on the graphite-epoxy-AChE biosensor is shown in Figures 5(a₁), 5(b₁), 5(c₁), 5(d₁), and 5(e₁). Relationships between percentage inhibition and the inhibitory pesticide concentration can usually be characterized by linear, nonlinear, logarithmic, or other types of equation [11]. As it can be seen in Figures 5(a₂), 5(b₂), 5(c₂), 5(d₂), and 5(e₂), a linear relationship between inhibition percentage and log [pesticide] was obtained. The results obtained showed that biosensors with 20% graphite loading do not allow determining low inhibitor concentrations. Although inhibition occurs in the same manner in surface of all the biosensors studied (all have the same fixed amount of enzyme), the electrochemical characteristics of the biosensor with the standard composition (nonoptimized composition with

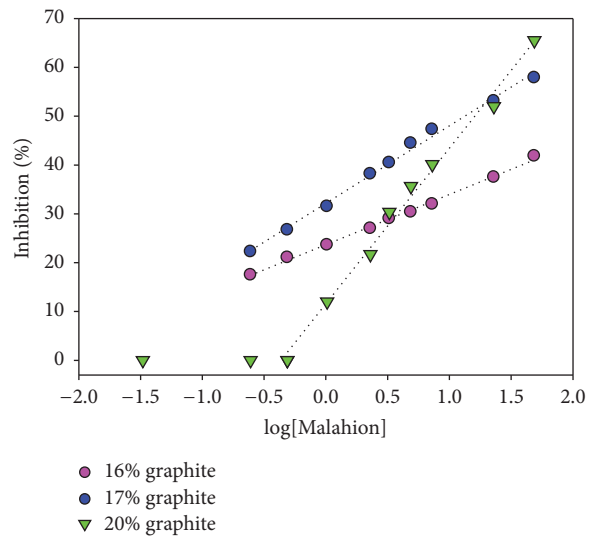
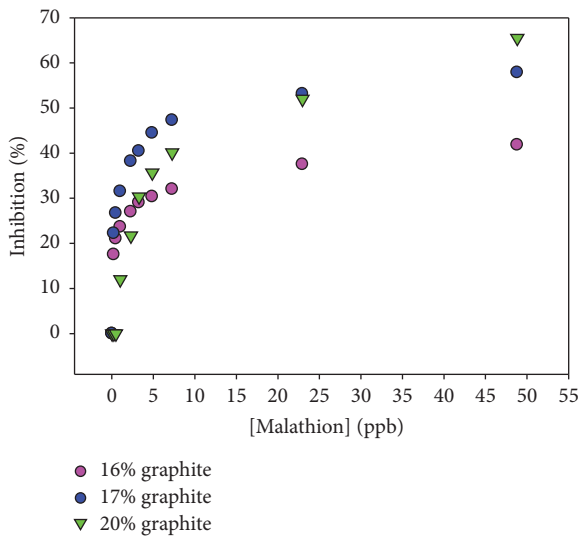
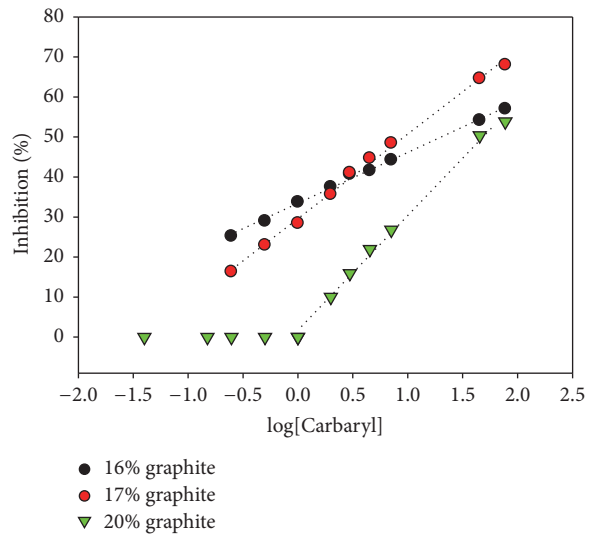
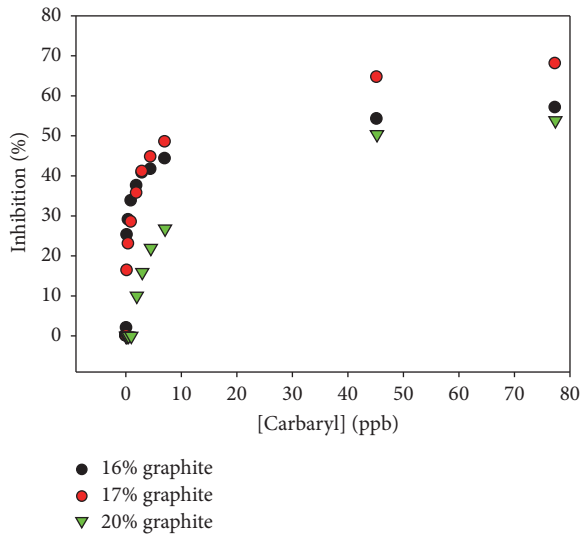
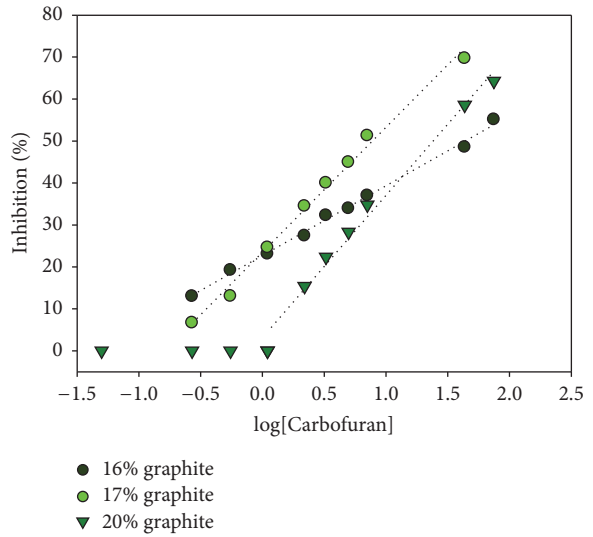
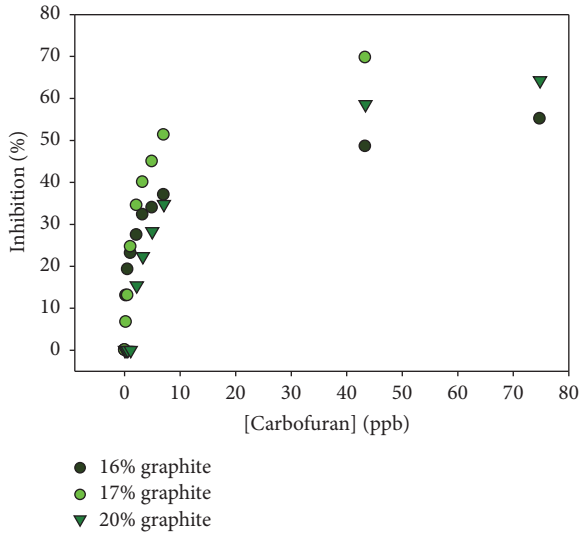


FIGURE 5: Continued.

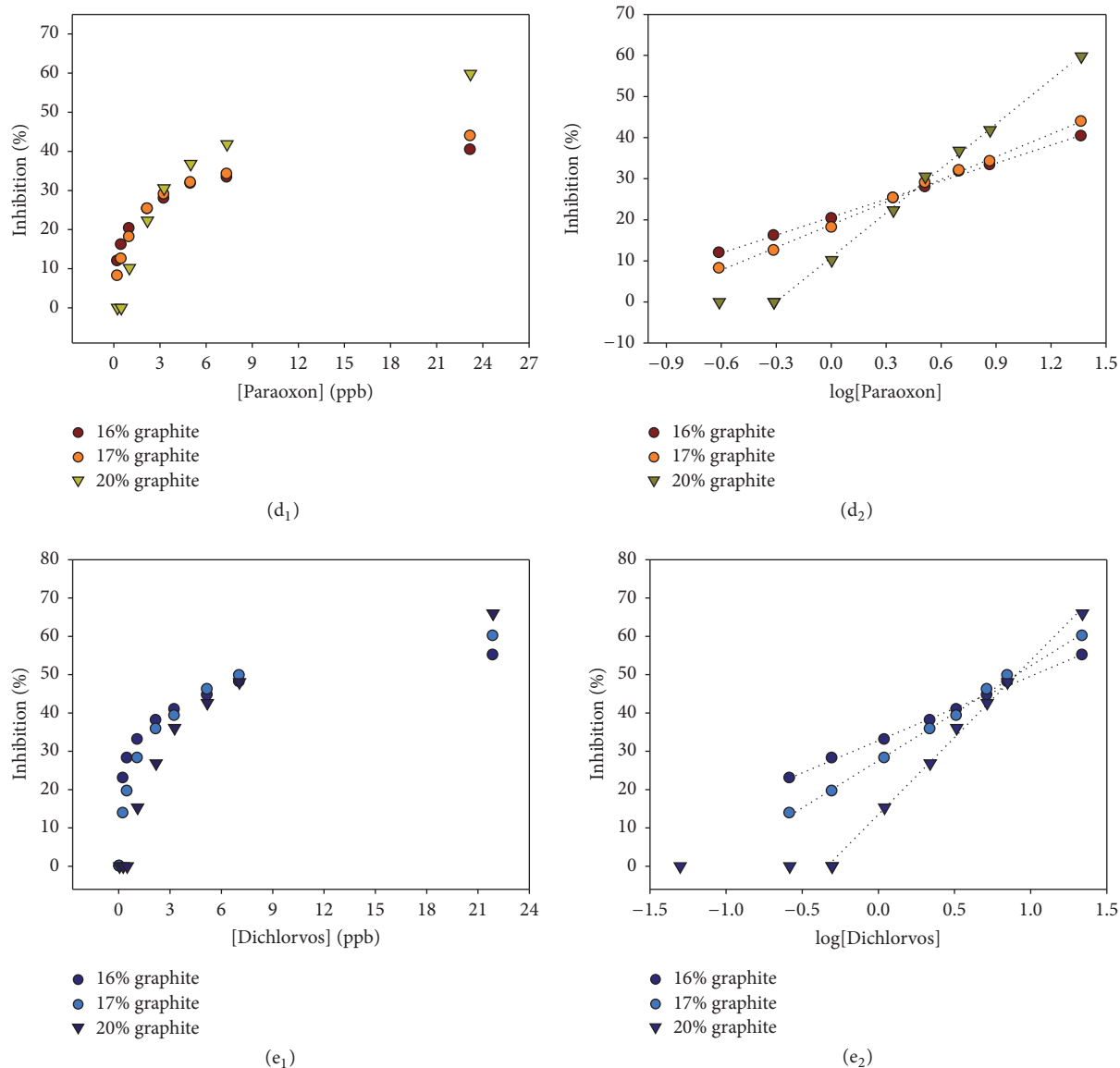


FIGURE 5: Direct relationship between inhibition and pesticide concentration for (a₁) carbofuran, (b₁) carbaryl, (c₁) malathion, (d₁) paraoxon, and (e₁) dichlorvos using biosensors with 16% of graphite, 17% graphite, and 20% of graphite loading. Linear relationship between inhibition and log pesticide concentration for (a₂) carbofuran, (b₂) carbaryl, (c₂) malathion, (d₂) paraoxon, and (e₂) dichlorvos using biosensors with 16% of graphite, 17% graphite, and 20% of graphite loading. Measurements were carried out in 0.1 M phosphate solution at pH = 7.0 and 0.1 M KCl using [ATCh] = $5.5 \cdot 10^{-4}$ M. EAPP = 700 mV.

20% of graphite loading) cannot distinguish small intensity variations caused by a minimum variation of the enzyme activity at low concentrations of pesticide (inhibitor). This fact is directly related to the capacity for determining smaller concentrations of enzymatic product (thiocholine) produced. However, optimized biosensors, with 16% and 17% of graphite loading, present enhanced electrochemical properties such as high signal/noise ratio values. Consequently, the detection limits achieved may significantly improve, being able to distinguish small variations in the thiocholine concentration (enzymatic reaction product) generated by the small reduction of enzyme activity (see Figure 3(a)). The enzymatic activity decrease is directly related to pesticides concentration. The

limits of detection and the parameters of calibration curves for the different pesticides studied are shown in Table 2. For the optimized biosensors, it can be observed that the limit of detection achieved is one decade of concentration lower. Moreover, as it can be observed, the slope of the inhibition plots increases when the graphite loading increases. This behaviour is observed for both pesticide families, as organophosphorus and carbamates.

Regarding the biocomposites which are in the optimal composition range (16%-17%), there are no significant differences in the limit of detection achieved for each pesticide studied. However, biosensors with 17% of graphite loading presented better sensibility for low pesticide concentrations

TABLE 2: Parameters obtained from the inhibition plots for the different biocomposite composition biosensors and pesticides evaluated.

| Inhibitor | Graphite (%) | Slope (% Inhibition · decade ⁻¹) | Limit of detection (µg·L ⁻¹) | Regression coefficient (n = 9) |
|------------|--------------|--|--|--------------------------------|
| Carbofuran | 16 | 16.6 ± 0.4 | 0.25 ± 0.08 | 0.996 |
| | 17 | 30 ± 1 | 0.27 ± 0.01 | 0.992 |
| | 20 | 32 ± 1 | 2.03 ± 0.07 | 0.996 |
| Carbaryl | 16 | 12.7 ± 0.3 | 0.23 ± 0.09 | 0.997 |
| | 17 | 21 ± 1 | 0.24 ± 0.04 | 0.997 |
| | 20 | 27.9 ± 0.9 | 1.82 ± 0.09 | 0.996 |
| Paraoxon | 16 | 14.6 ± 0.3 | 0.25 ± 0.03 | 0.998 |
| | 17 | 18.4 ± 0.4 | 0.26 ± 0.07 | 0.998 |
| | 20 | 36.4 ± 0.9 | 0.96 ± 0.07 | 0.999 |
| Malathion | 16 | 10.3 ± 0.2 | 0.25 ± 0.03 | 0.997 |
| | 17 | 15.7 ± 0.5 | 0.24 ± 0.03 | 0.994 |
| | 20 | 31 ± 1 | 1.03 ± 0.05 | 0.992 |
| Dichlorvos | 16 | 16.8 ± 0.4 | 0.28 ± 0.06 | 0.997 |
| | 17 | 24.7 ± 0.5 | 0.26 ± 0.01 | 0.997 |
| | 20 | 40.3 ± 0.9 | 1.05 ± 0.05 | 0.997 |

TABLE 3: Comparison of the analytic performance of the biosensor with few of the contemporary AChE sensors applied to the same analyte.

| Analyte | Electrode | Limit of detection (ppb) | Reference |
|------------|-----------------------------------|--------------------------|------------|
| Carbofuran | AChE/Nafion/BSA/CoPc-SPE | 0.108 | [13] |
| | AChE-TCNQ/SPE | 1.1 | [11] |
| | AuNP/AChE/Au | 7.26 | [14] |
| | PPy-AChE-Geltn-Glut/Pt | 0.12 | [15] |
| | Biocomposite 16% graphite | 0.25 | This paper |
| | Biocomposite 17% graphite | 0.27 | This paper |
| Paraoxon | AChE/Fe ³⁺ -BSA-Nafion | 10 | [16] |
| | AChE/PAN-AuNPs/Pt | 0.739 | [17] |
| | AChE/Geltn-Cellulose/SPE | 7.975 | [18] |
| | AChE-Carbon Paste/Cu | 0.86 | [19] |
| | PPy-AChE-Geltn-Glut/Pt | 1.1 | [15] |
| | Biocomposite 16% graphite | 0.25 | This paper |
| Dichlorvos | Biocomposite 17% graphite | 0.26 | This paper |
| | AChE/(MWCNTs/ALB)n/GCE | 61.87 | [5] |
| | Biocomposite 16% graphite | 0.28 | This paper |
| Carbaryl | Biocomposite 17% graphite | 0.26 | This paper |
| | AChE/TMOS/graphite | 2.01 | [3] |
| | Biocomposite 16% graphite | 0.23 | This paper |
| Malathion | Biocomposite 17% graphite | 0.24 | This paper |
| | AChE/TMOS/carbon paste | 58 | [3] |
| | Biocomposite 16% graphite | 0.25 | This paper |
| | Biocomposite 17% graphite | 0.24 | This paper |

with respect to the biocomposites with 16% of graphite loading. This fact can be attributed to the improvement of the charge-transfer rate, so the biocomposite with 16% of graphite loading was more sensitive biosensor for small variations of intensity measurements.

On the other hand, performance of the fabricated biosensor has been compared with other contemporary AChE based

biosensors reported in the literature. The comparison of the detection limits is shown in Table 3. As it can be observed, the limit of detection achieved for the optimized biocomposites is comparable to the others achieved with biosensors based on AChE when they are tested with the same pesticides. It is important to highlight that the optimized biosensors presented in this work have achieved lower pesticide concentration.

TABLE 4: Results obtained in the spiked tap water samples with pesticides (carbofuran and paraoxon) using the optimized biosensors.

| Pesticide (inhibitor) | Graphite (%) | Concentration added (ppb) | Biosensor (ppb) | RDS (%) | Recovery (%) |
|-----------------------|--------------|---------------------------|-----------------|---------|--------------|
| Carbofuran | 16 | 0.403 | 0.43 ± 0.05 | 12 | 107 |
| | | 4.03 | 3.9 ± 0.6 | 15 | 101 |
| | | 40.32 | 39.4 ± 0.3 | 1 | 98 |
| | 17 | 0.403 | 0.42 ± 0.03 | 7 | 104 |
| | | 4.03 | 4.0 ± 0.1 | 3 | 99 |
| | | 40.32 | 41 ± 2 | 4 | 102 |
| Paraoxon | 16 | 0.301 | 0.30 ± 0.01 | 3 | 100 |
| | | 3.01 | 3.2 ± 0.1 | 5 | 106 |
| | | 30.08 | 30.8 ± 0.1 | 4 | 102 |
| | 17 | 0.301 | 0.32 ± 0.03 | 4 | 107 |
| | | 3.01 | 3.2 ± 0.3 | 10 | 106 |
| | | 30.08 | 30.9 ± 0.2 | 1 | 103 |

3.3.2. Sample Water Analysis. Analysis of carbofuran and paraoxon pesticide in tap water samples was carried out using the optimized biosensor electrodes, biocomposites with 16%–17% of graphite loading. This study has been performed in tap water samples which have been collected after a plant was watered with commercial ground and then it has been spiked with different pesticide concentrations. For these pesticides, three concentrations have been studied which include as a upper limit the legal maximum allowed by EPA [36], one intermediate concentration, and one closer to the detection limit (for each pesticide evaluated). The measurements were carried out in triplicate. The results obtained are shown in Table 4. As it can be observed, the precision obtained with this method is adequate and the recovery percentages are in all the cases near 100%. Moreover, these results confirm that there is no pesticide presence in the ground susceptible to be swept along in the collected water process before the doping. So, the results obtained with the biosensor coincide with the pesticide additions made in the real samples and it is confirmed that there is no interference associated with other inhibitors.

4. Conclusions

Amperometric biosensors based on graphite-epoxy-AChE have been constructed, characterized, and optimized by means of EIS and CV techniques. This study has demonstrated the viability of these electrochemical techniques of characterization in the development of biosensors based on biocomposites. By means of EIS technique, the optimal composition range of conductive phase and enzyme for the biocomposite system based on graphite-epoxy-AChE that is near to a composition between 16% and 17% of graphite loading with 0.12% AChE has been estimated.

In addition, it has been demonstrated that the optimal composition allows constructing more robust amperometric biosensors based on biocomposites. Moreover, they are useful for applications that require more sensitive devices, with optimized signal-to-noise ratio, in order to determine lower analyte concentrations.

Regarding the inhibitors determination by indirect method, the optimized biocomposite sensor allows achieving lower pesticide concentrations, being these concentrations lower than the achieved ones by the standard composition electrode. Furthermore, the detection limits were lowest compared to other biosensors reported in the literature. On the other hand, in the analysis of spiked water samples with pesticides (organophosphorus and carbamates), there were no significant differences in the results obtained with the biosensors with 16% and 17% graphite loading with 0.12% AChE. In all the cases, the recovery percentage is around 100%. This fact leads to the conclusion that the sample matrices did not interfere with pesticide determination and thus they were used for the analysis of spiked samples.

It is important to highlight that these electrochemical characterization strategies allow optimizing both conductive particles loading and biological material ratio present on the (bio)sensors based on rigid (bio)composites. So, after these results, it is possible to set a methodology for the composition optimization in order to improve the biosensors electroanalytical properties.

Conflicts of Interest

The authors confirm that this article content has no conflicts of interest.

Acknowledgments

R. Montes acknowledges Universitat Autònoma de Barcelona (UAB) for the award of PIF studentship. This work was supported by the research project from the Spanish Ministerio de Economía y Competitividad (MINECO), CTQ2015-69802-C2-1-R.

Supplementary Materials

Supplementary information associated with this article can be found in the attached file. These data include the influence

of the enzyme loading on the electrochemical parameters, lineal voltammetry measurements, and the electroanalytical evaluation with acetylthiocholine. Table S1: comparison of the electrochemical parameters obtained by electrochemical impedance spectroscopy (R_{Ω} , R_{ct} , and C_{dl}) for the biocomposites with 16% and 17% of graphite loading and 0.12% of AChE and 0.24% of AChE. Figure S1: linear sweep voltammetry response to acetylthiocholine from 0 to 10 mM in phosphate buffer solution (PBS 0.1 M and pH = 7.0). Scan rate 10 mV/s. Table S2: the calibration parameters for 20%, 17%, and 16% of graphite biocomposite electrode with 0.12% of AChE using amperometric measurements with acetylthiocholine (ATCh) as analyte and PBS 0.1 M at pH = 7.0 as background electrolyte ($n = 3$, 95% confidence level). Figure S2: linear response for biosensors with (A) 16% and 17% of graphite and (B) 20% of graphite loading. Measurements were carried out in 0.1 M phosphate solution at pH = 7.0 and 0.1 M KCl. EAPP = 700 mV. (*Supplementary Materials*)

References

- [1] A. Aparecido, P. Ferreira, C. V. Uliana, M. D. S. Castilho, N. C. Pesquero, and M. V. Foguel, "Amperometric Biosensor for Diagnosis of Disease," in *State of the Art in Biosensors - Environmental and Medical Applications*, T. Rincken, Ed., pp. 10–5772, doi, 10.5772/53656, 2013.
- [2] L. M. D. C. Silva, V. P. S. Dos Santos, A. M. Salgado, and K. S. Pereira, "Biosensors for Contaminants Monitoring in Food and Environment for Human and Environmental Health," in *State of the Art in Biosensors - Environmental and Medical Applications*, pp. 151–168, 2013.
- [3] N. Xia and Y. Gao, "Carbon nanostructures for development of acetylcholinesterase electrochemical biosensors for determination of pesticides," *International Journal of Electrochemical Science*, vol. 10, no. 1, pp. 713–724, 2015.
- [4] M. M. Musameh, Y. Gao, M. Hickey, and I. L. Kyratzis, "Application of carbon nanotubes in the extraction and electrochemical detection of organophosphate pesticides: a review," *Analytical Letters*, vol. 45, no. 8, pp. 783–803, 2012.
- [5] G. Zhao, H. Wang, and G. Liu, "Advances in biosensor-based instruments for pesticide residues rapid detection," *International Journal of Electrochemical Science*, vol. 10, no. 12, pp. 9790–9807, 2015.
- [6] C. S. Pundir and N. Chauhan, "Acetylcholinesterase inhibition-based biosensors for pesticide determination: a review," *Analytical Biochemistry*, vol. 429, no. 1, pp. 19–31, 2012.
- [7] R. Ramachandran, V. Mani, S.-M. Chen, G. Gnanakumar, and M. Govindasamy, "Recent developments in electrode materials and methods for pesticide analysis - An overview," *International Journal of Electrochemical Science*, vol. 10, no. 1, pp. 859–869, 2015.
- [8] P. Raghunath, T. M. Reddy, K. Reddaiah, B. E. K. Swamy, and M. Sreedhar, "Acetylcholinesterase based biosensor for monitoring of malathion and acephate in food samples: a voltammetric study," *Food Chemistry*, vol. 142, pp. 188–196, 2014.
- [9] S. P. Sharma, L. N. S. Tomar, J. Acharya, A. Chaturvedi, M. V. S. Suryanarayan, and R. Jain, "Acetylcholinesterase inhibition-based biosensor for amperometric detection of Sarin using single-walled carbon nanotube-modified ferrule graphite electrode," *Sensors & Actuators: B. Chemical*, Article ID 166167, pp. 616–623, 2012.
- [10] J. S. Van Dyk and B. Pletschke, "Review on the use of enzymes for the detection of organochlorine, organophosphate and carbamate pesticides in the environment," *Chemosphere*, vol. 82, no. 3, pp. 291–307, 2011.
- [11] B. Bucur, D. Fournier, A. Danet, and J.-L. Marty, "Biosensors based on highly sensitive acetylcholinesterases for enhanced carbamate insecticides detection," *Analytica Chimica Acta*, vol. 562, no. 1, pp. 115–121, 2006.
- [12] M. Stoytcheva and R. Zlatev, "Organophosphorus Pesticides Determination by Electrochemical Biosensors," in *Pesticides - Strategies for Pesticides Analysis, InTech*, M. Stoytcheva, Ed., pp. 359–372, 2011.
- [13] S. Laschi, D. Ogończyk, I. Palchetti, and M. Mascini, "Evaluation of pesticide-induced acetylcholinesterase inhibition by means of disposable carbon-modified electrochemical biosensors," *Enzyme and Microbial Technology*, vol. 40, no. 3, pp. 485–489, 2007.
- [14] O. Shulga and J. R. Kirchhoff, "An acetylcholinesterase enzyme electrode stabilized by an electrodeposited gold nanoparticle layer," *Electrochemistry Communications*, vol. 9, no. 5, pp. 935–940, 2007.
- [15] R. Dutta and P. Puzari, "Amperometric biosensing of organophosphate and organocarbamate pesticides utilizing polypyrrole entrapped acetylcholinesterase electrode," *Biosensors and Bioelectronics*, vol. 52, pp. 166–172, 2014.
- [16] E. Suprun, G. Evtugyn, H. Budnikov, F. Ricci, D. Moscone, and G. Palleschi, "Acetylcholinesterase sensor based on screen-printed carbon electrode modified with prussian blue," *Analytical and Bioanalytical Chemistry*, vol. 383, no. 4, pp. 597–604, 2005.
- [17] I. Marinov, Y. Ivanov, K. Gabrovska, and T. Godjevargova, "Amperometric acetylthiocholine sensor based on acetylcholinesterase immobilized on nanostructured polymer membrane containing gold nanoparticles," *Journal of Molecular Catalysis B: Enzymatic*, vol. 62, no. 1, pp. 66–74, 2010.
- [18] M. Pohanka, M. Hrabínova, J. Fusek et al., "Electrochemical biosensor based on acetylcholinesterase and indoxylacetate for assay of neurotoxic compounds represented by paraoxon," *International Journal of Electrochemical Science*, vol. 7, no. 1, pp. 50–57, 2012.
- [19] D. Di Tuoro, M. Portaccio, M. Lepore et al., "An acetylcholinesterase biosensor for determination of low concentrations of Paraoxon and Dichlorvos," *New Biotechnology*, vol. 29, no. 1, pp. 132–138, 2011.
- [20] F. Céspedes and S. Alegret, "New materials for electrochemical sensing II. Rigid carbon-polymer biocomposites," *TrAC - Trends in Analytical Chemistry*, vol. 19, no. 4, pp. 276–285, 2000.
- [21] S. Ramírez-García, S. Alegret, F. Céspedes, and R. J. Forster, "Carbon Composite Microelectrodes: Charge Percolation and Electroanalytical Performance," *Analytical Chemistry*, vol. 76, no. 3, pp. 503–512, 2004.
- [22] R. Olivé-Monllau, M. J. Esplandiú, J. Bartrolí, M. Baeza, and F. Céspedes, "Strategies for the optimization of carbon nanotube/polymer ratio in composite materials: applications as voltammetric sensors," *Sensors and Actuators B: Chemical*, vol. 146, no. 1, pp. 353–360, 2010.
- [23] R. Montes, J. Bartrolí, F. Céspedes, and M. Baeza, "Towards to the improvement of the analytical response in voltammetric sensors based on rigid composites," *Journal of Electroanalytical Chemistry*, vol. 733, pp. 69–76, 2014.

- [24] R. Montes, J. Bartrolí, M. Baeza, and F. Céspedes, "Improvement of the detection limit for biosensors: advances on the optimization of biocomposite composition," *Microchemical Journal*, vol. 119, pp. 66–74, 2015.
- [25] J. Muñoz, J. Bartrolí, F. Céspedes, and M. Baeza, "Influence of raw carbon nanotubes diameter for the optimization of the load composition ratio in epoxy amperometric composite sensors," *Journal of Materials Science*, vol. 50, no. 2, pp. 652–661, 2014.
- [26] M. Pacios, M. del Valle, J. Bartrolí, and M. J. Esplandiu, "Electrochemical behavior of rigid carbon nanotube composite electrodes," *Journal of Electroanalytical Chemistry*, vol. 619–620, no. 1–2, pp. 117–124, 2008.
- [27] M. J. Esplandiu, M. Pacios, L. Cyganek, J. Bartrolí, and M. del Valle, "Enhancing the electrochemical response of myoglobin with carbon nanotube electrodes," *Nanotechnology*, vol. 20, no. 35, Article ID 355502, 2009.
- [28] F. Céspedes, E. Martínez-Fàbregas, and S. Alegret, "New materials for electrochemical sensing I. Rigid conducting composites," *TrAC - Trends in Analytical Chemistry*, vol. 15, no. 7, pp. 296–304, 1996.
- [29] M. Pohanka, D. Jun, and K. Kuca, "Amperometric biosensors for real time assays of organophosphates," *Sensors*, vol. 8, no. 9, pp. 5303–5312, 2008.
- [30] S. Zhang, Z. Gu, Y. Hu, S. Qu, and Y. Liu, "Study on the highly sensitive AChE electrode based on multiwalled carbon nanotubes," *Journal of Nanomaterials*, vol. 2014, Article ID 828141, 2014.
- [31] Sigma Aldrich, <http://www.sigmaaldrich.co>, 2015.
- [32] D. Martorell, F. Céspedes, E. Martínez-Fàbregas, and S. Alegret, "Amperometric determination of pesticides using a biosensor based on a polishable graphite-epoxy biocomposite," *Analytica Chimica Acta*, vol. 290, no. 3, pp. 343–348, 1994.
- [33] Y. Gao, I. Kyratzis, R. Taylor, C. Huynh, and M. Hickey, "Immobilization of acetylcholinesterase onto carbon nanotubes utilizing streptavidin-biotin interaction for the construction of amperometric biosensors for pesticides," *Analytical Letters*, vol. 42, no. 16, pp. 2711–2727, 2009.
- [34] J. Wang, "Practical Considerations," in *Analytical Electrochemistry*, John Wiley & Sons, Inc., New York, USA, 2000.
- [35] S. Solé, A. Merkoçi, and S. Alegret, "Determination of toxic substances based on enzyme inhibition. Part II. Electrochemical biosensors for the determination of pesticides using flow systems," *Critical Reviews in Analytical Chemistry*, vol. 33, no. 2, pp. 127–143, 2003.
- [36] Environmental Protection Agency (EPA), <http://www.epa.gov/>, 2015.

Research Article

Rapid Adsorption of Proinflammatory Cytokines by Graphene Nanoplatelets and Their Composites for Extracorporeal Detoxification

Yishan Zheng,¹ Nicholas Pescatore,² Yury Gogotsi,^{2,3} Boris Dyatkin,^{2,3} Ganesh Ingavle,¹ Vadym Mochalin ,⁴ Tochukwu Ozulumba,¹ Sergey Mikhailovsky,¹ and Susan Sandeman ¹

¹School of Pharmacy and Biomolecular Sciences, University of Brighton, Brighton BN2 4GJ, UK

²Department of Materials Science & Engineering and A. J. Drexel Nanomaterials Institute, Drexel University, Philadelphia, PA 19104, USA

³Chemistry Division, U.S. Naval Research Laboratory, Washington, DC 20375, USA

⁴Department of Chemistry and Department of Materials Science & Engineering, Missouri University of Science & Technology, Rolla, MO 65409, USA

Correspondence should be addressed to Susan Sandeman; s.sandeman@brighton.ac.uk

Received 19 July 2017; Revised 11 January 2018; Accepted 22 January 2018; Published 21 February 2018

Academic Editor: Renyun Zhang

Copyright © 2018 Yishan Zheng et al. This is an open access article distributed under the Creative Commons Attribution License, which permits unrestricted use, distribution, and reproduction in any medium, provided the original work is properly cited.

Sepsis is a complex clinical syndrome that features excessive release of cytokines and other inflammatory mediators that could lead to organ dysfunction. Despite different treatment and management options, sepsis associated high morbidity and mortality rates remain. This has prompted intensive research into alternative therapeutic approaches such as targeted removal of sepsis related molecules using extracorporeal hemoperfusion. In this study, we explore the use of graphene nanoplatelets (GNP) as low-cost alternative hemosorbents for rapid removal of a broad spectrum of proinflammatory cytokine markers. Firstly, the physical characteristics, cytotoxicity, and cytokine marker adsorption profile of GNP were assessed. The results not only confirmed the surface characteristics of GNP and their ability to rapidly remove cytokine markers, but also indicated a low cytotoxicity towards the hepatic cell line HepG2. GNP were then incorporated into a freestanding flexible GNP-poly(tetrafluoroethylene) film with preserved surface characteristics and cytokine adsorption profile for potential use in hemoperfusion applications.

1. Introduction

Sepsis is a life-threatening condition caused by the body's dysregulated host response to infection. Between 1993 and 2003, the number of hospitalizations for severe sepsis doubled in the United States [1]. Sepsis is the primary cause of death for children and infants [2, 3], and the number of incidences was estimated at over 19 million cases worldwide annually [4]. Sepsis conditions progress as a function of the cytokine cascade, an exaggerated immune response to the incident infection [5]. Although the exact mechanism of sepsis remains poorly understood, it is believed that high concentrations of proinflammatory cytokines, such as IL-6, IL-8, and TNF- α contribute to the progression of sepsis in patients [6, 7].

Current sepsis treatment methods consist of treating the underlying infection using broad spectrum antibiotics and remediating hemodynamic changes through fluid resuscitation [8]. Recently, the use of extracorporeal blood purification has been investigated as an alternative approach to sepsis treatment through the removal of substances linked to the pathogenesis of sepsis. Endotoxins have been identified as key substances in sepsis progression, and polymyxin B-immobilized columns have been designed for the removal of endotoxins through direct hemoperfusion [9]. Despite the successful targeted removal of endotoxins from septic patients, clinical trials have shown an inconclusive benefit in the removal of endotoxins alone [10, 11]. The removal of inflammatory cytokines has also attracted increasing

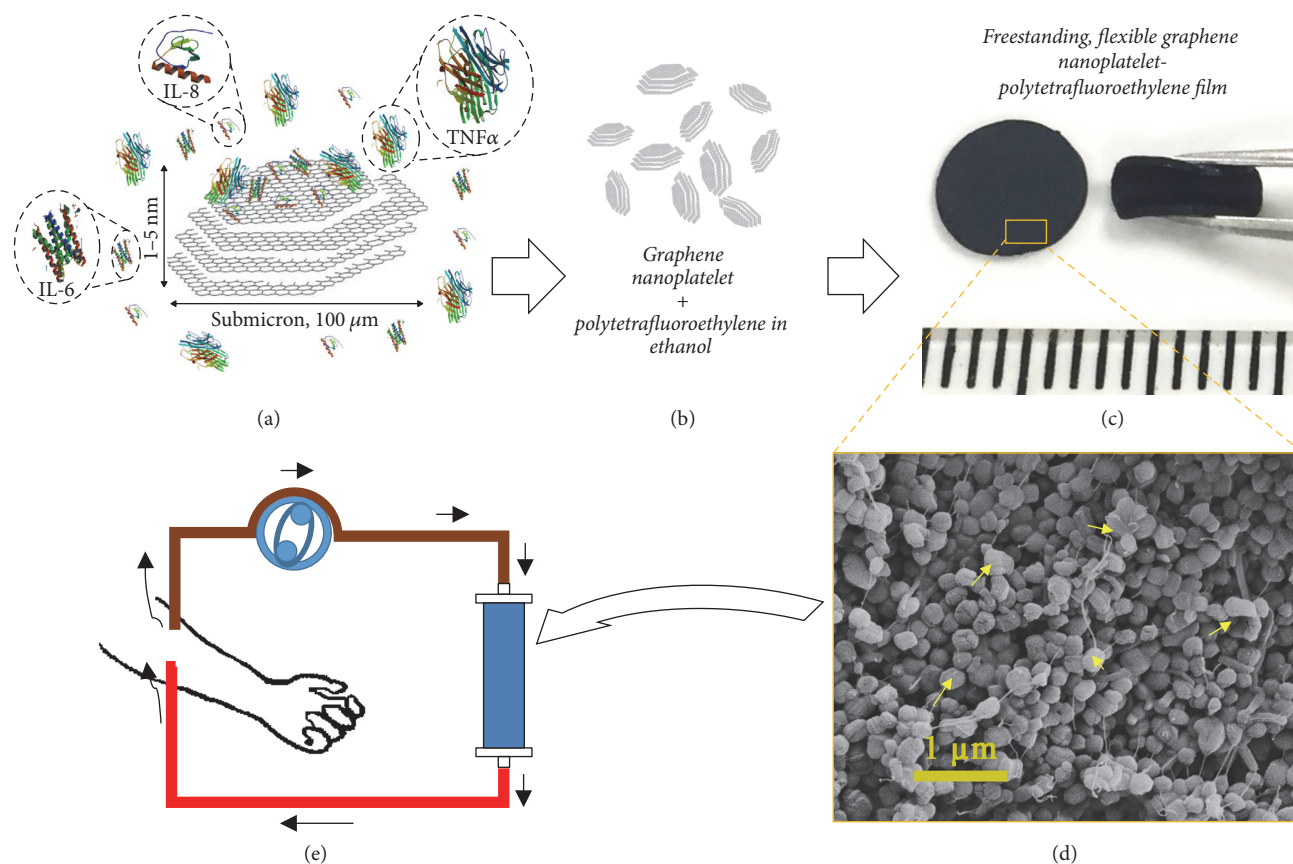


FIGURE 1: Schematic diagrams showing (a) the layered, open structure of graphene nanoplatelets (GNP) which are suitable for broad spectrum proinflammatory cytokine removal and (b) the use of PTFE, as a binder to produce the (c) freestanding flexible GNP-PTFE film with (d) exposed GNP surfaces and PTFE holding the GNP (indicated by yellow arrow), indicating a potential route for use in (e) hemoperfusion.

attention as an option for sepsis treatment. Polymeric porous adsorbents such as CytoSorb® (CytoSorbents Corporation, USA) have been developed for target removal of molecules between 10 and 50 kDa and have shown some success in both animal studies and clinical case studies [12, 13]. Furthermore, synthetic activated carbon (AC) is also an attractive adsorbent for hemoperfusion systems, as its inert character and tunable porosity (e.g., mesoporous texture) allow for optimal adsorption of proteins with different dimensions. Recent work has utilized carbon in the form of AC [14], carbide-derived carbons [15, 16], and polymer-pyrolyzed carbon monoliths [17] for use in adsorbing overexpressed cytokines and other toxins inherent in septic patients. These amorphous and graphitic carbons rely on an internally accessible surface area and entrapment of proteins by slit-shaped pores for adsorption [18].

While the results of these previous investigations have shown a viable proof-of-concept and efficient adsorption of these cytokines, these adsorbents lack rapid kinetics due to a complex adsorption model [14, 19]. More advanced synthetic materials have a high manufacturing cost. Graphene nanoplatelets (GNP) are a new, commercially available, low-cost graphene material that consists of stacks of graphene layers 1–5 nm in thickness and tunable lateral dimensions ranging from submicron scale to over 100 μm, as determined

by milling and processing [20]. GNP have an openly accessible and large specific surface area ($\sim 500 \text{ m}^2/\text{g}$) [21], making them an ideal material for rapid protein adsorption (Figure 1(a)). Typical GNP synthesis involves mechanical exfoliation of expanded graphite prepared from natural graphite [22, 23]. Previous report has tested the suitability of expanded graphite materials with inert surface and abundant macropores for large molecule adsorption and bacteriostatic properties and, subsequently, demonstrated potential for medical applications as wound dressings [24]. Owing to the abundant supply and low price of the source natural graphite material, GNP warrants further investigation as a potential cost-effective medical adsorbent. In this paper, we explore the use of noncytotoxic graphene nanoplatelets for rapid removal of a broad spectrum of proinflammatory cytokines identified as instigators of sepsis progression and the preparation of a freestanding flexible GNP-poly(tetrafluoroethylene) film (Figures 1(b) and 1(c)) with preserved surface (Figure 1(d)) and cytokine adsorption characteristics for practical use in hemoperfusion applications (Figure 1(e)).

2. Materials and Methods

2.1. Material Synthesis. The GNP used in this study was Grade C-500 xGnPTM obtained from XG Sciences© (Lansing, MI,

USA). GNP was vacuum annealed (10^{-6} torr) at 1800°C for eight hours in a vacuum furnace (Solar Atmospheres, PA, USA) to remove functional groups, graphitize the surface of the GNP, and produce vacuum annealed GNP (VA-GNP). VA-GNP-PTFE film was prepared by mixing defunctionalized VA-GNP with PTFE (60% w/w in water) solution (Sigma-Aldrich, US) in ethanol at a ratio of 19 : 1. Evaporation of ethanol left a homogenous VA-GNP-PTFE dense slurry which was rolled out into a cohesive, freestanding $100\ \mu\text{m}$ thick film. The resulting film was then subjected to nitrogen adsorption analysis and cytokine removal assessments to establish its efficacy as a hemoadsorbent.

2.2. Material Characterization. GNP particle size was determined by dynamic light scattering (DLS) using Zetasizer Nano ZS (Malvern, UK). High magnification images of GNP were obtained using transmission electron microscopy (TEM) (JEM2100, JEOL, Japan). The surface and internal porous morphologies of GNP powder and GNP-PTFE film were characterized by scanning electron microscopy (SEM) (Zeiss Supra 50VP field-emission SEM, USA). Quadrasorb pore size analyzer (Quantachrome, FL, USA) was used to measure specific surface area and porosity by carrying out N_2 adsorption-desorption measurements at 0.05–0.99 P/P_0 relative pressures at 77.4 K. The data was analyzed using Quantachrome data analysis software (Quantachrome QuadraWin™ 5.1). The specific surface areas were calculated using the Brunauer, Emmett, and Teller (BET) method while the pore size distribution was estimated using quenched solid density functional theory (QSDFT) modelling.

2.3. Biocompatibility Assessment. To ensure the safety of GNP, its cytotoxicity was also assessed. The liver, as the main organ for detoxification, has been reported to accumulate nanoparticles after their injection in the bloodstream [25, 26]. A human hepatic epithelial cell line HepG2 (CRL-11997™, ATCC®, VA, USA) was used for the assessment of GNP cytotoxicity, with silver nanoparticles as a positive control due to their widely reported cytotoxicity and hepatocytotoxicity [27, 28]. HepG2 cell viability after treatments was determined by comparing cellular 3-(4,5-dimethylthiazol-2-yl)-5-(3-carboxymethoxyphenyl)-2-(4-sulfophenyl)-2H-tetrazolium (MTS) conversion using CellTiter 96® Aqueous One Solution Cell Proliferation Assay (Promega, Southampton, UK), while the material cytotoxicity was assessed through the level of lactate dehydrogenase (LDH) released by the HepG2 cells using CytoTox 96® Non-Radioactive Cytotoxicity Assay (Promega, Southampton, UK).

2.4. Cytokine Adsorption Experiments. The cytokine marker adsorption profile of GNP was first evaluated by incubating 10% v/v of GNP with fresh frozen human blood plasma (Cambridge Bioscience Ltd., Cambridge, UK) spiked with 1 ng/mL IL-8, IL-1 β , IL-6, IL-10, and TNF- α (BD Biosciences, UK) for 60 minutes. Concentrations of the selected cytokine marker were determined using BD Cytometric Bead Array (CBA) Human Inflammatory Cytokines Kit (BD Biosciences, UK). The GNP-PTFE film adsorption kinetics of selected

cytokine markers IL-8, IL-6, and TNF- α was compared with PTFE film and GNP powder. The selected cytokine marker concentrations were measured by enzyme-linked immunosorbent assay (ELISA) using BD Biosciences ELISA set. Two-way ANOVA statistical analysis was performed using Prism 6 version 6.05 (GraphPad Software, Inc.).

3. Results and Discussion

3.1. Material Morphology and Surface Characteristics. In the untreated GNP samples, loose agglomerates of GNP can be observed under SEM (Figure 2(a)). At a higher magnification, SEM images revealed that these agglomerates consisted of submicron size particles (Figure 2(b)). After sonication in ethanol, smaller agglomerates of GNP and single nanoplatelets were observed under TEM (Figure 2(c)), revealing their multilayer-stacked graphene structure. Under higher magnification, a single nanoplatelet can be observed from a top-down perspective in TEM (Figure 2(c)). VA-GNP showed a 2.7-fold decrease in specific surface area and pore volume as compared to GNP. This was observed along with a 3-fold increase in VA-GNP particle size as compared to GNP determined by dynamic light scattering (DLS) analysis. The decrease in surface area is caused by the restacking of graphene planes during annealing [29]. However, increased agglomeration of defunctionalized hydrophobic VA-GNP in water is mainly responsible for the DLS-observed increase in their particle sizes. SEM and TEM images revealed the small particle size and tightly stacked layered structure of the GNP with high electron density between graphene layers, preventing access of N_2 molecules to internal voids in the material. The large BET surface area of the GNP is attributed predominantly to its outer accessible surface area. When VA-GNP was bound by PTFE (VA-GNP-PTFE) (Figure 2(d)), the film showed a slight decrease in the adsorbed nitrogen volume (Figure 3(a)) and micropore (<2 nm diameter pores) volume (Figure 3(b)), while the shape of the isotherm and the overall pore size distribution remained similar to the VA-GNP. The specific surface area and micropore volume of the VA-GNP-PTFE film remained as high as $210\ \text{m}^2/\text{g}$ and $0.30\ \text{cm}^3/\text{g}$, respectively, and only slightly lower than the VA-GNP alone at $294\ \text{m}^2/\text{g}$ and $0.39\ \text{cm}^3/\text{g}$, respectively (Table 1). This decrease in the specific surface area and micropore volume measured by the nitrogen adsorption analysis could be attributed to the addition of nonporous PTFE polymer that reduced the accessible VA-GNP surface to N_2 molecules.

3.2. Cytokine Markers Removal Profile of GNP. Following materials characterization, cytokine adsorption efficacy of the GNP-PTFE film was subsequently assessed. The cytokine marker adsorption profile of GNP showed rapid and efficient removal of cytokines from human plasma spiked with a cytokine cocktail. The concentration of smaller cytokines IL-8 (8 kDa) and IL-1 β (17 kDa) in the spiked plasma was reduced from over 1500 pg/mL to 20 pg/mL within 5 minutes of direct contact (Figure 4(a)). In comparison, GNP removal of larger cytokine markers IL-10 (18.5 kDa) and IL-6 (20.5 kDa) by GNP appeared to be slightly slower. However,

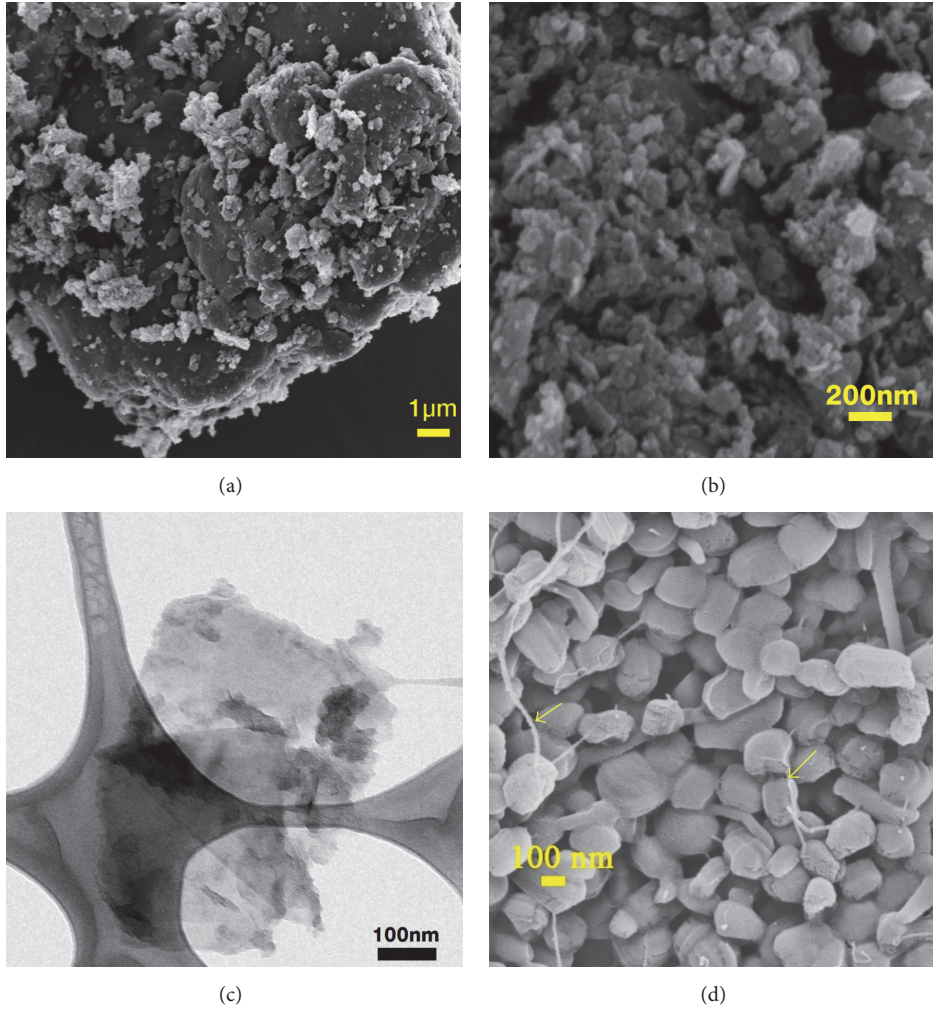


FIGURE 2: (a) SEM image of a GNP agglomerate; (b) higher magnification SEM image revealing submicron GNP particles; (c) TEM image of a single GNP, indicating a single GNP particle consists of stacks of graphene layers; and (d) SEM image of the GNP-PTFE film in which GNP particles were held together by PTFE (indicated by arrows).

TABLE 1: Porosity of GNP, VA-GNP, and VA-GNP-PTFE film determined using low temperature nitrogen adsorption analysis. Sample specific surface area (S_{BET}) and pore volume (V_{QSDFT})/size (D_{mode}) were calculated using BET and QSDFT, respectively. Equivalent particle diameter (d) was determined using dynamic light scattering.

| Sample | S_{BET} (m^2/g) | V_{QSDFT} (cm^3/g) | D_{mode} (nm) | d (nm) |
|-------------|--|---|------------------------|----------|
| Initial GNP | 797 | 0.807 | 0.785 | 547 |
| VA-GNP | 294 | 0.397 | 0.723 | 1670 |
| VA-GNP-PTFE | 210 | 0.301 | 0.852 | -- |

even in these cases 60% and 50% removal, respectively, were achieved within the first 5 min of contact. The TNF- α trimer (51 kDa) is, reportedly, the most challenging molecule to remove in conventional blood purification techniques using carbon sorbents [30–32]. However, a reduction in the plasma TNF- α concentration from 868 pg/mL to 55 pg/mL after 5 min contact with GNP indicated a rapid and efficient removal of the TNF- α by GNP. The fast adsorption kinetics can be attributed to direct contact with a completely accessible surface area and minimal diffusion barriers to and on

the surface. These results demonstrated GNP's potential for broad spectrum cytokine removal.

3.3. Biocompatibility of GNP. The LDH and MTT cytotoxicity assay results indicated that at lower tested concentrations GNP caused no or minimal cytotoxic effect (<20% cytotoxicity and >80% cell viability) towards HepG2 cells, while the silver nanoparticles were cytotoxic at concentrations as low as 0.01% (v/v) (Figures 4(b) and 4(c)). HepG2 cell viability fell below 60% after 0.06% GNP treatment, indicating a

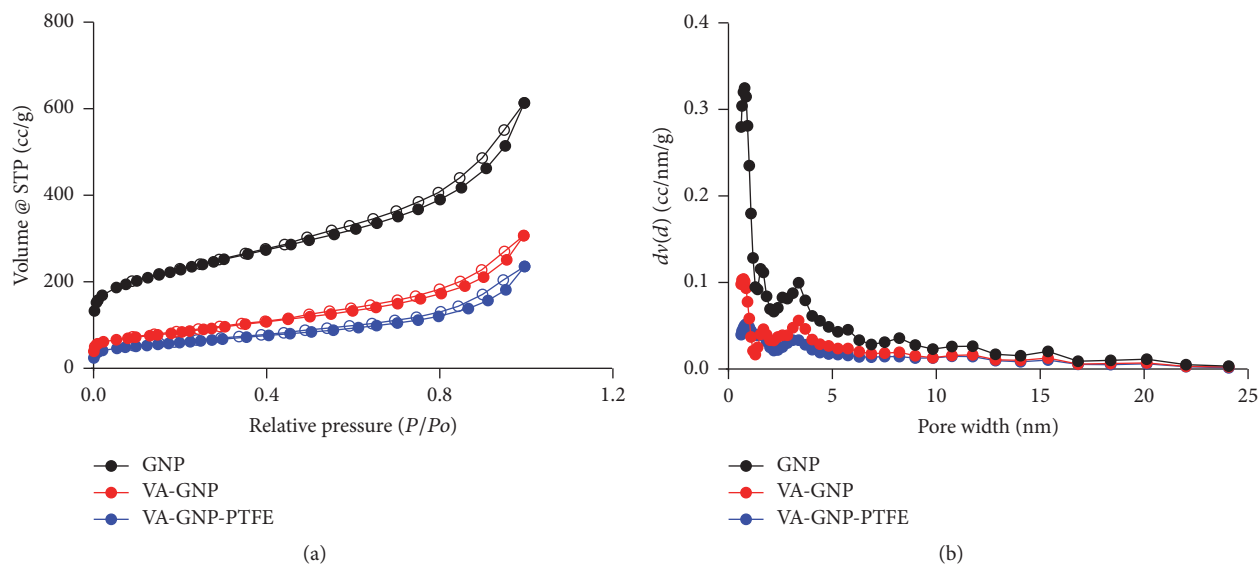


FIGURE 3: (a) Low temperature nitrogen adsorption isotherms (closed circles denote the adsorption branch and open circles denote the desorption branch) and (b) pore size distributions of the GNP, VA-GNP, and VA-GNP-PTFE film.

suppression of metabolic activity (Figure 4(b)). The cytotoxicity of GNP determined using LDH assay appeared to be dose-dependent and was significantly ($p < 0.01$) lower than the silver nanoparticles at the same concentration (Figure 4(c)). The slight cytotoxic effects of GNP at the concentrations of 0.03% and 0.06% are likely attributed to the large absolute volume of GNP in the two-dimensional culture system, which blocked cellular access to vital oxygen and nutrients.

3.4. Cytokine Markers Removal Efficiency of GNP-PTFE Film.

The adsorption data for cytokine markers IL-8 and IL-6 and TNF- α revealed that the PTFE film alone did not reduce the cytokine concentration in the spiked plasma compared to the control within the 90 min incubation cycle. In contrast, when the spiked plasma was incubated with the GNP particles, IL-8 concentration reduced from 633 pg/mL to 7 pg/mL within 5 min. IL-6 decreased from 477 pg/mL to 22 pg/mL after 5 min and further dropped to 8 pg/mL after 30 min (Figures 5(a) and 5(b)). The VA-GNP-PTFE film showed a slower and slightly less efficient adsorption of IL-8 from the spiked plasma as compared to the GNP, but with 95% removal of IL-8 over 90 min of incubation (Figure 5(a)). A significantly lower adsorption efficacy of IL-6 was observed with VA-GNP-PTFE film as compared to the GNP particles, but VA-GNP-PTFE film removed over 50% of IL-6 from the spiked plasma over the 90 min incubation period (Figure 5(b)). Incorporation of GNP into the PTFE film reduced TNF- α removal compared to the GNP particles alone (Figure 5(c)). This could be due to the packing of GNP particles, which reduced the exposed particle outer surface area. Alternatively, PTFE limited accessibility between the particles and potentially contributed to this effect. We have previously highlighted the need for pores with diameters that exceed protein molecule size [33]. From a practical perspective, this translated to meso-/macropores

in activated carbon adsorbents with predominant 70–120 nm diameter pores as necessary for significant TNF- α adsorption [17, 34, 35]. Although GNP with a similar specific surface area did not feature such large pores, it still demonstrated superior TNF- α adsorption, which was reduced after incorporation of PTFE. This indicated the benefit of GNP's large, outer surface area and underscored the importance of accessible surface just as much as the internal porosity of ACs. Overall, the incorporation of GNP in the PTFE film largely preserved the GNP surface for the adsorption of mid-range molecular weight cytokine markers IL-6 and IL-8 and demonstrated significantly lower removal capacity of plasma TNF- α as compared to unbound GNP. Future experiments may further improve GNP surface area exposure by preparing VA-GNP-PTFE film with reduced thickness and thus improve TNF- α adsorption. This development could yield significant cost benefits to optimize and use GNP for sepsis in blood detoxification devices.

Novel materials developed for direct blood contacting applications often raise hemocompatibility concerns such as fine particle release and blood cell activation. Several of our previously published studies have demonstrated the safe use of carbon-based materials for direct blood contacting applications [34, 36, 37]. Our efforts have developed a commercially viable composite material that utilized PTFE not only to produce a flexible freestanding film structure, but also to hold the GNP particles in place, eliminating fine particle release. In addition to the noncytotoxic nature of the GNP established in this study, further research that delves into the assessments of material hemocompatibility will be beneficial. In particular, future efforts must ensure that the use of this cost-effective adsorbent does not trigger complement cascade, excessive platelet adhesion/activation, or granulocyte activation in *ex vivo* setups. The GNP-PTFE adsorbent could also be used in the plasma circuit of systems

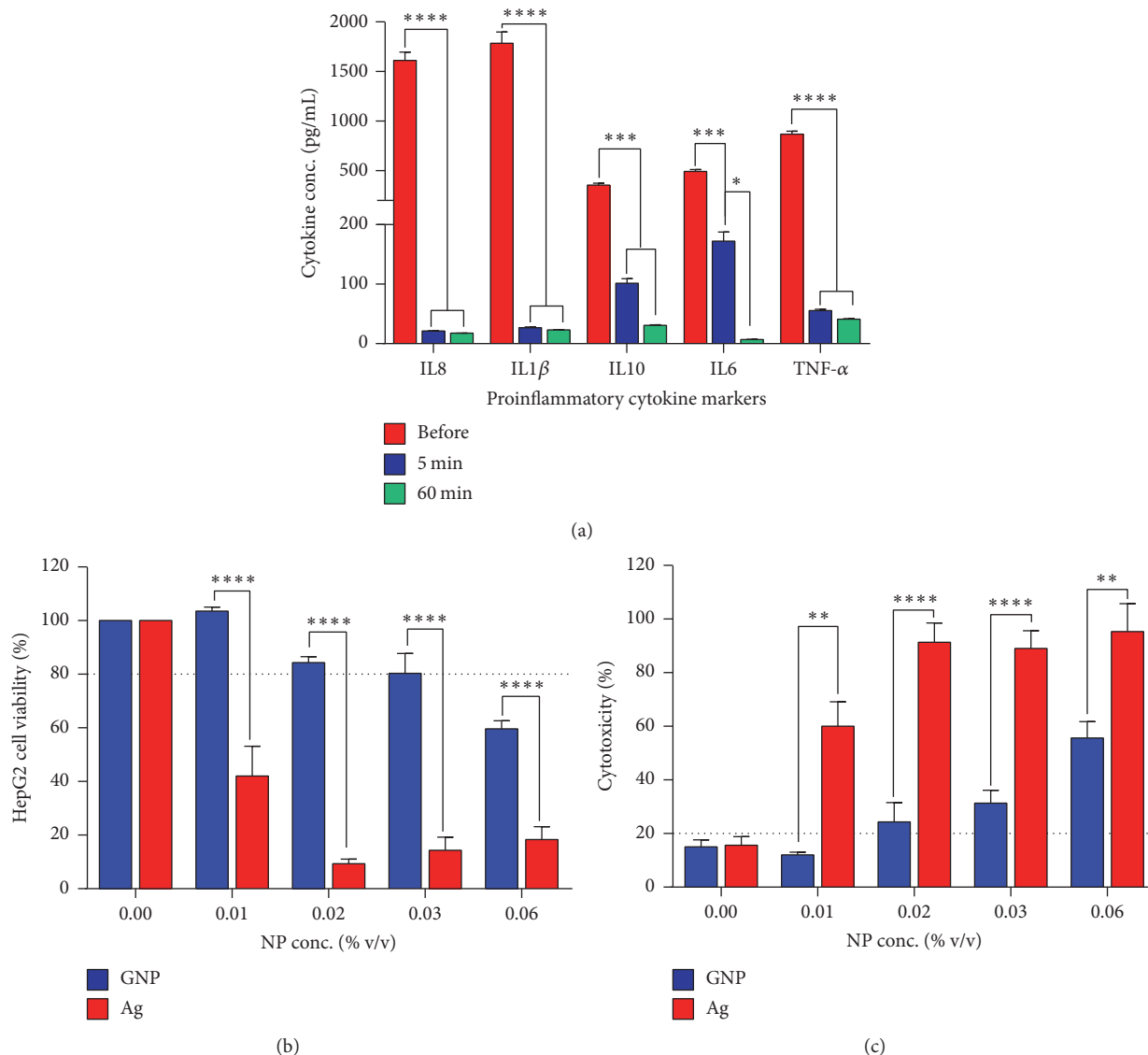


FIGURE 4: (a) The removal efficiency of inflammatory cytokine markers in spiked human plasma samples; GNP cytotoxicity assessments after 24 hours of direct contact using (b) MTS and (c) LDH assays. * represents $p < 0.05$; ** represents $p < 0.01$; *** represents $p < 0.001$; **** represents $p < 0.0001$ estimated using two-way ANOVA statistic test (\pm standard error of mean, $n = 3$).

such as MARS[®] [38] or Prometheus[®] [39] where adsorbent materials do not come into direct contact with patient blood and, therefore, mitigate issues of blood cell activation and hemocompatibility.

4. Conclusions

In summary, we have demonstrated the use of GNP as a fast and very efficient adsorbent with low cytotoxicity for rapid removal of proinflammatory cytokines including IL-8, IL-1 β , IL-6, IL-10, and TNF- α from human plasma on a clinically relevant scale. The material reported in this study shows faster adsorption compared to all other carbons reported so far, combined with a very high sorption capacity.

Furthermore, we also developed a flexible freestanding GNP-PTFE composite material with high accessible surface area for targeted adsorption of cytokines and showed its potential as hemoperfusion adsorbent. Further development of these graphene-based sorbents should aim to confirm their *ex vivo* hemocompatibility. Subsequently, future research efforts will enhance accessible surface area for improved adsorption of the high molecular weight cytokines including TNF- α and bring forth a cost-effective materials solution for hemoperfusion systems for treatment of sepsis.

Conflicts of Interest

The authors declare that there are no conflicts of interest regarding the publication of this paper.

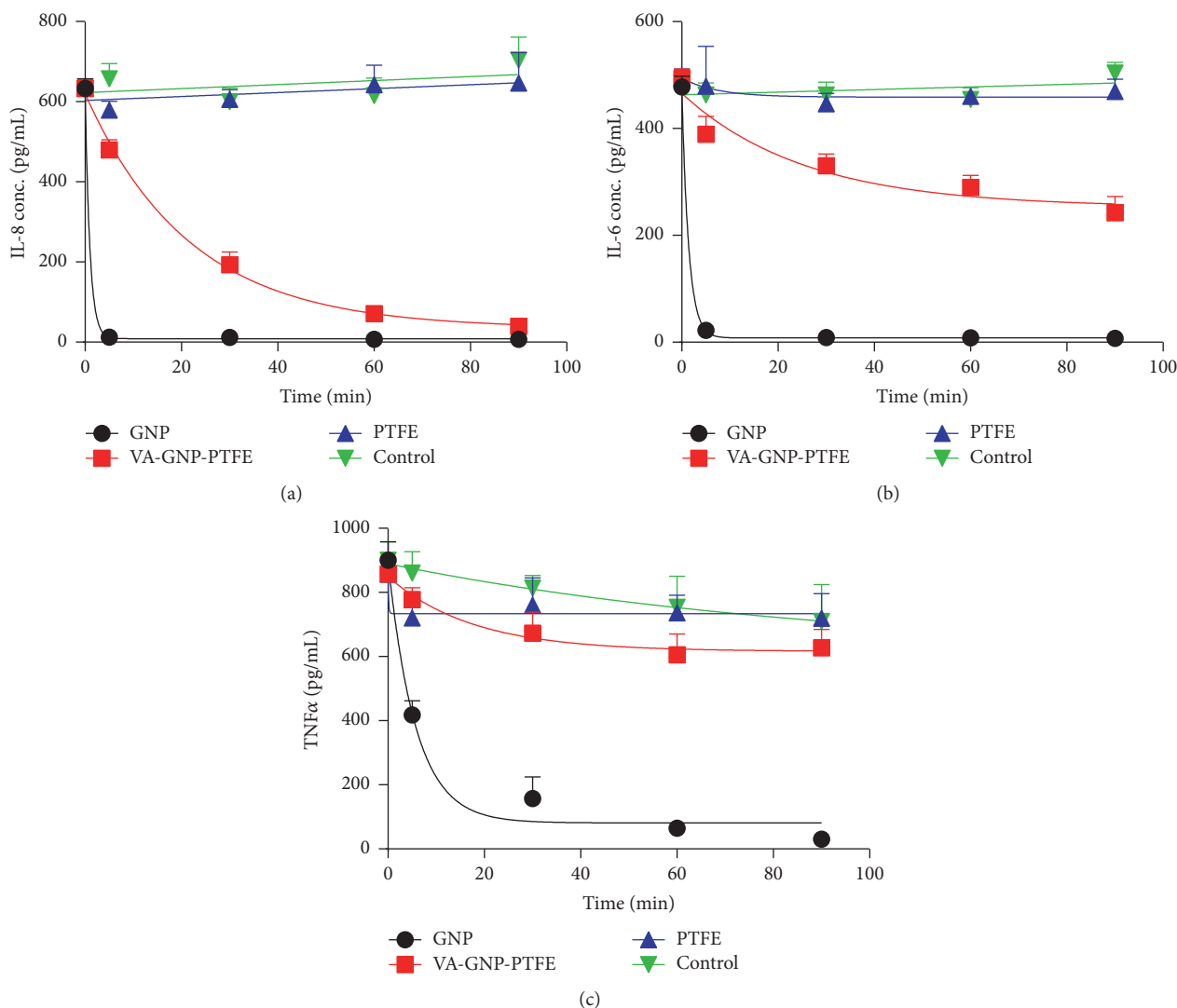


FIGURE 5: Removal efficiency of inflammatory cytokine markers IL-8 (a), IL-6 (b), and TNF- α (c) from spiked human plasma sample of GNP, VA-GNP-PTFE film, and plain PTFE film (\pm SEM, $n = 3$).

Acknowledgments

This material is based upon work carried out by the NOMAD project supported by the British Council and the UK Department for Business, Innovation and Skills through the Global Innovation Initiative.

References

- [1] V. Y. Dombrovskiy, A. A. Martin, J. Sunderram, and H. L. Paz, "Rapid increase in hospitalization and mortality rates for severe sepsis in the United States: a trend analysis from 1993 to 2003," *Critical Care Medicine*, vol. 35, no. 5, pp. 1244–1250, 2007.
- [2] A. R. Bedford Russell, "Neonatal sepsis," *Paediatrics and Child Health (United Kingdom)*, vol. 25, no. 6, pp. 271–275, 2015.
- [3] B. Tiru, E. K. DiNino, A. Orenstein et al., "The economic and humanistic burden of severe sepsis," *PharmacoEconomics*, vol. 33, no. 9, pp. 925–937, 2015.
- [4] N. K. J. Adhikari, R. A. Fowler, S. Bhagwanjee, and G. D. Rubenfeld, "Critical care and the global burden of critical illness in adults," *The Lancet*, vol. 376, no. 9749, pp. 1339–1346, 2010.
- [5] D. C. Angus and T. van der Poll, "Severe sepsis and septic shock," *The New England Journal of Medicine*, vol. 369, no. 9, pp. 840–851, 2013.
- [6] K. Baghel, R. N. Srivastava, A. Chandra et al., "TNF- α , IL-6, and IL-8 cytokines and their association with TNF- α -308 G/A polymorphism and postoperative sepsis," *Journal of Gastrointestinal Surgery*, vol. 18, no. 8, pp. 1486–1494, 2014.
- [7] B. G. Chousterman, F. K. Swirski, and G. F. Weber, "Cytokine storm and sepsis disease pathogenesis," *Seminars in Immunopathology*, vol. 39, no. 5, pp. 517–528, 2017.
- [8] A. M. Taeb, M. H. Hooper, and P. E. Marik, "Sepsis: Current definition, pathophysiology, diagnosis, and management," *Nutrition in Clinical Practice*, vol. 32, no. 3, pp. 296–308, 2017.
- [9] H. Aoki, M. Kodama, T. Tani, and K. Hanasawa, "Treatment of sepsis by extracorporeal elimination of endotoxin using

- polymyxin B-immobilized fiber," *The American Journal of Surgery*, vol. 167, no. 4, pp. 412–417, 1994.
- [10] C. Ronco and D. J. Klein, "Polymyxin B hemoperfusion: A mechanistic perspective," *Critical Care*, vol. 18, no. 3, article no. 309, 2014.
- [11] T. Terayama, K. Yamakawa, Y. Umemura, M. Aihara, and S. Fujimi, "Polymyxin B hemoperfusion for sepsis and septic shock: A systematic review and meta-analysis," *Surgical Infections*, vol. 18, no. 3, pp. 225–233, 2017.
- [12] T. Taniguchi, F. Hirai, Y. Takemoto et al., "A novel adsorbent of circulating bacterial toxins and cytokines: The effect of direct hemoperfusion with CTR column for the treatment of experimental endotoxemia," *Critical Care Medicine*, vol. 34, no. 3, pp. 800–806, 2006.
- [13] K. Kogelmann, D. Jarczak, M. Scheller, and M. Drüner, "Hemoadsorption by CytoSorb in septic patients: a case series," *Critical Care*, vol. 21, no. 1, 2017.
- [14] S. Inoue, K. Kiriya, Y. Hatanaka, and H. Kanoh, "Adsorption properties of an activated carbon for 18 cytokines and HMGB1 from inflammatory model plasma," *Colloids and Surfaces B: Biointerfaces*, vol. 126, pp. 58–62, 2015.
- [15] S. Yachamaneni, G. Yushin, S.-H. Yeon et al., "Mesoporous carbide-derived carbon for cytokine removal from blood plasma," *Biomaterials*, vol. 31, no. 18, pp. 4789–4794, 2010.
- [16] V. Presser, S. Yeon, C. Vakifahmetoglu et al., "Hierarchical porous carbide-derived carbons for the removal of cytokines from blood plasma," *Advanced Healthcare Materials*, vol. 1, no. 6, pp. 682–682, 2012.
- [17] S. R. Sandeman, C. A. Howell, S. V. Mikhalovsky et al., "Inflammatory cytokine removal by an activated carbon device in a flowing system," *Biomaterials*, vol. 29, no. 11, pp. 1638–1644, 2008.
- [18] S. V. Mikhalovsky, "Emerging technologies in extracorporeal treatment: Focus on adsorption," *Perfusion*, vol. 18, no. 1, pp. 47–54, 2003.
- [19] V. M. Gun'ko, V. V. Turov, O. P. Kozynchenko et al., "Activation and structural and adsorption features of activated carbons with highly developed micro-, meso- and macroporosity," *Adsorption*, vol. 17, no. 3, pp. 453–460, 2011.
- [20] X. Li, S. Biswas, and L. T. Drzal, "High temperature vacuum annealing and hydrogenation modification of exfoliated graphite nanoplatelets," *Journal of Engineering (United States)*, vol. 2013, Article ID 638576, 2013.
- [21] L. T. Drzal, *Graphene Nanoplatelets: A Multi-Functional Nanomaterial Additive for Polymers and Composites*, I. XG Sciences, 2015.
- [22] S. Y. Choi, M. Mamak, E. Cordola, and U. Stadler, "Large scale production of high aspect ratio graphite nanoplatelets with tunable oxygen functionality," *Journal of Materials Chemistry*, vol. 21, no. 13, pp. 5142–5147, 2011.
- [23] A. V. Melezhyk and A. G. Tkachev, "Synthesis of graphene nanoplatelets from peroxosulfate graphite intercalation compounds," *Nanosystems: Physics, Chemistry, Mathematics*, vol. 5, no. 2, p. 13, 2014.
- [24] W. Shen, S. Wen, N. Cao et al., "Expanded graphite - a new kind of biomedical material," *Carbon*, vol. 37, no. 2, pp. 356–358, 1999.
- [25] S. Hirn, M. Semmler-Behnke, C. Schleh et al., "Particle size-dependent and surface charge-dependent biodistribution of gold nanoparticles after intravenous administration," *European Journal of Pharmaceutics and Biopharmaceutics*, vol. 77, no. 3, pp. 407–416, 2011.
- [26] N. Kurantowicz, B. Strojny, E. Sawosz et al., "Biodistribution of a high dose of diamond, graphite, and graphene oxide nanoparticles after multiple intraperitoneal injections in rats," *Nanoscale Research Letters*, vol. 10, no. 1, article no. 398, 2015.
- [27] Y. Xue, T. Zhang, B. Zhang, F. Gong, Y. Huang, and M. Tang, "Cytotoxicity and apoptosis induced by silver nanoparticles in human liver HepG2 cells in different dispersion media," *Journal of Applied Toxicology*, vol. 36, no. 3, pp. 352–360, 2016.
- [28] B. K. Gaiser, S. Hirn, A. Kermanzadeh et al., "Effects of silver nanoparticles on the liver and hepatocytes in vitro," *Toxicological Sciences*, vol. 131, no. 2, pp. 537–547, 2013.
- [29] S. Osswald, J. Chmiola, and Y. Gogotsi, "Structural evolution of carbide-derived carbons upon vacuum annealing," *Carbon*, vol. 50, no. 13, pp. 4880–4886, 2012.
- [30] B. R. Glick, T. L. Delovitch, and C. L. Patten, "9.1.3 tumor necrosis factor," in *Medical Biotechnology*, American Society for Microbiology (ASM).
- [31] P. Heering, S. Morgera, F. J. Schmitz et al., "Cytokine removal and cardiovascular hemodynamics in septic patients with continuous venovenous hemofiltration," *Intensive Care Medicine*, vol. 23, no. 3, pp. 288–296, 1997.
- [32] S. Harm, F. Gabor, and J. Hartmann, "Characterization of adsorbents for cytokine removal from blood in an in vitro model," *Journal of Immunology Research*, vol. 2015, Article ID 484736, 2015.
- [33] G. Yushin, E. N. Hoffman, M. W. Barsoum et al., "Mesoporous carbide-derived carbon with porosity tuned for efficient adsorption of cytokines," *Biomaterials*, vol. 27, no. 34, pp. 5755–5762, 2006.
- [34] C. A. Howell, S. R. Sandeman, G. J. Phillips et al., "Nanoporous activated carbon beads and monolithic columns as effective hemoadsorbents for inflammatory cytokines," *The International Journal of Artificial Organs*, vol. 36, no. 9, pp. 624–632, 2013.
- [35] S. R. Tennison et al., "Carbon and its use in blood cleansing applications," US Pat., 20130072845 A1, 2013.
- [36] S. R. Sandeman, Y. Zheng, G. C. Ingavle et al., "A haemocompatible and scalable nanoporous adsorbent monolith synthesised using a novel lignin binder route to augment the adsorption of poorly removed uraemic toxins in haemodialysis," *Biomedical Materials*, vol. 12, no. 3, Article ID 035001, 2017.
- [37] S. R. Sandeman, C. A. Howell, G. J. Phillips et al., "An adsorbent monolith device to augment the removal of uraemic toxins during haemodialysis," *Journal of Materials Science: Materials in Medicine*, vol. 25, no. 6, pp. 1589–1597, 2014.
- [38] S. R. Mitzner, J. Stange, S. Klammt, S. Koball, H. Hickstein, and E. C. Reisinger, "Albumin dialysis MARS: Knowledge from 10 years of clinical investigation," *ASAIO Journal*, vol. 55, no. 5, pp. 498–502, 2009.
- [39] M. Oppert, S. Rademacher, K. Petrasch, and A. Jörres, "Extracorporeal liver support therapy with prometheus in patients with liver failure in the intensive care unit," *Therapeutic Apheresis and Dialysis*, vol. 13, no. 5, pp. 426–430, 2009.

Research Article

Biofabrication of Zinc Oxide Nanoparticle from *Ochradenus baccatus* Leaves: Broad-Spectrum Antibiofilm Activity, Protein Binding Studies, and *In Vivo* Toxicity and Stress Studies

Nasser A. Al-Shabib ¹, Fohad Mabood Husain ¹, Iftexhar Hassan,²
Mohd Shahnawaz Khan,³ Faheem Ahmed ⁴, Faizan Abul Qais,⁵ Mohammad Oves ⁶,
Mashihur Rahman,⁷ Rais Ahmad Khan ⁸, Altaf Khan,⁹ Afzal Hussain,¹⁰
Ibrahim M. Alhazza,² Shazia Aman,¹¹ Saba Noor,¹² Hossam Ebaid,²
Jameel Al-Tamimi,² Javed Masood Khan,¹ Abdul Rehman M. Al-Ghadeer,⁷
Md Khurshid Alam Khan,⁷ and Iqbal Ahmad⁵

¹ Department of Food Science and Nutrition, College of Food and Agriculture, King Saud University, Riyadh 11451, Saudi Arabia

² Department of Zoology, College of Science, King Saud University, Riyadh 11451, Saudi Arabia

³ Protein Research Chair, Department of Biochemistry, College of Science, King Saud University, Riyadh 11451, Saudi Arabia

⁴ College of Science & General Studies, Alfaisal University, Riyadh 11533, Saudi Arabia

⁵ Department of Agricultural Microbiology, Aligarh Muslim University, Aligarh 202002, India

⁶ Center of Excellence in Environmental Studies (CEES), King Abdulaziz University, Jeddah, Saudi Arabia

⁷ School of Life Sciences, B. S. Abdur Rahman University, Vandalur, Chennai 600048, India

⁸ Department of Chemistry, College of Science, King Saud University, Riyadh 11451, Saudi Arabia

⁹ Central Laboratory Research Center, College of Pharmacy, King Saud University, Riyadh 11451, Saudi Arabia

¹⁰ Department of Pharmacognosy, College of Pharmacy, King Saud University, Riyadh 11451, Saudi Arabia

¹¹ Department of Biochemistry, J. N. Medical College and Hospital, Aligarh Muslim University, Aligarh 202002, India

¹² Rajiv Gandhi Centre for Diabetes and Endocrinology, J. N. Medical College and Hospital, Aligarh Muslim University, Aligarh 202002, India

Correspondence should be addressed to Nasser A. Al-Shabib; nalshabib@ksu.edu.sa
and Fohad Mabood Husain; fhussain@ksu.edu.sa

Received 20 July 2017; Revised 15 November 2017; Accepted 5 December 2017; Published 7 February 2018

Academic Editor: Piersandro Pallavicini

Copyright © 2018 Nasser A. Al-Shabib et al. This is an open access article distributed under the Creative Commons Attribution License, which permits unrestricted use, distribution, and reproduction in any medium, provided the original work is properly cited.

Biofilms are complex aggregation of cells that are embedded in EPS matrix. These microcolonies are highly resistant to drugs and are associated with various diseases. Biofilms have greatly affected the food safety by causing severe losses due to food contamination and spoilage. Therefore, novel antibiofilm agents are needed. This study investigates the antibiofilm and protein binding activity of zinc nanoparticles (ZnNPs) synthesized from leaf extract of *Ochradenus baccatus*. Standard physical techniques, including UV-visible spectroscopy Fourier transform infrared spectroscopy and X-ray diffraction and transmission electron microscopy, were used to characterize the synthesized OB-ZnNPs. Synthesized OB-ZnNPs demonstrated significant biofilm inhibition in human and food-borne pathogens (*Chromobacterium violaceum*, *Escherichia coli*, *P. aeruginosa*, *Klebsiella pneumoniae*, *Serratia marcescens*, and *Listeria monocytogenes*) at subinhibitory concentrations. OB-ZnNPs significantly reduced the virulence factors like violacein, prodigiosin, and alginate and impaired swarming migration and EPS production. OB-ZnNPs demonstrated efficient binding with HSA protein and no change in their structure or stability was observed. In addition, *in vivo* toxicity evaluation confirmed that OB-ZnNPs possessed no serious toxic effect even at higher doses. Moreover, they were found to have excellent antioxidant properties that can be employed in the fields of food safety and medicine. Hence, it is envisaged that the OB-ZnNPs can be used as potential nanomaterials to combat drug resistant bacterial infections and prevent contamination/spoilage of food.

1. Introduction

Biofilms are a complex aggregation of bacteria that colonize and are found embedded, in self-secreted exopolysaccharide (EPS) matrix, which contains polysaccharides, proteins, lipids, and nucleic acids. Biofilms are more resistant to antibiotics as compared to their planktonic forms [1]. Apart from making the inhabitants more resistant, biofilms also increase retention of water and nutrients and absorption of nutrients, protect against host immune responses, and facilitate horizontal gene transfer. Biofilm inhabitants demonstrate multicellular behavior similar to higher multicellular organisms [2]. Implications of biofilm formation in medical field are well known, as it is associated with various diseases, infections caused by medical devices and nosocomial infections [3, 4]. Biofilms have also become problematic in the food industries, including brewing [5], seafood processing [6], dairy processing [7], poultry processing [8], and meat processing [9] leading to food safety issues by causing spoilage and contamination of food and food contact materials. There is an urgent need to find nontoxic, stable antibiofilm agents to improve public health and minimize economic losses.

Advent of nanotechnology has made nanomaterials as an effective alternative antimicrobial strategy to treat drug-resistant infections [10]. Particles with less than 100 nm in size are termed as nanoparticles (NPs) and their potent biocidal properties are attributed to their small size and high surface-to-volume ratio [11, 12]. In addition, stability of metal and metal oxides than organic compounds make them better antimicrobial agents [13, 14]. Among metal oxides, ZnO has attracted attention as antibacterial agent and ZnO nanoparticles (ZnO-NPs) are known to exhibit broad-spectrum antibacterial activity and can reduce the attachment and viability of microbes [15, 16]. Further, it is well established that the nanoparticles, after entry into the host system interact with biomolecules like proteins, lipids, and nucleic acids. Therefore, the effects of NPs are combined actions of nanoparticle-protein “corona” rather than nanoparticle alone [17]. Therefore, understanding of protein NPs interaction is very important for its future applications in medical and food industry [18, 19]. However, minimal work has been carried out to synthesize nontoxic ZnO nanoparticles and study their interactions with proteins and effects on biofilm formed by human and foodborne pathogens.

Green synthesis of NPs using plants is preferred over other chemical and physical methods as it is cost-effective, ecofriendly, and safe for human therapeutic use [20] and can be utilized for large-scale NPs synthesis [21]. ZnO nanoparticles (ZnONPs) from plants have been synthesized using green chemistry approaches by several workers [22–24].

Ochradenus baccatus Del. belongs to family Resedaceae and is widely distributed in South-West and central regions of Saudi Arabia. *O. baccatus* (Del.) is a shrub and is very important medicinally as it contains high contents of antioxidants and anti-inflammatory agents [25]. Leaves of *Ochradenus baccatus* have been used in the treatment of microbial infections, diphtheria, ganglions, and allergies [26].

In this study, aqueous leaf extract of *Ochradenus baccatus* was used as reducing, capping, and stabilizing agent for the

formation of zinc oxide nanoparticles (OB-ZnNPs). These nanoparticles were investigated for their ability to inhibit biofilm formed by bacterial pathogens. We also assessed its effect on the production of virulence factors like exopolysaccharide production, and motility associated with biofilm formation in the test pathogens. Further, the biofabricated OBZnNPs were examined for their protein (HSA) binding and toxicity studies were also performed *in vivo*. In our knowledge, this is probably the first report on the synthesis of nontoxic zinc oxide nanoparticles from the leaves of *Ochradenus baccatus* and characterization of their antibiofilm and protein binding properties.

2. Material Methods

2.1. Bacterial Strains. The bacterial strains used in this study included *Chromobacterium violaceum* ATCC 12472, *Escherichia coli* ATCC 25922, *P. aeruginosa* PAO1, *Klebsiella pneumoniae* ATCC 700603, *Serratia marcescens* ATCC 13880, and *Listeria monocytogenes* (laboratory strain). All bacterial strains were cultivated on Luria-Bertani (LB) medium and maintained at 37°C, except *C. violaceum* and *S. marcescens*, for which the temperature was 30°C.

2.2. Preparation of *Ochradenus baccatus* (OB) Seed Extract. *Ochradenus baccatus* leaves were collected and washed several times with distilled water to remove the dust particles and then sun-dried to remove the residual moisture. Leaf extract was prepared by crushing leaves in a grinder and the resultant powder (10 g) was homogenized completely in 50 ml double-distilled water and incubated with constant stirring (100 rpm) at 80°C for 20 min. The resultant mixture was then filtered using Whatman filter papers No. 1 to remove debris. This extract was used for generating green zinc nanoparticles.

2.3. Zinc Nanoparticle Synthesis. All the reagents involved in the experiments were of analytical grade purity and utilized as received without further purification. Zinc nitrate (99.999%) was purchased from Sigma-Aldrich. The synthesis was carried out in a domestic microwave oven (Samsung, 750 W). We followed the method described by Al-Shabib et al. (2016); briefly, 0.05 M aqueous solution of zinc nitrate in 100 ml distilled water was prepared in which 10 ml *O. baccatus* leaf extract was added to obtain a mixture solution in a round-bottom flask and then put into a domestic microwave oven. Microwave irradiation proceeded at 100% power for 20 min. After microwave processing, the solution was cooled to room temperature. The resulting precipitate was separated by centrifugation, then washed with deionized water and absolute ethanol several times, and dried in an oven at 80°C for 24 h. Finally, the product was calcined at 800°C for 2 h [24].

2.4. UV-Visible Spectroscopy. The UV-visible spectral analysis was performed by using UV-Vis spectrophotometer (UV5704S from Electronics, India Ltd.) for surface plasmon resonance. The absorbance spectra was recorded in the range of 250–800 nm at room temperature in 1 cm path length

quartz cuvettes. Double distilled water was used as reference to correct the background absorption.

2.5. X-Ray Diffraction. The XRD of synthesized OB-ZnNPs nanoparticles were obtained using MiniFlex II benchtop XRD system (Rigaku Corporation, Tokyo, Japan). The diffraction pattern was acquired by CuK α radiation ($k = 1.54 \text{ \AA}$) at 30 mA current and operating at 40 kV. The angle of direction (2θ) data was recorded in the range of 20° – 80° . Average crystalline size was calculated by Debye-Scherrer's equation:

$$D = \frac{K\lambda}{\beta \cos \theta}, \quad (1)$$

where D is average crystal size of nanoparticle, β is full width at half maximum of the diffraction peak, λ is wavelength of X-ray source used (1.54060 \AA), and K is constant of Debye-Scherrer equation with value ranging from 0.9 to 1.0 [27].

2.6. Fourier Transform Infrared Spectroscopy (FTIR). The transmittance spectra recorded by placing the dried powder of ZnO nanoparticles to spectroscopic grade KBr (mass ratio of about 1 : 100). FTR analysis was performed on Perkin Elmer FT-IR spectrometer Spectrum Two (Perkin Elmer Life and Analytical Sciences, CT, USA) at 4 cm^{-1} resolutions in diffuse reflectance mode in KBr pellets.

2.7. Scanning Electron Microscopy and EDX. Scanning electron micrographs of ZnO nanoparticles were obtained using JSM 6510LV scanning electron microscope (JEOL, Tokyo, Japan) equipped with Oxford Instruments INCAx-sight EDAX spectrometer to carry out analysis of constituting elements. The electron beams were accelerated at 15 kV. Images were obtained at 2500–35000x magnification.

2.8. Transmission Electron Microscopy (TEM). Transmission electron microscopy was done using EOL 100/120 kV TEM (JEOL, Tokyo, Japan). Aqueous suspension of ZnO nanoparticles was made in double distilled water followed by sonication at 30% amplitude for 15 min. About $10 \mu\text{l}$ of the suspension was transferred to TEM grid for analysis and excess amount of suspension was removed by soft filter paper. The grid was then allowed to dry at 80° for 6 h. Imaging was done at 200 kV in the magnification range of 300000–100000x magnification.

2.9. Determination of Minimal Inhibitory Concentration (MIC) of OB-ZnNPs. The MIC of OB-ZnNPs against each test pathogen was determined by the method of Clinical and Laboratory Standards Institute, USA with some modifications [28].

2.10. Violacein Inhibition Assay. Violacein production by *C. violaceum* (CV12472) in presence of OB-ZnNPs was studied using method of Blosser and Gray [29]. Briefly, CV12472 culture in the absence and presence of sub-MICs of OB-ZnNPs was grown overnight. 1 ml culture from each flask was centrifuged at $13000 \times g$ for 10 min and the pellet was

dissolved in 1 ml DMSO. The solution was vortexed vigorously for 30 seconds to completely solubilize violacein and again centrifuged. Absorbance of the soluble violacein was read at 585 nm using microplate reader (Thermo Scientific, Multiskan Ex, India). Reduction in violacein production in the presence of mango extracts was measured in terms of % inhibition as $[(\text{OD of control} - \text{OD of treated})/\text{OD of control}] \times 100$.

2.11. Alginate Inhibition in PAOI. Overnight culture of *P. aeruginosa* (1%) was added to Luria-Bertani broth medium supplemented with or without OB-ZnNPs (25 – $200 \mu\text{g/ml}$) and incubated overnight at 37°C under shaking. After incubation alginate production was estimated as described by Gopu et al. [30]. Briefly, $70 \mu\text{l}$ of test sample was mixed with $600 \mu\text{l}$ of boric acid-sulphuric acid solution (4 : 1) in an ice bath. The mixture was vortexed for 10 seconds and placed back again in ice bath. $20 \mu\text{l}$ of 0.2% carbazole dissolved in ethanol was added to the above mixture and vortexed for 10 s. The mixture was incubated for 30 min at 55°C and quantification was done at 530 nm using a microplate reader.

2.12. Prodigiosin Inhibition in *S. marcescens*. Prodigiosin production in *S. marcescens* was assayed using the method of Morohoshi et al. [31]. Briefly, 1% of *S. marcescens* cells (0.4 OD at 600 nm) were inoculated into 2 ml of fresh LB medium and incubated with and without sub-MICs of OB-ZnNPs (25 – $100 \mu\text{g/ml}$). Late stationary phase cultures were collected and centrifuged at 10,000 rpm for 10 min. Prodigiosin from the cell pellet was extracted with acidified ethanol solution (4% 1 M HCl in ethanol) and absorbance was read at 534 nm using a UV-visible spectrophotometer.

2.13. Swarming Motility Assay. Swarming motility of the test pathogens was determined by the method of Husain and Ahmad [32]. Briefly, overnight cultures of test pathogens were point inoculated at the center of the 0.5% Luria-Bertani agar medium with or without sub-MICs of synthesized OB-ZnNPs.

2.14. Extraction and Quantification of Exopolysaccharide (EPS). Test pathogens (*P. aeruginosa*, *E. coli*, *L. monocytogenes*, *S. marcescens*, and *C. violaceum*) grown in the presence and absence of sub-MICs of OB-ZnNPs were centrifuged and supernatant was filtered. Three volumes of chilled ethanol (100%) were added to the resultant supernatant and incubated overnight at 4°C to precipitate EPS [33]. EPS was then quantified by measuring sugars following the method of Dubois et al. [34].

2.15. Assay for Biofilm Inhibition. Polyvinyl chloride microtiter plate assay was adopted to study the effect of OB-ZnNPs on biofilm formation of the test pathogens [35]. Briefly, overnight cultures of test pathogens were resuspended in fresh LB medium in the presence and the absence of OB-ZnNPs and incubated at 30°C for 24 h. The biofilms in the microtiter plates were stained with a crystal violet solution

and quantified by solubilizing the dye in ethanol and measuring the absorbance at OD₄₇₀.

2.16. Protein (HSA) Binding Studies with OB-ZnNPs

2.16.1. Binding of OB-ZnNPs to Human Serum Albumin: Tryptophan Fluorescence Analysis. Tryptophan fluorescence analysis of HSA in the absence and presence of NPs was measured according to previously mentioned procedure [36, 37] with minor modifications. Briefly, intrinsic fluorescence measurement of HSA (2 μ M) was performed by titration with NPs (0–1 mg/ml) on a Jasco FP-750 fluorescence spectrophotometer at 25°C. The excitation wavelength was set as 295 nm and the emission spectra obtained were in the wavelength range of 300–400 nm. The excitation and emission slit widths were set as 5 nm. Respective blanks were subtracted; inner filter contribution was minimal and was less than 3%.

2.16.2. Stability of HSA in the Presence of NPs: Circular Dichroism Analysis. NPs induced secondary structural changes in HSA were measured by circular dichroism (CD) spectroscopy technique. Far UV-CD spectra of HSA (0.2 mg/ml) in the absence and presence of various concentrations of NPs (0.4 and 1 mg/ml) were recorded [38]. The samples were scanned from 200 to 250 nm three times, and the obtained data was averaged.

2.16.3. Nanoparticles-HSA Interaction: Hydrophobicity Measurement. 8-Anilinoanthracene-1-sulfonic acid (ANS) is a frequently used extrinsic fluorophore having the propensity to interact with the exposed hydrophobic patches and is used for the determination of surface hydrophobicity in proteins. ANS fluorescence measurement of HSA (2 μ M) incubated in the absence and presence of NPs (0–1 mg/ml) was performed on Jasco FP-750 spectrofluorometer. The excitation wavelength for ANS fluorescence measurements was set at 380 nm and emission spectra were recorded in the wavelength range of 400–600 nm. Both excitation and emission slits were set at 5 nm. Prior to measurements, aliquots were incubated at room temperature with 50-fold molar excess of ANS for 30 min in the dark [39].

2.17. Toxicity Studies

2.17.1. Animal Treatment Strategy. Twenty-four adult Swiss albino male adult mice (48–50 g, 6 months old) were bought from the central animal house, Department of Pharmacy, King Saud University, Riyadh, KSA. They were kept and treated under hygienic conditions maintained with 25 \pm 5°C with 12 h day : night cycle as per the institutional guidelines. The animals were acclimatized for 10 days before beginning the treatment on standard pellet mice diet and fresh drinking water ad libitum. All the animals were randomly divided into four groups: control (normal without any treatment) named CN–, control positive (CN+), and CCl₄ treated (single dose of 1 mL/kg in liquid paraffin in ratio of 1:1 by volume). The zinc nanoparticles were administered four times (once a week) at the dose of 2 mg/kg and 4 mg/kg of body weight

denoted by OB-ZnNPs and OB-ZnNPs', respectively. All the doses were given by intraperitoneal mode using 1 ml insulin syringe. Carbon tetrachloride (CCl₄), an established hepatotoxicant, was chosen as positive control for liver damage [40]. In the present study, dose and the duration of treatment were chosen to investigate if the nanoparticles induced any toxicity in the animals after repeated dose or not. After the treatment, all the animals were sacrificed on the same day under light ether anesthesia. Their livers and blood (with anticoagulant) were stored at –20°C until analysis.

2.17.2. Preparation of Samples. The serum was collected after centrifugation of blood samples at 1000 \times g for 10 min. The liver samples were homogenized separately at 3000 \times g in tris-HCl buffer (pH 7.36, 0.1 M) from which their supernatants were collected for biochemical assays and estimations.

2.17.3. Assay of Superoxide Dismutase (SOD) and Reduced Glutathione (GSH). The specific activity of SOD was assayed by autoxidation of pyrogallol in tris-succinate buffer by the method of S. Marklund and G. Marklund [41]. The level of GSH was estimated by method of Jollow et al. [42] based on DTNB reagent.

2.17.4. Estimation of Lipid Peroxidation. The lipid peroxidation was estimated by the method of Buege and Aust [43] involving the measurement of total malondialdehyde (MDA) based on reaction with TCA and TBA.

Estimation of SGOT and SGPT as Liver Function Markers. The activity of serum glutamate pyruvate transferase (SGPT) and serum glutamate oxaloacetate transferase (GOT) in the serum was assayed by commercially available estimation kits (Linear or QCA, Spain).

2.18. Statistical Analysis. All microbiological studies were performed in triplicate and the data obtained from experiments were presented, as mean values, and the difference between control and test was analysed using Student's *t*-test. All the data for the toxicity studies have been expressed as mean \pm standard error of mean (SEM) for 6 different preparations in duplicate. Their statistical significance was evaluated by one-way ANOVA followed by Tuckey's method based software (Graph Pad prism 5). The treatment and the experiments were repeated twice to check the reproducibility of the results.

3. Results and Discussion

3.1. UV-Visible Spectral Analysis. The reducing ability of *Ochradenus baccatus* aqueous extract was evaluated for the synthesis of Zn nanoparticles. The UV-visible spectra of microwave assisted synthesis of ZnO nanoparticles are shown in Figure 1(a). The colour of reaction mixture, that is, 10 ml of *Ochradenus baccatus* aqueous extract and 100 ml of 0.05 mM zinc nitrate, was initially yellowish brown. When the reaction mixture was allowed for radiation in microwave for 20 min at 100% power, the colour of solution changed to off-white.

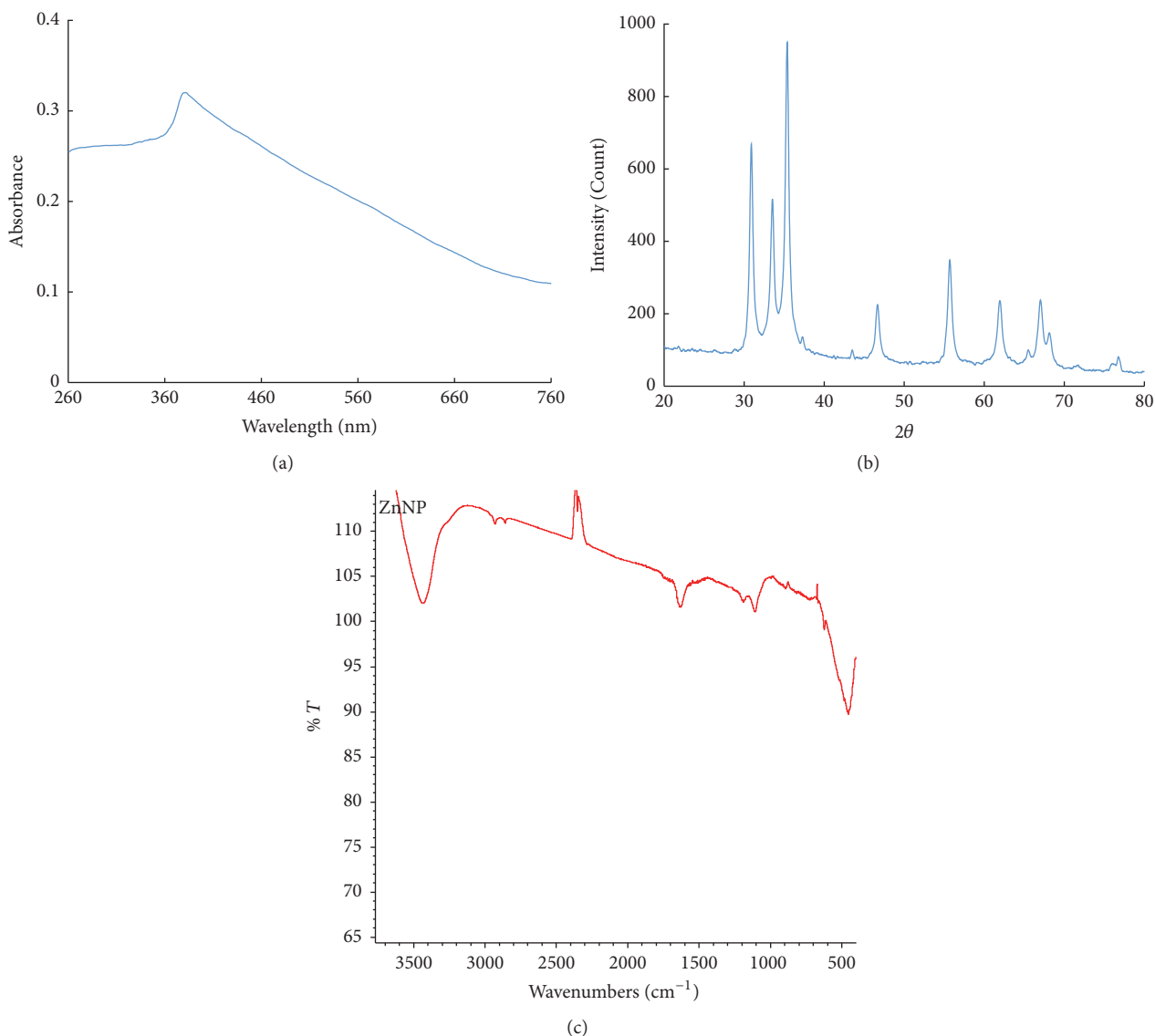


FIGURE 1: (a) UV-Vis absorption spectrum of ZnO nanoparticles *Ochradenus baccatus* leaf extract; (b) XRD patterns of ZnO nanoparticles using *Ochradenus baccatus* leaf extract; (c) FT-IR spectrum of synthesized ZnO nanoparticles.

Change in colour and absorption spectra with λ_{\max} at 385 nm is considered as the preliminary characterization for synthesis of ZnO nanoparticles which is due to the reduction of Zn^{2+} ions. Similar result has been reported for synthesis of ZnO nanoparticles with characteristic peak around 372 nm [44]. ZnO nanoparticles synthesized for the leaf extract of *Aloe barbadensis* showed the absorption maxima in the range of 358–375, due to surface plasmon resonance [22].

3.2. X-Ray Diffraction. The XRD analysis was carried out for the determination of average particle of ZnO nanoparticles. Figure 1(b) shows the XRD pattern of synthesized ZnO nanoparticles. XRD profile shows that the Bragg reflection was found to be prominent at 2θ values of 30.8° , 33.5° , and 35.3° with intensity of 668.4, 516.6, and 950.7. The full-width-at-half-maximum (FWHM) value at 35.3° was used for

particle's size calculation. The average particle size was found to be 16.02 nm which was determined using Debye-Scherrer's equation.

3.3. Fourier Transform Infrared Spectroscopy (FTIR). FTIR analysis was carried out to evaluate the presence of various phytochemicals responsible for the synthesis as well as stabilization of ZnO nanoparticles (Figure 1(c)). The appearance of peak around 521 cm^{-1} is characteristic of hexagonal phase vibrations of ZnO nanoparticles [4]. Broad peak approximately at 3441 cm^{-1} is attributed to the vibrations of -OH group of phenols that might have acted as one of the capping agents of ZnO nanoparticles [5]. Another transmittance maxima around 1652 cm^{-1} were due to vibrations of primary amide of proteins. A short peak at 1085 cm^{-1} might be due to stretching of primary alcohols $\{\text{R}-\text{CH}_2-\text{OH} (1^\circ)\}$. Thus, FTIR

TABLE 1: Minimum inhibitory concentrations (MICs) of OB-ZnNPs against test pathogens.

| Strains | MIC of OB-ZnNPs ($\mu\text{g/ml}$) | Sub-MICs of OB-ZnNPs selected for assays ($\mu\text{g/ml}$) | | | |
|-------------------------|--------------------------------------|---|-------------------------|-------------------------|-------------------------|
| | | $1/16 \times \text{MIC}$ | $1/8 \times \text{MIC}$ | $1/4 \times \text{MIC}$ | $1/2 \times \text{MIC}$ |
| <i>P. aeruginosa</i> | 400 | 25 | 50 | 100 | 200 |
| <i>E. coli</i> | 50 | 3.125 | 6.25 | 12.5 | 25 |
| <i>C. violaceum</i> | 200 | 12.5 | 25 | 50 | 100 |
| <i>K. pneumoniae</i> | 200 | 12.5 | 25 | 50 | 100 |
| <i>S. marcescens</i> | 100 | 6.25 | 12.5 | 25 | 50 |
| <i>L. monocytogenes</i> | 100 | 6.25 | 12.5 | 25 | 50 |

analysis indicates that various phytoconstituents present in *Ochradenus baccatus* extract such as phenols, enzymes, proteins, and alcohols would have been responsible for synthesis and stabilization of ZnO nanoparticles. The capping of ZnO nanoparticles by these phytochemicals resulted in formation of protein corona that enhances its dispersibility and ultimately lowers the agglomeration rate in aqueous medium. In addition to the above-mentioned phytochemicals, free amino and carboxylic groups have also been reported for their role in the stabilization of ZnO nanoparticles [22].

3.4. SEM and EDX Analysis. Scanning electron microscopy is one of the most routinely used techniques for the identification of shape of nanoparticles. Figures 2(a) and 2(b) show the scanning electron micrograph (SEM) of ZnO nanoparticles at 15000x and 35000x magnifications at 15 and 20 kV, respectively. It is evident from the surface scanning that the nanoparticles were predominantly found to be spherical and oval in shape. Although the particle size is not determined by SEM but it can be visualized that the nanoparticles are <100 nm. Figure 2(c) shows EDX pattern in which the highest elemental weight percent detected was of zinc with 62.0%. From Figure 2(d), oxygen, carbon, and sulphur were found to be 13.47, 23.37, and 1.16%, respectively. Nanoparticles with similar morphology from *Aloe barbadensis* [22] and *Nigella sativa* [24] have been reported.

3.5. Transmission Electron Microscopy. TEM images of ZnO nanoparticles are illustrated in Figure 2(e) at 30000x and 100000x magnification, respectively. The nanoparticle's micrograph shows that there was variation in shape and size of nanoparticles. The two-dimensional geometry of nanoparticles was found to be circular, elliptical, and somewhat hexagonal or irregular. The particles size is less than 50 nm and is consistent with the results of XRD.

3.6. Minimum Inhibitory Concentration. Minimum inhibitory concentrations (MIC) of OB-ZnNPs were assessed for all test pathogens and the results are summarized in Table 1. Concentrations below MIC, that is, sub-MICs, were considered for all assays.

3.7. Violacein Inhibition Assay in *C. violaceum* 12472. The result of the violacein assay is shown in Figure 3(a). The sub-MICs of OB-ZnNPs exhibited concentration-dependent

inhibitory activity and all tested concentrations of OB-ZnNPs led to a statistically significant ($p \leq 0.05$) reduction in violacein production of *C. violaceum* compared to that of the untreated control. Our findings on violacein inhibition are in accordance with reports with silver nanowires [45] and zinc oxide nanostructures synthesized from the seed extract of *Nigella sativa* [24].

3.8. Inhibition of Alginate Production in *P. aeruginosa* PAO1. Alginate is a major constituent of the EPS of PAO1 biofilm; the effect of sub-MICs of OB-ZnNPs was studied for its efficacy to reduce the production of alginate. The obtained results showed that the alginate production was reduced significantly with increasing concentration of the synthesized zinc nanoparticles. At concentrations ranging 25–200 $\mu\text{g/ml}$, OB-ZnNPs inhibited alginate production by 34–74% in PAO1 (Figure 3(b)). The concentration-dependent inhibition of alginate by sub-MICs of OB-ZnNPs depicted in Figure 3(b) is an important finding as alginate confers resistance to the pathogens against antimicrobial agents. Inhibition of alginate production would reduce the rate of resistance among bacteria and make them susceptible to the drugs. Previously, mycofabricated biosilver nanoparticles have been shown to inhibit alginate production in *P. aeruginosa* [46].

3.9. Effect on Prodigiosin Production of *S. marcescens*. Dose-dependent decrease in the production of prodigiosin by *S. marcescens* was recorded at the sub-MICs ranging from 6.25–50 $\mu\text{g/ml}$. Though the inhibition was statistically insignificant at lower concentrations (6.25 and 12.5 $\mu\text{g/ml}$) but at higher concentrations, that is, 25 and 50 $\mu\text{g/ml}$ significant ($p \leq 0.05$) reduction of 55 and 60%, respectively, was recorded (Figure 3(c)). Prodigiosin is considered as a major virulence factor of the *S. marcescens* and is quorum sensing regulated [31]. Hence, inhibition of prodigiosin will reduce the pathogenicity of *S. marcescens*. Prodigiosin inhibition is previously reported with natural products [47] and bacterial supernatant [48] but this is probably the first report on zinc nanoparticle impairing prodigiosin production in *S. marcescens*.

3.10. Biofilm Inhibition by OB-ZnNPs. In the present study, subinhibitory concentrations ($1/16 \times \text{MIC}$ – $1/2 \times \text{MIC}$) of OB-ZnNPs were tested against biofilm formation of six human and foodborne bacterial pathogens, namely, *P. aeruginosa*

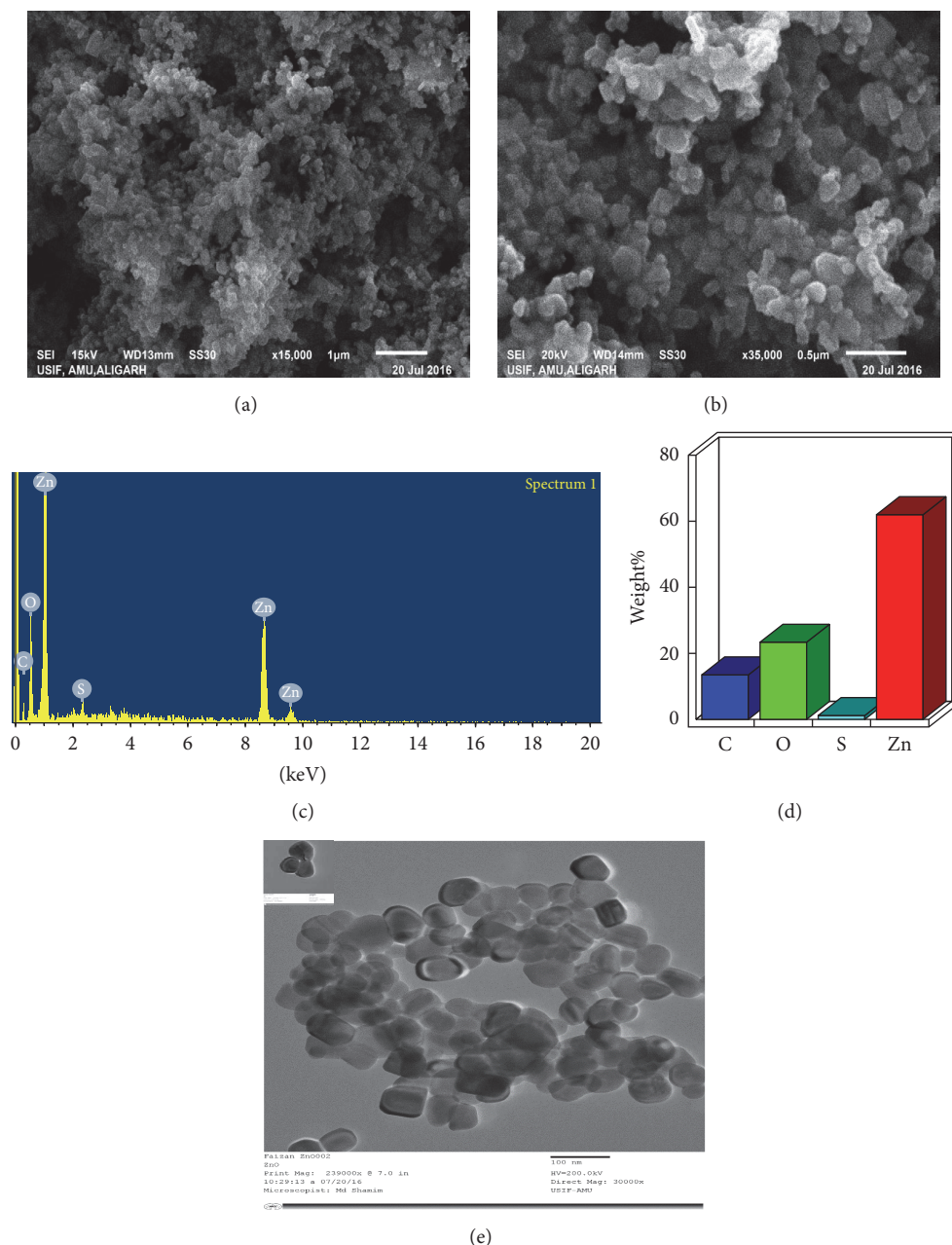


FIGURE 2: (a) and (b) show the SEM micrograph of ZnO nanoparticles at 15000x and 35000x magnifications, respectively; (c) and (d) show EDX pattern; (e) TEM micrograph of ZnO nanoparticles. Inset shows the corresponding HRTEM image of the synthesized nanoparticles.

PAO1, *E. coli* 25922, *L. monocytogenes*, *K. pneumoniae*, *S. marcescens*, and *C. violaceum* 12472. Figure 4 shows the representative micrographs indicating that OB-ZnNPs inhibit biofilm formation in all the test pathogens in a dose-dependent manner. The data revealed 32, 52, 68, and 84% inhibition of biofilm in *P. aeruginosa* PAO1; 18, 28, 49, and 67% in *E. coli* 25922; 28, 41, 63, and 78% in *L. monocytogenes*; 16, 30, 52, and 70% in *K. pneumoniae*; 39, 57, 69, and 80% in *S. marcescens*; and 24, 38, 54, and 64% in *C. violaceum* 12472, as compared to untreated control (Figure 4).

Formation of biofilm not only plays an important role in the pathogenesis but also is responsible for food contamination

and spoilage. Biofilm development is often regulated by signal-mediated quorum sensing phenomenon [49]. Cells residing in biofilm are more than 1000 times more resistant to their planktonic forms. Therefore, biofilm poses a great threat to the current drug therapy. The result of biofilm biomass assay in the current investigation indicated reduced production of biofilm biomass in test pathogens when treated with OB-ZnNPs (Figure 4). Our results are agreement with previously published report of Kalishwaralal et al. [50], wherein biologically synthesized Ag nanoparticle (NPs) showed an antibiofilm activity against *P. aeruginosa* and *S. epidermidis*. In an another study, Al-Shabib et al. [24]

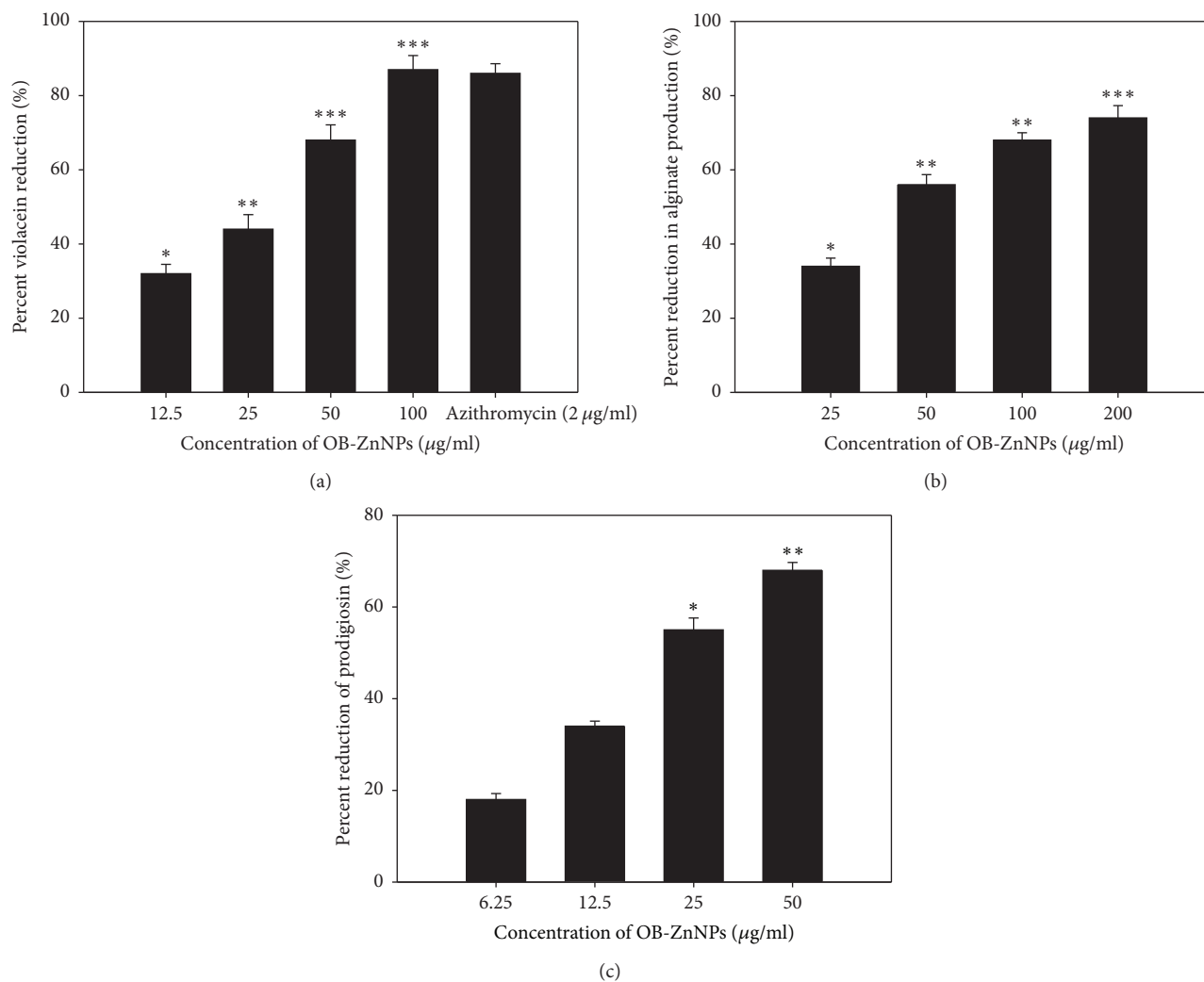


FIGURE 3: Quantitative assessment of virulence factors in test pathogens at sub-MICs. (a) Violacein inhibition in CV12472 by sub-MICs of OB-ZnNPs; (b) reduction in alginate production in *P. aeruginosa* PAO1; (c) reduction in prodigiosin production in *S. marcescens*. Data are represented as percentage of inhibition. All of the data are presented as mean \pm SD. *Significance at $p \leq 0.05$; **significance at $p \leq 0.005$; ***significance at $p \leq 0.001$.

demonstrated broad-spectrum biofilm inhibition in *P. aeruginosa* PAO1, *E. coli* 25922, *L. monocytogenes*, and *C. violaceum* 12472 after treatment with sublethal doses of zinc nanostructures synthesized from the seed extract of *Nigella sativa*.

3.11. Inhibition of EPS and Swarming Motility. Exopolysaccharides (EPS) maintain biofilm architecture and microcolony formation [51]. In addition, EPS acts as a protective barrier and confers resistance to pathogens by preventing the entry of antibiotics into bacterial cells [52]. Further, increased EPS secretion means increased resistance to antimicrobials due to altered biofilm architecture [53]. Hence, inhibition of EPS production will expose biofilms cells and thus help in the eradication of biofilm. Owing to this positive correlation between biofilm formation and EPS production, an attempt was made to assess the effect of OB-ZnNPs on EPS production by test pathogens. EPS extracted from OB-ZnNPs treated

and untreated cultures of test pathogens was spectrometrically analysed. EPS production in all pathogens decreased with increasing concentration of OB-ZnNPs (Figure 5(a)). OB-ZnNPs at highest sub-MICs of 200, 50, 100, 200, and 50 $\mu\text{g/ml}$ exhibited 81, 69, 67, 59, and 68% decrease in EPS production in *P. aeruginosa* PAO1, *E. coli*, *L. monocytogenes*, *K. pneumoniae*, and *S. marcescens*, respectively. At lower concentrations also, significant reduction in EPS production was recorded for all pathogens (Figure 5(a)). Hsueh et al. [54] have observed 92% reduced production of EPS by *P. aeruginosa* upon treatment with 100 ng/ml concentration of copper oxide nanoparticles. LewisOscar et al. [55] also reported significant reduction of EPS produced by zinc oxide nanoparticle treated *Bacillus subtilis* strains.

Swarming motility of bacteria is also considered to be an important virulence factor, as it helps to initiate the attachment of bacterial cells to the surface [56]. Therefore, any interference with the swarming motility is bound to effect

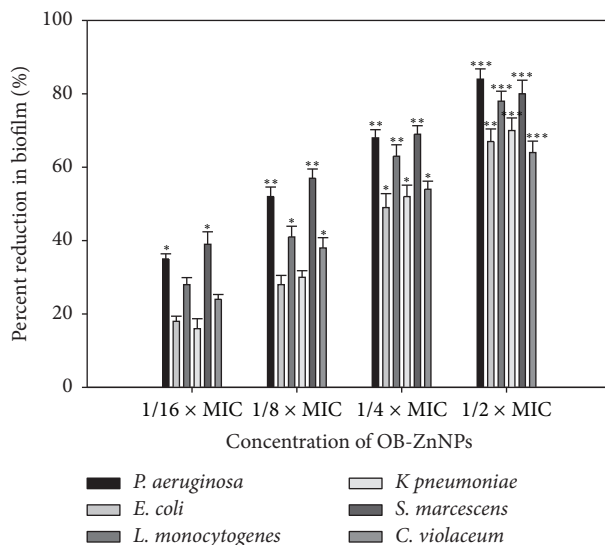


FIGURE 4: Quantitative measurement of biofilm inhibition as quantified by crystal violet staining. Data are represented as percentage of biofilm inhibition. All of the data are presented as mean \pm SD. *Significance at $p \leq 0.05$; **significance at $p \leq 0.005$; ***significance at $p \leq 0.001$.

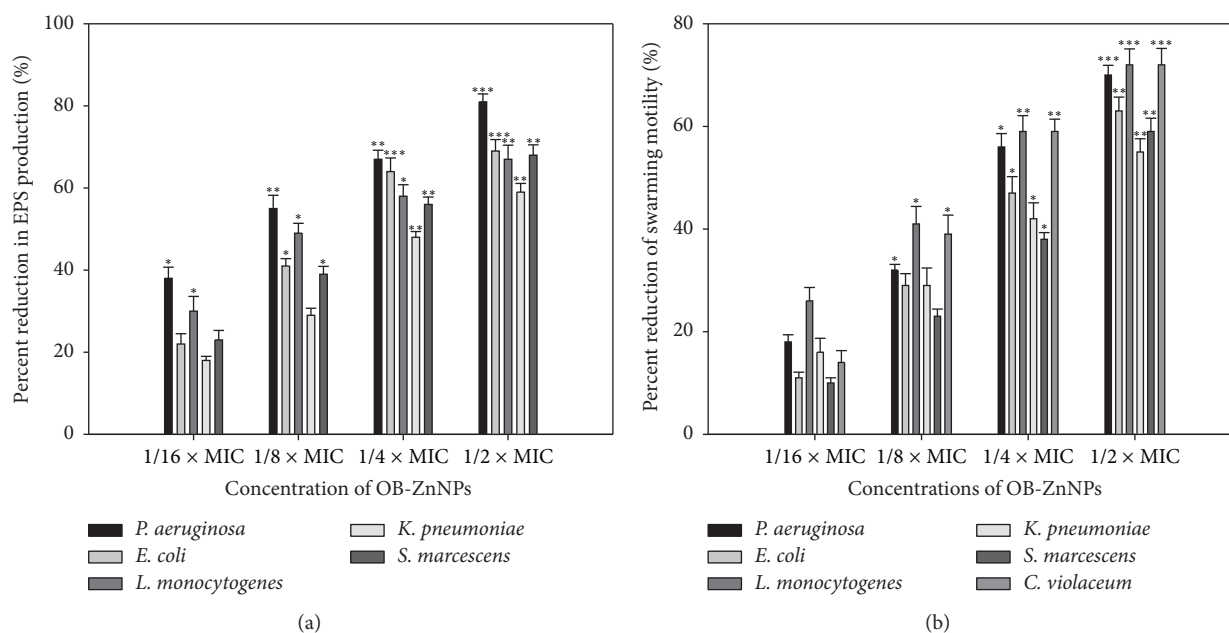


FIGURE 5: (a) Quantitative analysis of EPS inhibition by sub-MICs of OB-ZnNPs. (b) Inhibition of swarming motility of bacterial pathogens. Data are represented as percentage of inhibition over untreated control. All of the data are presented as mean \pm SD. *Significance at $p \leq 0.05$; **significance at $p \leq 0.005$; ***significance at $p \leq 0.001$.

the biofilm formation. The OB-ZnNPs induced reduction in swarming migration of *P. aeruginosa*, *E. coli*, *L. monocytogenes*, *K. pneumoniae*, *S. marcescens*, and *C. violaceum* is shown in Figure 5(b). The test pathogens, *P. aeruginosa*, *E. coli*, *L. monocytogenes*, *K. pneumoniae*, *S. marcescens*, and *C. violaceum* demonstrated 18–70%, 11–63%, 26–72%, 16–55%, 10–59%, and 14–72% reduction in swarming migration in presence of sub-MICs (1/16 \times MIC–1/2 \times MIC) of OB-ZnNPs (Figure S1). Results obtained in the present study are comparable to the decrease in swarming motility reported in recent studies for mycofabricated silver nanoparticles [46],

Ag nanoparticles synthesized from *Sargassum polyphyllum* [57], and green zinc oxide nanostructures [24].

3.12. HSA Binding Studies. The quenching in Trp fluorescence of HSA has been widely used to determine the mechanism by which a ligand interacts with HSA. In the present study, a progressive decrease in the fluorescence intensity (85%) of HSA upon NP binding was observed. The results suggested a perturbation in the microenvironment of Trp-214 which became less hydrophobic due to the binding of NP (Figure 6(a)).

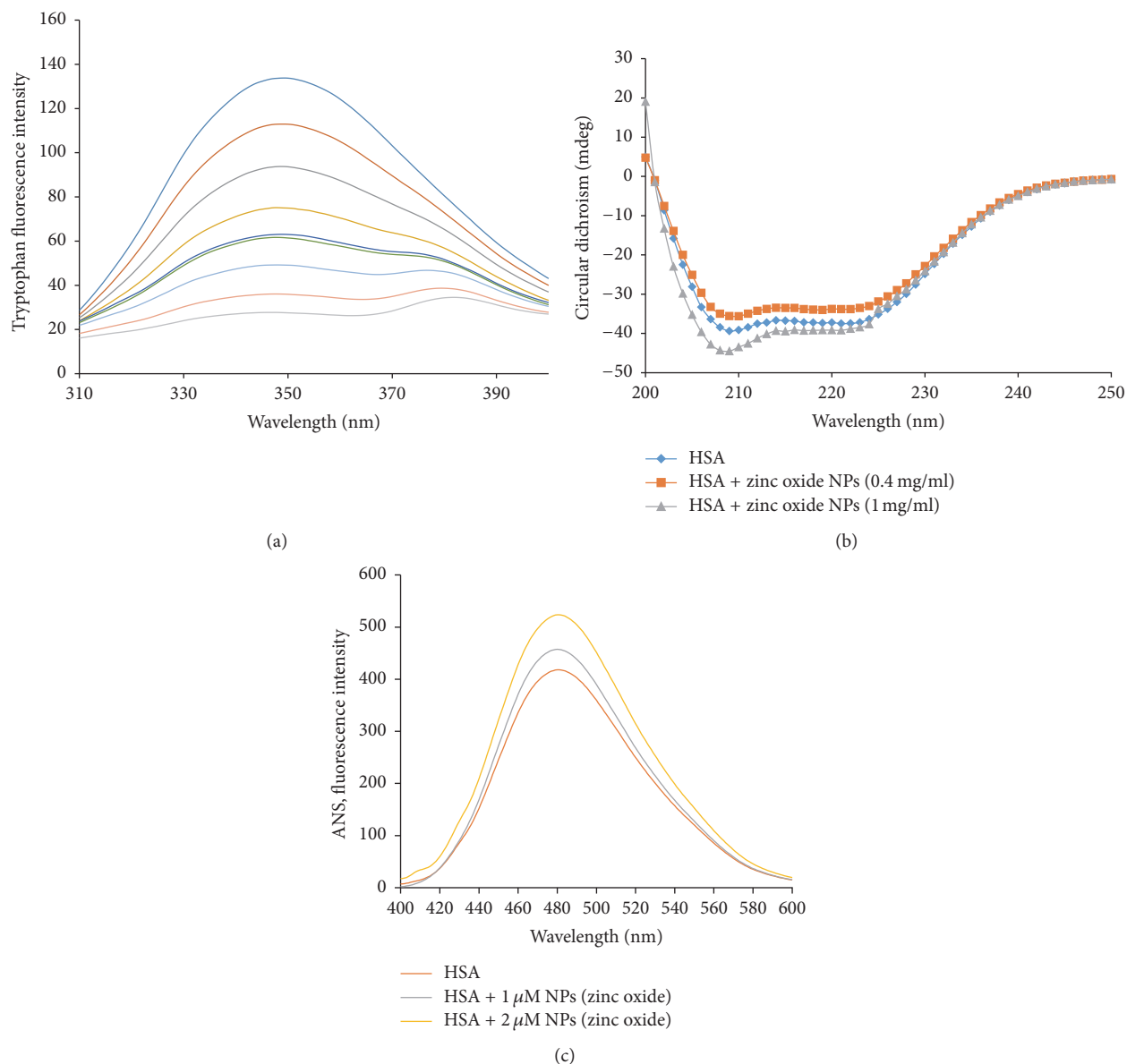


FIGURE 6: Binding studies of OB-ZnNPs with human serum albumin protein. (a) Tryptophan fluorescence analysis; (b) stability of HSA in the presence of NPs: circular dichroism analysis; (c) hydrophobicity measurement.

A change in far UV-CD spectra is generally followed to monitor any change in the secondary structure of the proteins. The far-UV spectra of HSA in the absence of OB-ZnNPs showed characteristic negative bands at 208 nm and 222 nm. Upon binding at 0.4 mg/ml concentration, a marginal decrease in the far-UV CD spectra of HSA was observed, suggesting a partial loss in the secondary structure of HSA. However, as the concentration of NP was increased to 1 mg/ml, the overall secondary structure of HSA also increased, thereby indicating a gain in the stability of the protein (Figure 6(b)). The imparted stability of the protein might be due to preferential exclusion of NPs from the surface of HSA. The results clearly suggested that the stability of secondary structure of HSA in the presence of OB-ZnNPs is concentration-dependent.

ANS dye is commonly used to map the hydrophobic patches of a protein exposed to the solvent. The results indicate that OB-ZnNPs binding to HSA induced a marginal decrease in the overall hydrophobicity of the protein (Figure 6(c)). These results are in good agreement with the results of Trp fluorescence which suggested that the microenvironment of Trp-214 became less hydrophobic upon NP binding.

3.13. In Vivo Toxicity Studies

3.13.1. Effect on Liver Function Tests (LFT). SGOT and SGPT are chief markers for toxic burden on liver. In the present study, SGOT was found elevated by 119.42% in the positive control (CCl₄ treated animals) as compared to the control. However, OB-ZnNPs and OB-ZnNPs' groups showed

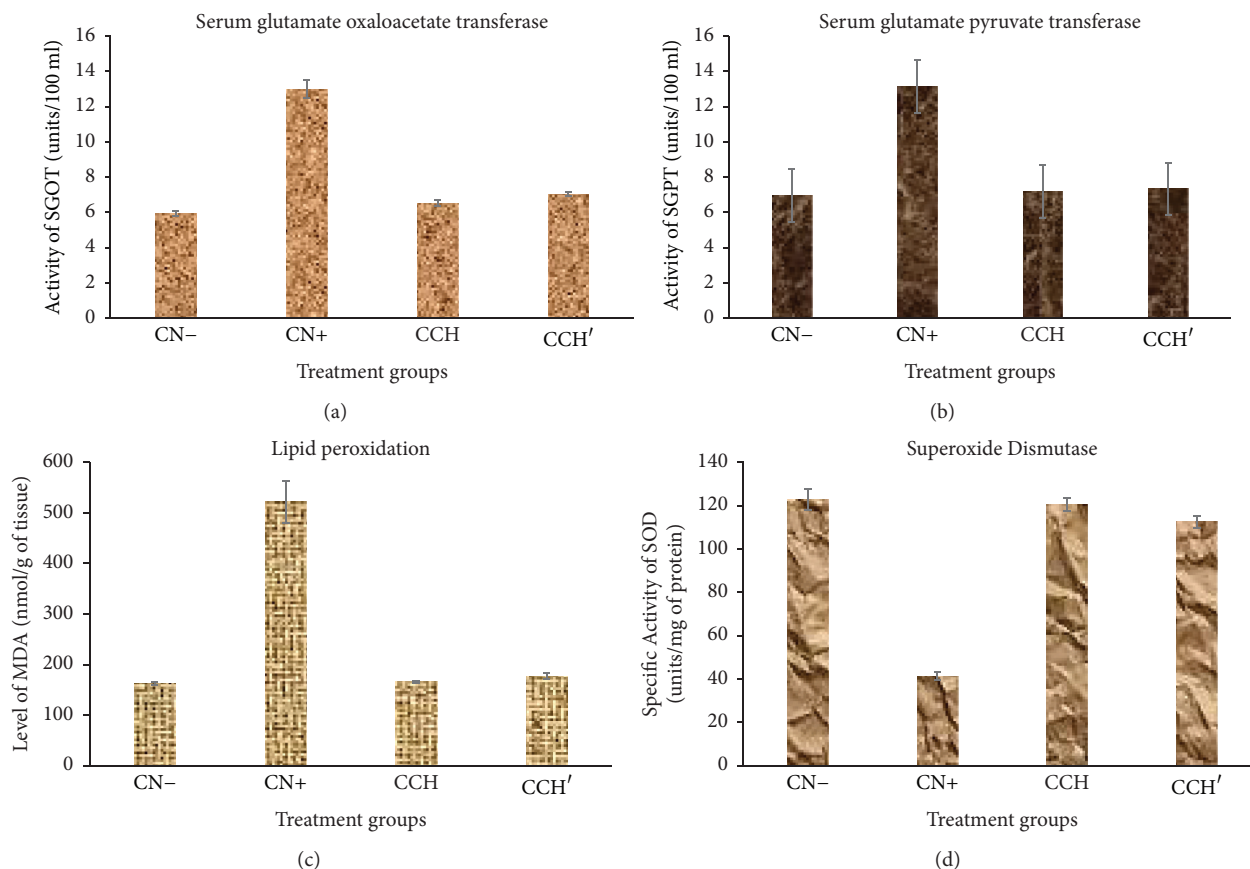


FIGURE 7: *In vivo* toxicity studies with OB-ZnNPs. (a, b) Effect on liver function tests (LFT), serum glutamate pyruvate transferase (SGPT), and serum glutamate oxaloacetate transferase (GOT) assay; (c) effect on MDA levels; (d) effect on antioxidant parameters.

increase in its activity by 10.14% and 18.91% with respect to the control (Figure 7(a)).

SGPT activity enhanced in CN+ by 89.46% while it increased in OB-ZnNPs and OB-ZnNPs' groups by 3.32% and 5.62% and this is statistically insignificant as compared to the control (Figure 7(b)).

3.13.2. Effect on MDA Levels. The CN+ group demonstrated elevation in MDA level by staggering 221.35% while OB-ZnNPs and OB-ZnNPs' showed merely 2.2% and 9.15% increase as compared to the control, CN-, group (Figure 7(c)).

3.13.3. Effect on Antioxidant Parameters. In the present study, SOD and GSH were chosen as antioxidant markers to assess stress level in the animals after the treatment with test nanoparticles. The CN+ group showed compromise by 66.35% and 64.34% in the activity of SOD and the level of GSH, respectively. OB-ZnNPs and OB-ZnNPs' groups exhibited decrease in SOD activity by 1.80% and 8.30% while GSH levels declined by 7.60% and 15.12% as compared to the control. This reduction was found to be statistically insignificant (Figure 7(d)).

In the present study, we were interested to know if the newly synthesized zinc oxide nanoparticles pose any toxic insults *in vivo* or to check its suitability for usage as drug

or drug adjuvant. For this we chose CCl_4 as positive control which is an established hepatotoxicant in many previous investigations [58, 59]. From the *in vivo* results, it is evident that CCl_4 caused severe toxicity in the parameters to assess liver health status based on significantly enhanced LFTs and MDA level concomitant with highly compromised activity of SOD and GSH. As compared to CCl_4 , both experimental groups, OB-ZnNPs and OB-ZnNPs', showed minor toxicity *in vivo* (Figure S2).

LFTs and MDA levels in the OB-ZnNPs and OB-ZnNPs' groups were slightly elevated while GSH level and SOD activity were quite comparable to the control (CN-). However, the minor toxicity was observed in OB-ZnNPs' group as the dose of nanoparticles was higher than that in OB-ZnNPs group. Interestingly, OB-ZnNPs group showed all the toxicity assessing parameters quite comparable to CN-. It entails that the dose of 2 mg/kg of the nanoparticles is well tolerated in the rodent system. It also suggests that the particles at this dose can be used as adjuvant with established or new drugs.

It is well established that zinc is an important trace element for all biological systems as it is involved in various biochemical and metabolic functions including copper zinc superoxide dismutase, digestion and absorption of food, hormonal homeostasis, immunity, general growth, and development [40, 60]. In the present work, it seems that the green synthesized nanoparticles improve SOD activity and assist in

absorption and digestion of the food in the treated animals. That might also improve the GSH level. Our study is well supported by earlier work done by Choi et al. [61] who showed that the zinc nanoparticles are quite tolerable at higher doses in animals. These particles hence possessed no serious toxic effect at the dose 2 mg/kg and can be used in further animal model studies for the improvement of established drugs. However, further studies are required to know the exact mechanism of action of these particles.

The findings of the current investigation highlight the broad-spectrum antibiofilm and antivirulence properties of synthesized OB-ZnNPs against human and food-borne bacterial pathogens. Efficient binding with HSA protein without changing the structure and stability augurs well for future use. Moreover, the nontoxic nature of these biofilm inhibiting nanoparticles present a possibility for use as potential nanomaterials to combat drug resistant bacterial infections and prevent contamination/spoilage of food. Exact molecular mechanism of action for these nanoparticles still needs to be unearthed.

Conflicts of Interest

The authors declare that they have no conflicts of interest.

Authors' Contributions

Nasser A. Al-Shabib and Fohad Mabood Husain contributed equally to this work.

Acknowledgments

The authors wish to acknowledge the Agricultural Research Centre, College of Food and Agricultural Sciences, and the Deanship of Scientific Research, King Saud University, Riyadh, Saudi Arabia, for funding this research.

Supplementary Materials

Supplementary material for this article includes figures for swarming motility inhibition and histopathology studies. Following is the description of the figures, FIGURE S1: effect of OB-ZnNPs on swarming motility of food pathogens. (A–F) Untreated strains and (e–h) OB-ZnNPs treated ($1/2 \times \text{MIC}$) plates of *C. violaceum*, *E. coli*, *L. monocytogenes*, *P. aeruginosa*, *K. pneumoniae*, and *S. marcescens*, respectively. FIGURE S2: histopathological slides of various groups. A: control showing normal microstructures of the liver with well-maintained contour, hepatocytes with normal sinusoids. B: CCl_4 treated group showing disturbed microanatomy of the liver including blurred cells with prominent cytoplasmic vacuolation. Enlargement of the cells is indicative of the necrosis. C and D: representative images of liver after dose-dependent treatment with OB-ZnNPs. Both show comparable microanatomy to the control. Slight distortion is observed in image D that might be due to the usage of higher dose of nanoparticles. (*Supplementary Materials*)

References

- [1] J. W. Costerton, K. J. Cheng, G. G. Geesey et al., "Bacterial biofilms in nature and disease," *Annual Review of Microbiology*, vol. 41, pp. 435–464, 1987.
- [2] L. Hall-Stoodley, J. W. Costerton, and P. Stoodley, "Bacterial biofilms: from the natural environment to infectious diseases," *Nature Reviews Microbiology*, vol. 2, no. 2, pp. 95–108, 2004.
- [3] R. L. E. Castrillón, R. A. Palma, and D. M. C. Padilla, "Interferencia de las biopelículas en el proceso de curación de heridas," *Dermatología Rev Mex*, vol. 55, pp. 127–139, 2011.
- [4] R. M. Donlan and J. W. Costerton, "Biofilms: survival mechanisms of clinically relevant microorganisms," *Clinical Microbiology Reviews*, vol. 15, no. 2, pp. 167–193, 2002.
- [5] H.-C. Flemming and H. Ridgway, "Biofilm control: conventional and alternative approaches," *Marine and Industrial Biofouling*, vol. 4, pp. 103–117, 2009.
- [6] M. N. Shikongo-Nambabi, A. Shoolongela, and M. Schneider, "Control of bacterial contamination during marine fish processing," *Journal of Biology and Life Science*, vol. 3, no. 1, pp. 1–17, 2011.
- [7] R. A. N. Chmielewski and J. F. Frank, "Inactivation of *Listeria monocytogenes* biofilms using chemical sanitizers and heat," in *Biofilms in The Food Environment*, H. P. Blaschek, H. H. Wang, and M. E. Agle, Eds., pp. 73–104, Blackwell Publishing, Ames, Iowa, USA, 2007.
- [8] J. Harvey, K. P. Keenan, and A. Gilmour, "Assessing biofilm formation by *Listeria monocytogenes* strains," *Food Microbiology*, vol. 24, no. 4, pp. 380–392, 2007.
- [9] J. N. Sofos and I. Geornaras, "Overview of current meat hygiene and safety risks and summary of recent studies on biofilms, and control of *Escherichia coli* O157:H7 in nonintact, and *Listeria monocytogenes* in ready-to-eat, meat products," *Meat Science*, vol. 86, no. 1, pp. 2–14, 2010.
- [10] U. Desselberger, "Emerging and re-emerging infectious diseases," *Infection*, vol. 40, no. 1, pp. 3–15, 2000.
- [11] R. P. Allaker, "The use of nanoparticles to control oral biofilm formation," *Journal of Dental Research*, vol. 89, no. 11, pp. 1175–1186, 2010.
- [12] J. R. Morones, J. L. Elechiguerra, A. Camacho et al., "The bactericidal effect of silver nanoparticles," *Nanotechnology*, vol. 16, no. 10, pp. 2346–2353, 2005.
- [13] J. Sawai, "Quantitative evaluation of antibacterial activities of metallic oxide powders (ZnO, MgO and CaO) by conductimetric assay," *Journal of Microbiological Methods*, vol. 54, no. 2, pp. 177–182, 2003.
- [14] I. Sondi and B. Salopek-Sondi, "Silver nanoparticles as antimicrobial agent: a case study on *E. coli* as a model for gram-negative bacteria," *Journal of Colloid and Interface Science*, vol. 275, no. 1, pp. 177–182, 2004.
- [15] R. Brayner, R. Ferrari-Iliou, N. Brivois, S. Djediat, M. F. Benedetti, and F. Fievet, "Toxicological impact studies based on *Escherichia coli* bacteria in ultrafine ZnO nanoparticles colloidal medium," *Nano Letters*, vol. 6, no. 4, pp. 866–870, 2006.
- [16] O. Yamamoto, "Influence of particle size on the antibacterial activity of zinc oxide," *International Journal of Inorganic Materials*, vol. 3, no. 7, pp. 643–646, 2001.
- [17] E. Casals, T. Pfaller, A. Duschl, G. J. Oostingh, and V. Puntès, "Time evolution of the nanoparticle protein corona," *ACS Nano*, vol. 4, no. 7, pp. 3623–3632, 2010.

- [18] S. Laera, G. Ceccone, F. Rossi et al., "Measuring protein structure and stability of protein-nanoparticle systems with synchrotron radiation circular dichroism," *Nano Letters*, vol. 11, no. 10, pp. 4480–4484, 2011.
- [19] W. Shang, J. H. Nuffer, J. S. Dordick, and R. W. Siegel, "Unfolding of ribonuclease a on silica nanoparticle surfaces," *Nano Letters*, vol. 7, no. 7, pp. 1991–1995, 2007.
- [20] V. Kumar and S. K. Yadav, "Plant-mediated synthesis of silver and gold nanoparticles and their applications," *Journal of Chemical Technology and Biotechnology*, vol. 84, no. 2, pp. 151–157, 2009.
- [21] K. Jeeva, M. Thiyagarajan, V. Elangovan, N. Geetha, and P. Venkatachalam, "*Caesalpinia coriaria* leaf extracts mediated biosynthesis of metallic silver nanoparticles and their antibacterial activity against clinically isolated pathogens," *Industrial Crops and Products*, vol. 52, pp. 714–720, 2014.
- [22] G. Sangeetha, S. Rajeshwari, and R. Venkatesh, "Green synthesis of zinc oxide nanoparticles by *aloe barbadensis miller* leaf extract: structure and optical properties," *Materials Research Bulletin*, vol. 46, no. 12, pp. 2560–2566, 2011.
- [23] M. Sundrarajan, S. Ambika, and K. Bharathi, "Plant-extract mediated synthesis of ZnO nanoparticles using *Pongamia pinnata* and their activity against pathogenic bacteria," *Advanced Powder Technology*, vol. 26, no. 5, pp. 1294–1299, 2015.
- [24] N. A. Al-Shabib, F. M. Husain, F. Ahmed et al., "Biogenic synthesis of Zinc oxide nanostructures from *Nigella sativa* seed: prospective role as food packaging material inhibiting broad-spectrum quorum sensing and biofilm," *Scientific Reports*, vol. 6, article 36761, 2016.
- [25] F. A. Qurainy, M. Nadeem, S. Khan, S. Alansi, and M. Tarroum, "Efficient regeneration of a potential medicinal plant *Ochradeus baccatus* delile from cotyledon and shoot axis," *Pakistan Journal of Botany*, vol. 45, no. 2, pp. 501–505, 2013.
- [26] A. Hassan-Abdallah, A. Merito, S. Hassan et al., "Medicinal plants and their uses by the people in the Region of Randa, Djibouti," *Journal of Ethnopharmacology*, vol. 148, no. 2, pp. 701–713, 2013.
- [27] A. L. Patterson, "The scherrer formula for X-ray particle size determination," *Physical Review A: Atomic, Molecular and Optical Physics*, vol. 56, no. 10, pp. 978–982, 1939.
- [28] CLSI, *Performance Standards for Antimicrobial Susceptibility Testing: Seventeenth Informational Supplement: M100-S17*, Clinical and Laboratory Standards Institute, Wayne, Pa, USA, 2007.
- [29] R. S. Blosser and K. M. Gray, "Extraction of violacein from *Chromobacterium violaceum* provides a new quantitative bioassay for N-acyl-homoserine lactone autoinducers," *Journal of Microbiological Methods*, vol. 40, no. 1, pp. 47–55, 2000.
- [30] V. Gopu, C. K. Meena, P. H. Shetty, and Y. He, "Quercetin influences quorum sensing in food borne bacteria: in-vitro and in-silico evidence," *PLoS ONE*, vol. 10, no. 8, Article ID e0134684, 2015.
- [31] T. Morohoshi, T. Shiono, K. Takidouchi et al., "Inhibition of quorum sensing in *Serratia marcescens* AS-1 by synthetic analogs of N-acylhomoserine lactone," *Applied and Environmental Microbiology*, vol. 73, no. 20, pp. 6339–6344, 2007.
- [32] F. M. Husain and I. Ahmad, "Doxycycline interferes with quorum sensing-mediated virulence factors and biofilm formation in Gram-negative bacteria," *World Journal of Microbiology and Biotechnology*, vol. 29, no. 6, pp. 949–957, 2013.
- [33] A. L. Huston, B. Methé, and J. W. Deming, "Purification, characterization, and sequencing of an extracellular cold-active aminopeptidase produced by marine psychrophile *Cohwellia psychrerythraea* strain 34H," *Applied and Environmental Microbiology*, vol. 70, no. 6, pp. 3321–3328, 2004.
- [34] M. K. Dubois, J. K. Gils, P. A. Hanniton, and F. Smith, "Use of phenol reagent for the determination of total sugar," *Analytical Chemistry*, vol. 28, pp. 350–356, 1956.
- [35] G. A. O'Toole and R. Kolter, "Initiation of biofilm formation in *Pseudomonas fluorescens* WCS365 proceeds via multiple, convergent signalling pathways: a genetic analysis," *Molecular Microbiology*, vol. 28, no. 3, pp. 449–461, 1998.
- [36] R. Wahab, S. Dwivedi, M. S. Khan et al., "Optical analysis of zinc oxide quantum dots with bovine serum albumin and bovine hemoglobin," *Journal of Pharmaceutical Innovation*, vol. 9, no. 1, pp. 48–52, 2014.
- [37] M. T. Rehman, S. Ahmed, and A. U. Khan, "Interaction of meropenem with 'N' and 'B' isoforms of human serum albumin: a spectroscopic and molecular docking study," *Journal of Biomolecular Structure and Dynamics*, vol. 34, no. 9, pp. 1849–1864, 2016.
- [38] M. T. Rehman, H. Shamsi, and A. U. Khan, "Insight into the binding mechanism of imipenem to human serum albumin by spectroscopic and computational approaches," *Molecular Pharmaceutics*, vol. 11, no. 6, pp. 1785–1797, 2014.
- [39] R. P. Honda, K.-I. Yamaguchi, and K. Kuwata, "Acid-induced molten globule state of a prion protein: Crucial role of strand 1-Helix 1-Strand 2 Segment," *The Journal of Biological Chemistry*, vol. 289, no. 44, pp. 30355–30363, 2014.
- [40] H. Ebaid, J. Al-Tamimi, I. Hassan, I. Alhazza, and M. Al-Khalifa, "Antioxidant bioactivity of samsum Ant (*Pachycondyla sennaarensis*) Venom protects against CCL₄-induced nephrotoxicity in mice," *Oxidative Medicine and Cellular Longevity*, vol. 2014, Article ID 763061, 2014.
- [41] S. Marklund and G. Marklund, "Involvement of the superoxide anion radical in the autoxidation of pyrogallol and a convenient assay for superoxide dismutase," *European Journal of Biochemistry*, vol. 47, no. 3, pp. 469–474, 1974.
- [42] D. J. Jollow, J. R. Mitchell, N. Zampaglione, and J. R. Gillette, "Bromobenzene induced liver necrosis. Protective role of glutathione and evidence for 3,4 bromobenzene oxide as the hepatotoxic metabolite," *Pharmacology*, vol. 11, no. 3, pp. 151–169, 1974.
- [43] J. A. Buege and S. D. Aust, "Microsomal lipid peroxidation," *Methods in Enzymology*, vol. 52, pp. 302–310, 1978.
- [44] S. Nagarajan and K. Arumugam Kuppasamy, "Extracellular synthesis of zinc oxide nanoparticle using seaweeds of gulf of Mannar, India," *Journal of Nanobiotechnology*, vol. 11, no. 1, article 39, 2013.
- [45] M. S. Wagh, R. H. Patil, D. K. Thombre, M. V. Kulkarni, W. N. Gade, and B. B. Kale, "Evaluation of anti-quorum sensing activity of silver nanowires," *Applied Microbiology and Biotechnology*, vol. 97, no. 8, pp. 3593–3601, 2013.
- [46] B. R. Singh, B. N. Singh, A. Singh, W. Khan, A. H. Naqvi, and H. B. Singh, "Mycofabricated biosilver nanoparticles interrupt *Pseudomonas aeruginosa* quorum sensing systems," *Scientific Reports*, vol. 5, Article ID 13719, 2015.
- [47] I. A. S. V. Packiavathy, S. Priya, S. K. Pandian, and A. V. Ravi, "Inhibition of biofilm development of uropathogens by curcumin - An anti-quorum sensing agent from *Curcuma longa*," *Food Chemistry*, vol. 148, pp. 453–460, 2014.
- [48] C. Nithya, C. Aravindraja, and S. K. Pandian, "*Bacillus pumilus* of Palk Bay origin inhibits quorum-sensing-mediated virulence

- factors in Gram-negative bacteria," *Research in Microbiology*, vol. 161, no. 4, pp. 293–304, 2010.
- [49] B. V. Jones, R. Young, E. Mahenthiralingam, and D. J. Stickler, "Ultrastructure of *Proteus mirabilis* swarmer cell rafts and role of swarming in catheter-associated urinary tract infection," *Infection and Immunity*, vol. 72, no. 7, pp. 3941–3950, 2004.
- [50] K. Kalishwaralal, S. BarathManiKanth, S. R. K. Pandian, V. Deepak, and S. Gurunathan, "Silver nanoparticles impede the biofilm formation by *Pseudomonas aeruginosa* and *Staphylococcus epidermidis*," *Colloids and Surfaces B: Biointerfaces*, vol. 79, no. 2, pp. 340–344, 2010.
- [51] K. Sauer and A. K. Camper, "Characterization of phenotypic changes in *Pseudomonas putida* in response to surface-associated growth," *Journal of Bacteriology*, vol. 183, no. 22, pp. 6579–6589, 2001.
- [52] C. A. Fux, J. W. Costerton, P. S. Stewart, and P. Stoodley, "Survival strategies of infectious biofilms," *Trends in Microbiology*, vol. 13, no. 1, pp. 34–40, 2005.
- [53] F. H. Yildiz and G. K. Schoolnik, "Vibrio cholerae O1 El Tor: identification of a gene cluster required for the rugose colony type, exopolysaccharide production, chlorine resistance, and biofilm formation," *Proceedings of the National Academy of Sciences of the United States of America*, vol. 96, no. 7, pp. 4028–4033, 1999.
- [54] Y. Hsueh, W. Ke, C. Hsieh et al., "ZnO nanoparticles affect *Bacillus subtilis* cell growth and biofilm formation," *PLoS ONE*, vol. 10, no. 6, Article ID e0128457, 2015.
- [55] F. LewisOscar, D. MubarakAli, C. Nithya et al., "One pot synthesis and anti-biofilm potential of copper nanoparticles (CuNPs) against clinical strains of *Pseudomonas aeruginosa*," *Biofouling*, vol. 31, no. 4, pp. 379–391, 2015.
- [56] L. A. Pratt and R. Kolter, "Genetic analysis of *Escherichia coli* biofilm formation: roles of flagella, motility, chemotaxis and type I pili," *Molecular Microbiology*, vol. 30, no. 2, pp. 285–293, 1998.
- [57] M. Arunkumar, K. Suhashini, N. Mahesh, and R. Ravikumar, "Quorum quenching and antibacterial activity of silver nanoparticles synthesized from *Sargassum polyphyllum*," *Bangladesh Journal of Pharmacology*, vol. 9, no. 1, pp. 54–59, 2014.
- [58] M. Boll, L. W. D. Weber, E. Becker, and A. Stampfl, "Mechanism of carbon tetrachloride-induced hepatotoxicity. Hepatocellular damage by reactive carbon tetrachloride metabolites," *Zeitschrift fur Naturforschung - Section C Journal of Biosciences*, vol. 56, no. 7-8, pp. 649–659, 2001.
- [59] H. Ebaid, I. Hassan, S. Bashandy et al., "Zinc improves the immune function and the proliferation of lymphocytes in Cadmium-treated rats," *Central European Journal of Immunology*, vol. 39, no. 4, pp. 441–448, 2014.
- [60] A. Malhotra and D. K. Dhawan, "Current view of zinc as a hepatoprotective agent in conditions of chlorpyrifos induced toxicity," *Pesticide Biochemistry and Physiology*, vol. 112, no. 1, pp. 1–6, 2014.
- [61] J. Choi, H. Kim, P. Kim et al., "Toxicity of zinc oxide nanoparticles in rats treated by two different routes: single intravenous injection and single oral administration," *Journal of Toxicology and Environmental Health, Part A. Current Issues*, vol. 78, no. 4, pp. 226–243, 2015.

Research Article

Embedding of Bacterial Cellulose Nanofibers within PHEMA Hydrogel Matrices: Tunable Stiffness Composites with Potential for Biomedical Applications

Radka Hobzova ¹, Jakub Hrib,¹ Jakub Sirc,¹ Evgeny Karpushkin,¹ Jiri Michalek,¹ Olga Janouskova,¹ and Paul Gatenholm²

¹Institute of Macromolecular Chemistry, Czech Academy of Sciences, Heyrovsky Sq. 2, 16206 Prague 6, Czech Republic

²Department of Chemical and Biological Engineering/Biopolymer Technology and Wallenberg Wood Science Center, Chalmers University of Technology, Kemivagen 10, 41296 Gothenburg, Sweden

Correspondence should be addressed to Radka Hobzova; hobzova@imc.cas.cz

Received 20 July 2017; Revised 30 November 2017; Accepted 18 December 2017; Published 17 January 2018

Academic Editor: Faheem Ahmed

Copyright © 2018 Radka Hobzova et al. This is an open access article distributed under the Creative Commons Attribution License, which permits unrestricted use, distribution, and reproduction in any medium, provided the original work is properly cited.

Bacterial cellulose (BC) and poly(2-hydroxyethyl methacrylate) (PHEMA) hydrogels are both considered as biocompatible materials with potential use in various biomedical applications including cartilage, cardiovascular stent, and soft tissue engineering. In this work, the “ever-wet” process based on in situ UV radical polymerization of HEMA monomer in BC nanofibrous structure impregnated with HEMA was used, and a series of BC-PHEMA composites was prepared. The composite structures were characterized by ATR FT-IR spectroscopy, WAXD, SEM, and TEM techniques. The strategy of using densified BC material of various cellulose fiber contents was applied to improve mechanical properties. The mechanical properties were tested under tensile, dynamic shear, and relaxation modes. The final composites contained 1 to 20 wt% of BC; the effect of the reinforcement degree on morphology, swelling capacity, and mechanical properties was investigated. The biocompatibility test of BC-PHEMA composites was performed using mouse mesenchymal stem cells.

1. Introduction

Bacterial cellulose (BC) has gained considerable attention in recent years because of its unique structure and properties. BC is produced by bacteria *Gluconacetobacter xylinus* in the form of tree-dimensional network of nanosized fibrils (fiber diameter 20–100 nm). The remarkable features of BC, which set it apart from common plant cellulose, are the very high purity, high crystallinity (80–90%), high water holding capacity (99% water), and good mechanical stability [1, 2]. Moreover, the possibility of direct control of the biosynthesis process in terms of final structure and shape together with inherent biocompatibility and nontoxicity of BC makes this biopolymer a promising candidate for various biomedical applications such as wound dressings, artificial skin, scaffolds for tissue engineering, and soft tissue replacement [3–9].

A number of researchers focused on preparation of mechanically enhanced BC composites [10] as the scaffolds

fabricated directly from pure BC show mechanical anisotropy with a high tensile modulus ($E = 2.9$ MPa) along the fibril layer direction but a low compression modulus ($E = 0.007$ MPa) perpendicular to the stratified direction [11]. BC composites have been prepared by addition of reinforcing agents during the BC biosynthesis (e.g., using silica [12], titania [13], or silver [14] nanoparticles as fillers), by blending of BC with various polymers (e.g., with chitosan [15], polyvinyl alcohol [16, 17], or acrylic resin [18]) or by in situ polymerization of monomers within the BC network (e.g., (meth)acrylates [19–23] or (meth)acrylamides [24–26]).

In our previous work [21] we have demonstrated a successful preparation of various BC-methacrylate composites by UV radical crosslinking polymerization of monomer/crosslinker mixtures by the “ever-wet” process by impregnating the BC nanofibrous structures with the monomers (2-hydroxyethyl methacrylate, glycerol monomethacrylate, and/or 2-ethoxyethyl methacrylate). We have shown that the

final properties of the composites, especially the swelling and mechanical properties, can be adjusted in a relatively wide range of values. The properties of such composites were controlled by the chemical composition of the hydrogel matrix (i.e., by monomer ratio, crosslink density, or diluent concentration) while keeping the BC content at the level of 1 wt%. Other authors [19, 27, 28] studied BC composites of different BC content and showed that mechanical improvement can be achieved, so that these densified BC scaffolds almost approached the mechanical requirements of the native tissue.

The objective of this work was the preparation of mechanically enhanced BC-methacrylate composites, where the final properties will be mainly adjusted by the degree of reinforcement, that is, by the BC content in composites. As a suitable monomer for hydrogel matrix, 2-hydroxyethyl methacrylate (HEMA) was chosen because HEMA hydrogels are nontoxic and biocompatible with longtime and widespread use in the biomedical applications such as contact lenses, intraocular lenses, or implants for tissue engineering [29]. Therefore, combined with BC the high attractiveness in the field of biomaterials is ensured. The high-modulus and strength composites described here are considered for candidates for cartilage, stent, and certain wound-dressing materials. The PHEMA-based ointment has been commercialized (HEMAGEL®) as a successful wound-healing and eczema-healing material [30].

The BC-PHEMA composites studied here were prepared by UV radical polymerization using “ever-wet” process. The amount of water present in the BC sheets was adjusted mechanically, and water was subsequently replaced by the monomer mixture. In this way, the BC/PHEMA ratio in the composite was controlled. The composite materials were characterized by swelling; morphology; mechanical properties in tensile, shear, and relaxation modes; biocompatibility.

2. Materials and Methods

2.1. Chemicals and Materials. 2-Hydroxyethyl methacrylate (HEMA) (Roehm GmbH), ethylene dimethacrylate (EDMA) (Aldrich), and Darocur® 1173 (2-hydroxy-2-methylpropio-phenone) were supplied by Sigma-Aldrich (Czech Republic) and used as received. Phosphate buffered saline (PBS, pH 7.4) was prepared from tablets (Sigma-Aldrich, Czech Republic). Cell culture Dulbecco’s modified Eagle medium (DMEM) and AlamarBlue Assay were purchased from ThermoFisher Scientific (Czech Republic), 24-well plates from TPP (Techno Plat Product, iBioTech, Czech Republic), and biopsy punch Stiefel from Servoprax (Wesel, Germany). Mouse mesenchymal stem cells were kindly provided by Dr. Jendelova (Institute of Experimental Medicine AS CR, Prague, Czech Republic).

2.2. Preparation of BC. A corn steep liquor medium was used for cultivation of precultures and bacterial cellulose production as described elsewhere [31]. Precultures of *A. xylinum* subsp. *sucrofermentans*, BRP2001, trade number 700 178™, purchased from the American Type Culture Collection (LGC Promochem AB, Borås, Sweden), were prepared as described by Bodin and coworkers [31]. Bacteria preculture

suspension (2.5 ml, cell density 3.7–10 cfu/ml) was added to each glass bioreactor, and reactors were then put into an incubator at 30°C and cultivated for 7 days. Fermented BC sheets were removed from bioreactors and purified using 0.1 M NaOH at 60°C and then rinsed with distilled water.

The BC sheets of the original cellulose content of 1 wt% were compressed to obtain BC material with increased cellulose content of 5, 10, and 20 wt%, using the protocol described elsewhere [9].

2.3. Preparation of BC-PHEMA Composites. The BC-PHEMA composites were prepared by crosslinking radical polymerization of mixture impregnated into the BC nanofibrous network. We followed the methods described in our previous work [21]. The polymerization mixture consisted of monomer (HEMA), crosslinker (EDMA, 0.7 wt% relative to monomer), UV initiator (Darocur, 0.5 wt% relative to monomer), and diluent (water). The water present in BC sheet was included into the overall calculation of diluent amount to keep the monomer/diluent (HEMA/water) ratio constant at 60/40.

BC sheets in the form of discs 8 cm in diameter were immersed into the polymerization mixtures, bubbled with nitrogen for 10 min, and left for 24 h at room temperature under shaking to allow the liquid interchange. To obtain samples with defined BC content, the sheets were examined gravimetrically; the excess of monomer mixture was expelled to obtain the same sheet weight as before immersion.

The sheets were placed on a glass plate and confined with a silicone rubber frame of 1.0 mm thickness, covered with a polypropylene plate, and firmly closed with screw clamps into the mold. The polymerization was carried out by illumination with a UV lamp ReptiGlo 8.0 (60 W) for 20 min. The obtained composites were washed in distilled water for five days (water was changed twice per day) to acquire an equilibrium swollen state. During the swelling, unreacted residues present in samples after the polymerization were washed out. The washing efficiency was checked by UV spectroscopy. The values of absorbance of the aqueous extract after 5 days were below the detection limit. The neat PHEMA hydrogel matrix was prepared under the same polymerization conditions as the BC-PHEMA composites.

2.4. Characterization of BC-PHEMA Composites. The equilibrium water content (EWC) was determined using weighing method. Specimens (1 × 1 cm approx.) were cut from each equilibrium swollen material at room temperature. Excess surface liquid was gently blotted with tissue paper, and the samples were weighed (m_{sw}), then dried in free air at room temperature for 1 day, and finally dried under vacuum at elevated temperature (30 Pa at 100°C) to constant weight (m_{dry}). The EWC is defined as $EWC = 100 \times (m_{sw} - m_{dry}) / m_{sw}$. The resulting EWC is expressed as the average of at least six values (three values of at least two independently prepared materials of the same composition) ± standard deviation ($n = 6$).

ATR FT-IR spectra were measured on a Perkin-Elmer PARAGON 1000PC spectrometer equipped with Specac MKII Golden Gate Single Reflection ATR System with diamond crystal (angle of incidence 45°). Wide-angle X-ray

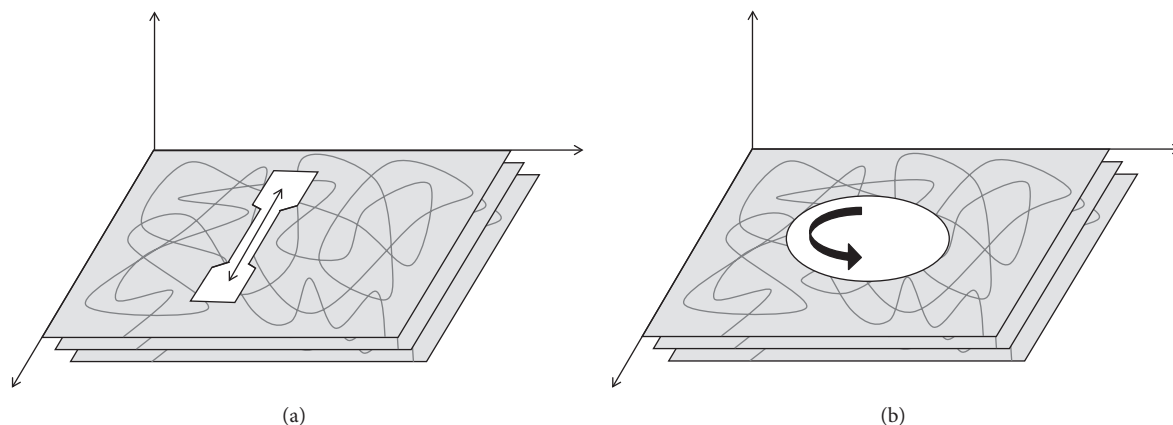


FIGURE 1: Schematic sketch of cut specimens and the direction of applied mechanical stresses in (a) static tensile and (b) dynamic shear measurements.

diffraction (XRD) patterns were obtained using high resolution diffractometer Explorer (GNR Analytical Instruments, Italy). Instrument was equipped with one-dimensional silicon strip detector Mythen 1K (Dectris, Switzerland). Samples were measured in reflection mode. The radiation $\text{CuK}\alpha$ (wavelength $\lambda = 1.54 \text{ \AA}$) monochromatized by Ni foil (β filter) was used for diffraction. The measurement was done in range $2\theta = 8\text{--}30^\circ$ with step 0.1° . Exposure time at each step was 10 seconds. Peak deconvolution procedure was made using the SASfit software [32]. The peak positions were employed to obtain periodicities and distinguish various phases according to Bragg's law, $d = \lambda/2 \sin \theta$, where λ is the X-ray wavelength and 2θ is the scattering angle.

2.5. Morphology. Scanning electron microscopy (SEM) was carried out with a SEM microscope Quanta 200 FEG (FEI, Czech Republic). Samples in dry state were fractured in liquid nitrogen (in order to avoid plastic deformations during fracture) perpendicularly to the stratified structure of BC. The fractured surfaces were sputtered with 4 nm thin platinum layer (vacuum sputter coater SCD 050, Leica). Samples were observed in the SEM microscope using secondary electrons detector either at medium accelerating voltage of 15 kV in low-vacuum (80 Pa) or at low accelerating voltage of 5 kV in high vacuum (10^{-3} Pa).

Transmission electron microscopy (TEM) was made with a TEM microscope Tecnai G2 Spirit (FEI, Czech Republic). The ultrathin sections (40 nm) of the investigated samples were cut with ultramicrotome (Ultratome III, LKB) at room temperature. The sections were transferred to the TEM microscope and observed at 120 kV using bright field imaging.

2.6. Mechanical Properties. The uniaxial extension test was done using the Instron 5800 with a crosshead speed of 10 mm/min until failure. The dumbbell-shaped samples of width of 2 mm and thickness of 1 mm (ISO527-2/5B) were measured in their water-swollen state at room temperature.

The tests were carried out in the direction parallel to the stratified BC layers embedded in the hydrogel matrix (Figure 1(a)). The standard deviations of tensile strength (σ_b), elongation at break (ε_b), and Young modulus (E) average were below 10%.

The dynamic mechanical properties were characterized using the oscillation-shear rheometer Gemini HR Nano (Malvern/Bohlin) and the plate-plate geometry. The cylindrical-shaped samples (12.7 mm in diameter) were fixed between two parallel metal plates and measured in their equilibrium swollen state in water using a solvent chamber at 25°C . The shear was introduced in the direction parallel to the stratified BC layers embedded in the hydrogel matrix (Figure 1(b)). The shear moduli (G' and G'') were determined in the frequency range 0.01–100 Hz. The measurements were done in the experimentally determined linear-viscoelastic limit of deformations below 0.05% strain.

The relaxation measurements were performed in both tensile and shear modes. The equilibrium swollen samples were strained to 0.05% and held for 3 h (shear measurements) or to 5% and held for 10 min (tensile measurements).

2.7. Biocompatibility Test. For biocompatibility test, equilibrium water-swollen samples were cut by biopsy punch 4 mm in diameter, and cut discs were sterilized under UV light for 30 min. Mouse mesenchymal stem cells (rMSCs) were resuspended in fresh DMEM and seeded in the 24-well plates at a density of 5×10^4 cells/well. The insert (porosity 0.45 mm, translucent PET membrane, Becton Dickinson, Czech Republic) with sample disc in 0.5 ml of media was added above the cells. The cells were cultivated for 72 h. The evaluation of growth and viability of cells was done by AlamarBlue Assay. The insert with sample was discarded, and AlamarBlue reagent was added to the medium with cells and incubated for 4 h at 37°C . The viable/metabolically active cells reduced the active component of AlamarBlue reagent resazurin to resorufin, whose fluorescence was detected in a plate reader Synergy Neo (BioTek, Czech Republic) using excitation at 570 nm and emission at 60 nm. The fluorescence intensity directly correlates with the number of

TABLE 1: Specification and equilibrium swelling of BC-PHEMA composites.

| Material code | BC content [wt%] | | Equilibrium water content [%] | |
|---------------|----------------------|--------------------|-------------------------------|--------------------|
| | Initial ^a | Final ^b | EWC-1 ^c | EWC-2 ^d |
| M | - | - | 40.6 ± 0.1 | 40.7 ± 0.1 |
| C1 | 1 | 2 | 40.0 ± 0.3 | 40.1 ± 0.2 |
| C5 | 5 | 8 | 39.8 ± 0.3 | 39.7 ± 0.3 |
| C10 | 10 | 16 | 39.9 ± 0.6 | 39.8 ± 0.5 |
| C20 | 20 | 30 | 39.5 ± 0.1 | 39.6 ± 0.3 |

^aBC content in the initial water-swollen BC; ^bBC content in composite in dry state; ^cEWC determined after preparation of composite prior to drying; ^dEWC determined after drying of composite and its reswelling in water.

growing/viable cells. The acquired fluorescence was recalculated using a calibration curve to determine absolute number of viable cells under the sample. For calibration curve, 24-well plates were seeded with various numbers of cells, and the fluorescence of metabolized component resorufin was measured. Then, the cells were washed with PBS and incubated in 0.2 mL of trypsin solution (0.05% trypsin, 0.5 mM EDTA in PBS) at 37°C for 5–10 min. The trypsin was deactivated by addition of 0.2 ml of media. The cells were pipetted out from the well, transferred into the Eppendorf vial, and centrifuged for 3 minutes at 1200 rpm at room temperature. The deactivated trypsin solution was then aspirated, and the pellet fraction (composed of cell and gel debris) was resuspended in 30 μ L of the PBS. The Bürker chamber was used to determine the number of cells per 1 mL of solution. To determine the number of viable cells, the 0.2% Trypan blue and lethal dyes were added in a 1:1 ratio. The numbers of viable cells were added to graph against fluorescent intensities, which gave us calibration curve and equation for the calculation of cell number growing under the insert with samples adequate to their fluorescent intensity. Each sample was conducted in triplicate, and the average values and their standard deviations were calculated.

The morphologies of cell growth under the insert with the samples and cell growth without sample (control) were visualized after 72 h of growth using the Olympus microscope equipped with camera Infinity 2 and FV10-ASW viewer software (Olympus, Japan). The images were evaluated using Quick photo 3.0 software.

3. Results and Discussion

3.1. Preparation of BC-PHEMA Composites. In our previous study [21], we demonstrated that by the combination of hydrophilic and hydrophobic monomers, it was possible to obtain composites having properties in a wide range of values. To achieve high level of compression modulus (6–8 MPa) and strength, addition of hydrophobic monomer (2-ethoxyethyl methacrylate) to hydrophilic major monomer was necessary. However, low swelling (2% of water) renders biomedical application of such composite material difficult. Using softer gels (e.g., based on HEMA monomer), an acceptable compromise between mechanical properties and swelling can be achieved. Here, we show that much stronger BC composites

of a wide application range can be obtained by varying the BC content in the PHEMA matrix. As starting materials, BC gels with 99, 95, 90, and 80% of water were used (see Table 1, column “BC Content Initial”). If water present initially in the BC is completely replaced by the polymerization mixture, the BC content in the dry composite ranged from 2 to 30 wt% (see Table 1, column “BC Content Final”).

The character of the samples is shown at Figure 2. The BC-PHEMA composites were considerably more translucent than the pure BC, but still slightly opaque compared to neat PHEMA hydrogel matrix.

Figure 3 shows the ATR-IR spectra of pure BC, PHEMA matrix, and BC-PHEMA composites of various BC contents. The successful polymerization of HEMA monomer impregnated into the nanofibrous BC structure was confirmed by the appearance of peaks typical for methacrylate polymers at around 1720 cm^{-1} (carbonyl ester group), 1456 cm^{-1} , and 750 cm^{-1} (CH_2 group) and absence of the peak at 1630 attributed to the monomer. Comparing the spectra of composites, the intensity of peaks corresponding to PHEMA decreased with increased BC content. The presence of BC is demonstrated by the appearance of the peak at 1110 cm^{-1} corresponding to -C-O-C- vibration within the glucose ring which is evident in the spectra of both BC and composites. Finally, in all spectra the characteristic O-H group stretching peaks at 3350 cm^{-1} were detected as a contribution of both PHEMA and BC component.

The crystallinity character of the materials was examined by XRD, and the diffractograms are shown in Figure 4. For pure BC the main diffraction peaks are apparent at 2θ 14.5, 16.7, and 22.6°, while PHEMA matrix (M) is characterized by a broad peak centered at around 2θ 18.5° as typical for fully amorphous material. All BC-PHEMA composites exhibit the diffraction profiles very similar to that of pure BC regardless on BC content (therefore, only data for composites C5 and C10 are presented).

The equilibrium water content (EWC) of all prepared materials is given in Table 1. Only a slight decrease in swelling is observed when comparing hydrogel matrix (M) and composite materials (marked as C with number corresponding to initial BC content). The EWC of composites are nearly the same with no obvious dependence on the BC content. Presumably, PHEMA matrix is a major determinant of the final EWC of the composites materials, irrespectively of the

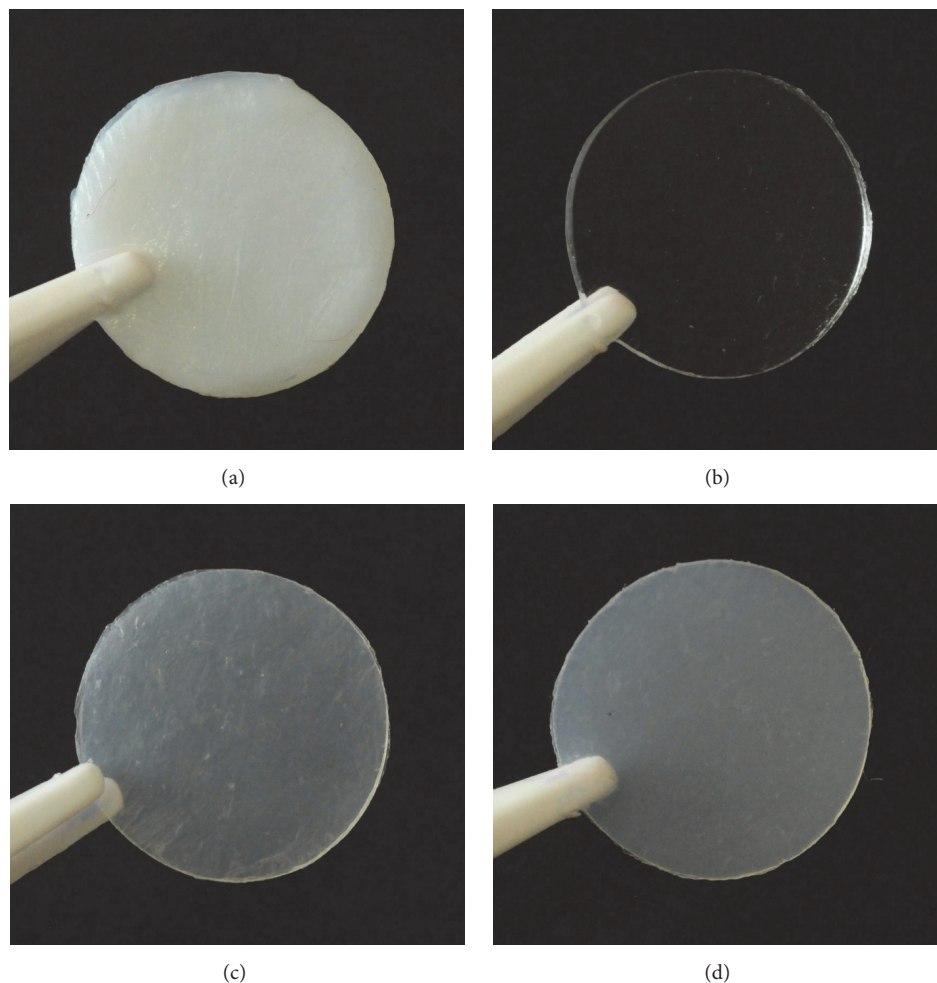


FIGURE 2: Photographs of water-swollen BC (90% H₂O) (a), PHEMA hydrogel matrix swollen in water (b), BC-PHEMA composite C10 in dry (c) and swollen state (d).

BC content in the matrix. The composites as well as PHEMA matrix swelled reversibly after drying; compare the EWC-1 and EWC-2 values in Table 1. The formation of PHEMA matrix within BC nanofibrous network prevents the collapse of the BC structure and provides the materials with repeatable ability to swell. This is a favorable feature of the material enabling the storage of composites in the dry form to ensure easier sterility.

3.2. Morphology. The morphology of BC-PHEMA composites was examined by SEM. Figures 5(a)–5(c) illustrate the structure of the composites varying in BC content. The micrographs show darker PHEMA matrix background with light BC nanofibers protruding to the surface. There are no apparent fibers in the structure, but only white dots distributed in the hydrogel matrix, whose number increases with the increasing BC content in the matrix. To prove that the “light dots” represent the BC fibers, we specially prepared hybrid sample of a two-layer structure. The BC sheet swollen in the polymerization mixture was polymerized “in air” contrary to the standard preparation of the composite

which is carried out in closed mold. Oxygen present in polymerization mixture acts as an inhibitor of the radical polymerization and causes that polymerization not to be complete in the surface layer, and therefore no compact hydrogel matrix is formed as in the inner layers of the composites. The structure of such a sample is shown in Figure 5(d); the lower part of the image represents a surface layer of the sample with the partially preserved BC fiber structure and the upper part of the image shows the structure of the inner layer. This is consistent with the structures of the composites C5–C20. It can be concluded that the light dots really do represent BC fibers, where individual BC nanofibers are well wrapped by the PHEMA and are uniformly dispersed in compact hydrogel matrix. The homogenous distribution of the BC fibers within the hydrogel matrix without noticeable aggregates formation is also clearly seen in TEM images of sample cross-section showing lighter PHEMA matrix with darker spots or fibers of BC (Figure 6). The results obtained by the morphological analysis confirm successful impregnation of BC nanofibrous network by HEMA monomer and in particular the excellent compatibility between the BC and

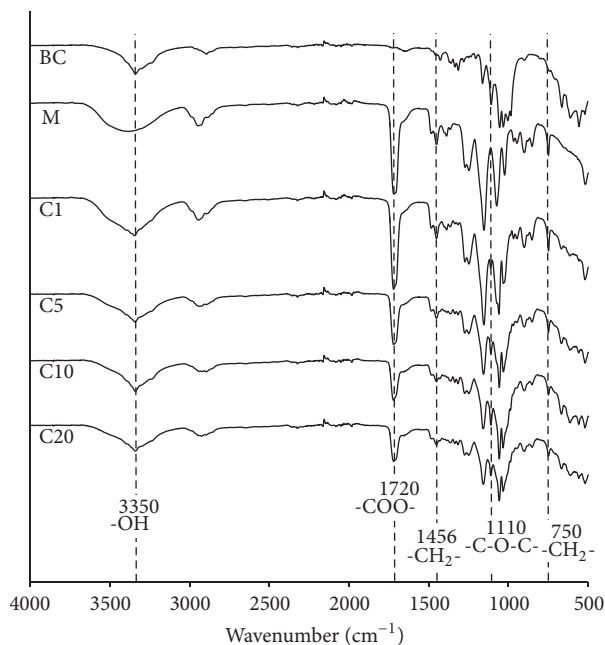


FIGURE 3: IR spectra of BC, PHEMA hydrogel matrix (M), and CB-PHEMA composites (C1, C5, C10, and C20).

PHEMA matrix with strong interfacial adhesion arising from the presence of hydroxyl groups in both materials.

3.3. Mechanical Properties

Static Tensile Properties. Measurements in uniaxial tension were performed for PHEMA hydrogel matrix M and BC-PHEMA composite C10 (Figure 7). The shapes of both curves are characteristic for viscoelastic materials that do not exhibit linear stress/strain behavior at low deformations. The difference in stress (Young modulus) is enormous (see the insert in Figure 7).

The mechanical parameters are presented in Table 2 together with those for pure BC [11]. The introduction of BC fibers improved the strength and stiffness of PHEMA and BC significantly. Taking the composite C10, the tensile strength increased by a factor of 80 and 10, respectively, compared to hydrogel matrix and BC; for Young modulus, E , the factors were 120 and 40, respectively. The elongation at break decreased only by a factor of 2 compared to the hydrogel matrix and was even slightly higher than that of the parent BC. Such improvement in mechanical properties for hydrogel composites is not associated with a change in swelling, because EWC values are practically the same compared with PHEMA matrix (see Table 1). The considerable reinforcement by incorporation of BC into PHEMA is apparently caused by good wetting of BC fibers with HEMA and their good adhesion to the matrix. The strength and modulus are almost of an order of magnitude better than that for interpenetrating polymer networks or fiber-reinforced hydrogels [33], but the latter contain much more water. The compact structure with good interfacial adhesion between matrix and BC fibers was also proved by electron microscopy.

TABLE 2: Mechanical properties of hydrogels.

| Material code | Extension | | E (MPa) | Oscillatory shear ^c | |
|---------------|---------------------|---------------------|------------------|--------------------------------|----------------|
| | σ_b (MPa) | ϵ_b (%) | | G' (kPa) | G'' (kPa) |
| BC | 2.2 ^a | 21.0 ^a | 2.9 ^a | 0.63 | 0.07 |
| M | 0.3 | 51.4 | 1.0 | 117 | 16 |
| C1 | 8.7 | 38.7 | 15.2 | 510 | 70 |
| C10 | 25.3 | 25.5 | 120 | 1450 | 187 |
| ligament | 38.6 ^b | 17.0 ^b | 332 ^b | | |

^aValues of tensile properties for pure BC taken from [11]. ^bValues of tensile properties for natural ligament taken from [25]. ^cModuli values at 1 Hz.

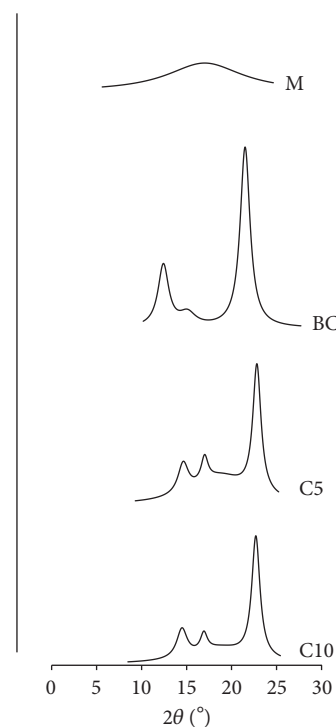


FIGURE 4: X-ray diffractograms of BC, PHEMA hydrogel matrix (M), and CB-PHEMA composites (C1, C5, C10, and C20).

The values of tensile properties of composite C10 approach the values for natural ligament [25] (Table 2). It can be concluded that the composite C10 mimics well the structure of the ligament; that is, both materials are composed of a soft hydrated matrix reinforced by filaments.

Dynamic Mechanical Properties. Dynamic mechanical behavior can be characterized by storage modulus (G') which is associated with the elastic energy stored in the material and loss modulus (G'') which describes the viscous behavior and is associated with the dissipation of the energy caused by structural rearrangements within the material.

Oscillatory shear measurements of equilibrium water-swollen hydrogel materials offer frequency dependences of G' and G'' (Figures 8 and 9). A slight increase in G' with frequency was observed for both the PHEMA matrix M and composites C1 and C10. The increase in G'' with frequency

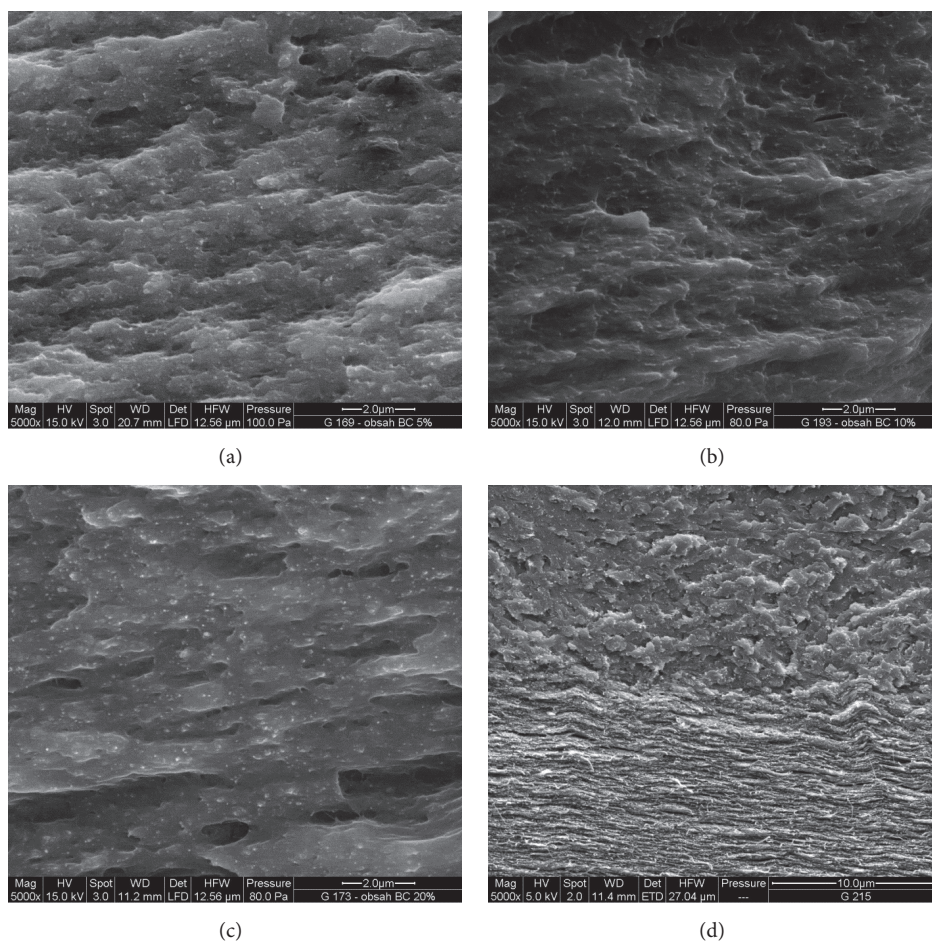


FIGURE 5: SEM micrographs of the fracture surface of dry BC-PHEMA composites with various BC contents: (a) composite C5, (b) composite C10, and (c) composite C20 (for the codes, see Table 1). (d) SEM micrograph of the composite with two-layer structure.

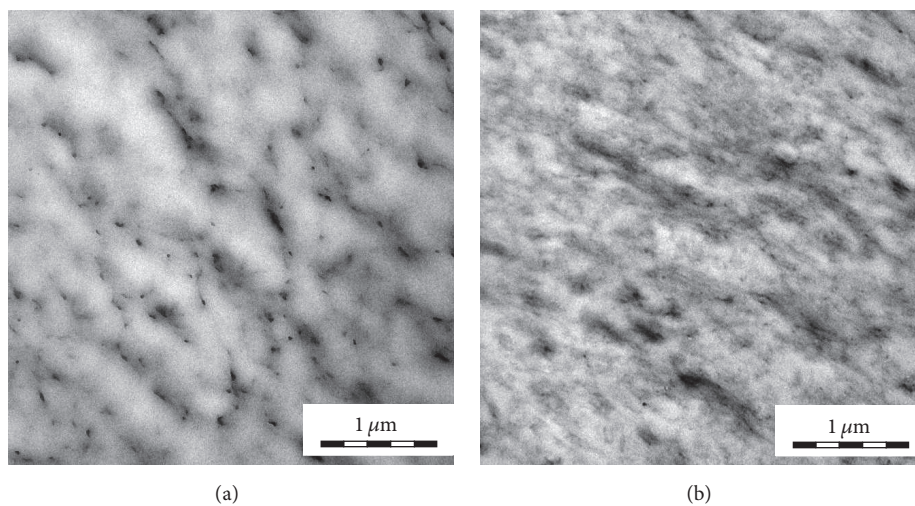


FIGURE 6: TEM micrographs of the fracture surface of dry BC-PHEMA composites (a) C5 and (b) C10 (for the codes, see Table 1).

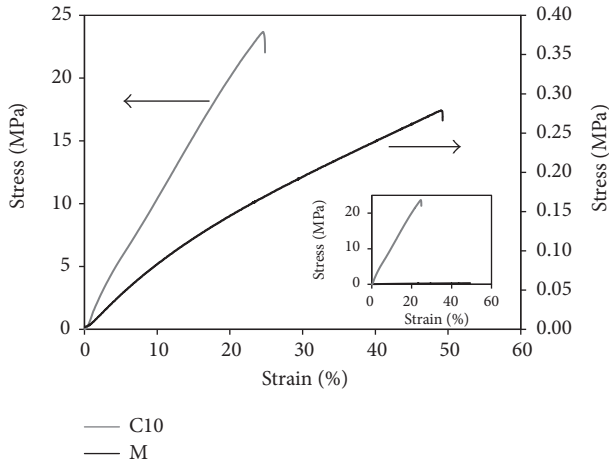


FIGURE 7: Tensile stress-strain curves for PHEMA hydrogel matrix M (black line, right y axis) and BC-PHEMA composite C10 (grey line, left y axis).

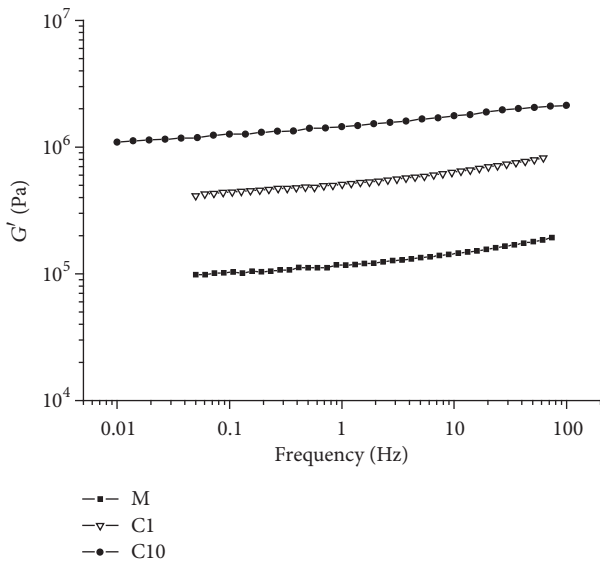


FIGURE 8: Frequency dependence of the storage moduli G' for PHEMA matrix M (symbol ■), BC-PHEMA composite C1 (symbol ▽), and C10 (symbol ●).

implies the rubbery-like behavior of the materials (Figure 9). Similarly to tensile measurements, improvement of G' by BC reinforcement is evident (Table 2); the increase in G' (factor 12) is lower than the increase in E (factor 120). This difference can be explained by the fact that oscillatory shear measurements are limited to small strains where the matrix is still disoriented, whereas in the (nonoscillatory) extension mode the chains can get oriented aided by the adhesion to nanofibers. The losses (G'') are relatively low and the ratio G''/G' (loss-angle tangent) is almost the same.

Relaxation Properties Measurements. Since most natural soft tissues are of viscoelastic nature, the time-dependent properties of the designed material are very important. The

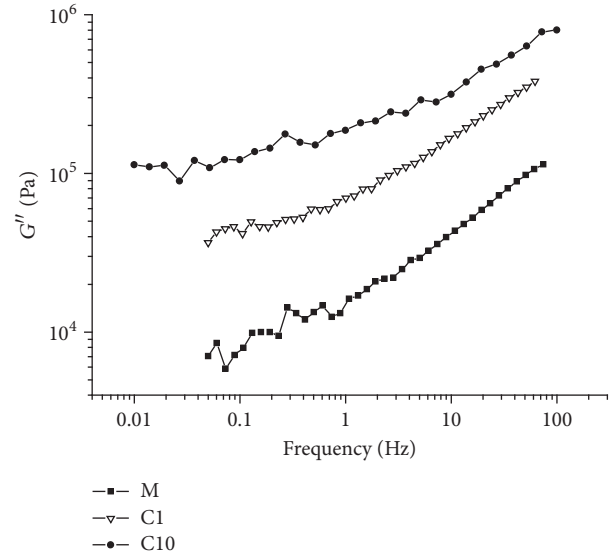


FIGURE 9: Frequency dependence of the loss moduli G'' for PHEMA matrix M (symbol ■), BC-PHEMA composite C1 (symbol ▽), and C10 (symbol ●).

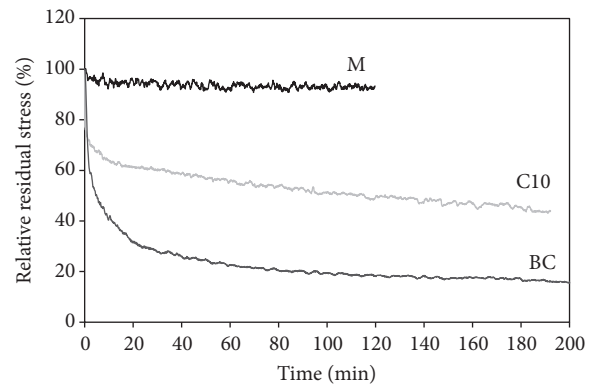


FIGURE 10: Change in relative residual shear relaxation stress over the time period of 3 h for pure BC, PHEMA matrix M, and BC-PHEMA composite C10.

stress relaxation measurements were performed for pure BC, PHEMA matrix M, and the composite C10. An instantaneous oscillatory deformation in shear was applied and the time dependence of the stress required for maintaining that deformation was recorded.

Very low deformations (0.05%) were applied. For PHEMA hydrogel matrix almost no decrease in stress over the time was recorded (Figure 10), and the material showed almost ideal rubbery network behavior with immediate response to the applied deformation. On the other hand, a pronounced time-dependent relaxation behavior of both parent BC and composites was observed. BC relaxed much faster and to the lower final stress (20% of residual stress) compared to composite C10 (45% of residual stress). Such a behavior suggests that even small mechanical loading causes the structural rearrangements (reorientation of BC nanofibers). These rearrangements take place much

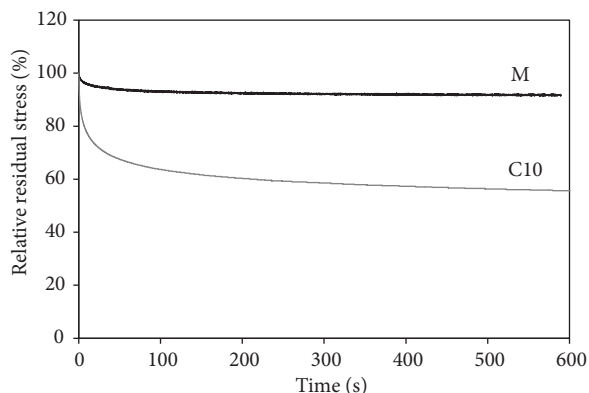


FIGURE 11: Change in relative residual tensile relaxation stress over the period time of 10 min for PHEMA matrix M and BC-PHEMA composite C10.

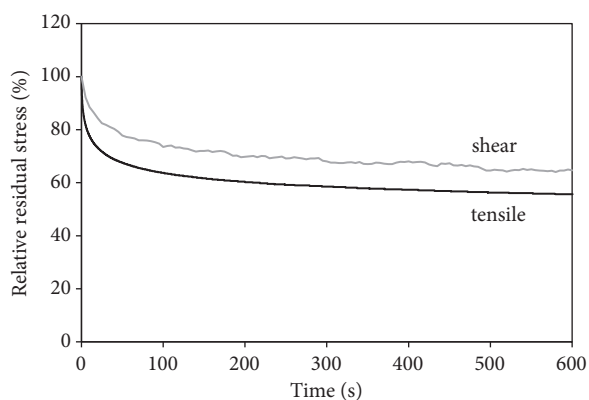


FIGURE 12: Comparison of relaxation response under tensile and shear deformation for BC-PHEMA composite C10.

easier in neat BC scaffold than in the composite material where the fibers are anchored in a hydrogel matrix. This interpretation was also supported by the results obtained from relaxation measurements under tensile deformation as shown in Figure 11. Comparing the relaxation response of BC-PHEMA composite under tensile and shear deformation, the tensile relaxation proceeds faster and to a lower residual stress (Figure 12). The observed viscoelastic behavior of BC-PHEMA composites can be considered similar to those of other composite natural tissues such as ligament, tendon, or cartilage [34, 35]. It would be interesting to strain the composite in extension or compression during the process of network formation (irradiation), so as to reorient continuously the fibers and chains and to fix by crosslinking the reoriented structure. This may lead to further enhancement of mechanical properties.

3.4. Biocompatibility. The nontoxicity of BC and PHEMA hydrogel is known, nevertheless we performed the biocompatibility test with our BC-PHEMA composites using rMSCs. The behavior of these cells is an important indicator in terms of tissue engineering because they can be differentiated into a

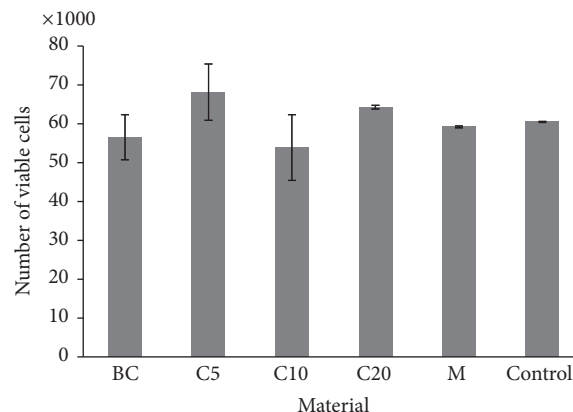


FIGURE 13: Number of viable rMSCs after 72 h of growth on BC-PHEMA composites determined by cell viability AlamarBlue Assay.

variety of cell types, including osteocytes, adipocytes, or also chondrocytes.

We determined the number of growing/viable cells after 72 h under the BC, PHEMA matrix M, and BC-PHEMA composites incubated with the cells in the inserts. The influence of the sample presence on cell growing compared to the control test (without insert and any sample) is shown in Figure 13. It is apparent that the differences in number of viable cells between the samples and control as well as between the materials are not significant. Further, we observed the morphology of growing cells, and the microscopy images are shown in Figure 14. It can be concluded that the BC-PHEMA composites regardless of the composition did not influence the morphology and proliferation of the rMSCs.

4. Conclusions

Composite hydrogels based on poly(2-hydroxyethyl methacrylate) (PHEMA) matrix and bacterial cellulose nanofibers (BC) were successfully prepared by in situ UV radical polymerization of HEMA monomer impregnated into wet BC nanofibrous structure. The final properties of composites were tuned by varying the BC content ranging from 1 to 20 wt% relative to swollen composite. The SEM images confirmed complete and uniform distribution of BC nanofibers in the hydrogel matrix. A significant improvement in mechanical properties was achieved. Comparing the PHEMA matrix and BC with the composite containing 10 wt% of BC, the tensile strength increased by factors of 80 and 10, respectively, and Young modulus by factors of 120 and 40, respectively. By varying the composition of BC-PHEMA composites, the mechanical properties can be adjusted to achieve the mechanical requirements of soft and semisoft native tissues. Biocompatibility tests demonstrated that BC-PHEMA composites are nontoxic providing a favorable environment for rMSCs proliferation. Therefore, our composites can be seen as promising for application in the tissue engineering area, particularly in tissue replacement and wound healing.

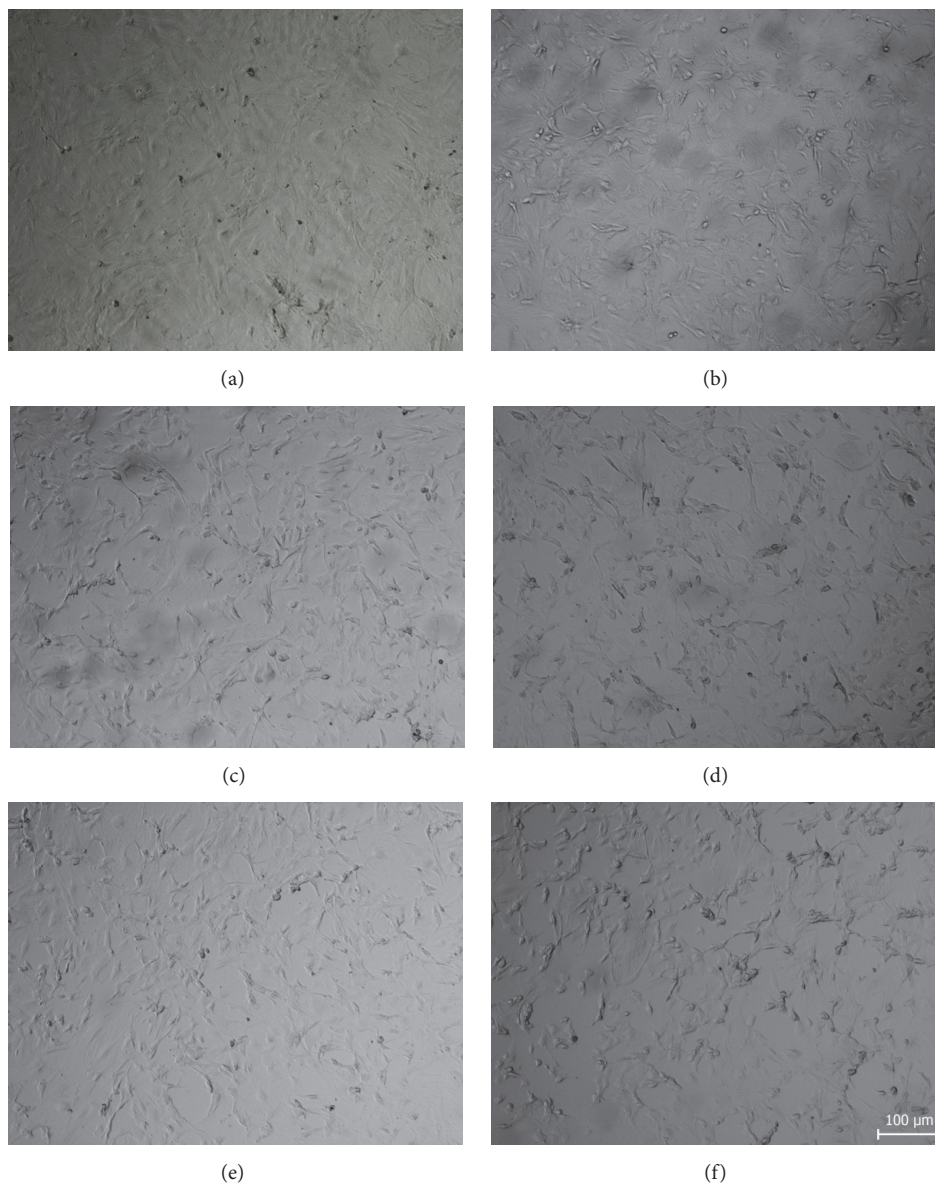


FIGURE 14: Light microscopy images of morphology of growing rMSCs at 72 h after seeding in the presence of (a) BC, (b) PHEMA matrix, and BC-PHEMA composites (c) C5, (d) C10, and (e) C20. Image (f) represents a controlling cell growth. Scale bar 100 μm is the same for all images.

Conflicts of Interest

The authors declare that there are no conflicts of interest regarding the publication of this paper.

Acknowledgments

This work was supported by the Grant Agency of the Czech Republic (Project 16-04863S) and by the Ministry of Education, Youth and Sports of the Czech Republic within the National Sustainability Program II (Project BIOCEV-FAR LQ1604) and the Project “BIOCEV” (CZ.1.05/1.1.00/02.0109). The authors thank Jiri Hodan for measuring the tensile mechanical properties and Dr. Miroslav Slouf for microscopy

measurements. Professor Karel Dusek is acknowledged for his contribution to the article finalization.

References

- [1] D. Klemm, F. Kramer, S. Moritz et al., “Nanocelluloses: a new family of nature-based materials,” *Angewandte Chemie International Edition*, vol. 50, no. 24, pp. 5438–5466, 2011.
- [2] I. Siró and D. Plackett, “Microfibrillated cellulose and new nanocomposite materials: a review,” *Cellulose*, vol. 17, no. 3, pp. 459–494, 2010.
- [3] J. M. Rajwade, K. M. Paknikar, and J. V. Kumbhar, “Applications of bacterial cellulose and its composites in biomedicine,” *Applied Microbiology and Biotechnology*, vol. 99, no. 6, pp. 2491–2511, 2015.

- [4] Y. Dahman, "Nanostructured biomaterials and biocomposites from bacterial Cellulose nanofibers," *Journal of Nanoscience and Nanotechnology*, vol. 9, no. 9, pp. 5105–5122, 2009.
- [5] N. Hoenich, "Cellulose for medical applications: past, present, and future," *BioResources*, vol. 1, pp. 270–280, 2006.
- [6] S. Thomas, "A review of the physical, biological and clinical properties of a bacterial cellulose wound," *Journal of Wound Care*, vol. 17, no. 8, pp. 349–352, 2008.
- [7] L. Fu, J. Zhang, and G. Yang, "Present status and applications of bacterial cellulose-based materials for skin tissue repair," *Carbohydrate Polymers*, vol. 92, no. 2, pp. 1432–1442, 2013.
- [8] A. Svensson, E. Nicklasson, T. Harrah et al., "Bacterial cellulose as a potential scaffold for tissue engineering of cartilage," *Biomaterials*, vol. 26, no. 4, pp. 419–431, 2005.
- [9] L. Nimeskern, H. Martínez Ávila, J. Sundberg, P. Gatenholm, R. Müller, and K. S. Stok, "Mechanical evaluation of bacterial nanocellulose as an implant material for ear cartilage replacement," *Journal of the Mechanical Behavior of Biomedical Materials*, vol. 22, pp. 12–21, 2013.
- [10] C. Chang and L. Zhang, "Cellulose-based hydrogels: present status and application prospects," *Carbohydrate Polymers*, vol. 84, no. 1, pp. 40–53, 2011.
- [11] A. Nakayama, A. Kakugo, J. P. Gong et al., "High mechanical strength double-network hydrogel with bacterial cellulose," *Advanced Functional Materials*, vol. 14, no. 11, pp. 1124–1128, 2004.
- [12] S. Yano, H. Maeda, M. Nakajima, T. Hagiwara, and T. Sawaguchi, "Preparation and mechanical properties of bacterial cellulose nanocomposites loaded with silica nanoparticles," *Cellulose*, vol. 15, no. 1, pp. 111–120, 2008.
- [13] S. Yamanaka and J. Sugiyama, "Structural modification of bacterial cellulose," *Cellulose*, vol. 7, no. 3, pp. 213–225, 2000.
- [14] T. Maneerung, S. Tokura, and R. Rujiravanit, "Impregnation of silver nanoparticles into bacterial cellulose for antimicrobial wound dressing," *Carbohydrate Polymers*, vol. 72, no. 1, pp. 43–51, 2008.
- [15] S. C. M. Fernandes, C. S. R. Freire, A. J. D. Silvestre, C. Pascoal Neto, and A. Gandini, "Novel materials based on chitosan and cellulose," *Polymer International*, vol. 60, no. 6, pp. 875–882, 2011.
- [16] S. Gea, E. Bilotti, C. T. Reynolds, N. Soykeabkeaw, and T. Peijs, "Bacterial cellulose-poly(vinyl alcohol) nanocomposites prepared by an in-situ process," *Materials Letters*, vol. 64, no. 8, pp. 901–904, 2010.
- [17] L. E. Millon, C. J. Oates, and W. Wan, "Compression properties of polyvinyl alcohol-bacterial cellulose nanocomposite," *Journal of Biomedical Materials Research Part B: Applied Biomaterials*, vol. 90, no. 2, pp. 922–929, 2009.
- [18] E. Trovatti, L. Oliveira, C. S. R. Freire et al., "Novel bacterial cellulose-acrylic resin nanocomposites," *Composites Science and Technology*, vol. 70, no. 7, pp. 1148–1153, 2010.
- [19] F. Kramer, D. Klemm, D. Schumann et al., "Nanocellulose polymer composites as innovative pool for (Bio)material development," *Macromolecular Symposia*, vol. 244, pp. 136–148, 2006.
- [20] A. G. P. R. Figueiredo, A. R. P. Figueiredo, A. Alonso-Varona et al., "Biocompatible bacterial cellulose-poly(2-hydroxyethyl methacrylate) nanocomposite films," *BioMed Research International*, vol. 2013, Article ID 698141, pp. 1–14, 2013.
- [21] R. Hobzova, M. Duskova-Smrckova, J. Michalek, E. Karpushkin, and P. Gatenholm, "Methacrylate hydrogels reinforced with bacterial cellulose," *Polymer International*, vol. 61, no. 7, pp. 1193–1201, 2012.
- [22] W. Zhao, Z. Shi, X. Chen, G. Yang, C. Lenardi, and C. Liu, "Microstructural and mechanical characteristics of PHEMA-based nanofibre-reinforced hydrogel under compression," *Composites Part B: Engineering*, vol. 76, pp. 292–299, 2015.
- [23] A. R. P. Figueiredo, A. G. P. R. Figueiredo, N. H. C. S. Silva et al., "Antimicrobial bacterial cellulose nanocomposites prepared by in situ polymerization of 2-aminoethyl methacrylate," *Carbohydrate Polymers*, vol. 123, pp. 443–453, 2015.
- [24] A. L. Buyanov, I. V. Gofman, L. G. Revel'skaya, A. K. Khripunov, and A. A. Tkachenko, "Anisotropic swelling and mechanical behavior of composite bacterial cellulose-poly(acrylamide or acrylamide-sodium acrylate) hydrogels," *Journal of the Mechanical Behavior of Biomedical Materials*, vol. 3, no. 1, pp. 102–111, 2010.
- [25] Y. Hagiwara, A. Putra, A. Kakugo, H. Furukawa, and J. P. Gong, "Ligament-like tough double-network hydrogel based on bacterial cellulose," *Cellulose*, vol. 17, no. 1, pp. 93–101, 2010.
- [26] M. Pandey, N. Mohamad, and M. C. I. M. Amin, "Bacterial cellulose/acrylamide pH-sensitive smart hydrogel: Development, characterization, and toxicity studies in ICR mice model," *Molecular Pharmaceutics*, vol. 11, no. 10, pp. 3596–3608, 2014.
- [27] M. L. Tanaka, N. Vest, C. M. Ferguson, and P. Gatenholm, "Comparison of biomechanical properties of native menisci and bacterial cellulose implant," *International Journal of Polymeric Materials and Polymeric Biomaterials*, vol. 63, no. 17, pp. 891–897, 2014.
- [28] H. Martínez Ávila, S. Schwarz, E.-M. Feldmann et al., "Biocompatibility evaluation of densified bacterial nanocellulose hydrogel as an implant material for auricular cartilage regeneration," *Applied Microbiology and Biotechnology*, vol. 98, no. 17, pp. 7423–7435, 2014.
- [29] J. Michalek, M. Pradny, and K. Dusek, "Hydrogels in biology and medicine," *Bioceramics Development and Applications*, pp. 177–230, 2010.
- [30] J. Labsky, J. Vacik, and P. Hosek, *Preparations for Prevention And Healing of Inflammation Affections*, US6610284-B1, 2003.
- [31] A. Bodin, H. Bäckdahl, H. Fink, L. Gustafsson, B. Risberg, and P. Gatenholm, "Influence of cultivation conditions on mechanical and morphological properties of bacterial cellulose tubes," *Biotechnology and Bioengineering*, vol. 97, no. 2, pp. 425–434, 2007.
- [32] I. Breßler, J. Kohlbrecher, and A. F. Thünemann, "SASfit: A tool for small-angle scattering data analysis using a library of analytical expressions," *Journal of Applied Crystallography*, vol. 48, pp. 1587–1598, 2015.
- [33] C. Azuma, K. Yasuda, Y. Tanabe et al., "Biodegradation of high-toughness double network hydrogels as potential materials for artificial cartilage," *Journal of Biomedical Materials Research Part A*, vol. 81A, no. 2, pp. 373–380, 2007.
- [34] L. Ambrosio, R. De Santis, S. Iannace, P. A. Netti, and L. Nicolais, "Viscoelastic behavior of composite ligament prostheses," *Journal of Biomedical Materials Research Part B: Applied Biomaterials*, vol. 42, no. 1, pp. 6–12, 1998.
- [35] P. Netti, A. D'Amore, D. Ronca, L. Ambrosio, and L. Nicolais, "Structure-mechanical properties relationship of natural tendons and ligaments," *Journal of Materials Science: Materials in Medicine*, vol. 7, no. 9, pp. 525–530, 1996.

Review Article

Heparin-Based Nanoparticles: An Overview of Their Applications

Maria del Pilar Rodriguez-Torres ¹, **Laura Susana Acosta-Torres** ¹,
and Luis Armando Diaz-Torres ²

¹Laboratorio de Investigación Interdisciplinaria, Área de Nanoestructuras y Biomateriales, Escuela Nacional de Estudios Superiores Unidad León, Universidad Nacional Autónoma de México (UNAM), Boulevard UNAM No. 2011, Predio El Saucillo y El Potrero, 37684 León, GTO, Mexico

²Centro de Investigaciones en Óptica, AP 1-948, 37150 León, GTO, Mexico

Correspondence should be addressed to Maria del Pilar Rodriguez-Torres; pilar.rdz.torres@gmail.com

Received 26 June 2017; Accepted 19 November 2017; Published 14 January 2018

Academic Editor: Faheem Ahmed

Copyright © 2018 Maria del Pilar Rodriguez-Torres et al. This is an open access article distributed under the Creative Commons Attribution License, which permits unrestricted use, distribution, and reproduction in any medium, provided the original work is properly cited.

This review deals with nanoparticles synthesized using heparin. Such nanoparticles have been widely studied since a long time ago, obtaining satisfactory outcomes. An outstanding aspect of these nanoparticles is that they possess good biocompatible characteristics, and since heparin is produced in the human body within the mast cells, this makes these nanoparticles useful for future applications like imaging, disease and cancer treatment, and antibacterial activity. They can also be used for applications that are not oriented directly to the medical and biological areas such as in the case of analyte detection in aqueous solution, although such studies are very few. These nanoparticles synthesis is mainly through wet chemistry methods, using heparin that could have been modified or not.

1. Introduction

Nanoparticles are defined as dispersions of particles or solid particles with nanoscale sizes. There are different nanoparticles types; they can be classified as nanopores, nanotubes, quantum dots, nanoshells, dendrimers, liposomes, nanorods, fullerenes, nanospheres, nanowires, nanobelts, nanorings, and nanocapsules. Such categories are pretty general and are based on dimensionality, morphology, composition, uniformity, and agglomeration [1].

Nanoparticles have been widely studied for many years and they have also generated an intense scientific interest due to a wide variety of potential applications in biomedical, optical, and electronic fields. Nanoparticles have drawn attention based on the few properties they exhibit like their surface to mass ratio and the reactivity of their surface [2]. In general, metal nanoparticles are prepared by top-down or bottom-up approaches; such methods are useful for obtaining nanoparticles which are good in their particle size and particle size distribution but because most of the

reactants used are hazardous, there are times in which they are not useful for certain further applications, so another step has to be performed to modify their surface, which also implies an extra cost and use. Thereupon, another pathway has to be found to carry out the synthesis procedure to avoid these problems [2]. Nanoparticles can be prepared from a variety of materials such as proteins, polysaccharides, and synthetic polymers. The selection of material depends on factors such as (a) required size of nanoparticles; (b) aqueous solubility and stability; (c) surface characteristics as charge and permeability; or (d) degree of biodegradability, biocompatibility, and toxicity [3, 4].

Glycosaminoglycans are biomaterials also known as mucopolysaccharides or polysaccharides, such as heparin, keratan sulfate, chondroitin sulfate, heparan sulfate, and hyaluronic acid. They are usually composed of a repeating disaccharide unit along their structure. In such disaccharide units, which are variable according to the glycosaminoglycan being referred to, the amino sugar is always hexosamine,

either D-glucosamine or D-galactosamine, mostly in the N-acetylated form; the other monosaccharide is mainly D-glucuronic acid or L-iduronic acid, except of keratan sulfate, in which D-galactose replaces the uronic acid [5]. In the specific case of heparin, it is composed of repeating units of 1→4 linked pyranosyl uronic acid and 2-amino-deoxyglucopyranose (glucosamine) residues. The uronic acid is composed of L-idopyranosyluronic acid (L-iduronic acid) and D-glucopyranosyluronic acid (D-glucuronic acid) and it possesses a high negative charge [5–7].

Heparin was discovered in 1916 in Toronto, Canada, by Jay McLean under the guidance of William H. Howell. Later, heparin has been extensively studied and commercialized and even nowadays there are several aspects about it that are to be disclosed. Heparin is mainly used as an anticoagulant and antithrombotic in medicine, although it is used and still studied for other uses in other therapeutic fields as well, for example, wound healing, burn injury treatment, inhibition of inflammation, and metastatic spread of tumor cells [8–11]. Also, it is found within the human body and of animals [12], specifically, in the mast cells granules where it interacts with histamine, proteases, and inflammatory mediators. It can also be synthesized synthetically [6].

Heparin is also known as unfractionated heparin (UHF); it is polydisperse, mostly obtained from porcine and bovine mucosa and has been normally utilized for the treatment and prevention of thrombotic events. Heparin is composed of molecular chains of varying lengths from 2000 to 40,000 kDa; its use is restricted to an in-hospital setting, where its dosage can be strictly supervised. On the other hand, low molecular weight heparins (LMWHs) are smaller chains of UFH that can be obtained by various chemical and enzymatic depolymerization processes, and their weight ranges from 2000 to 15000 kDa. They have reduced inhibitory activity against thrombin and they exhibit more predictable pharmacokinetic properties compared with UFH. Other subcategories of LMWH involve low and ultra-low molecular weight heparins (ULMWHs) [13].

Apart from its noble anticoagulant properties, heparin and its derivatives can interact and modulate proteins involved in different biological process such as inflammation and angiogenesis [14]. Still, its mechanisms of action are still under debate. Furthermore, heparin broader use is still impaired due to its strong anticoagulant activity and hemorrhagic complications [15, 16]. This work is devoted to review research on heparin-based nanoparticles for different applications.

2. Heparin-Based Nanoparticles

Heparin has been used in nanoparticle synthesis procedures since some time ago. Heparin-based nanoparticles own enhanced properties when heparin is integrated to them because of its biological properties [17, 18]. Some works are related to synthesis with no specific applications, the synthesis procedure is proposed only, and some other works aim to mention the potential ones as follows.

Nobel metal nanoparticles, for example, gold and silver [19–22] and metal oxide ones [23]; conjugates: silica [24]

and chitosan [25, 26]; and poly(lactide-co-glycolide) [27], complexes [28, 29], and magnetic particles have been synthesized using heparin [30]. When it comes to specifics and applications, the most relevant works are related to the health field, especially cancer treatment, imaging, and detection [31], and they are many and varied taking advantage of heparin uses as an anticoagulant for treatment and prophylaxis of various thromboembolic disease processes, to maintain anticoagulated states in patients on extracorporeal circulation or hemodialysis and to help maintain patency of indwelling vascular catheter [32].

2.1. Cancer Diagnosis and Therapy. Cancer is a quite spread disease nowadays. It was the leading cause of death worldwide, accounting for 8.8 million deaths in 2015 [33]. Therefore, there is an increasing necessity for the development of treatments beside the ones already available, which are surgery, chemotherapy, radiation, and targeted, photodynamic, and immunotherapies. There are some other procedures which include stem cell transplants, hyperthermia, photodynamic and photothermal therapies, blood transfusion and donation, and laser treatment [34].

To understand how cancer develops, it has to be mentioned that healthy cells usually divide in an ordered way and they die when damaged or worn down but when cells divide and grow uncontrollably, they continue forming new ones that replace the normal cells leading to the growth of a tumor. Cancer cells can spread to other parts of the body and infect them, too [35]; therefore, early detection is necessary to avoid it.

Nanoparticles have been studied since some years ago to detect and treat cancer [36, 37]. Work has been devoted to use heparin as a part of a multifunctional nanosystem [38] to detect and treat cancer since it is a biocompatible substance and it is well absorbed by the body due to its biological interactions with proteins, growth factors, chemokines, cytokines, enzymes, and lipoproteins, involved in a variety of biological processes [14]. Also, previous studies have been on the usage of heparin alone on the treatment of cancer and the effects that heparin produces [39–42]. There is a list of drugs that are used for cancer treatment as stated by the National Cancer Institute [43]. Among them, doxorubicin, docetaxel (taxotere), paclitaxel (taxol), and sorafenib have been employed, for example, as part of nanosystems intended for therapeutic purposes. In all cases, after nanoparticle synthesis and the usual characterization (UV-Vis spectra and either TEM/SEM, DLS, or zeta potential), they are tested for cytotoxicity, biocompatibility, antiangiogenic effect, differentiation, drug loading efficiency, apoptosis analysis, cell uptake, and pharmacokinetics, among others. Next, some works devoted to this topic will be mentioned briefly.

Park et al. synthesized an amphiphilic conjugate made of heparin and deoxycholic acid within which doxorubicin was encapsulated in a two-step procedure intended for action on SCC (squamous cell carcinoma). Then, the as-produced nanoparticles were tested for toxicity (to assess their safety as a drug carrier), antitumor effect, and cytotoxicity. The conjugate was proved to have high loading efficiency and release promoting an elevated antitumor effect [44].

Khaliq et al. designed a composite system in which heparin was used to form the heparin/DOX/DEVD-S-DOX complex first. Then, Pluronic F-68 was used to form the composite and to stabilize it. The task of this system is to deliver doxorubicin and the DEVD-S-DOX in a specific tumor site, once being there DOX (doxorubicin) is exposed in the tumor cells triggering apoptosis that subsequently leads to the repetitive activation of caspase-3. Caspases are proteases that control the death and inflammation of cells; they execute apoptosis, and so in the case of this nanosystem, an amplified apoptosis is induced. Murine squamous cell carcinoma (SCC-7) cancer cells were used in this study [45]. Zhang et al. developed an interesting system which comprises two anticancer drugs, ATRA (all trans retinoic acid) and DOX (doxorubicin), the first one being conjugated to LMWH (low molecular weight heparin) and the second one loaded physically, such system was named as DOX-loaded LMWH-ATRA. The most relevant assets in this work are that the cytotoxicity effect on epithelial MCF-7 cells used was maintained and they possessed much higher anticancer activity compared to the free drugs in solution and side effects were reduced [46]. Kim et al. conjugated LMWH (low molecular weight heparin) to (SA) stearylamine in order to create, first, a polymer that was used to synthesize self-assembled nanoparticles, and then, docetaxel was loaded within them. The cell lines used in the study were MCF-7 and MDAM2 231 (human breast carcinoma). From the results, it was concluded that heparin conserved 30% of its anticoagulant activity that the half-life of docetaxel was improved with the formulation used and the growth of the MDAM2 231 cell line was inhibited greatly [47]. In other studies, doxorubicin and letrozole were used to treat this cancer type, too [48–51]. In one study, doxorubicin was combined with curcumin to be delivered by heparin modified poly(L-lactide) grafted polyethylenimine nanoparticles [52]. Yang et al. worked on an immobilized chitosan/heparin Pluronic-coated system for the delivery of sorafenib in gastric cancers. The line cell used for the study was the BCG-823 (gastric adenocarcinoma). It was discovered that these nanoparticles worked better than sorafenib alone for inhibition of cancer cells [53]. Other studies related to gastric cancer were developed by Lai et al. [54].

There is more research that has been carried out concerning cancer but not only of the types already mentioned. For instance, as for liver cancer, Sun et al. synthesized heparin-coated gold nanoparticles for liver specific imaging through computed tomography in vivo [55] and Lin et al. made a combination of nanoparticles, Emodin-Loaded PLGA-TPGS and Heparin Sodium-Loaded PLGA-TPGS ones for chemotherapeutic purposes [56]; colon cancer (oral absorption mechanism and antiangiogenesis effect of taurocholic acid linked heparin docetaxel conjugates) [57]; lung, melanoma, and ovarian cancers [58–61]; melanoma [62]; and heart, spleen, lung, and kidney [63–65]. HeLa cells were also used for a study in which the synthesized nanoparticles did not show an apparent cytotoxicity indicating good biocompatibility [66].

Some research has been directed to coupling already existing therapies, photodynamic, photothermal, and chemotherapy with heparin-based nanoparticles [67] and

photodynamic therapy [68–71]. Some studies have only proved that heparin-based nanosystems have potential as drug carriers but they do not focus on a specific cancer kind (heparin-based nanocapsules as potential drug delivery systems) [72]. There are other works related to potential drug delivery for cancer treatment, although they do not focus on a specific kind. They only point out biocompatibility as well as anticoagulant activity [73].

2.2. Disease Treatment. There are some works on heparin-based nanoparticles, which has been focused on other disease types, for example, bacteria-provoked ones. The *Helicobacter pylori* bacterium was discovered by Warren and Marshall in 1982 from patients with peptic ulcer (*Helicobacter pylori*) [74]. It is a type of microorganism which enters the gastric mucosa and triggers its inflammation. It is responsible for the development of duodenal or gastric ulcers, gastric cancer, and gastric mucosa-associated lymphoid tissue (MALT) lymphoma [75, 76]. Heparin-based nanoparticles have been synthesized with the purpose of treating *H. pylori* producing complexes that attack this microorganism. For *H. pylori* to be eradicated, the agent that is used to attack it has to penetrate the gastric mucosa layer and hold a certain concentration for antibacterial activity within a fixed amount of time. However, the available treatments cause undesired side effects such as bad mouth taste and nausea. Besides this, bacterial resistance is another issue due to patients leaving treatment too soon [77, 78]. Chang et al. synthesized a complex formed by berberine, chitosan, and heparin. Berberine is an alkaloid derived from the barberry plant and it is known to treat gastroenteritis and diarrhea; it has also been shown to inhibit *H. pylori*. Chitosan was employed in this work because of its biocompatibility and adhesion properties and heparin was used because of its ability to bind to cell receptors and to promote ulcer healing [79]. Lin et al. have developed works on this *H. pylori* treatment topic, too. In one of them, a chitosan heparin complex was developed to encapsulate and protect a drug from the gastric acids to treat the *H. pylori* infection specific sites. It showed good stability at 1.2–2.5 pH values and the latter was the follow-up drug model [80]. In another study, genipin was used. Genipin is a natural cross-linker, for its choleric action in liver diseases and its inhibition of *H. pylori*. Their results showed that amoxicillin was successfully released in the specific site avoiding most of its contact with gastric acids, much better than in the previous work [81]. There are other more interesting works related to disease treatment using heparin-based nanoparticles as drug carriers for the treatment of specific illnesses. Ciprofloxacin is an antibiotic used to treat a variety of bacterial infections, for example, typhoid fever, diarrhea, intestinal infection, and pneumonia [82]. Kumara et al. came up with a ciprofloxacin loaded genipin cross-linked chitosan/heparin nanoparticle system to target enteropathogenic bacteria in a simulated gastrointestinal system [83]. Other systems have been developed for multipurpose treatment; Lembo et al.'s heparin nanoassemblies were based on the autoassociation of O-palmitoyl-heparin and α -cyclodextrin in water; it was found that they possessed antiviral activity against herpes simplex viruses of types 1 and 2 (HSV-1 and HSV-2), human

papilloma virus 16 (HVP-16), and the respiratory syncytial virus (SRV) and that this antiviral activity was affected by the sulphation degree of heparin [84]. More research has been carried out on the treatment of antithrombosis [85] and some more on the development of nanosystems although without mentioning a specific disease to be treated, like in the case of stealth nanoparticles (PEGylated nanoparticles) (Heparin-Engineered Mesoporous Iron Metal-Organic Framework Nanoparticles: Toward Stealth Drug Nanocarriers) [86, 87].

2.3. Other Potential Applications. As it has been described so far, heparin-based nanoparticles are potential useful tools in the medicine area, specifically in the cancer and disease treatment area. Some more applications will be covered in this section. Most of them still have to do with the medical area but the studies are fewer than the ones mentioned in the previous sections. As for the rest, they are focused on antimicrobial activity, biosensing, and analyte detection. Medical imaging refers to different technologies used to view the human body to diagnose, monitor, or treat medical conditions. Each type of technology gives different information about the area of the body being studied or treated, related to possible disease, injury, or the effectiveness of medical treatment [88]. Nanoparticles have been engineered for this purpose to improve the technique [89]. In the case of heparin-based ones, some studies have been carried out with good results by using quantum dots (QDs) in *in vitro* studies to assess their interaction with different cell lines, first. For example, in the case of THP-1, A549 and Caco-2 cell lines, it is proved that the QDs show affinity for the nuclear compartment of fixed permeabilised THP-1 and A549 cell lines but that they also remain confined to the cytoplasm of fixed permeabilised Caco-2 cell lines. This study is particularly interesting because, among the disadvantages that QDs pose, they provoke thrombosis and cell death in *in vivo* studies, and these heparin-based gelatin QDs may be useful in the future because of heparin reducing the presence of thrombogenic complications [90]. In another study, the QDs were loaded in heparin-deoxycholic acid conjugates, their oral administration showed no significant toxicity showing that, like in the aforementioned study, the use of QDs is being much less limited. This study was carried out using a rat model [91]. In one more study, QDs were loaded in heparin-deoxycholic acid (DOCA) nanoparticles for the imaging of the gastrointestinal tract, which could be orally administered [92]. On the other hand, not only QDs have been used for imaging purposes, but also other conjugate types, for instance, folate-heparin ones which were loaded with fluorescent dyes within them for tumor imaging as well [93]. Heparin-based nanoparticles have also been included in labeling and targeting investigations. Cell labeling studies have been carried out using superparamagnetic iron oxide nanoparticles that are coated with heparin (HSPIO). These nanoparticles were conjugated to a collagen matrix of cell surface using a polymer linker which remained stable in *in vivo* conditions and used as a Magnetic Resonance Imaging (MRI) agent, offering an alternative to endocytosis [94]. As for targeting, Gonçaves et al. developed heparin-chitosan nanoparticles labeled with rhodamine activated derivative

(5[6]-carboxy-X-rhodamine N-succinimidyl ester (ROX)). The entire system was named CHROX. It was used to target drugs *in vivo* to the sciatic nerve, and such system showed no inflammation issues and good biocompatibility, although the authors mention that nerve regeneration is the topic that will be a follow-up to this research [95]. Bone and tissue-oriented studies have been worked on, too, for example, bone formation [96] and scaffold [97]; tissue engineering [98]; and regeneration [99]. Some other potential applications that are understudied are as follows: antimicrobial activity [100, 101], glucose biosensing [102], analyte detection in solution using a colorimetric approach [103], and surface enhanced Raman spectroscopy [104].

3. Conclusions

The use of heparin-based nanoparticles is an important issue because although it is a material that was discovered many years ago, it has been improved and it continues to be studied to disclose its properties and structure. Additionally, new uses for it are being explored besides the antithrombotic and anti-inflammation ones. The most important and relevant applications are focused on the treatment of cancer and other diseases, followed by bone and tissue engineering, antimicrobial activity, biosensing, and detection. Therefore, the range of potential applications is large and tempting.

As for heparin-based nanoparticles impact, it has to be pointed out that heparin is a biocompatible material that can be obtained naturally and synthetically. Its derivatives are also useful because they have been created to widen its uses in the medical area or to overcome disadvantages or perils. When used for nanoparticle synthesis, it can be chemically modified in several ways, for example, through conjugation and cross-linking to produce nanobiomaterials that can be potentially used for different applications giving them certain functionality for a specific purpose. Heparin can be used for nanoparticle synthesis without being modified at all, too. The studies that have been carried out *in vitro* and *in vivo* for medical applications show that in the near future these heparin-based products could be an excellent option for the development of other alternatives to treat, detect, and prevent diseases in human beings. On the other hand, as for imaging, detection, antimicrobial activity, and biosensing, despite the fact that there are a few studies, they are areas that can be worked on further in order to develop very useful materials. As for nanobiomaterials heparin-based nanoparticles could be integrated to already existing materials to improve their antibacterial and antifungal activities, especially because nowadays several microorganisms have developed a strong resistance to the available common antibiotics. As for detection and biosensing, since heparin structure allows it to interact with other materials such as dyes and biomolecules, there can be a chance to boost the existing detection and sensing techniques available even at very low concentrations. The most relevant heparin-based nanoparticles are the conjugated and cross-linked ones because they are usually synthesized incorporating different materials, but each one of them has a defined role in the specific application, for example, adhesion, biocompatibility, cell uptake, and drug release. In the case

of heparin, it is usually to promote angiogenesis control, antithrombotic, and anti-inflammation activities.

Conflicts of Interest

The authors declare no conflicts of interest.

Acknowledgments

Maria del Pilar Rodriguez-Torres wishes to thank DGAPA (Dirección General de Asuntos de Personal Académico) for the Postdoctoral Stay Scholarship granted at ENES UNAM Unidad Leon; the funding is provided by Projects PAPIME PE-210616 and PAPIIT-IN225516. The authors also wish to acknowledge Red de Farmoquímicos (CONACYT).

References

- [1] P. Heera and S. Shanmugan, "Nanoparticle characterization and application: an overview," *International Journal of Current Microbiology and Applied Sciences*, vol. 4, no. 8, pp. 379–386, 2015.
- [2] S. Hasan, "Review on nanoparticles: their synthesis and types," *Research Journal of Recent Sciences*, vol. 4, pp. 1–3, 2014, Uttar Pradesh (Lucknow Campus).
- [3] L. M. Liz-Marzán and P. V. Kamat, *Nanoscale Materials*. In *Nanoscale Materials*, p. 1–3, Springer US, 1st edition, 2003.
- [4] J. M. Patra, D. Gitishree, and K. H. Baek, "Towards a greener environment: Synthesis and applications of green nanoparticles," *Pakistan Journal of Agricultural Sciences*, vol. 53, no. 2, pp. 345–354, 2016.
- [5] K. Prydz, "Determinants of glycosaminoglycan (GAG) structure," *Biomolecules*, vol. 5, no. 3, pp. 2003–2022, 2015.
- [6] M. Mende, C. Bednarek, M. Wawryszyn et al., "Chemical Synthesis of Glycosaminoglycans," *Chemical Reviews*, vol. 116, no. 14, pp. 8193–8255, 2016.
- [7] B. Casu, A. Naggi, and G. Torri, "Re-visiting the structure of heparin," *Carbohydrate Research*, vol. 403, pp. 60–68, 2015.
- [8] T. W. Barrowcliffe, "Heparin: A Century of Progress. In: Heparin: A Century of Progress," in *Mulloy B. CPP*, pp. 4–17, Springer Berlin, Berlin, Germany, 1st edition, 2012.
- [9] J. Hirsh and V. Fuster, "Guide to anticoagulant therapy part I: heparin," *English J*, pp. 933–938, 2001.
- [10] L. Galvan, "Effects of heparin on wound healing," *Journal of Wound Ostomy & Continence Nursing*, vol. 23, no. 4, pp. 224–226, 1996.
- [11] R. J. Ludwig, "Therapeutic use of heparin beyond anticoagulation," *Current Drug Discovery Technologies*, vol. 6, no. 4, pp. 281–289, 2009.
- [12] "Methods in molecular biology," in *Glycosaminoglycans: Chemistry and Biology*, pp. 3–619, Springer New York Heidelberg Dordrecht London, New York, USA, 2015.
- [13] E. Gray, B. Mulloy, and T. W. Barrowcliffe, "Heparin and low-molecular-weight heparin," *Thrombosis and Haemostasis*, vol. 99, no. 5, pp. 807–818, 2008.
- [14] N. S. Gandhi and R. L. Mancera, "The structure of glycosaminoglycans and their interactions with proteins," *Chemical Biology & Drug Design*, vol. 72, no. 6, pp. 455–482, 2008.
- [15] H. B. Nader, C. C. Lopes, H. A. O. Rocha, E. A. Santos, and C. P. Dietrich, "Heparins and heparinoids: Occurrence, structure and mechanism of antithrombotic and hemorrhagic activities," *Current Pharmaceutical Design*, vol. 10, no. 9, pp. 951–966, 2004.
- [16] J. Hirsh, T. E. Warkentin, S. G. Shaughnessy et al., "Heparin and low-molecular-weight heparin: mechanisms of action, pharmacokinetics, dosing, monitoring, efficacy, and safety," *CHEST*, vol. 119, no. 1, pp. 64S–94S, 2001.
- [17] M. M. Kemp and R. J. Linhardt, "Heparin-based nanoparticles," *Wiley Interdisciplinary Reviews: Nanomedicine and Nanobiotechnology*, vol. 2, no. 1, pp. 77–87, 2010.
- [18] S. E. Sakiyama-Elbert, "Incorporation of heparin into biomaterials," *Acta Biomaterialia*, vol. 10, no. 4, pp. 1581–1587, 2014.
- [19] Y. Guo and H. Yan, "Preparation and characterization of heparin-stabilized gold nanoparticles," *Journal of Carbohydrate Chemistry*, vol. 27, no. 5, pp. 309–319, 2008.
- [20] H. Huang and X. Yang, "Synthesis of polysaccharide-stabilized gold and silver nanoparticles: a green method," *Carbohydrate Research*, vol. 339, no. 15, pp. 2627–2631, 2004.
- [21] M. D. P. Rodríguez-Torres, L. A. Díaz-Torres, P. Salas, C. Rodríguez-González, and M. Olmos-López, "UV photochemical synthesis of heparin-coated gold nanoparticles," *Gold Bulletin*, vol. 47, no. 21, pp. 21–31, 2014.
- [22] H.-S. Kim, S. H. Jun, Y. K. Koo, S. Cho, and Y. Park, "Green synthesis and nanotopography of heparin-reduced gold nanoparticles with enhanced anticoagulant activity," *Journal of Nanoscience and Nanotechnology*, vol. 13, no. 3, pp. 2068–2076, 2013.
- [23] E. Vismara, A. Valerio, A. Coletti et al., "Non-covalent synthesis of metal oxide nanoparticle-heparin hybrid systems: a new approach to bioactive nanoparticles," *International Journal of Molecular Sciences*, vol. 14, no. 7, pp. 13463–13481, 2013.
- [24] B. Silvestri, A. Pezzella, G. Luciani, A. Costantini, F. Tescione, and F. Branda, "Heparin conjugated silica nanoparticle synthesis," *Materials Science and Engineering C: Materials for Biological Applications*, vol. 32, no. 7, pp. 2037–2041, 2012.
- [25] M.-A. Shahbazi and M. Hamidi, "The impact of preparation parameters on typical attributes of chitosan-heparin nanohydrogels: Particle size, loading efficiency, and drug release," *Drug Development and Industrial Pharmacy*, vol. 39, no. 11, pp. 1774–1782, 2013.
- [26] M.-A. Shahbazi, M. Hamidi, and S. Mohammadi-Samani, "Preparation, optimization, and in-vitro/in-vivo/ex-vivo characterization of chitosan-heparin nanoparticles: Drug-induced gelation," *Journal of Pharmacy and Pharmacology*, vol. 65, no. 8, pp. 1118–1133, 2013.
- [27] Y.-C. Kuo and K.-H. Shih, "Loading efficiency and surface conductance of heparin-modified poly(lactide-co-glycolide) nanoparticles," *Colloids and Surfaces B: Biointerfaces*, vol. 71, no. 2, pp. 282–287, 2009.
- [28] S. Boddohi, N. Moore, P. A. Johnson, and M. J. Kipper, "Polysaccharide-based polyelectrolyte complex nanoparticles from chitosan, heparin, and hyaluronan," *Biomacromolecules*, vol. 10, no. 6, pp. 1402–1409, 2009.
- [29] Z. Liu, Y. Jiao, F. Liu, and Z. Zhang, "Heparin/chitosan nanoparticle carriers prepared by polyelectrolyte complexation," *Journal of Biomedical Materials Research Part A*, vol. 83, no. 3, pp. 806–812, 2007.
- [30] S. C. Wuang, K. G. Neoh, E.-T. Kang, D. W. Pack, and D. E. Leckband, "Heparinized magnetic nanoparticles: In-vitro assessment for biomedical applications," *Advanced Functional Materials*, vol. 16, no. 13, pp. 1723–1730, 2006.

- [31] M. Nurunnabi, Z. Khatun, W. C. Moon, G. Lee, and Y. K. Lee, "Heparin based nanoparticles for cancer targeting and noninvasive imaging," *Quant Imaging Med Surg*, vol. 2, no. 3, pp. 219–226, 2012.
- [32] N. M. Acquisto, "Reference module in biomedical sciences," in *Encyclopedia of Toxicology Michael Caplan*, pp. 837–839, Elsevier, 3rd edition, 2014.
- [33] M. H. Forouzanfar et al., "GBD 2015 Risk Factors Collaborators. Global, regional, and national comparative risk assessment of 79 behavioural, environmental and occupational, and metabolic risks or clusters of risks, 1990–2015: a systematic analysis for the global burden of disease," *Lancet*, vol. 388, no. 10053, pp. 1659–1724, 2016.
- [34] A. Sudhakar, "History of cancer, ancient and modern treatment methods," *Journal of Cancer Science and Therapy*, vol. 1, no. 2, pp. 1–4, 2010.
- [35] D. Hanahan and R. A. Weinberg, "The hallmarks of cancer," *Cell*, vol. 100, no. 1, pp. 57–70, 2000.
- [36] K. B. Sutradhar and M. L. Amin, "Nanotechnology in Cancer Drug Delivery and Selective Targeting," *ISRN Nanotechnology*, vol. 2014, pp. 1–12, 2014.
- [37] V. Sanna, N. Pala, and M. Sechi, "Targeted therapy using nanotechnology: focus on cancer," *International Journal of Nanomedicine*, vol. 9, no. 1, pp. 467–483, 2014.
- [38] L. Li, K. M. Huh, Y. Lee, and S. Y. Kim, "Design of a multifunctional heparin-based nanoparticle system for anticancer drug delivery," *Macromolecular Research*, vol. 18, no. 2, pp. 153–161, 2010.
- [39] L. R. Zacharski and J. T. Loynes, "The heparins and cancer," *Current Opinion in Pulmonary Medicine*, vol. 8, no. 1070–5287, pp. 379–382, 2002.
- [40] R. Castelli, F. Porro, and P. Tarsia, "The heparins and cancer: review of clinical trials and biological properties," *Vascular Medicine*, vol. 9, no. 3, pp. 205–213, 2004.
- [41] S. Noble, "Heparins and cancer survival: where do we stand?" *Thrombosis Research*, vol. 133, Supplement 2, pp. S133–S138, 2014.
- [42] T. M. H. Niers, C. P. W. Klerk, M. DiNisio et al., "Mechanisms of heparin induced anti-cancer activity in experimental cancer models," *Critical Review in Oncology/Hematology*, vol. 61, no. 3, pp. 195–207, 2007.
- [43] (NIH) NCI, *A to Z List of Cancer Drugs [Internet]*, 2017, <https://www.cancer.gov/about-cancer/treatment/drugs>.
- [44] K. Park, G. Y. Lee, Y.-S. Kim et al., "Heparin-deoxycholic acid chemical conjugate as an anticancer drug carrier and its antitumor activity," *Journal of Controlled Release*, vol. 114, no. 3, pp. 300–306, 2006.
- [45] N. U. Khaliq, F. C. Sandra, D. Y. Park et al., "Doxorubicin/heparin composite nanoparticles for caspase-activated prodrug chemotherapy," *Biomaterials*, vol. 101, pp. 131–142, 2016.
- [46] T. Zhang, H. Xiong, F. Z. Dahmani et al., "Combination chemotherapy of doxorubicin, all-trans retinoic acid and low molecular weight heparin based on self-assembled multifunctional polymeric nanoparticles," *Nanotechnology*, vol. 26, no. 14, Article ID 145101, 2015.
- [47] K. Park, K. Kim, I. C. Kwon et al., "Preparation and characterization of self-assembled nanoparticles of heparin-deoxycholic acid conjugates," *Langmuir*, vol. 20, no. 26, pp. 11726–11731, 2004.
- [48] L. Mei, Y. Liu, C. Xia, Y. Zhou, Z. Zhang, and Q. He, "Polymer-drug nanoparticles combine doxorubicin carrier and heparin bioactivity functionalities for primary and metastatic cancer treatment," *Molecular Pharmaceutics*, vol. 14, no. 2, pp. 513–522, 2017.
- [49] W. She, N. Li, K. Luo et al., "Dendronized heparin-doxorubicin conjugate based nanoparticle as pH-responsive drug delivery system for cancer therapy," *Biomaterials*, vol. 34, no. 9, pp. 2252–2264, 2013.
- [50] T. Y. Cheang, Z. H. Xing, Z. L. Li et al., "Delivery of AIB1 siRNA by Ca²⁺/PEI/heparin composite nanoparticles effectively inhibits the growth of human breast cancer," *Journal of Materials Chemistry B*, vol. 3, no. 38, pp. 7623–7630, 2015.
- [51] W. Hu, L. Cheng, L. Cheng et al., "Redox and pH-responsive poly (amidoamine) dendrimer-poly (ethylene glycol) conjugates with disulfide linkages for efficient intracellular drug release," *Colloids and Surfaces B: Biointerfaces*, vol. 123, pp. 254–263, 2014.
- [52] Q. Guo, X. Li, Y. Yang et al., "Enhanced 4T1 breast carcinoma anticancer activity by co-delivery of doxorubicin and curcumin with core-shell drug-carrier based on heparin modified poly(l-lactide) grafted polyethylenimine cationic nanoparticles," *Journal of Biomedical Nanotechnology*, vol. 10, no. 2, pp. 227–237, 2014.
- [53] Y.-C. Yang, J. Cai, J. Yin, J. Zhang, K.-L. Wang, and Z.-T. Zhang, "Heparin-functionalized Pluronic nanoparticles to enhance the antitumor efficacy of sorafenib in gastric cancers," *Carbohydrate Polymers*, vol. 136, Article ID 10325, pp. 782–790, 2016.
- [54] C.-K. Lai, Y.-L. Lu, J.-T. Hsieh et al., "Development of chitosan/heparin nanoparticle-encapsulated cytolethal distending toxin for gastric cancer therapy," *Nanomedicine*, vol. 9, no. 6, pp. 803–817, 2014.
- [55] I.-C. Sun, D.-K. Eun, J. H. Na et al., "Heparin-Coated gold nanoparticles for liver-specific CT imaging," *Chemistry - A European Journal*, vol. 15, no. 48, pp. 13276–13347, 2009.
- [56] H. Liu, H. Xu, C. Zhang et al., "Emodin-Loaded PLGA-TPGS Nanoparticles Combined with Heparin Sodium-Loaded PLGA-TPGS Nanoparticles to Enhance Chemotherapeutic Efficacy Against Liver Cancer," *Pharmaceutical Research*, vol. 33, no. 11, pp. 2828–2843, 2016.
- [57] Z. Khatun, M. Nurunnabi, K. J. Cho, Y. Byun, Y. H. Bae, and Y.-K. Lee, "Oral absorption mechanism and anti-angiogenesis effect of taurocholic acid-linked heparin-docetaxel conjugates," *Journal of Controlled Release*, vol. 177, no. 1, pp. 64–73, 2014.
- [58] A. Garg, V. Patel, R. Sharma, A. Jain, and A. K. Yadav, "Heparin-appended polycaprolactone core/corona nanoparticles for site specific delivery of 5-fluorouracil," *Artificial Cells, Nanomedicine and Biotechnology*, vol. 4, pp. 1–10, 2016.
- [59] M. Fazilati, "Anti-neoplastic Applications of Heparin Coated Magnetic Nanoparticles Against Human Ovarian Cancer," *Journal of Inorganic and Organometallic Polymers and Materials*, vol. 24, no. 3, pp. 551–559, 2014.
- [60] P. Liu, M. Gou, T. Yi et al., "The enhanced antitumor effects of biodegradable cationic heparin-polyethyleneimine nanogels delivering HSulf-1 gene combined with cisplatin on ovarian cancer," *International Journal of Oncology*, vol. 41, no. 4, pp. 1504–1512, 2012.
- [61] F. Yang, M. Gou, H. Deng et al., "Efficient inhibition of ovarian cancer by recombinant CXC chemokine ligand 10 delivered by novel biodegradable cationic heparin-polyethyleneimine nanogels," *Oncology Reports*, vol. 28, no. 2, pp. 668–676, 2012.

- [62] L. Hou, J. Yao, J. Zhou, and Q. Zhang, "Pharmacokinetics of a paclitaxel-loaded low molecular weight heparin-all-trans-retinoid acid conjugate ternary nanoparticulate drug delivery system," *Biomaterials*, vol. 33, no. 21, pp. 5431–5440, 2012.
- [63] L. Dai, J. Li, B. Zhang, J. Liu, Z. Luo, and K. Cai, "Redox-responsive nanocarrier based on heparin end-capped mesoporous silica nanoparticles for targeted tumor therapy in vitro and in vivo," *Langmuir*, vol. 30, no. 26, pp. 7867–7877, 2014.
- [64] Y. Yang, Q. F. Guo, J. R. Peng et al., "Doxorubicin-conjugated heparin-coated superparamagnetic iron oxide nanoparticles for combined anticancer drug delivery and magnetic resonance imaging," *Journal of Biomedical Nanotechnology*, vol. 12, no. 11, pp. 1963–1974, 2016.
- [65] X.-H. Peng, Y. Wang, D. Huang et al., "Targeted delivery of cisplatin to lung cancer using ScFvEGFR-heparin- cisplatin nanoparticles," *ACS Nano*, vol. 5, no. 12, pp. 9480–9493, 2011.
- [66] P. Liang, D. Zhao, C.-Q. Wang, J.-Y. Zong, R.-X. Zhuo, and S.-X. Cheng, "Facile preparation of heparin/CaCO₃/CaP hybrid nano-carriers with controllable size for anticancer drug delivery," *Colloids and Surfaces B: Biointerfaces*, vol. 102, pp. 783–788, 2013.
- [67] T. H. Tran, B.-C. Bae, Y.-K. Lee, K. Na, and K. M. Huh, "Heparin-folate-retinoic acid bioconjugates for targeted delivery of hydrophobic photosensitizers," *Carbohydrate Polymers*, vol. 92, no. 2, pp. 1615–1624, 2013.
- [68] V. Revuri, J. Cho, and Y. Lee, "Photosensitizer conjugated iron oxide nanoparticles for simultaneous in vitro magneto-fluorescent imaging guided photodynamic therapy," *Chemical Communications*, vol. 51, pp. 5687–5690, 2015.
- [69] K. H. Bae, H. Mok, and T. G. Park, "Synthesis, characterization, and intracellular delivery of reducible heparin nanogels for apoptotic cell death," *Biomaterials*, vol. 29, no. 23, pp. 3376–3383, 2008.
- [70] L. Li, B.-C. Bae, T. H. Tran, K. H. Yoon, K. Na, and K. M. Huh, "Self-quenchable biofunctional nanoparticles of heparin-folate-photosensitizer conjugates for photodynamic therapy," *Carbohydrate Polymers*, vol. 86, no. 2, pp. 708–715, 2011.
- [71] M. Nafujjaman, V. Revuri, M. Nurunnabi, K. Jae Cho, and Y. Lee, "Photosensitizer conjugated iron oxide nanoparticles for simultaneous in vitro magneto-fluorescent imaging guided photodynamic therapy," *Chemical Communications*, vol. 51, pp. 5687–5690, 2015.
- [72] G. Baier, S. Winzen, C. Messerschmidt et al., "Heparin-based nanocapsules as potential drug delivery systems," *Macromolecular Bioscience*, vol. 15, no. 6, pp. 765–776, 2015.
- [73] C. Argyo, V. Cauda, H. Engelke, J. Rädler, G. Bein, and T. Bein, "Heparin-coated colloidal mesoporous silica nanoparticles efficiently bind to antithrombin as an anticoagulant drug-delivery system," *Chemistry - A European Journal*, vol. 18, no. 2, pp. 428–432, 2012.
- [74] B. E. Dunn, H. Cohen, and M. J. Blaser, "Helicobacter pylori," *Clinical Microbiology Reviews*, vol. 10, no. 4, pp. 720–724, 1997.
- [75] J. G. Kusters, A. H. M. van Vliet, and E. J. Kuipers, "Pathogenesis of *Helicobacter pylori* infection," *Clinical Microbiology Reviews*, vol. 19, no. 3, pp. 449–490, 2006.
- [76] S. Suerbaum and P. Michetti, "Helicobacter pylori infection," *The New England Journal of Medicine*, vol. 347, no. 15, pp. 1175–1186, 2002.
- [77] P. Malfertheiner, F. Megraud, C. A. O'Morain et al., "Management of *Helicobacter pylori* infection—the Maastricht IV/Florence consensus report," *Gut*, vol. 61, no. 5, pp. 646–664, 2012.
- [78] B. Stenström, A. Mendis, and B. Marshall, "Helicobacter pylori: The latest in diagnosis and treatment," *Australian Family Physician*, vol. 37, no. 8, pp. 608–612, 2008.
- [79] C.-H. Chang, W.-Y. Huang, C.-H. Lai et al., "Development of novel nanoparticles shelled with heparin for berberine delivery to treat *Helicobacter pylori*," *Acta Biomaterialia*, vol. 7, no. 2, pp. 593–603, 2011.
- [80] Y.-H. Lin, J.-H. Lin, S.-C. Chou et al., "Berberine-loaded targeted nanoparticles as specific *Helicobacter pylori* eradication therapy: In vitro and in vivo study," *Nanomedicine*, vol. 10, no. 1, pp. 57–71, 2015.
- [81] Y.-H. Lin, S.-C. Tsai, C.-H. Lai, C.-H. Lee, Z. S. He, and G.-C. Tseng, "Genipin-cross-linked fucose-chitosan/heparin nanoparticles for the eradication of *Helicobacter pylori*," *Biomaterials*, vol. 34, no. 18, pp. 4466–4479, 2013.
- [82] K. Vance-Bryan, D. R. P. Guay, and J. C. Rotschafer, "Clinical Pharmacokinetics of Ciprofloxacin," *Clinical Pharmacokinetics*, vol. 19, no. 6, pp. 434–461, 1990.
- [83] G. V. Kumar, C.-H. Su, and P. Velusamy, "Ciprofloxacin loaded genipin cross-linked chitosan/heparin nanoparticles for drug delivery application," *Materials Letters*, vol. 180, no. 2016, pp. 119–122, 2016.
- [84] C. Chen, S. Li, K. Liu, G. Ma, and X. Yan, "Co-Assembly of Heparin and Polypeptide Hybrid Nanoparticles for Biomimetic Delivery and Anti-Thrombus Therapy," *Small*, vol. 34, pp. 4719–4725, 2016.
- [85] E. Bellido, T. Hidalgo, M. V. Lozano et al., "Heparin-Engineered Mesoporous Iron Metal-Organic Framework Nanoparticles: Toward Stealth Drug Nanocarriers," *Advanced Healthcare Materials*, vol. 4, no. 8, pp. 1246–1257, 2015.
- [86] S. Salmaso and P. Caliceti, "Stealth Properties to Improve Therapeutic Efficacy of Drug Nanocarriers," *Journal of Drug Delivery*, vol. 2013, pp. 1–19, 2013.
- [87] M. Socha, P. Bartecki, C. Passirani et al., "Stealth nanoparticles coated with heparin as peptide or protein carriers," *Journal of Drug Targeting*, vol. 17, no. 8, pp. 575–585, 2009.
- [88] P. Suetens, "Fundamentals of medical imaging," in *Fundamentals of Medical Imaging*, pp. 128–158, 2009.
- [89] S. K. Nune, P. Gunda, P. K. Thallapally, Y.-Y. Lin, M. Laird Forrest, and C. J. Berkland, "Nanoparticles for biomedical imaging," *Expert Opinion on Drug Delivery*, vol. 6, no. 11, pp. 1175–1194, 2009.
- [90] C. M. Maguire, O. K. Mahfoud, T. Rakovich et al., "Heparin conjugated quantum dots for in vitro imaging applications," *Nanomedicine: Nanotechnology, Biology and Medicine*, vol. 10, no. 8, pp. 1853–1861, 2014.
- [91] Z. Khatun, M. Nurunnabi, D. Y. Lee et al., "Optical imaging, biodistribution and toxicity of orally administered quantum dots loaded heparin-deoxycholic acid," *Macromolecular Research*, vol. 23, no. 7, pp. 686–695, 2015.
- [92] Z. Khatun, M. Nurunnabi, K. J. Cho, and Y. Lee, "Imaging of the GI tract by QDs loaded heparin-deoxycholic acid (DOCA) nanoparticles," *Carbohydrate Polymers*, vol. 90, no. 4, pp. 1461–1468, 2012.
- [93] J. Wang, D. Ma, Q. Lu et al., "An unusual role of folate in the self-assembly of heparin-folate conjugates into nanoparticles," *Nanoscale*, vol. 7, no. 37, pp. 15185–15190, 2015.
- [94] Y. H. Hwang and D. Y. Lee, "Magnetic resonance imaging using heparin-coated superparamagnetic iron oxide nanoparticles for cell tracking in vivo," *Quantitative Imaging in Medicine and Surgery*, vol. 2, no. 2, pp. 118–123, 2012.

- [95] N. P. Gonçalves, H. Oliveira, A. P. Pêgo, and M. J. Saraiva, "A novel nanoparticle delivery system for in vivo targeting of the sciatic nerve: Impact on regeneration," *Nanomedicine*, vol. 7, no. 8, pp. 1167–1180, 2012.
- [96] O. Jeon, S. J. Song, S. Kang, A. J. Putnam, and B. Kim, "Enhancement of ectopic bone formation by bone morphogenetic protein-2 released from a heparin-conjugated poly(l-lactic-co-glycolic acid) scaffold," *Biomaterials*, vol. 28, no. 17, pp. 2763–2771, 2007.
- [97] S. E. Kim, O. Jeon, J. B. Lee et al., "Enhancement of ectopic bone formation by bone morphogenetic protein-2 delivery using heparin-conjugated PLGA nanoparticles with transplantation of bone marrow-derived mesenchymal stem cells," *Journal of Biomedical Science*, vol. 15, no. 6, pp. 771–777, 2008.
- [98] Y. Yang, H. Tang, A. Köwitsch et al., "Novel mineralized heparin-gelatin nanoparticles for potential application in tissue engineering of bone," *Journal of Materials Science: Materials in Medicine*, vol. 25, no. 3, pp. 669–680, 2014.
- [99] B. Wang, L. Tan, D. Deng et al., "Novel stable cytokine delivery system in physiological pH solution: Chitosan oligosaccharide/heparin nanoparticles," *International Journal of Nanomedicine*, vol. 10, pp. 3417–3427, 2015.
- [100] K. Vijaya Sudhakar, D. Srinivasa Rao, and P. Naga Babu, "K.R.S.Samba Siva Rao SP. Polysaccharide based synthesis characterization of heparin stabilized silver nanoparticles and its antibacterial activity," *Drug Invention Today*, vol. 6, no. 1, pp. 77–83, 2014.
- [101] M. M. Kemp, A. Kumar, D. Clement, P. Ajayan, S. Mousa, and R. J. Linhardt, "Hyaluronan- and heparin-reduced silver nanoparticles with antimicrobial properties," *Nanomedicine*, vol. 4, no. 4, pp. 421–429, 2009.
- [102] C. Sun, Y. Niu, F. Tong et al., "Preparation of novel electrochemical glucose biosensors for whole blood based on antibiofouling polyurethane-heparin nanoparticles," *Electrochimica Acta*, vol. 97, pp. 349–356, 2013.
- [103] Y. Park, A.-R. Im, Y. N. Hong, C.-K. Kim, and Y. S. Kim, "Detection of malathion, fenthion and methidathion by using heparin-reduced gold nanoparticles," *Journal of Nanoscience and Nanotechnology*, vol. 11, no. 9, pp. 7570–7578, 2011.
- [104] M. D. P. Rodríguez-Torres, L. A. Díaz-Torres, and S. Romero-Servin, "Heparin assisted photochemical synthesis of gold nanoparticles and their performance as SERS substrates," *International Journal of Molecular Sciences*, vol. 15, no. 10, pp. 19239–19252, 2014.

Research Article

Practical Solution for Effective Whole-Body Magnetic Fluid Hyperthermia Treatment

Hiroaki Mamiya,¹ Yoshihiko Takeda,^{1,2} Takashi Naka,¹ Naoki Kawazoe,¹
Guoping Chen,^{1,2} and Balachandran Jeyadevan³

¹National Institute for Materials Science, Sengen 1-2-1, Tsukuba 305-0047, Japan

²University of Tsukuba, 1-1-1 Tennodai, Tsukuba, Ibaraki 305-8577, Japan

³The University of Shiga Prefecture, Hikone 522-8533, Japan

Correspondence should be addressed to Hiroaki Mamiya; mamiya.hiroaki@nims.go.jp

Received 21 June 2017; Accepted 20 November 2017; Published 13 December 2017

Academic Editor: Mohammad Mansoob Khan

Copyright © 2017 Hiroaki Mamiya et al. This is an open access article distributed under the Creative Commons Attribution License, which permits unrestricted use, distribution, and reproduction in any medium, provided the original work is properly cited.

Magnetic fluid hyperthermia therapy is considered as a promising treatment for cancers including unidentifiable metastatic cancers that are scattered across the whole body. However, a recent study on heat transfer simulated on a human body model showed a serious side effect: occurrences of hot spots in normal tissues due to eddy current loss induced by variation in the irradiated magnetic field. The indicated allowable upper limit of field amplitude H_{ac} for constant irradiation over the entire human body corresponded to approximately 100 Oe at a frequency f of 25 kHz. The limit corresponds to the value $H_{ac}f$ of 2.5×10^6 Oe·s⁻¹ and is significantly lower than the conventionally accepted criteria of 6×10^7 Oe·s⁻¹. The present study involved evaluating maximum performance of conventional magnetic fluid hyperthermia cancer therapy below the afore-mentioned limit, and this was followed by discussing alternative methods not bound by standard frameworks by considering steady heat flow from equilibrium responses of stable nanoparticles. Consequently, the clarified potentials of quasi-stable core-shell nanoparticles, dynamic alignment of easy axes, and short pulse irradiation indicate that the whole-body magnetic fluid hyperthermia treatment is still a possible candidate for future cancer therapy.

1. Introduction

In principle, “if a steel pan made for induction heating (IH) cooking appliances is diced up into ultra-small pieces (magnetic nanoparticles) and selectively delivered to metastasized tiny cancers, and if the entire human body is then placed on a cooking top, all cancers including unidentifiable ones will be burned without long-term side effects, resulting in a complete cure.” The realization of this scenario corresponds to an ideal therapy, and thus complete body magnetic fluid hyperthermia cancer therapy is intensively investigated by previous studies as an option in new cancer treatments to replace surgery, radiation therapy, and chemotherapy [1–8]. However, the selective annihilation of cancer cells, leaving the normal cells safe, is debatable since normal tissues are also warmed up due to eddy current loss.

The International Commission on Non-Ionizing Radiation Protection has established guidelines that are intended to protect the human body from harmful health effects by restricting exposure to electromagnetic waves [9]. The basic limit for occupational exposure to the entire body in terms of specific absorption rate (which is equal to the amount of heat generated) corresponds to 0.4 mW/cm³ based on the guidelines [9]. A safety limit based on some clinical tolerance tests on healthy volunteers has been known as Brezovich criterion where $H_{ac}f$ product should not go beyond 6×10^6 Oe·s⁻¹ [10]. However, this value applies to healthy individuals, and it may not be applicable to individuals who face serious health issues. Therefore, Hergt et al. [11] proposed a maximum of approximately $H_{ac}f$ of 6×10^7 Oe·s⁻¹ that can be permitted for localized hyperthermia treatments of patients with serious health conditions. This value is referenced by numerous studies

and is considered as a de facto standard for magnetic fluid hyperthermia cancer therapy. Thus, magnetic nanoparticles corresponding to an ultrasmall IH cooking pan were developed based on this irradiation condition.

Recently, Dössel and Bohnert [12] simulated the electromagnetic field distribution and the flow of heat from irradiation on a detailed human body model. The results at $f = 100$ kHz and $H_{ac} = 100$ Oe indicated that hot spots appeared in certain portions of muscles and fat in which the temperature elevation reached 10°C after 5 min despite considering the cooling effects of blood flow. The temperature elevation curves were used to estimate the thermal relaxation time τ of the hot spots that corresponded to several tens of minutes. This indicated that thermal insulation could be the reason for the existence of the hot spots. The study surmised that the allowable upper limit of H_{ac} for constant irradiation over the entire human body corresponded to 100 Oe at f of 25 kHz. The limit corresponds to the value $H_{ac}f$ of 2.5×10^6 Oe·s $^{-1}$. It should be noted that the condition estimated in the practical simulation significantly deviates from the long-accepted criteria. This finding is important because we cannot measure the deep body temperature during the treatment, although the improvement in accuracy for the simulation is an issue for future research.

In the present study, the new limit is considered to clarify whether or not the heating power of the present magnetic nanoparticles is sufficient to annihilate cancer cells including unidentifiable metastatic tiny cancerous areas scattered throughout the body via conventional magnetic fluid hyperthermia therapy. This is followed by a discussion on alternative strategies that are not bound by conventional frameworks of magnetic fluid hyperthermia cancer treatment. It should be noted that, with the exception of W , Gaussian-cgs units are used in the relationship with respect to the tissue size.

2. Model

2.1. Heating Power of Magnetic Nanoparticles. Magnetic hysteresis and eddy current losses heat a pan during IH cooking. Additionally, an ultrasmall pan (magnetic nanoparticles) can rotate in the applied magnetic field unlike a *regularly used* pan due to its small size. These rotations generate frictional heat [13]. Thus, the study begins by reexamining each heating mechanism briefly. First, with respect to magnetic hysteresis losses, the amount of heat generated, P_h , for a unit volume of magnetic nanoparticles per unit time is derived as follows:

$$P_h = 4\pi \cdot f \int_{\text{Loop}} \mathbf{H} d\mathbf{M}, \quad (1)$$

for irradiation of the ac magnetic field, $H = H_{ac} \sin(2\pi ft)$, where \mathbf{H} denotes the magnetic field and \mathbf{M} denotes the magnetization. The value of the integral corresponds to the area of the hysteresis loop, and it is maximized at $4M_s H_{ac}$ in the case where the magnetization reversal occurs coherently in all nanoparticles when H corresponds to $\pm H_{ac}$, and M_s denotes the saturation magnetization. In other words, P_h , is largest when the magnetic hysteresis loop is a square with width of

$2H_{ac}$. However, it should be noted that it is not possible to realize such ideal reversals in actual systems. Hence, the ratio, η_{sq} , of $\int_{\text{Loop}} \mathbf{H} d\mathbf{M}$ to $4M_s H_{ac}$ is considered as an index that represents the squareness of the magnetic hysteresis loop and the equation is reexpressed as follows:

$$P_h = 16\pi M_s \eta_{sq} H_{ac} f. \quad (2)$$

At this stage, it is necessary to consider the relaxation loss of magnetic nanoparticles that is generated when the magnetic response is given by $M = \chi' H_{ac} \sin(2\pi ft) - \chi'' H_{ac} \cos(2\pi ft)$, where χ' and χ'' denote the in-phase and out-of-phase components, respectively, of the ac susceptibility. This loss can be expressed as $4\pi^2 \chi'' H_{ac}^2 f$ by substituting M into (1). It should be noted that the relaxation loss is actually a type of hysteresis loss and $\eta_{sq} = \pi \chi'' H_{ac} / 4M_s$ is always less than unity.

Friction heat generated from the rotation of particles is considered. The work ΔW_T performed by the friction torque \mathbf{T} while a small rotation of $\Delta\theta$ occurs corresponds to $\mathbf{T} \cdot \Delta\theta$. For the purpose of simplicity, it is assumed that the magnetization vector $\boldsymbol{\mu}$, which is equal to $\mathbf{M}V$, is fixed in the direction of the easy axis of particles in a manner similar to a small permanent magnet, where V denotes volume of the particle. In this case, the friction dominates the rotation with respect to the inertia-less limit, and \mathbf{T} always balances the magnetic torque corresponding to $4\pi\boldsymbol{\mu} \times \mathbf{H}$. Thus, the following expression is obtained:

$$\begin{aligned} \Delta W_T &= -4\pi\boldsymbol{\mu}H \sin\theta \Delta\theta = 4\pi H \Delta(\boldsymbol{\mu} \cos\theta) \\ &= 4\pi H V \Delta M_z, \end{aligned} \quad (3)$$

where θ denotes the angle between \mathbf{H} and $\boldsymbol{\mu}$ (which is in the direction of the easy axis). The amount of friction heat P_f generated per unit volume per unit time is therefore expressed as follows:

$$P_f = f \cdot \int_{\text{Loop}} \frac{dW_T}{V} = 4\pi f \int_{\text{Loop}} \mathbf{H} d\mathbf{M}. \quad (4)$$

This equation is equivalent to (1) and indicates that the amount of energy dissipated by friction is equal to the input magnetic energy. Thus, only the names that describe the evolved heat vary depending on the focus of attention, that is, hysteresis loss or friction heat as described above.

Conversely, an eddy current loss P_e exists that corresponds to a heat source derived from electromagnetic induction. The induced electromotive force in any closed circuit is equal to the negative of the time rate of change of the magnetic flux enclosed by the circuit, and thus the per unit volume and unit time average of P_e for a spherical particle with electrical conductivity σ and radius R are as follows:

$$P_e = \frac{4}{5} \pi^2 \sigma R^2 \int \left[2\pi f H_{ac} + \left(\frac{\partial M}{\partial t} \right) \right]^2 dt. \quad (5)$$

Thus, the total amount of heat generated in magnetic nanoparticles can be expressed as $P_h + P_e$, since sources of heat in the above two cases are completely different.

2.2. Thermal Models of Tumor and Hot Spot Portion. To discuss the effectiveness of hyperthermia treatments, it is necessary to model the heat flow generated in the magnetic nanoparticles accumulated in a tumor. To consider the tumor, it is not necessary to use finite element method despite the significant dependence of thermal conductivity λ on the organ type (typically, $0.003\text{--}0.006\text{ WK}^{-1}\text{ cm}^{-1}$ [14]) because a feature of this therapy includes treatments of small unidentifiable metastatic cancers with an approximate diameter d_c of 1 cm, within which thermal properties are assumed homogeneous. According to Andr a et al. [15], the heat at $2\pi\lambda\Delta Td_c$ is roughly dissipated by conduction when such a tumor is steadily maintained at a temperature that exceeds the temperature of the surrounding area by ΔT . Conversely, the blood flow in tumor tissues transfers heat at the rate $F_b(\pi d_c^3/6)c_{vb}\Delta T$, where C_{vb} denotes the blood specific heat and approximately corresponds to $4\text{ JK}^{-1}\text{ cm}^{-3}$, while F_b corresponds to the tumor tissue blood perfusion rate and it varies based on the type, phase, size, and temperature of the tumor. Typically, F_b is lower than that of the corresponding normal tissue and is less than 0.01 s^{-1} [16]. Therefore, the heating power density required to elevate the temperature of tumor with a d_c of 1 cm corresponds to $(12\lambda d_c^{-2} + F_b C_b)\Delta T \sim 0.1\Delta T\text{ W/cm}^3$ by assuming higher values for F_b and λ as 0.01 s^{-1} and $0.006\text{ WK}^{-1}\text{ cm}^{-1}$, respectively. For the purposes of subsequent discussion, it is necessary to remember that the thermal relaxation time in such cancers $\tau_c = (d_c^2 \cdot c_c)/27\lambda$ corresponds to 23 s [17] when specific heat, c_c , is assumed to correspond to $3.7\text{ JK}^{-1}\text{ cm}^{-3}$.

Now, the model of the hot spot portions proposed by D ssel and Bohnert is considered. Specifically, it is necessary to simulate the temperature distributions in a human body that is exposed to ac magnetic fields by using Bio-heat equation. However, it is possible to roughly estimate the temperature of the hot spot portion T_h by using the following simple equation because the temperature variation for each organ, reported by D ssel and Bohnert, is actually approximated by single exponential relaxation, respectively. This is expressed as follows:

$$C_n \frac{dT_h}{dt} = P_n - \frac{C_n}{\tau_h} (T_h - T_0), \quad (6)$$

where P_n , C_n , and τ_h denote the nominal heat generation, the specific heat, and relaxation time at the hot spot portions, respectively, and T_0 denotes the original temperature. For example, the results of curve fitting for the temperature variations of the hot spot portion in the muscle indicate that P_n and τ_h , correspond to 0.034 W/cm^3 and $1.2 \times 10^3\text{ s}$, respectively, for $H_{ac}f = 5 \times 10^6\text{ Oe}\cdot\text{s}^{-1}$. For $H_{ac}f = 1 \times 10^7\text{ Oe}\cdot\text{s}^{-1}$, P_n and τ_h correspond to 0.137 W/cm^3 and $1.2 \times 10^3\text{ s}$, respectively. C_n is set as $3.7\text{ JK}^{-1}\text{ cm}^{-3}$ for the above cases. It should be noted that long relaxation times indicate thermal insulation of the hot spot portion. The fact that P_n is almost proportional to $(H_{ac}f)^2$ is consistent with the feature of the eddy current loss, although details of actual current circuits are unknown. This indicates the validity of the approximation, and thus the hot spot temperature can be approximately

calculated by using (6) with above parameters derived from the simulated results.

3. Results and Discussion

3.1. Conventional Magnetic Fluid Hyperthermia. For the purposes of biosafety, magnetic nanoparticles consisting of iron were examined as various types of nanomedicine because a high amount of iron (0.1 mg/cm^3) is always stored in the body. Specifically, iron oxides, such as magnetite, were actually used since metallic iron is easily oxidized in the nanoform. Therefore, the survey of the conventional method is initiated by calculating the heating power of the magnetite nanoparticles by implementing actual figures. Presently, $4\pi M_s$, σ , R , and the density are set as 5 kG , 10^4 Sm^{-1} , 10 nm , and 5.2 g/cm^3 , respectively. Simple analyses on the results of typical hyperthermia studies indicate that the values of η_{sq} are typically in the range of $0.2\text{--}0.3$ [18]; and thus η_{sq} is corresponding to 0.3 . With respect to the condition of irradiating magnetic field, the value of $H_{ac}f = 2.5 \times 10^6\text{ Oe}\cdot\text{s}^{-1}$ is selected as an upper limit as stated above. The substitution of these values in (2) indicates that P_h in this instance corresponds to 120 W/cm^3 (which is 23 W/g) when P_e corresponds to $1 \times 10^{-4}\text{ W/cm}^3$ on the assumption that μ is reversed in the time scale comparable to Larmor precession $\sim 10^{-9}\text{ s}$. Therefore, it is possible to ignore the eddy current loss in magnetite nanoparticles in contrast to the hysteresis loss.

Conversely, it is considered that hyperthermia treatments are conventionally performed in the range of $42\text{--}43^\circ\text{C}$ although an established value does not exist [1, 3]. The calculation shown in the prior section indicates that the heating power density for increasing the temperature of tumor with a d_c of 1 cm by $\Delta T = 5\text{ K}$ approximately corresponds to 0.5 W/cm^3 . The heating power density can be achieved when a large amount of magnetite with P_h of 23 W/g is accumulated at a concentration of 22 mg/cm^3 in tumor tissues. In contrast, Huang and Hainfeld [19] reported that they injected ferric oxide nanoparticles intravenously via a tail vein, and, consequently, the results indicated that nanoparticles accumulated in the tumor at a concentration of approximately 1.9 mg/cm^3 . This concentration corresponds to the top class performance at present. However, it is significantly less than the required figures. Thus, the current discussion indicates that conventional hyperthermia treatment using magnetite nanoparticles is impractical for unidentifiable tiny cancers areas scattered throughout the body without significant advancements in drug delivery technology in the future.

An easy method involves eliminating the focus on the whole-body treatment by drug delivery techniques and focusing instead on identified larger cancer treatments in a local area by direct injection. This is because the heat generated by eddy current loss in hot spot portions is proportional to the cross-sectional area through which the magnetic flux passes as discussed above. Hence, restricting an irradiation range to local area suppresses temperature elevation in the hot spot portion. Furthermore, the temperature elevation of tumors can become significant as the size of tumors increases

because the heat dissipation is proportional to the area of the cancer surface while the heating power afforded by the accumulated nanoparticles is proportional to the volume. Additionally, a direct injection on the identified cancers enables the enhancement of the concentration of nanoparticles inside tumors when compared with that in other drug delivery techniques. However, we know that larger cancerous area at known positions can be also removed through surgery. Therefore, it is still important to examine other solutions for the whole-body treatment by considering points overlooked in conventional magnetic fluid hyperthermia treatments.

3.2. Alternative Strategies. As described in the preceding section, the conventional hyperthermia treatment using magnetite nanoparticles is ineffective with respect to tiny cancers scattered throughout the body. To resolve this, it is necessary to shift the standpoint by considering steady heating by using the equilibrium response of stable nanoparticles to those for temporary heating from a nonequilibrium response of quasi-stable nanoparticles in order to clarify the manners to maximize each factor in (2). First, the saturation magnetization M_s is considered. For example, only iron oxide nanoparticles were commercially used for magnetic fluids in machines due to their excellent oxidization resistance, although metallic iron has much higher M_s . This is because industrial products generally need durability exceeding ten years. On the basis of such experience, iron oxide nanoparticles have been examined for hyperthermia treatments. Nevertheless, it should be noticed that the hyperthermia treatment period is significantly shorter. Hence, the iron oxide shell, iron core nanoparticles can be considered as a candidate despite instability for long-term usage. This substance includes a large value of M_s for the iron core and biocompatibility of the iron oxide shell. Previous studies indicated that the nanoparticles with this type of structure possess a saturation magnetization $4\pi M_s$ of 12 kG at 14 nm [20] and 16 kG at 40 nm [21], which is twice that of iron oxide. Little is, however, known as to their long-term durability. Thus, the stability of magnetization for the commercially available core-shell nanoparticles ($4\pi M_s = 12$ kG) obtained from BoutiQ Nanoparticle Solutions was checked by using an extraction method (PPMS, Quantum Design). Consequently, the results indicated that the magnetization did not decline after six months from when the substance was received as shown in Figure 1. As expected, the iron oxide of the shell also serves as a surface protection layer. Hence, it is applicable for magnetic fluid hyperthermia treatments because such treatments are typically completed in half year at most, although it may become difficult to maintain excellent dispersion stability for over several months because the larger M_s strengthens effects of the interparticle interactions.

Subsequently, the squareness of magnetic hysteresis loop, η_{sq} , is considered. As is widely known, alignment of easy axes of single domain nanoparticles improves the squareness, and thus easy axes orientation in static magnetic fields are widely employed prior to sintering permanent magnets to improve their performance [22]. In contrast to these types of ceramics, the easy axes of nanoparticles, starts to thermally fluctuate immediately after cutting the static magnetic field in the

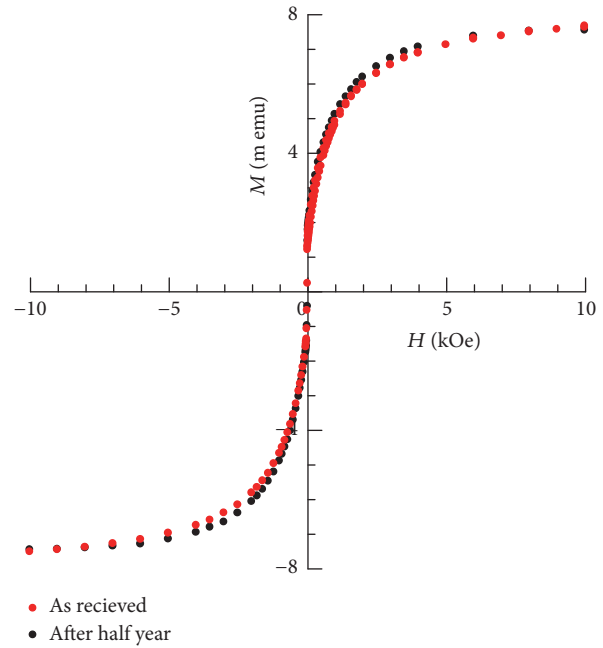


FIGURE 1: Magnetization curves of magnetic fluid containing Fe/FeO core/shell nanoparticles. The red dots indicate the curve immediately after the nanoparticles are received while the black dots show the curve after half a year has elapsed.

human body. On the other hand, the continuous application of a large static magnetic field biases the field variation range from the hysteresis loop. Therefore, it is actually difficult to increase the value by η_{sq} by using a static magnetic field. Recently, a study employed a Brownian dynamics simulation for rotatable magnetic nanoparticles and indicated that these types of nanoparticles form nonequilibrium structure in ac magnetic fields and the orientation of the easy axes occurs under a certain condition [13]. Therefore, the capability to steadily align the easy axes is examined by applying an ac magnetic field using an in situ small angle X-ray scattering experiment in static and ac magnetic fields. Insets in Figure 2 show the two-dimensional contour diagrams of the intensity of X-rays scattered by magnetite nanoparticles (a) in a zero magnetic field, (b) in static magnetic field of 1000 Oe, and (c) in an AC magnetic field with H_{ac} of 660 Oe and f of 100 kHz, where the average size, M_s , and the coercivity of the nanoparticles correspond to 17.4 nm, 3.5 kG, and 53 Oe, respectively. The findings readily indicate that the contour lines change from circles to diamonds when static as well as ac magnetic fields are applied. The intensity dependence of circumferential angle symmetry is fourfold not only in a static magnetic field, but also in an AC magnetic field with comparable oscillation in amplitude as shown in Figure 2. These results indicate that, apart from the details, the ac magnetic field can steadily align the cuboidal magnetite nanoparticles in a manner similar to the static magnetic field. This fact is consistent with the prediction of the previous Brownian dynamics simulation, which indicated that η_{sq} can be increased to 0.8 [13]. Consequently, the squareness of the magnetic hysteresis loop can be improved by increasing H_{ac}

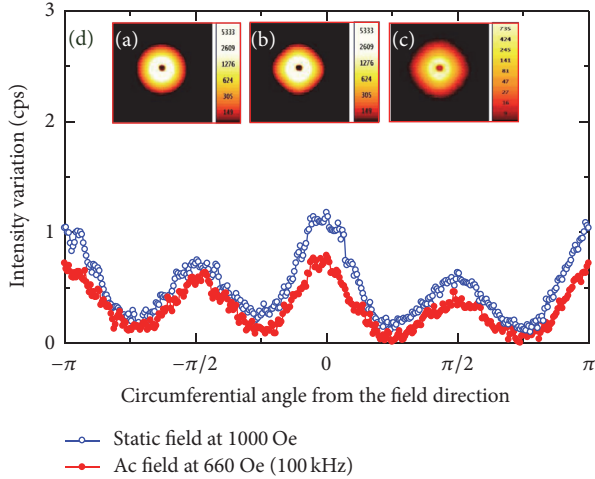


FIGURE 2: Two-dimensional contour diagrams of small angle X-ray scattering intensity for magnetite nanoparticles (a) in a zero magnetic field, (b) in static magnetic field of 1000 Oe, and (c) in ac magnetic field with H_{ac} of 660 Oe and f of 100 kHz. (d) Circumferential angle dependencies of small angle X-ray scattering intensities in a scattering vector range from 0.4 nm^{-1} to 0.6 nm^{-1} .

and decreasing f even when the value of $(H_{ac}f)^2$ is restricted to suppress the occurrence of hot spots.

Prior to examining the next topic, it is necessary to focus attention on the issue of the switching field distribution of magnetic nanoparticles. As widely known [22], the existence of the switching field distribution reduces the squareness of the magnetic hysteresis loop, and thus it is necessary to prepare magnetic nanoparticles without anisotropy dispersion. However, there is very little agreement with respect to the effective origin of magnetic anisotropy even for iron oxide nanoparticles that are widely used for over half a century, not to mention the recently developed core-shell nanoparticles. Hence, clarification of the origin is another critical issue.

Finally, it is necessary to consider the remaining parameters, H_{ac} and f , subject to the occurrence of hot spots. Recalling daily experiences, the main point here is that exposure to high temperatures even only for a short period of time leads to skin burns. For example, the time required for thermal damage corresponds to a couple of minutes at 50°C and to several hours at 44°C [23]. Interestingly, extant studies did not focus on this type of temporary heating by pulsed irradiation in the development of magnetic nanoparticles for hyperthermia treatments, although researchers in the field of hyperthermia treatments always considered irradiation duration. Hence, the present study does not consider the fixed idea that the treatments are performed in the steady state and considers the possibility of short pulse heating at high magnetic field amplitudes prior to storing the heat in the thermally insulated tissues. An example with $H_{ac}f$ of $1 \times 10^7 \text{ Oe}\cdot\text{s}^{-1}$ (10 kHz, 1000 Oe) is considered. With respect to this applied magnetic field, easy axes orientation with η_{sq} of 0.8 is assumed for the above-mentioned core-shell nanoparticles with $4\pi M_s$, of 16 kG considered as an ideal case. The concentration of nanoparticles in the tumor involves

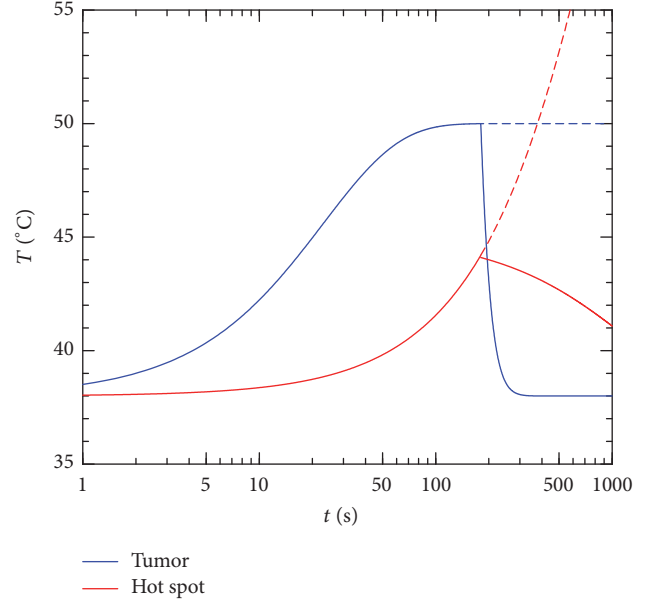


FIGURE 3: Calculated heating curves of tiny tumors and hot spot portions in normal tissues by pulsed irradiation of ac magnetic field. Details are described in the text.

setting the practical value at $2 \text{ mg}/\text{cm}^3$ [19]. Under these conditions, the maximum generated heat corresponds to $1.2 \text{ W}/\text{cm}^3$ inside the tiny tumor with a d_c of 1 cm. Under these conditions, a simple calculation using the above-mentioned τ_c of 23 s and c_c of $3.7 \text{ J K}^{-1} \text{ cm}^{-3}$ indicates that the temperature of tiny tumors would exceed 49°C for an exposure time corresponding to $t = 60 \text{ s}$ as shown in Figure 3. Then, when the irradiation ceases at a time t of 180 s, the temperature drops rapidly. In this case, the tumor is burned at 50°C for 2 min, which is sufficient to damage the tumor.

It is necessary to check the temperature at the hot spot portions in normal tissues under the afore-mentioned conditions. The temperature elevation under the same condition of $H_{ac}f = 1 \times 10^7 \text{ Oe}\cdot\text{s}^{-1}$ curve was calculated by using (6) and $0.137 \text{ W}/\text{cm}^3$, $3.7 \text{ J K}^{-1} \text{ cm}^{-3}$, and $1.2 \times 10^3 \text{ s}$ for P_n , C_n , and τ_h , respectively. The result shown in Figure 3 indicates that the temperature reaches 44°C at $t = 180 \text{ s}$. If the irradiation is continued constantly, then the temperature increases to 83°C finally. Conversely, the irradiation is terminated immediately after the temperature reached 44°C in the example. Consequently, the temperature of normal tissues does not exceed 44°C even at the hot spot portions as indicated by the solid line. The thermal damage for a couple of minutes is negligible below 44°C . Thus, this calculation indicates that it is possible to eradicate a metastatic cancer of roughly 1 cm that was not identified in the diagnosis without serious side effects on normal tissues if irradiation can be performed by using the ideal magnetic nanoparticles in this manner. The required concentration of the nanoparticles accumulated in this type of a metastatic cancer corresponds to $2 \text{ mg}/\text{cm}^3$, which is one tenth of that in the conventional method and it is achievable within the framework of the current drug delivery technology.

4. Conclusions

In a conventional magnetic fluid hyperthermia therapy for cancers including unidentifiable metastatic ones scattered in the whole body needs selective accumulation of the magnetic nanoparticles at a concentration of 22 mg/cm^3 , which is significantly higher than the value achieved by current drug delivery technique. Thus, the present study proposes a shift from techniques based on static, steady, and equilibrium to unstable, dynamic, and nonequilibrium scenario, although other kinds of approaches using assistance of ultrasonic or photothermal hyperthermic effects have been discussed [24, 25]. Therefore, the possibility of temporary heating of tumors was examined by pulsed irradiation using dynamically aligned structures of quasi-stable core-shell nanoparticles. Consequently, the results indicated that the proposed manner allows ideal whole-body cancer treatment at a realistic nanoparticle concentration via current drug delivery techniques. However, we must notice that much still remains to be done in each issue. First, it is not possible to control magnetic anisotropy even in widely used magnetite nanoparticles and especially in the recently developed core-shell nanoparticles. Additionally, there is a paucity of research on the dynamic alignment of easy axes of nanoparticles and especially of interacting nanoparticles. Furthermore, it is necessary to simulate heat transfers during temporary heating by pulsed irradiation in a detailed human body model in the next stage. These issues can be examined through cross-field collaboration since they are correlated with each other. For example, significance of the synthesis of core-shell nanoparticles with higher magnetization decreases if dynamic aligned structures are not formed due to an unbalance between the anisotropy field of the synthesized particles and the amplitude H_{ac} , which is optimized in the heat transfer simulation in a detailed human body. However, it is necessary for this simulation to input heating power of nanoparticles that depend on both M_s and η_{sq} . Although there are many technical challenges to overcome as discussed here, magnetic fluid hyperthermia therapy continues to be a promising candidate for ideal treatments of cancers including unidentifiable metastatic cancers scattered throughout the body, preventing the side effects of the occurrence of hot spots as pointed out recently.

Disclosure

The funders had no role in study design, data collection and analysis, decision to publish, or preparation of the manuscript.

Conflicts of Interest

The authors declare that they have no conflicts of interest.

Authors' Contributions

All authors conceived the study. Hiroaki Mamiya performed the experiments, analyzed the data, and wrote the paper.

Acknowledgments

This work was partly supported by Japan Society for the Promotion of Science (JSPS) KAKENHI Grants nos. 24310071 (Hiroaki Mamiya and Balachandran Jeyadevan) and 15K13278 (Hiroaki Mamiya).

References

- [1] Q. A. Pankhurst, N. K. T. Thanh, S. K. Jones, and J. Dobson, "Progress in applications of magnetic nanoparticles in biomedicine," *Journal of Physics D: Applied Physics*, vol. 42, Article ID 224001, 2009.
- [2] K. M. Krishnan, "Biomedical nanomagnetism: a spin through possibilities in imaging, diagnostics, and therapy," *IEEE Transactions on Magnetics*, vol. 46, no. 7, pp. 2523–2558, 2010.
- [3] B. Jeyadevan, "Present status and prospects of magnetite nanoparticles-based hyperthermia," *Nippon Seramikkusu Kyokai Gakujutsu Ronbunshi*, vol. 118, no. 1378, pp. 391–401, 2010.
- [4] H. Mamiya, "Recent advances in understanding magnetic nanoparticles in ac magnetic fields and optimal design for targeted hyperthermia," *Journal of Nanomaterials*, vol. 2013, Article ID 752973, 17 pages, 2013.
- [5] S. Dutz and R. Hergt, "Magnetic nanoparticle heating and heat transfer on a microscale: basic principles, realities and physical limitations of hyperthermia for tumour therapy," *International Journal of Hyperthermia*, vol. 29, no. 8, pp. 790–800, 2013.
- [6] E. A. Périgo, G. Hemery, O. Sandre et al., "Fundamentals and advances in magnetic hyperthermia," *Applied Physics Reviews*, vol. 2, no. 4, Article ID 041302, 2015.
- [7] M. Molcan, V. Petrenko, M. Avdeev et al., "Structure characterization of the magnetosome solutions for hyperthermia study," *Journal of Molecular Liquids*, vol. 235, pp. 11–16, 2017.
- [8] Y. Shlapa, S. Solopan, A. Bodnaruk et al., "Lanthanum-strontium manganites for magnetic nanohyperthermia: Fine tuning of parameters by substitutions in lanthanum sublattice," *Journal of Alloys and Compounds*, vol. 702, pp. 31–37, 2017.
- [9] International Commission on Non-Ionizing Radiation Protection, "Guide-lines for limiting exposure to time-varying electric, magnetic, and electro-magnetic fields (up to 300 GHz)," *Health Phys*, vol. 74, p. 494, 1998.
- [10] I. A. Brezovich, "Low frequency hyperthermia: Capacitive and ferromagnetic thermoseed methods," *Medical Physics Monograph*, vol. 16, pp. 82–111, 1988.
- [11] R. Hergt, S. Dutz, and M. Röder, "Effects of size distribution on hysteresis losses of magnetic nanoparticles for hyperthermia," *Journal of Physics: Condensed Matter*, vol. 20, no. 38, Article ID 385214, 2008.
- [12] O. Dössel and J. Bohnert, "Safety considerations for magnetic fields of 10 mT to 100 mT amplitude in the frequency range of 10 kHz to 100 kHz for magnetic particle imaging," *Biomedizinische Technik. Biomedical Engineering*, vol. 58, no. 6, pp. 611–621, 2013.
- [13] H. Mamiya and B. Jeyadevan, "Hyperthermic effects of dissipative structures of magnetic nanoparticles in large alternating magnetic fields," *Scientific Reports*, vol. 1, article 157, 2011.
- [14] C. Rossmanna and D. Haemmerich, "Review of temperature dependence of thermal properties, dielectric properties, and perfusion of biological tissues at hyperthermic and ablation temperatures," *Critical Reviews in Biomedical Engineering*, vol. 42, no. 6, pp. 467–492, 2014.

- [15] W. Andrä, C. G. D'Ambly, R. Hergt, I. Hilger, and W. A. Kaiser, "Temperature distribution as function of time around a small spherical heat source of local magnetic hyperthermia," *Journal of Magnetism and Magnetic Materials*, vol. 194, no. 1, pp. 197–203, 1999.
- [16] C. W. Song, "Effect of local hyperthermia on blood flow and microenvironment: a review," *Cancer Research*, vol. 44, pp. 4721s–4730s, 1984.
- [17] R. R. Anderson and J. A. Parrish, "Selective photothermolysis: precise microsurgery by selective absorption of pulsed radiation," *Science*, vol. 220, no. 4596, pp. 524–527, 1983.
- [18] E. Kita, T. Oda, T. Kayano et al., "Ferromagnetic nanoparticles for magnetic hyperthermia and thermoablation therapy," *Journal of Physics D: Applied Physics*, vol. 43, no. 47, Article ID 474011, 2010.
- [19] H. S. Huang and J. F. Hainfeld, "Intravenous magnetic nanoparticle cancer hyperthermia," *International Journal of Nanomedicine*, vol. 8, pp. 2521–2532, 2013.
- [20] D. A. J. Herman, P. Ferguson, S. Cheong et al., "Hot-injection synthesis of iron/iron oxide core/shell nanoparticles for T2 contrast enhancement in magnetic resonance imaging," *Chemical Communications*, vol. 47, no. 32, pp. 9221–9223, 2011.
- [21] Y. Qiang, J. Antony, A. Sharma, J. Nutting, D. Sikes, and D. Meyer, "Iron/iron oxide core-shell nanoclusters for biomedical applications," *Journal of Nanoparticle Research*, vol. 8, no. 3–4, pp. 489–496, 2006.
- [22] T. Maki and S. Hirosawa, "Analysis of squareness in demagnetization curve of Nd-Fe-B magnet produced by the hydrogenation-disproportionation-desorption-recombination process," *Journal of Applied Physics*, vol. 103, no. 4, Article ID 043904, 2008.
- [23] A. R. Moritz and F. C. Henriques, "Studies of thermal injury II. The relative importance of time and surface temperature in the causation of thermal burns," *American Journal of Pathology*, vol. 23, pp. 695–720, 1947.
- [24] A. Józefczak, K. Kaczmarek, T. Hornowski et al., "Magnetic nanoparticles for enhancing the effectiveness of ultrasonic hyperthermia," *Applied Physics Letters*, vol. 108, no. 26, Article ID 263701, 2016.
- [25] N. Alegret, A. Criado, and M. Prato, "Recent Advances of Graphene-based Hybrids with Magnetic Nanoparticles for Biomedical Applications," *Current Medicinal Chemistry*, vol. 24, no. 5, pp. 529–536, 2017.

Research Article

Evaluation of the Osteoblast Behavior to PGA Textile Functionalized with RGD as a Scaffold for Bone Regeneration

Mariné Ortiz,¹ Diana María Escobar-García,¹ Marco Antonio Álvarez-Pérez,² Amaury Pozos-Guillén,¹ Christian Grandfils,³ and Héctor Flores¹

¹Basic Sciences Laboratory, Faculty of Stomatology, San Luis Potosí University, San Luis Potosí, SLP, Mexico

²Tissue Bioengineering Laboratory, Postgraduate and Research Division Studies, Faculty of Dentistry, National University of Mexico, Mexico City, Mexico

³Interfaculty Research Center of Biomaterials, Institute of Chemistry, University of Liège, Liège, Belgium

Correspondence should be addressed to Héctor Flores; heflores@uaslp.mx

Received 25 May 2017; Revised 9 October 2017; Accepted 23 October 2017; Published 20 November 2017

Academic Editor: Samuel M. Mugo

Copyright © 2017 Mariné Ortiz et al. This is an open access article distributed under the Creative Commons Attribution License, which permits unrestricted use, distribution, and reproduction in any medium, provided the original work is properly cited.

The new era of biomaterials for repairing bone tissue injury continues to be a challenge in bone tissue engineering. The fiber scaffolds allow for cellular interconnection and a microenvironment close to the bone extracellular matrix. The aim of this study was to evaluate the osteoblast behavior on a 3D textile of PGA (polyglycolic acid) fibers functionalized with the RGD (R: arginine; G: glycine; D: aspartic acid) peptide. The cell morphology, proliferation, and calcium phosphate deposition ability were evaluated on textiles at different time intervals under a confocal laser scanning microscope. The osteoblast viability ranged from 92% to 98%, and cell proliferation was higher in PGA-RGD than control PGA (uncoated). In addition, the osteoblast calcium phosphate deposition was significantly greater on PGA-RGD in osteogenic inductor medium (OIM) in contrast to controls without inducing factors. The PGA-RGD fibers supported proliferation and viability of osteoblast and stimulated bone osteogenesis and mineralization. These results support the adoption of this 3D polymeric textile as a scaffold for bone tissue engineering.

1. Introduction

The healing of damaged or diseased bone is still a challenge issue for orthopedic surgeon and craniofacial surgeon. To overcome reduced bone formation and healing, many have turned to regenerative medicine. Usually, autogenous bone grafting is the first choice for bridging the bone defect. The advantages are free of immunogenic response and completely biocompatible since it comes from patient himself. The disadvantages are limited donor source, donor site morbidities, and variable bone graft survival. Xenograft and allograft are alternative choices for the treatment. However, immunogenic reaction and inadequate bone regeneration due to incomplete resorption result in nonunion or pathologic fracture. Recently tissue engineering becomes a promising matter to improve bone defect reparation [1–4].

The tissue engineering approach is a promising strategy added in the field of bone regenerative medicine, which aims

to generate new, cell-driven, functional tissues, rather than just to implant nonliving scaffolds. The manufacture of scaffolds mimicking the extracellular bone matrix, which is composed of collagen fibers, calcium, phosphorus, and other minerals, has not yet been resolved [5–7]. Scaffolds made from polymer fibers have many of the characteristics necessary for the adhesion, proliferation, and differentiation of mesenchymal stem cells and osteoblasts [8–11]. Cell behavior can be influenced by the topography of fiber scaffolds; the organization, alignment, and direction of the fibers allow cells to attach to multiple textile walls due to their close interconnectivity and larger surface-area [12–15].

One of the goals of bone tissue engineering is to reproduce the biological and physiological conditions of bone within the human body by mimicking the *in vivo* cellular microenvironment, which consists of multiple complex factors. The ideal scaffold for bone engineering should promote mineralization and support the new osteoid matrix to do

this; biomaterial surfaces are modified and functionalized with bioactive factors that stimulate and promote a cellular response [16].

To repair bone defects and regenerate bone, the induction of osteogenesis is key. It is also a key determining the capacity of osteoblasts to deposit extracellular matrix and bone mineralization. The new biomaterials replace not only the mechanical functions but also the biological characteristics of the bone tissue [12, 17, 18].

Previous work demonstrated that the biocompatibility of a 3D polymeric textile intended for use in tissue regeneration was tested by evaluating the viability, proliferation, and adhesion of dental pulp stem cells (DPSCs); morphological parameters were characterized using scanning electronic microscopy (SEM), X-ray photoelectron spectroscopy (XPS), and X-ray microtomography (μ CT) analyses. The textiles were functionalized with the RGD (R: arginine; G: glycine; D: aspartic acid) peptide, which is thought to be the principal peptide responsible for cell adhesion [19]. Because synthetic polymers do not have bioactive groups on their surfaces, they do not promote cellular adhesion and require surface functionalization [20]. The 3D polymeric textile has been shown to support cell viability; however, it is necessary to perform studies with cell lineages specific to the tissue that needs to be regenerated [19].

In this study the behavior of osteoblast on PGA 3D textile functionalized with RGD to determine their ability induced of calcium phosphate deposition by used as scaffold for bone regeneration was evaluated. Additionally, the capacity of the scaffolds to induce osteoid matrix synthesis followed directly by mineralization was examined. The proliferation of osteoblasts on the fibers was evaluated by [3-(4,5-dimethylthiazol-2-yl)-5-(3-carboxymethoxyphenyl)-2-(4-sulfophenyl)-2H-tetrazolium] (MTS) assay, cell viability was evaluated with the LIVE/DEAD[®] Viability/Cytotoxicity Kit assay under a fluorescence microscope, and mineral deposition was evaluated with the Osteogenesis Quantitation Kit (Millipore).

2. Materials and Methods

2.1. Textile Fabrication and RGD Textile Functionalization. The textiles were fabricated and characterized as described in previous work. Briefly, the textiles were knitted by Centexbel (Verviers, Belgium) from resorbable thread made from polyglycolic acid (PGA) multifilaments. After cutting, cleaning, drying, and undergoing 2 hours of UV sterilization and generating textile samples of an overall dimension of $0.2 \times 0.5 \times 0.5$ cm (*h w d*), the materials were stored under vacuum at -20°C until future use. The RGD (R: arginine; G: glycine; D: aspartic acid, A8052 Sigma-Aldrich) was physically absorbed by the textiles by incubating them in a solution of RGD (1 mg/mL) plus 0.1 M PBS (phosphate saline buffer) for 6 h at 4°C . Next, the textiles were washed with PBS and dried for 1 h under sterile conditions. The μ CT and XPS analyses were conducted to analyze the porosity and surface properties of the fabrics, respectively [19].

2.2. Osteoblast Culture. Human osteoblasts (hOB) were isolated from the maxillary tuberosity using the explant technique during third molar surgery. This study was approved by

the Institutional Ethics Committee (UASLP CEIFE-032-012). The hOB was cultured in 75 cm² cell culture flasks containing Dulbecco's Modified Eagle Media (DMEM, Sigma-Aldrich, St. Louis, USA) supplemented with 10% fetal bovine serum (FBS, Biosciences, USA) and antibiotic solution (streptomycin 100 $\mu\text{g}/\text{mL}$ and penicillin 100 U/mL, Sigma-Aldrich). The cell cultures were incubated in a 100% humidified environment at 37°C in an environment of 95% O₂ and 5% CO₂. The hOB from passages 2–6 were used for all of the experimental procedures. For *in vitro* osteogenic differentiation, cells were cultured in an osteogenic inductor medium (OIM) consisting of complete DMEM medium supplemented with 50 $\mu\text{g}/\text{mL}$ of ascorbic acid, 10 mM of b-Glycerophosphate, and 10^{-7} M of Dexamethasone (all from Sigma-Aldrich St. Louis, USA). During the experiment, the culture medium was changed twice per week.

2.3. Seeding on Textiles. The hOB were cultured in a 75 cm² cell culture flask upon reaching 90% confluence and then washed with PBS. The cell monolayer was detached using 1x Trypsin-EDTA (0.25%) solution (Gibco, Life Technologies, USA). The human osteoblastic cells were seeded at a concentration of 1×10^4 cells/textile onto the upper surface of the PGA textiles and allowed to infiltrate into the textiles within Millicell EZ SLIDE 8-well glass slides (Millipore-USA). The samples evaluated in the study were PGA-RGD and PGA with and without OIM induction. Cells were cultured without agitation at 37°C in a humidified atmosphere under 5% CO₂. Conventional polystyrene 24-well culture plates were used as a control. The medium was changed twice per week [19].

2.4. Cell Viability. The cell viability was determined at 3, 9, and 12 days of cell culture with the *in vitro* LIVE/DEAD Viability/Cytotoxicity Kit assay (Invitrogen) according to manufacturer's instructions. The cells were observed under a confocal laser scanning microscope (CLSM, Leica Model DMI4000B, Germany) using a laser beam emitted at 488 nm and 532 nm wavelengths. Images were processed and analyzed using the LASAF[®] software (Leica, Germany). Adherent live and dead cells were counted manually based on 10 images (1×1 mm) per textile acquired randomly. The percent viability was calculated using the following formula: number of live cells/number of total cells at each time $\times 100$.

2.5. Cell Proliferation. Proliferation of hOB cells seeded onto PGA at a concentration of 1×10^4 cells/textile was quantified at 3, 5, and 7 days of culture using the Cell Titer 96TM Aqueous One Solution Cell Proliferation Assay (Promega), also known as the MTS assay. This assay is based on the ability of mitochondrial dehydrogenases in living cells to oxidize the MTS tetrazolium compound forming a colored formazan product that is soluble in tissue culture medium. The concentration of colored product is directly proportional to the number of metabolically active cells. The hOB seeded at the indicated times onto PGA textile material and PGA textile material functionalized with RGD were washed with PBS, incubated with fresh culture medium containing 20 μL of the stock solution, and incubated for 3 h at 37°C . After incubation, the absorbance was quantified by spectrophotometry at 490 nm

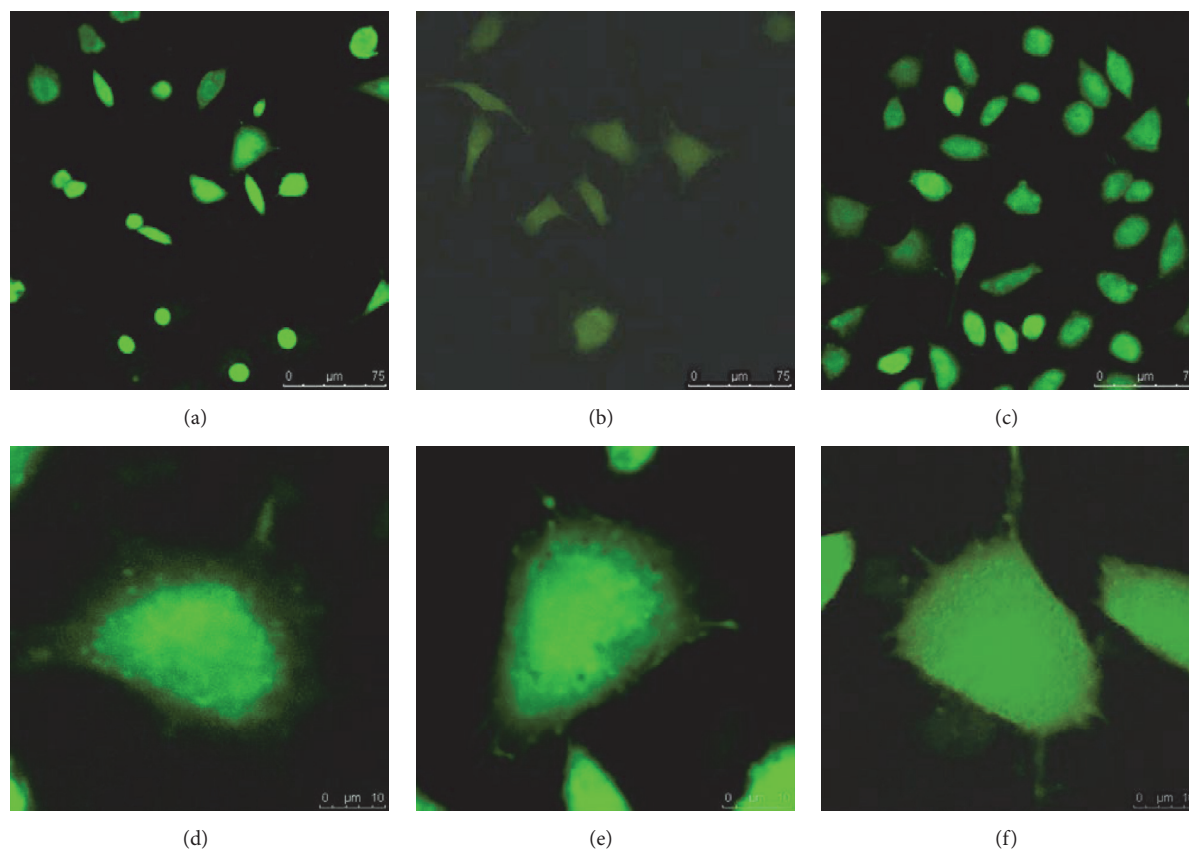


FIGURE 1: Image shows representative LIVE/DEAD fluorescent staining of osteoblasts seeded onto culture plates. 25% (a), 50% (b), and 75% (c) of osteoblasts showing flattened morphology at 3 days (d), 9 days (e), and 12 days (f).

with a plate reader (Epoch, BioTek). During the experiment, the culture medium was exchanged for fresh medium every two days. All MTS experiments were conducted in triplicate and repeated at least three times.

2.6. Mineralization Analysis and Calcium Phosphate Deposition. An osteogenesis quantization assay kit (Millipore) was used to determine the degree of mineralization, which is related to calcium content, during osteogenesis of human osteoblasts cultured onto the PGA textile for 4, 14, and 21 days with and without OIM. This assay is based on the quantification of Alizarin Red Stain (ARS), which binds selectively to calcium phosphate deposits (mineralization nodules). After incubation, the PGA textiles were carefully washed with PBS, fixed with 10% formaldehyde for 1 h at room temperature, carefully washed with distilled H₂O three times (5–10 minutes), and then stained with ARS solution (40 mM) for 30 min at room temperature. After several washes with distilled H₂O to remove excess dye, the PGA textiles were examined under an optical microscope (Leica DMIL LED), and images were processed and analyzed using the LAS EZ software (Leica, Germany). After microscopic analysis of ARS staining, the dye was extracted from the PGA textile by treatment with 10% acetic acid for 30 min. After neutralization with 10% ammonium hydroxide, the optical density of ARS was measured at 405 nm with a spectrophotometer

(Epoch, BioTek). The concentration of ARS was determined by correlating the absorbance of the experimental samples with a standard curve of known ARS dye concentrations.

2.7. Statistical Analysis. Significant differences between experimental groups were determined using the Kruskal-Wallis and Wilcoxon tests, with $p < 0.05$ considered significant. Data were analyzed using SigmaPlot Ver. 11.0 statistical software (SPSS Inc., Chicago, IL, USA).

3. Results

3.1. Cell Viability. The viability of human osteoblast cells isolated using the explant technique was evaluated by LIVE/DEAD Viability/Cytotoxicity Kit assay. The results show more than 92% viability with well-defined polygonal, spindle shaped cell morphology (Figures 1(a)–1(c)). The cell morphology was observed at different intervals throughout the viability assays (Figures 1(d)–1(f)). Our results showed that the viability of human osteoblasts cultured on PGA textile fibers functionalized with RGD peptide in the presence of OIM at 3, 9, and 12 days was significantly greater for all time intervals than viability of osteoblasts cultured on control PGA (Figures 2(a)–2(f)). However, no differences in biocompatibility were found when human osteoblasts were cultured onto PGA-RGD and PGA textile in normal complete medium

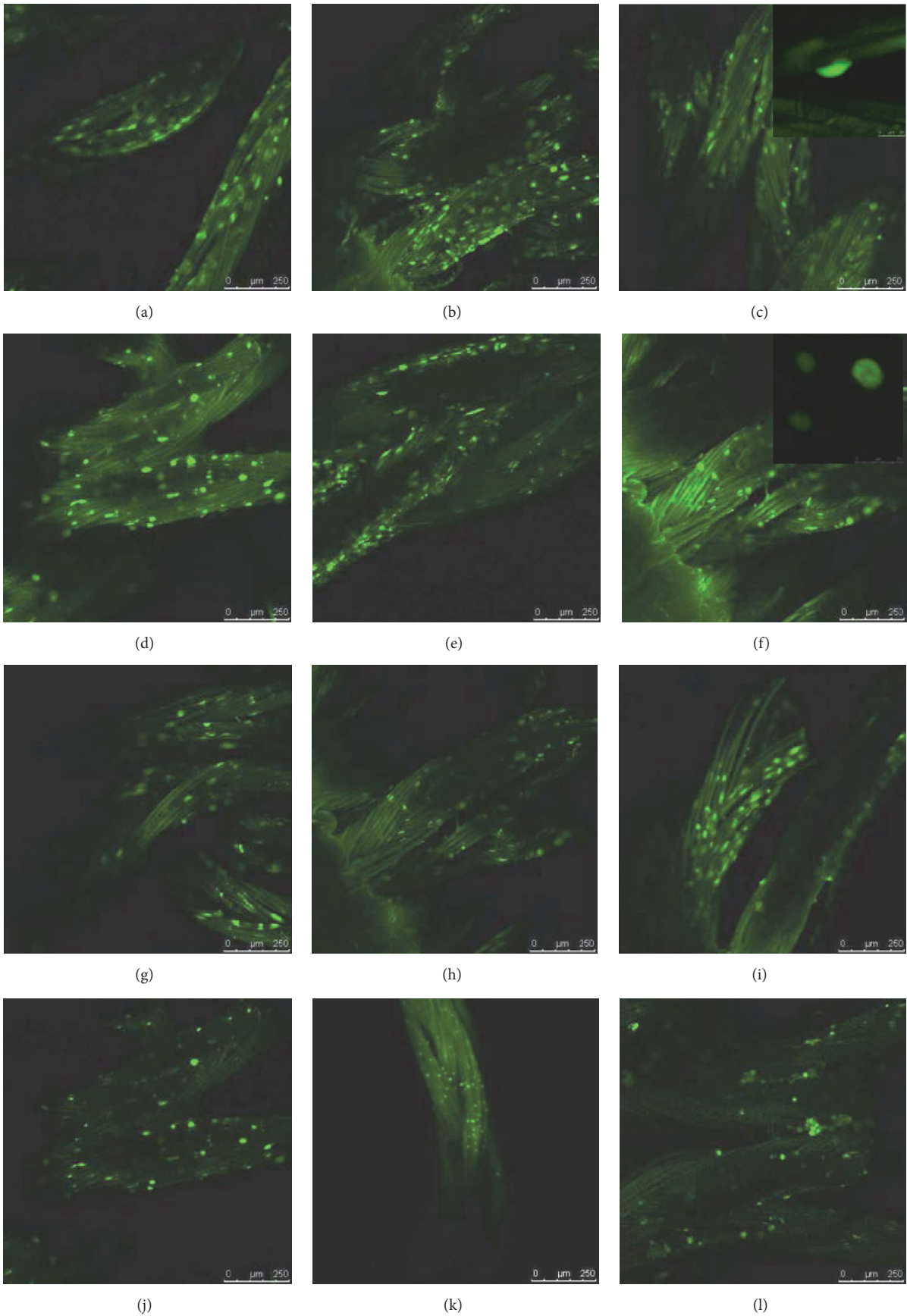


FIGURE 2: Images taken using a CLSM on PGA textiles at 3, 9, and 12 days. Osteoblasts were stained using the LIVE/DEAD Viability/Cytotoxicity Kit assay (10x). PGA-RGD-OIM at 3 days (a), 9 days (b), and 12 days (c). PGA-OIM at 3 days (d), 9 days (e), and 12 days (f). PGA-RGD control at 3 day (g), 9 days (h), and 12 days (i); control PGA at 3 days (j), 9 days (k), and 12 days (l).

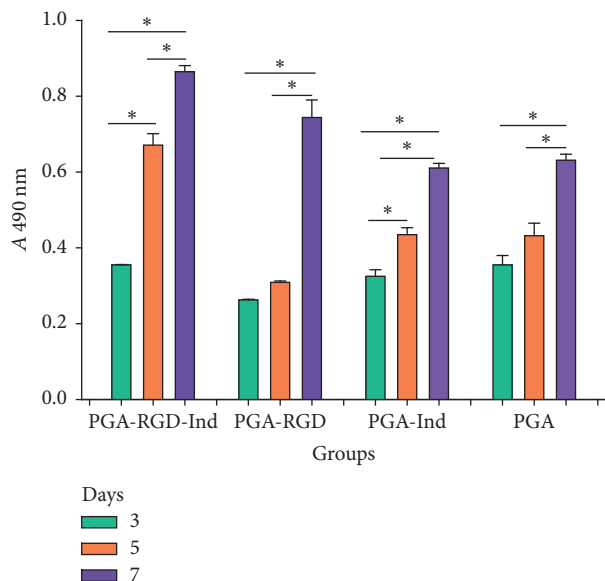


FIGURE 3: Osteoblast proliferation on the functionalized and non-functionalized textiles over time as measured by MTS assay, which represents active mitochondrial activity of living cells. Cell density was significantly higher on the PGA-RGD-OIM textile at 3, 5, and 7 days compared to control PGA * ($p < 0.05$). Cells proliferated faster on PGA-RGD than control PGA.

(Figures 2(g)–2(l)). The percent cell viabilities determined by image analysis of the PGA textiles ranged from 92% to 98%. Moreover, the morphology of human osteoblasts cultured on control PGA textiles were round to oval in shape compared to the flattened morphology of osteoblasts cultured on PGA-RGD (Figures 2(c) and 2(f)).

3.2. Cell Proliferation. Proliferation of osteoblasts cultured on both textile materials after 3, 5, and 7 days was evaluated using a proliferation assay kit. The absorbance level confirmed that human osteoblasts grow on PGA textiles in the presence and absence of OIM, indicating good proliferation without a cytotoxic response to the multifilament polymeric structures (Figure 3). The results showed that human osteoblasts grow faster on textiles of PGA functionalized with RGD peptide compared to the control PGA. Nevertheless, an increase in cell number was detected following growth on both surfaces during the course of the experiment. In the PGA-RGD-OIM group, there were significant differences between the three incubation times. The PGA-RGD only showed significant differences during the 3–7 day and 5–7 day intervals ($p < 0.05$). The PGA-OIM and PGA-RGD-OIM groups both showed significant differences at 3, 5, and 7 days. Comparing cell proliferation among the four groups at 3 days, there was a significant difference between PGA-RGD and control PGA. At 5 days, there were significant pairwise differences between all groups except PGA-OIM versus PGA. Lastly, at 7 days, there was also no significant difference for PGA-OIM versus PGA.

3.3. Mineralization Analysis and Calcium Phosphate Deposition. The amounts of calcium phosphate in the secreted

mineral matrix of osteoblasts were quantified using ARS. The osteoblasts cultured on both PGA-RGD and control PGA in the presence of OIM stained positive for the presence of mineral nodules of calcium by ARS staining assay at 4, 14, and 21 days. The results indicating that the mineral nodules increased in number and became larger with prolonged induction in OIM (Figures 4(a)–4(f)); in comparison with cells cultures on PGA-RGD and control PGA with complete normal medium, there was either a slight presence or absence of calcium phosphate deposits or mineral nodules (Figures 4(g)–4(l)). As a negative control, we used the osteoblasts cultured in plates with DMEM where calcium phosphate deposits did not form, and as a positive control, we used osteoblasts cultured in OIM.

Images of the mineral deposits were confirmed by quantitative analysis of ARS extraction, which indicated that polymeric textile scaffolds of PGA-RGD-OIM and control PGA-OIM have an enhanced calcium phosphate deposition in the extracellular matrix compared with cultures without OIM (Figure 5).

4. Discussion

Designing the ideal bone graft requires understanding the nature of the materials with which cells interact. Osteoinductive activity is one of the most important properties of the materials [21]. Methods exist to evaluate the behavior of cells on fibrous membrane surfaces tailored for bone tissue engineering [14]. In the present study, cell viability, proliferation, morphology, and calcium phosphate deposition by osteoblasts on the polymeric 3D textiles functionalized with RGD were evaluated.

The main characteristic of a biomaterial is its biocompatibility, and in our hands, the PGA-RGD fibers show a high level of cell viability (from 92% to 98%). This result could mean that the PGA-RGD fibers provide an appropriate environment for osteoblast cells where they can proliferate and migrate between multiple fibers and attach to the textile fibers and walls. In our previous studies, DPSCs were used and had a cell survival rate ranging from 94% to 100%. The parameters that probably play important roles in these textiles, such as surface roughness, 3D structure, and high interconnectivity, permit osteoblasts to migrate through the pores of the textiles and increase the surface available for protein adsorption, leading to cell attachment to the fibrous surface topographies of the PGA textile [19].

The morphology of the polymeric fiber textiles is a 3D structure with the fibers knitted in one orientation and aligned such that cells grow in the direction of the multifilaments. In previous studies that cultivated DPSCs on textiles, cells grew along the longitudinal axis of the fiber, which offers greater surface-area compared with monofilament mesh fabrics [19].

Studies have reported significantly higher cell mobility on aligned poly(methyl methacrylate) fibers than on random fibers, probably because there is less distance between the fibers and there is increased cell-cell communication [22]. Moreover, the cells orient, elongate, and spread along poly(styrene) fibers [16]. Alignment of cells is regulated by

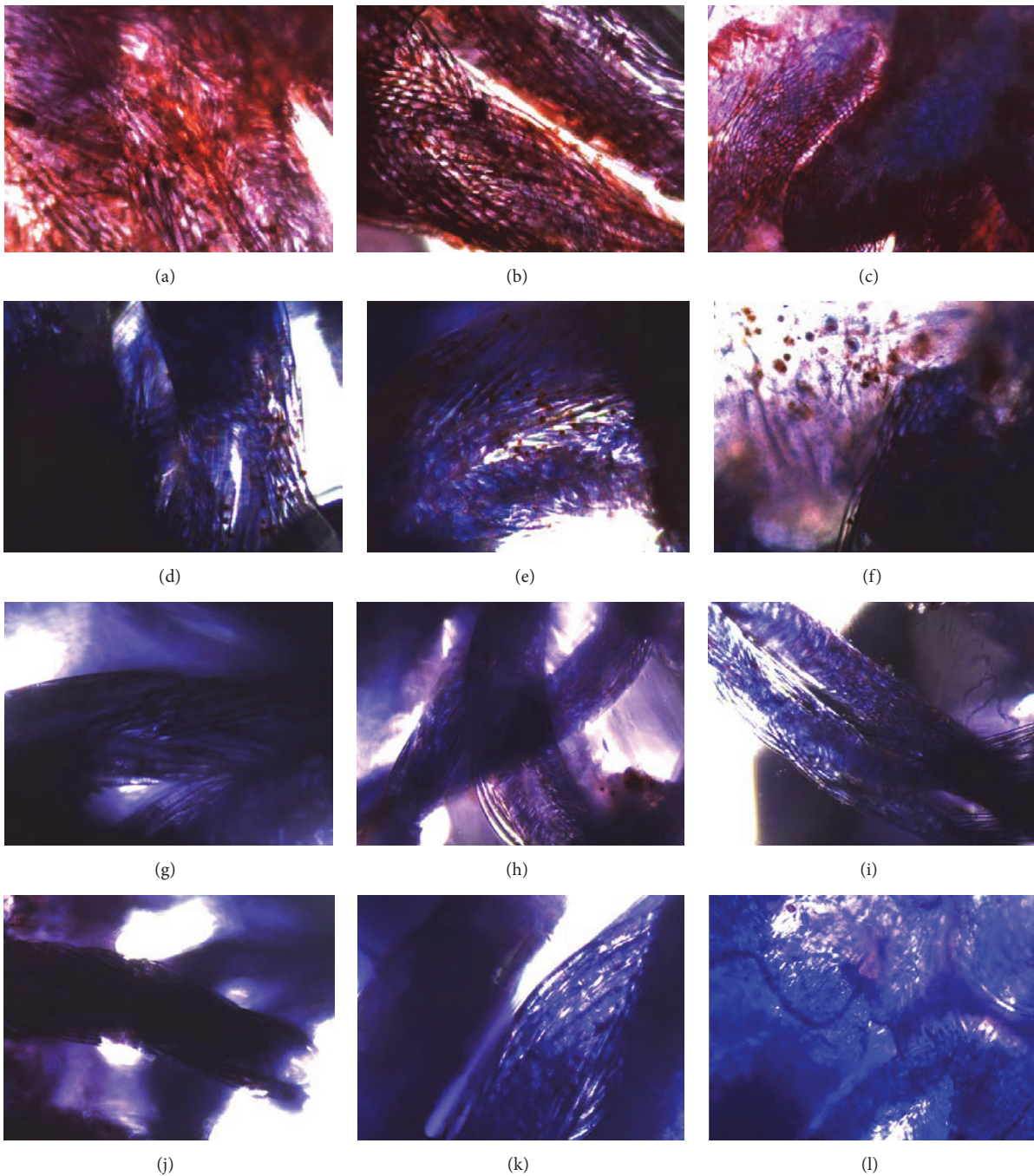


FIGURE 4: Cell aggregates grown in OIM stain positive with ARS solution, indicating osteoblast differentiation and mineralization. Phase contrast micrographs at a total magnification of 10x. PGA-RGD-OIM at 4 days (a), 14 days (b), and 21 days (c). PGA-OIM at 4 days (d), 14 days (e), and 21 days (f). In the case for the aggregates in non-OIM at 4, 14, and 21 days showed no calcium deposition; PGA-RGD at 4 days (g), 14 days (h), and 21 days (i). PGA at 4 days (j), 14 days (k), and 21 days (l).

fiber densities and patterns; therefore, the growth patterns depend on cell-cell communication and cell alignment [14].

The cell morphologies observed under CLSM include elongated and polygonal morphology and the presence of flattened and cytoplasmic extensions between the multifilaments. Cell infiltration is possible due to the porosity and the morphological parameters of the fiber. Cell morphology is one way to determine if the substrate is suitable for the cells.

The osteoblasts cultured on textiles had an elongated morphology with abundant cytoplasmic cell processes, filopodia, and lamellipodia, connected to the fiber matrix and to neighboring cells. These morphological characteristics are a key factor in many biological processes [23].

The proliferation assay demonstrated that all cells could proliferate after they adhered to the textiles. The fiber scaffold structures were shown to promote cell attachment;

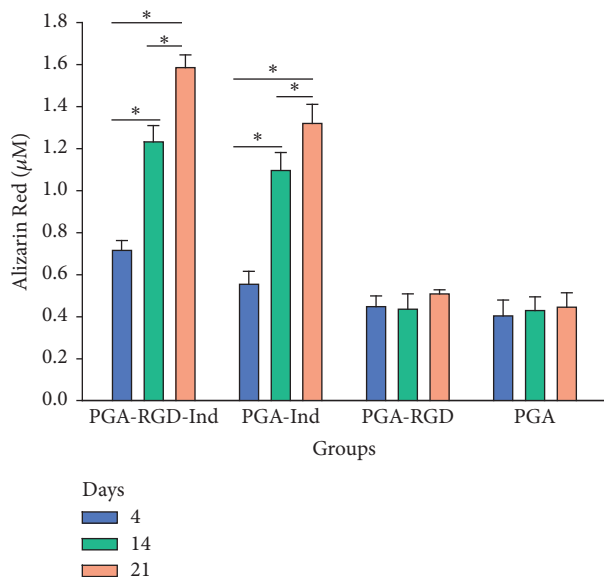


FIGURE 5: Quantitative Alizarin Red Staining after 4, 14, and 21 days of cell culture. There were significant differences on PGA-RGD and PGA with osteogenic inductor medium at 4, 14, and 21 days ($p < 0.05$).

nevertheless, surface functionalization stimulated protein adsorption, which represents the first step in cell adhesion. Studies have provided evidence that synthetic fibers may exhibit certain properties that are comparable to natural collagen fibers; thus, the nanofibrous architecture may be a superior scaffold versus the solid-walled architecture for promoting osteoblast differentiation and biomineralization [24–28].

Calcium phosphate deposition was evaluated by ARS staining, which is used to visually detect mineralization in bone tissue. In the textiles functionalized with RGD in the presence of OIM, the presence of ARS demonstrates calcium phosphate deposition throughout the multifilament polymeric textiles. In the case of control PGA without functionalization, but with osteoblasts cultured in OIM, lower amounts of ARS were observed. We supposed that RGD promotes the growth of osteoblasts and produces a greater amount of mineral nodules deposition on PGA-RGD. The growth rate of osteoblasts on control PGA textiles was slower than on functionalized textiles. This result may be related to the different degrees of cell spreading on these two surface types.

Studies have demonstrated that culturing osteoblast cells on nanofibers made of poly(L-lactic acid) results in much higher levels of alkaline phosphatase in cells than culturing on flat films in complete induction medium [29], while growth on polycaprolactone/gelatin electrospun scaffolds in medium with osteogenic supplementation promoted bone osteogenesis and mineralization [30]. In collagen/hydroxyapatite composite nanofibrous scaffolds, the mineralization reflects the functional activity of osteoblasts [31].

5. Conclusions

The interaction between osteoblasts and biomaterials depends on the biomaterial surface roughness, topography,

chemistry, and functionalization. The PGA textiles functionalized with RGD in inductive conditions tend to deposit calcium phosphate, which is an indicator of matrix formation. The osteoblast viability ranged from 92% to 98%, and cell proliferation was higher in PGA-RGD than control PGA. Our data showed that the adhesion and proliferation of osteoblasts cultured on PGA-RGD-OIM were significantly increased relative to control. In addition, the calcium phosphate deposition from osteoblasts was significantly greater on PGA-RGD-OIM. The PGA-RGD fibers supported proliferation and viability of osteoblast. These results suggest that this 3D polymeric textile can be employed as a scaffold for bone tissue regeneration. Future *in vivo* studies should be performed as well.

Conflicts of Interest

The authors declare that they have no conflicts of interest and any financial interest related to this study.

Acknowledgments

This work was partially supported by FNRS-CONACYT, Mexico-Belgium, Bilateral Collaboration “Biocompatibility of a New Polymeric Textile Proposed for Bone Tissue Regeneration,” Ref. V 4/285–NR/DeM–3.596, PIFI 2011-12, UASLP-C13-FAI-03-51.51, PFCE-UASLP 2016, PRODEP 2017, C15-FAI-10.78.78, and DGAPA-UNAM: PAPIIT-IN210815 Grants. Mariné Ortiz was a CONACYT Fellow 368667 and has received a grant from University of Liège, Belgium.

References

- [1] A. R. Amini, C. T. Laurencin, and S. P. Nukavarapu, “Bone tissue engineering: recent advances and challenges,” *Critical Reviews in Biomedical Engineering*, vol. 40, no. 5, pp. 363–408, 2012.
- [2] B. Schmidt-Rohlfing, C. Tzioupis, C. L. Menzel, and H. C. Pape, “Tissue engineering of bone tissue : PPPinciples and clinical applications,” *Der Unfallchirurg*, vol. 112, no. 9, pp. 785–795, 2009.
- [3] E. M. Younger and M. W. Chapman, “Morbidity at bone graft donor sites,” *Journal of Orthopaedic Trauma*, vol. 3, no. 3, pp. 192–195, 1989.
- [4] J. C. Banwart, M. A. Asher, and R. S. Hassanein, “Iliac crest bone graft harvest donor site morbidity: a statistical evaluation,” *The Spine Journal*, vol. 20, no. 9, pp. 1055–1060, 1995.
- [5] H. J. Park, K. D. Min, M. C. Lee et al., “Fabrication of 3D porous SF/ β -TCP hybrid scaffolds for bone tissue reconstruction,” *Journal of Biomedical Materials Research Part A*, vol. 104, no. 7, pp. 1779–1787, 2016.
- [6] H. J. Park, O. J. Lee, M. C. Lee et al., “Fabrication of 3D porous silk scaffolds by particulate (salt/sucrose) leaching for bone tissue reconstruction,” *International Journal of Biological Macromolecules*, vol. 78, pp. 215–223, 2015.
- [7] Z. Guo, J. Xu, S. Ding, H. Li, C. Zhou, and L. Li, “In vitro evaluation of random and aligned polycaprolactone/gelatin fibers via electrospinning for bone tissue engineering,” *Journal of Biomaterials Science, Polymer Edition*, vol. 26, no. 15, pp. 989–1001, 2015.

- [8] J. M. Holzwarth and P. X. Ma, "Biomimetic nanofibrous scaffolds for bone tissue engineering," *Biomaterials*, vol. 32, no. 36, pp. 9622–9629, 2011.
- [9] N. Wismer, S. Grad, G. Fortunato, S. J. Ferguson, M. Alini, and D. Eglin, "Biodegradable electrospun scaffolds for annulus fibrosus tissue engineering: Effect of scaffold structure and composition on annulus fibrosus cells in vitro," *Tissue Engineering Part: A*, vol. 20, no. 3–4, pp. 672–682, 2014.
- [10] W. Zhao, J. Li, K. Jin, W. Liu, X. Qiu, and C. Li, "Fabrication of functional PLGA-based electrospun scaffolds and their applications in biomedical engineering," *Materials Science & Engineering C: Materials for Biological Applications*, vol. 59, pp. 1181–1194, 2016.
- [11] H. Peng, Z. Yin, H. Liu et al., "Electrospun biomimetic scaffold of hydroxyapatite/chitosan supports enhanced osteogenic differentiation of mMSCs," *Nanotechnology*, vol. 23, no. 48, Article ID 485102, 2012.
- [12] W.-H. Lin, J. Yu, G. Chen, and W.-B. Tsai, "Fabrication of multi-biofunctional gelatin-based electrospun fibrous scaffolds for enhancement of osteogenesis of mesenchymal stem cells," *Colloids and Surfaces B: Biointerfaces*, vol. 138, pp. 26–31, 2016.
- [13] L. Terranova, R. Mallet, R. Perrot, and D. Chappard, "Polystyrene scaffolds based on microfibers as a bone substitute; development and in vitro study," *Acta Biomaterialia*, vol. 29, pp. 380–388, 2016.
- [14] J.-C. Chang, S. Fujita, H. Tonami, K. Kato, H. Iwata, and S.-H. Hsu, "Cell orientation and regulation of cell-cell communication in human mesenchymal stem cells on different patterns of electrospun fibers," *Biomedical Materials*, vol. 8, no. 5, Article ID 055002, 2013.
- [15] T. Schneider, B. Kohl, T. Sauter et al., "Influence of fiber orientation in electrospun polymer scaffolds on viability, adhesion and differentiation of articular chondrocytes," *Clinical Hemorheology and Microcirculation*, vol. 52, no. 2–4, pp. 325–336, 2012.
- [16] A. Serafim, R. Mallet, F. Pascaretti-Grizon, I.-C. Stancu, and D. Chappard, "Osteoblast-like cell behavior on porous scaffolds based on poly(styrene) fibers," *BioMed Research International*, vol. 2014, Article ID 609319, 2014.
- [17] M. Stoppato, H. Y. Stevens, E. Carletti, C. Migliaresi, A. Motta, and R. E. Guldborg, "Influence of scaffold properties on the inter-relationship between human bone marrow derived stromal cells and endothelial cells in pro-osteogenic conditions," *Acta Biomaterialia*, vol. 25, pp. 16–23, 2015.
- [18] M. Ngiam, L. T. Nguyen, S. Liao, C. K. Chan, and S. Ramakrishna, "Biomimetic nanostructured materials: potential regulators for osteogenesis?" *Annals Of the Academy of Medicine Singapore*, vol. 40, no. 5, pp. 213–222, 2011.
- [19] M. Ortiz, R. Rosales-Ibáñez, A. Pozos-Guillén et al., "DPSC colonization of functionalized 3D textiles," *Journal of Biomedical Materials Research Part B: Applied Biomaterials*, vol. 105, no. 4, pp. 785–794, 2017.
- [20] E. Ruoslahti, "RGD and other recognition sequences for integrins," *Annual Review of Cell and Developmental Biology*, vol. 12, pp. 697–715, 1996.
- [21] P. Janicki and G. Schmidmaier, "What should be the characteristics of the ideal bone graft substitute? Combining scaffolds with growth factors and/or stem cells," *Injury*, vol. 42, supplement 2, pp. S77–S81, 2011.
- [22] Y. Liu, A. Franco, L. Huang, D. Gersappe, R. A. F. Clark, and M. H. Rafailovich, "Control of cell migration in two and three dimensions using substrate morphology," *Experimental Cell Research*, vol. 315, no. 15, pp. 2544–2557, 2009.
- [23] E. Cukierman, R. Pankov, D. R. Stevens, and K. M. Yamada, "Taking cell-matrix adhesions to the third dimension," *Science*, vol. 294, no. 5547, pp. 1708–1712, 2001.
- [24] P. Jayakumar and L. Di Silvio, "Osteoblasts in bone tissue engineering," *Proceedings of the Institution of Mechanical Engineers, Part H: Journal of Engineering in Medicine*, vol. 224, no. 12, pp. 1415–1440, 2010.
- [25] J. M. Kanczler and R. O. Oreffo, "Osteogenesis and angiogenesis: the potential for engineering bone," *European Cells & Materials*, vol. 15, pp. 100–114, 2008.
- [26] K. M. Woo, J.-H. Jun, V. J. Chen et al., "Nano-fibrous scaffolding promotes osteoblast differentiation and biomineralization," *Biomaterials*, vol. 28, no. 2, pp. 335–343, 2007.
- [27] K. M. Woo, V. J. Chen, and P. X. Ma, "Nano-fibrous scaffolding architecture selectively enhances protein adsorption contributing to cell attachment," *Journal of Biomedical Materials Research. Part A*, vol. 67, no. 2, pp. 531–537, 2003.
- [28] M. P. Prabhakaran, J. Venugopal, and S. Ramakrishna, "Electrospun nanostructured scaffolds for bone tissue engineering," *Acta Biomaterialia*, vol. 5, no. 8, pp. 2884–2893, 2009.
- [29] J. Hu, X. Liu, and P. X. Ma, "Induction of osteoblast differentiation phenotype on poly(L-lactic acid) nanofibrous matrix," *Biomaterials*, vol. 29, no. 28, pp. 3815–3821, 2008.
- [30] M. A. Alvarez Perez, V. Guarino, V. Cirillo, and L. Ambrosio, "In vitro mineralization and bone osteogenesis in poly(ϵ -caprolactone)/gelatin nanofibers," *Journal of Biomedical Materials Research. Part A*, vol. 100, no. 11, pp. 3008–3019, 2012.
- [31] J. Venugopal, S. Low, A. T. Choon, T. S. S. Kumar, and S. Ramakrishna, "Mineralization of osteoblasts with electrospun collagen/hydroxyapatite nanofibers," *Journal of Materials Science: Materials in Medicine*, vol. 19, no. 5, pp. 2039–2046, 2008.

Research Article

Studies of the Influence of Gold Nanoparticles on Characteristics of Mesenchymal Stem Cells

Nataliia Volkova,¹ Olena Pavlovich,² Olena Fesenko,³ Oksana Budnyk,³
Serhii Kovalchuk,³ and Anatoliy Goltsev¹

¹Department of Cryopathophysiology and Immunology, Institute for Problems of Cryobiology and Cryomedicine, The National Academy of Sciences of Ukraine, Pereyaslavskaya Str. 23, Kharkov 61015, Ukraine

²Department of Reproductive Systems, Institute for Problems of Cryobiology and Cryomedicine, The National Academy of Sciences of Ukraine, Pereyaslavskaya Str. 23, Kharkov 61015, Ukraine

³International Surface Enhanced Spectroscopy (SES) Laboratory, Institute of Physics, The National Academy of Sciences of Ukraine, 46 Nauki Ave., Kyiv 03028, Ukraine

Correspondence should be addressed to Nataliia Volkova; volkovanatali2006@yandex.ua

Received 27 July 2017; Accepted 20 September 2017; Published 24 October 2017

Academic Editor: Faheem Ahmed

Copyright © 2017 Nataliia Volkova et al. This is an open access article distributed under the Creative Commons Attribution License, which permits unrestricted use, distribution, and reproduction in any medium, provided the original work is properly cited.

The aim of the present study is to determine what effect the different concentrations of 15 nm gold nanoparticles (AuNPs) will have on the immunophenotype, synthesis collagen type I, ability to direct differentiation and spectroscopic characteristics of bone marrow mesenchymal stem cells (MSCs). The AuNPs in concentrations of 1.5–9 $\mu\text{g/ml}$ did not lead to changes in the level of expression of CD 45, CD 90, and CD 73. It should be noted that AuNPs in concentrations of 6 and 9 $\mu\text{g/ml}$ led to a decrease in CD 44 cells by 6% and 9%, respectively. The content of CD 105 cells was reduced by 5% when AuNPs were applied at a concentration of 9 $\mu\text{g/ml}$. It was found that AuNPs in concentrations of 1.5–6 $\mu\text{g/ml}$ are safe for MSCs, while the increase up to 9 $\mu\text{g/ml}$ has a toxic effect, manifested by the reduction of synthesis collagen type I and ability of adipogenic differentiation. IR spectroscopy data have shown that the AuNPs at concentrations of 9 $\mu\text{g/ml}$ under conditions of adipogenic differentiation to MSCs lead to the destruction processes in the cells. The obtained results are related to the field of applied nanotechnology, which extends to regenerative medicine, especially in development of bioimplantology.

1. Introduction

Nanotechnology involves the design, characterization, and application of structures or systems at the nanometer scale (size range, 1–100 nm) which includes nanofibers, nanotubes, nanogels, and nanoparticles (NPs, e.g., rods, cubes, and spheres) [1–3]. Applications related to engineering, information technology, and diagnostics are examples of consumer applications that directly improve our lives. This technology is intrinsically multidisciplinary and is reliant on techniques and methodologies from many fields such as chemistry, physics, electrical engineering, material science, and molecular biology. Our current knowledge of the health effects of nanomaterials is limited and therefore this aspect deserves

special attention, particularly the potential long-term adverse effects on living organisms [4–6].

The gold nanoparticles (AuNPs) are very attractive for usage in biomedical products due to their unique physical and chemical properties and conventional methods of synthesis [4, 7]. Many approaches to development of medical nanotechnology are based on involvement of metal nanoparticles [8, 9]. These nanoscale metals can have different impact on both physical and chemical properties of cells, depending on their quantity or therapeutic dose [10]. AuNPs are used for cancer targeted therapy and as a contrast agent for biomedical imaging; hence, identification of their possible cytotoxic effects is an important direction of nanobiotechnological research [11, 12].

The impact of metal NPs on stem cells has been scarcely studied so far [3, 13]. Possible interaction could lead to unpredictable consequences in the functioning of organs and tissues as long as all the cells encountered in the primary division of stem cells do not cease to exist. In 2006 the International Society for Cellular Therapy (ISCT) proposed basic criteria for determining MSCs, namely, adhesive fibroblast-like cells that are CD105, CD73, and CD90 positive and CD45, CD34, CD14, or CD11b, CD19, or CD79a and HLA-DR negative, capable of directed differentiation into adipogenic, osteogenic, and chondrogenic lineages. This minimum set of phenotypic criteria for MSCs identification is not associated with their origin [14]. MSCs are normally taken from various tissues, such as bone marrow, fat, and muscles involved in tissue homeostasis and regeneration [15]. We selected bone marrow MSCs of rats as a model object for studying the effect of AuNPs on stem cells. It is likely that mesenchymal stem cells will come into close contact with any AuNPs coated implants. Furthermore, due to their high differentiation capacity, these cells represent an optimal cellular model for analysis of a possible influence of AuNP on cell differentiation. As it has been reported [13] AuNPs have a size-dependent cytotoxicity and NPs less than 15 nm are only considered to be toxic.

Determination of the metal NPs' influence on different types of cultured cells requires evaluation of morphological and functional parameters, namely, viability (membrane integrity) and capacity of adhesion and proliferation [16, 17]. To determine the biosafety and compatibility of metal NPs with cells, most researchers used cytological, biochemical, and biophysical methods. Infrared and Raman spectroscopies are complimentary informative and noninvasive techniques, able to provide the essential information for the diagnosis and evaluation of the cell's functionality without damaging it and use of additional markers [18]. Generic from them is the Single Cell Raman Spectroscopy (SCRS), a label-free method for the analysis of individual parameters of living cells both *in vivo* and *in vitro* [19], because obtained spectrum contains the marker bands (associated with characteristic functional groups) of nucleic acids, proteins, carbohydrates, and lipids, thus reflecting cellular genotypes, phenotypes, and physiological states.

Here we present the study of what effect different concentrations of 15 nm AuNPs will have on the immunophenotype, synthesis collagen type I, ability to direct differentiation and spectroscopic characteristics of bone marrow MSCs.

2. Materials and Methods

2.1. Obtaining and Cultivation of MSCs. MSCs were isolated from resected femur of rats ($n = 7$, weighing 220–225 g) by washing out with Hanks' solution (PAA, Pasching, Austria), followed by flushing through a needle with gradually decreased diameter. The next step was centrifugation at $834 \times g$ for 5 min. The cells were resuspended in culture medium and plated on culture flasks (PAA) with 10^3 cells per cm^2 density. Cultural medium contained: Iscove's Modified Dulbecco's Medium (PAA), 10% fetal bovine serum (FBS)

(HyClone, Logan, UT, USA), gentamicin (150 mg/mL) (Farmak, Kiev, Ukraine), and amphotericin B (10 mg/mL) (PAA). Cultural medium was changed every three days. We used standard culture conditions (37°C , 5% CO_2 , 95% humidity) in a CO_2 incubator (Sanyo, Osaka, Japan). MSCs were detached with 0.25% trypsin-EDTA (Hyclone), which was replanted in other flasks with 1:2 ratios at 80% confluence. Third-passage MSCs were used in all experiments.

2.2. Manipulations with AuNPs. AuNPs were obtained by citrate synthesis [20] with an initial metal concentration of $45 \mu\text{g}/\text{ml}$. The average size of AuNPs was 15 nm. The range of investigated concentrations was 1.5, 3, 6, and $9 \mu\text{g}/\text{ml}$. AuNPs were introduced in cells by passive diffusion at 37°C . Cells without AuNPs under the same conditions were taken as control ones.

2.3. MSCs Immunophenotyping. For immunophenotypic analysis MSCs after 1 hour incubation with AuNPs were stained with mouse -anti- rat CD45-FITC, CD44-FITC, CD73-FITC, CD90-FITC, and CD105-PE monoclonal antibodies (BD Biosciences, USA) according to the manufacturer's instructions. Measurements were performed on flow cytometer BD FACS Calibur (Becton Dickinson, USA). Data were analyzed using WinMDI v.2.8.

2.4. Immunohistochemical Study of Type I Collagen. Staining for collagen type I was performed using monoclonal antibodies to COL-1 (Sigma-Aldrich, USA) in dilution 1:2000 and CFTM488A (Sigma-Aldrich, USA) according to the manufacturer's instructions. The cells nuclei were additionally stained with DAPI (Sigma-Aldrich, USA) at a concentration of $1 \mu\text{g}/\text{mL}$ for 30 min. Fluorescent microscopy of MSCs was performed using confocal scanning microscope LSM 510 Meta (Carl Zeiss, Germany).

2.5. Directed Adipogenic Differentiation. For directed differentiation into adipogenic lineage standard nutrient medium in cultures after reaching confluency was changed for differentiation medium consisting of IMDM, 1% fetal bovine serum, 10^{-7} M dexamethasone, and 10^{-9} M insulin (all from PAA, Austria). Further cultivation was carried out for 3 weeks changing medium twice a week. To confirm the differentiation, the cells were stained with Oil red (Fluka, Germany) and under a light microscope we counted the number of cells with lipid droplets (orange stain), calculating the percentage of the total number of cells. The control ones for spontaneous differentiation were cells cultured without specific inductors.

2.6. Directed Chondrogenic Differentiation. For directed differentiation in chondrogenic lineage, standard nutrient medium in cultures after reaching confluency was changed for differentiation medium consisting of IMDM, 10^{-5} ascorbate-2-phosphate (PAA, Austria), and $10 \text{ ng}/\text{ml}$ TGF- β (Sigma, USA). Further cultivation was carried out for 3 weeks changing medium twice a week. To confirm the differentiation, the cultures were stained with Toluidine

TABLE 1: Immunophenotype of MSCs after 1 hr incubation with AuNPs.

| Sample | Expression level, % | | | | |
|------------------|---------------------|-------------|------------|------------|-------------|
| | CD 44 | CD 45 | CD 73 | CD 90 | CD 105 |
| Control | 97.7 ± 0.2 | 1.12 ± 0.11 | 97.3 ± 0.8 | 91.5 ± 1.2 | 95.4 ± 0.4 |
| Au_NPs_1.5 µg/ml | 97.2 ± 0.4 | 0.91 ± 0.12 | 96.5 ± 0.4 | 92.1 ± 0.5 | 93.4 ± 0.3 |
| Au_NPs_3 µg/ml | 97.1 ± 0.3 | 1.07 ± 0.13 | 96.5 ± 0.3 | 91.1 ± 0.3 | 93.1 ± 0.4 |
| Au_NPs_6 µg/ml | 92.5 ± 0.4* | 1.09 ± 0.08 | 96.7 ± 0.3 | 91.3 ± 0.2 | 93.2 ± 0.5 |
| Au_NPs_9 µg/ml | 89.5 ± 0.3* | 1.11 ± 0.15 | 96.5 ± 0.6 | 91.1 ± 0.1 | 90.3 ± 0.4* |

Note. * $p \leq 0.05$ is significant versus the control.

blue (Fluka, Germany) and we counted the number of cells with proteoglycans in the extracellular matrix (blue stain). Number of differentiated cells was counted under a light microscope and we calculated the percentage of the total number of cells. The control ones for spontaneous differentiation were cells cultured without specific inductors.

2.7. IR Spectroscopy. The spectroscopic characteristics were determined on the 21st day of adipogenic differentiation of MSCs. The IR spectra were acquired in reflection mode on a FTIR Spectrometer VERTEX-70 equipped with Hyperion 1000 Microscope (Bruker). For the data processing the following protocol has been adopted: (1) collecting IR spectrum, (2) baseline correction, (3) spectrum normalization in OH-NH range, (4) spectrum normalization in Amide I range, and (5) spectrum normalization in Amide II region.

2.8. Statistical Analysis. Testing of the normality was carried out using common test for asymmetry and kurtosis. At the normal distribution of variables, reliability of differences between groups was evaluated using Student's *t*-test. Differences are significant at $p \leq 0.05$. Analysis was performed using MS Excel (Microsoft, USA) and Statistica 8 (StatSoft Inc., USA) software.

3. Results and Discussion

3.1. Effect of AuNPs on Immunophenotype of MSCs. MSCs populations derived from bone marrow were characterized by immunophenotype presented in Table 1.

The cells revealed typical mesenchymal phenotype with high expression ($\geq 90\%$) of CD44, CD90, CD105, and CD73 and low expression ($\leq 1\%$) of hematopoietic marker CD45. Addition of the investigated concentrations of AuNPs did not lead to significant changes in the level of expression of CD 45, CD 90, and CD 73.

It should be noted that AuNPs in concentrations of 6 and 9 µg/ml led to a decrease in CD 44 cells by 6% and 9%, respectively. The content of CD 105 cells was reduced by 5% when AuNPs were applied at a concentration of 9 µg/ml. The effect of gold at a concentration of 6 and 9 µg/ml on the decrease in the expression level of the markers CD 44 and CD 105 (9 µg/ml of AuNPs) is probably due to the oppression of the functional state of cells when interacting with nanoparticles. It is known that the CD 44 marker is responsible for the basic functions of the cell, including cell

adhesion, cell homing in peripheral and lymphoid organs and inflammatory foci, cellular activation, and increased production of cytokines and growth factors [21]. When 9 µg/ml of AuNPs was applied, a decrease in the expression of the CD105 (endogen) marker of type I membrane glycoprotein was observed, which functions as an additional receptor for the transforming growth factor beta (TGF-β) superfamily, including TGF-β1 and TGF-β3, activin A, and BMP-7. Also, CD 105 is involved in the regulation of migration and the processes of reorganization of the cytoskeleton [14]. These changes in the immunophenotype of the MSC of the bone marrow when interacting with AuNPs give the prerequisites for the detection and prevention of disturbances in the processes of proliferation and differentiation.

3.2. Effect of AuNPs on Synthesis Collagen I Type of MSCs. Morphological characteristics of the studied cells and their ability to produce collagen type I are shown in Figure 1. The control samples of MSCs were characterized by the presence of spindle-shaped and sail-shaped cells, in which 89.6 ± 2.7% were positively stained for type I collagen. The relative number of cells that synthesized type I collagen, in cultures of MSCs with addition of AuNPs at a concentration of 1.5 and 3 µg/ml, did not differ significantly from the corresponding index in the control and was 87.4 ± 3.1% and 87.6 ± 1.9%, respectively. The glow in the green region of the spectrum was bright and intense. The use of AuNPs at concentrations of 6 and 9 µg/ml led to a decrease in the relative number of cells positively stained for type I collagen; they were 57.6 ± 2.1% and 53.4 ± 2.5%, respectively. The luminescence of MSCs cultured with the addition of AuNPs of 9 µg/ml was not intense and covered by small sections of cells (in most cases around the nucleus).

The results of the study of the effect of AuNPs on synthetic processes in MSCs bone marrow showed that the use of concentrations of 6 and 9 µg/ml led to a decrease in the relative number of cells positively stained with collagen type I. As is known, the decrease in the synthetic activity of MSCs of bone marrow is one of the main indicators of attenuation of their functioning [22]. Based on the results of our previous studies, by using confocal laser microscopy of bone marrow MSC culture preparations, it has been shown that low-frequency gold does not remain on the plasma membrane of cells. The localization was partially observed in the cytoplasm and in the cell nucleus [23, 24]. It can be assumed that the AuNPs, by binding to the nucleus cell membrane, have the potential

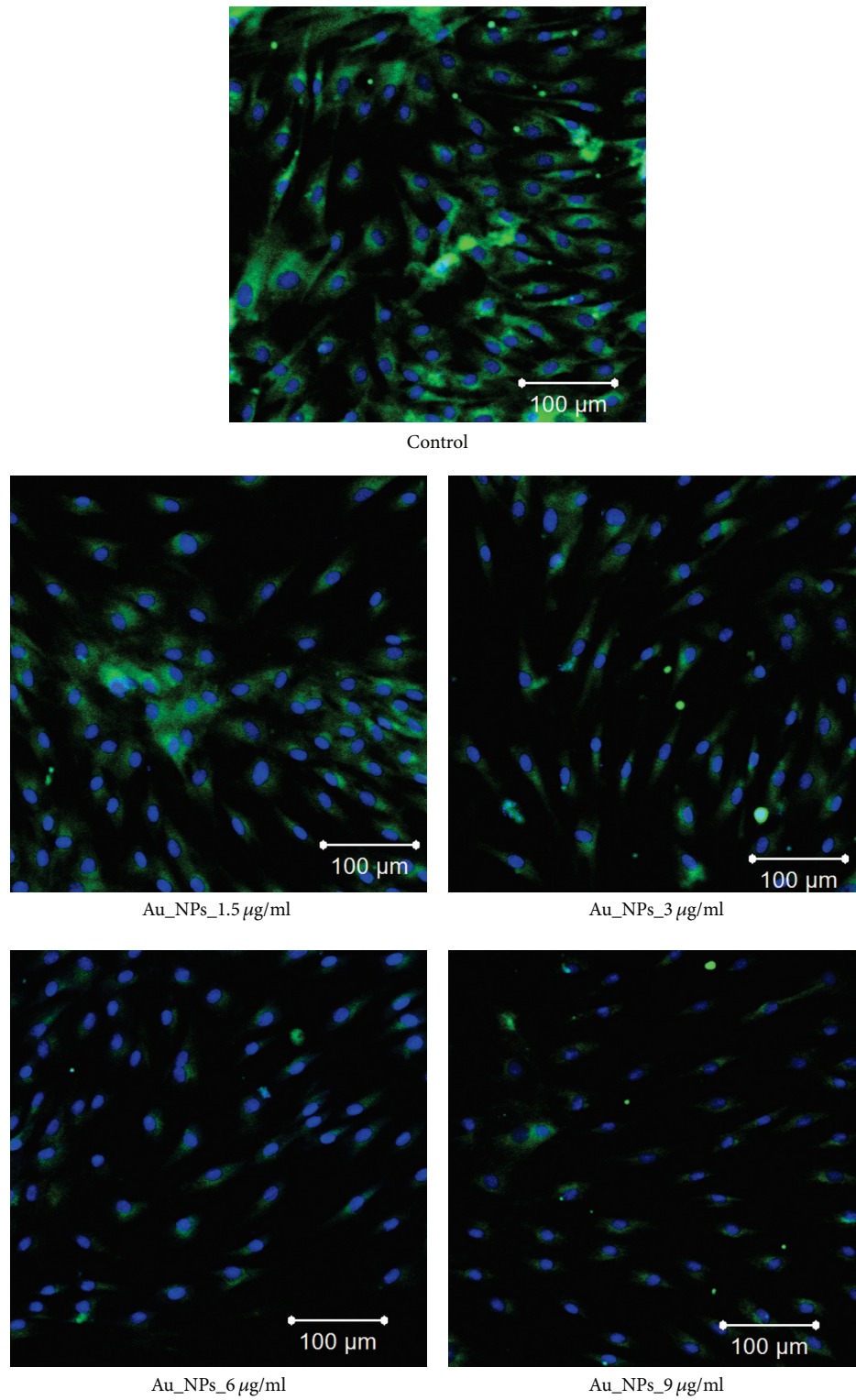


FIGURE 1: The effect of AuNPs on synthesis collagen I type of MSCs, 10th day. Control cells were not incubated with AuNPs. Fluorescent microscopy, immunological staining of MSCs on type I collagen (green light), nucleus stained of DAPI (blue light).

TABLE 2: Ability to direct adipogenic and chondrogenic differentiation of MSCs cultured with addition of AuNPs.

| Samples | Adipogenic differentiation, positive staining with Oil red | | Chondrogenic differentiation, positive staining with Toluidine blue | |
|-----------------------------|--|-------------------------|---|-------------------------|
| | Spontaneous differentiation | Induced differentiation | Spontaneous differentiation | Induced differentiation |
| Control | — | + | — | + |
| Au_NPs_1.5 $\mu\text{g/ml}$ | — | + | — | + |
| Au_NPs_3 $\mu\text{g/ml}$ | — | + | — | + |
| Au_NPs_6 $\mu\text{g/ml}$ | — | + | — | + |
| Au_NPs_9 $\mu\text{g/ml}$ | — | ± | — | + |

Notes. “+”: differentiation of more than 50% cells; “±”: differentiation of less than 50% cells; “—”: no differentiation.

to influence the synthetic processes in the MSCs of the bone marrow at the transcriptional and posttranscriptional levels.

3.3. Effect of AuNPs on Ability to Direct Adipogenic and Chondrogenic Differentiation of MSCs. Ability to direct adipogenic and chondrogenic differentiation of MSCs is presented in Table 2 and Figure 2.

The first signs of adipogenic differentiation, evidenced in changing the morphology of cells (roundness, cytoplasm granularity), were observed on 5–7th day in the case of control samples and at the addition of AuNPs at concentrations of 1.5–6 $\mu\text{g/ml}$.

Application of AuNPs at a concentration of 9 $\mu\text{g/ml}$ inhibited the process of adipogenic differentiation in the cultures studied, which was manifested in the delay in the appearance of the first signs of differentiation, which appeared on 9–10th days. In all investigated concentrations of AuNPs, spontaneous adipogenic differentiation was not observed. Cytochemical staining of MSCs with dye Oil red on 21st day after the initiation of adipocyte differentiation revealed the presence of orange lipid droplets in the cytoplasm of more than $64.7 \pm 6.2\%$ of cells. The use of AuNPs at concentrations of 1.5, 3, and 6 $\mu\text{g/ml}$ did not lead to significant changes in the number of cells with signs of adipogenic differentiation; namely, the index was $64.2 \pm 4.1\%$, $59.7 \pm 5.6\%$, and $61.3 \pm 5.7\%$ of the cells, respectively. In the culture of MSCs with the addition of AuNPs at a concentration of 9 $\mu\text{g/ml}$, the number of cells with signs of adipogenic differentiation was $32.6 \pm 6.5\%$.

In the study of directed chondrogenic differentiation, the first signs of a change in the morphology in the control samples were observed on the 3–4th day of cultivation and on the 5–6th day in the case of using AuNPs in all the concentrations studied. Since the 8th day of chondrogenic differentiation in cultures, we observed areas of high cells concentration. In further observations, cell density increased and on the 21st day there was creation of formed structures with large amount of extracellular matrix, which was confirmed by their staining with Toluidine blue for the proteoglycans. The total percentage of bone marrow cells differentiated in the chondrogenic direction of the control samples was $71.3 \pm 5.2\%$, with the addition of AuNPs of

1.5 $\mu\text{g/ml}$ - $68.7 \pm 7, 1\%$, AuNPs of 3 $\mu\text{g/ml}$ - $68.2 \pm 4.8\%$, AuNPs of 6 $\mu\text{g/ml}$ $62.5 \pm 5.3\%$, and AuNPs of 9 $\mu\text{g/ml}$ $62.7 \pm 7.4\%$. In all investigated concentrations of AuNPs, spontaneous chondrogenic differentiation was not observed.

In the studies of authors the effect of AuNPs on direct multilinear differentiation of MSCs was reported [16, 17, 25–28]. Yi et al. reported that uncoated AuNPs decrease the adipogenic differentiation of murine MSCs in a time and dose-dependent manner. The work of Fan et al. showed that although AuNPs had minor cytotoxicity to the cells, they suppressed osteogenic and adipogenic differentiation of hMSCs on days 7 and 14. In our study, we have shown that 15 nm AuNPs led to a decrease in lipid formation in dependency on the applied particle concentration. The MSCs were probably more fragile during adipogenic differentiation; hence, they may constitute a cell system to detect the cytotoxic effects of nanoparticles and other chemical substances [17].

3.4. Spectroscopic Data. With the aim of having more detailed information about how AuNPs influence the cell, the following issues should be addressed: (i) a possible impact of AuNPs on cellular metabolism; (ii) applicability of AuNPs as cellular markers; (iii) an identification of cellular components, which might get affected by AuNPs, for example, lipid membrane or macromolecular nucleic acids (DNA, RNA); and, finally, (iv) which cellular components give maximum contribution to the IR signal from a single cell with AuNPs. Working on solving this puzzle we analyzed the profiles of so-called marker bands of a cell's main components, which are presented in Table 3.

The results of the histochemical study showed no influence of AuNPs on MSCs under chondrogenic differentiation conditions (Table 2). Therefore the next step was to obtain more information about chemical and biochemical changes influenced by AuNPs in MSCs under adipogenic differentiation conditions. We proceeded by performing FTIR spectroscopy of MSCs as such (control set) and those cultivated with AuNPs in concentrations of 1.5, 3, 6, and 9 $\mu\text{g/ml}$ for 21 days of adipogenic differentiations.

The FTIR spectra presented on Figure 3 show a significant increase of the intensity of IR bands from cells with gold concentration of 1.5 $\mu\text{g/ml}$ due to the Surface Enhanced

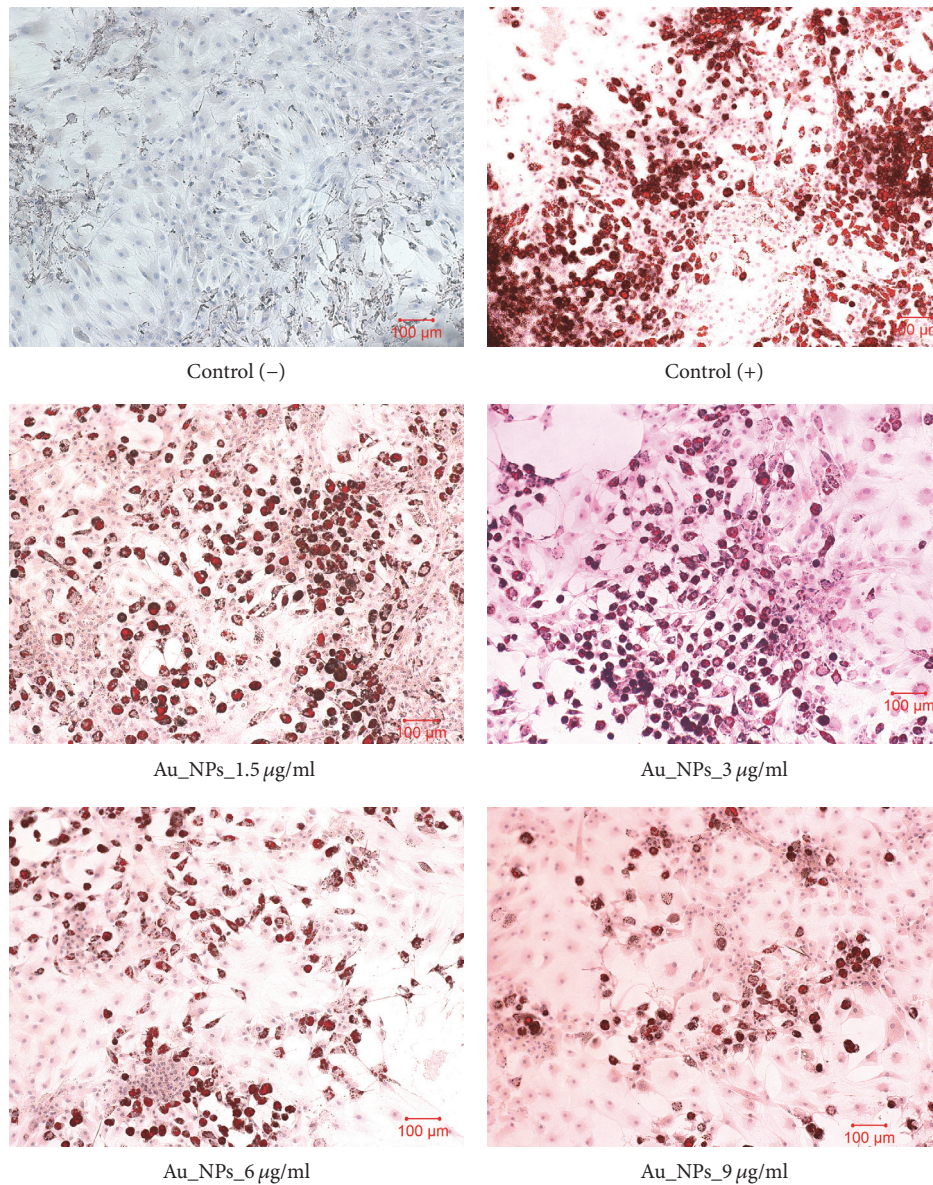


FIGURE 2: The effect of AuNPs on ability of adipogenic differentiation of MSCs, 21st day. Control cells were not incubated with AuNPs. Control (-) cells were not induced to differentiate and control (+) cells were induced to differentiate. Oil red O staining was used to assess adipogenic differentiation by staining for lipid deposits.

TABLE 3: The regions of marker bands for a cell.

| Amide I, cm^{-1} | Amide II, cm^{-1} | Nucleic acids, cm^{-1} | νCH_2 , cm^{-1} | νCH_3 , cm^{-1} |
|---------------------------|----------------------------|---------------------------------|-------------------------------------|-------------------------------------|
| 1600–1710 | 1483–1595 | 1000–1140 | 2900–2944 | 2945–2980 |

Infrared Absorption (SEIRA) effect. In case of SEIRA effect the enhancement of IR absorbance is provided by huge increasing of electromagnetic field in the area around AuNPs. Increase in intensity of IR bands from all cell components, especially enhancement of the signals from the cell nucleus, might indicate that at small concentration of $1.5 \mu\text{g/ml}$ AuNPs mostly pass through the membrane inside the cell. Further increase in gold concentration leads to decrease in IR spectral intensity, which is probably caused by excessive deposition of

AuNPs and cluster's formation of that on a cell membranes. In this case AuNPs still remain a good enhancement factor for cell membrane, which is revealed in strong lipid peaks, but prevent obtaining a good signal from the cell as a whole.

The results of analysis of the intensities of absorption bands of Amide I and Amide II in the IR spectra, which have been measured on the samples of cell cultures with directed adipogenic differentiation and different concentrations of AuNPs are given in Table 4. In the studied samples, the

TABLE 4: Calculated value of Amide I/Amide II ratio in MSC of bone marrow under adipogenic differentiation conditions.

| Sample | IR band for Amide I | | IR band for Amide II | | Amide I/Amide II | Standard deviation |
|------------------------------------|----------------------------|-----------------|----------------------------|-----------------|------------------|--------------------|
| | Position, cm^{-1} | Intensity, a.u. | Position, cm^{-1} | Intensity, a.u. | | |
| Control (no AuNPs) | 1645 | 0.126 | 1541 | 0.095 | 1.309 | ± 0.0007 |
| Au_NPs_1.5 $\mu\text{g}/\text{ml}$ | 1646 | 0.46 | 1545 | 0.38 | 1.269 | ± 0.0007 |
| Au_NPs_3 $\mu\text{g}/\text{ml}$ | 1645 | 0.196 | 1541 | 0.14 | 1.255 | ± 0.0007 |
| Au_NPs_6 $\mu\text{g}/\text{ml}$ | 1645 | 0.11 | 1536 | 0.095 | 1.408 | ± 0.0007 |
| Au_NPs_9 $\mu\text{g}/\text{ml}$ | 1642 | 0.14 | 1536 | 0.11 | 1.422 | ± 0.0007 |

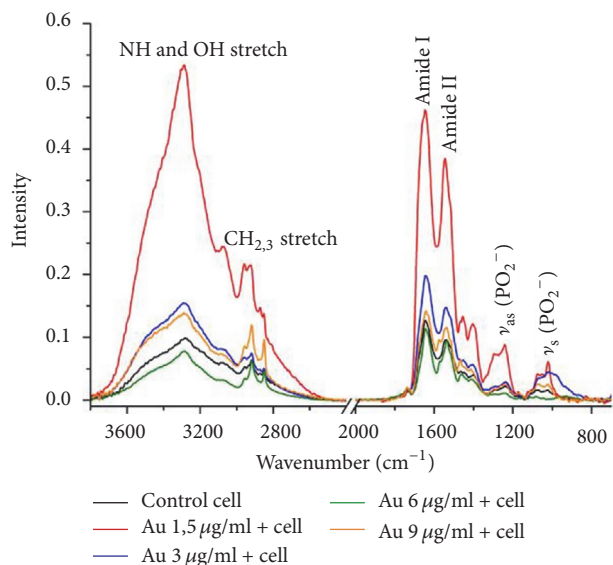


FIGURE 3: FTIR spectra of pristine MSCs (labeled as control cell, black) and of MSCs incubated with AuNPs in concentrations of 1.5 (red), 3 (blue), 6 (green), and 9 (magenta) $\mu\text{g}/\text{ml}$ for 21 days of adipogenic differentiations. Resolution 2 cm^{-1} ; 234 scans are collected. The spectra background are subtracted.

Amide I/Amide II ratio was higher by 7% and 8% for samples of AuNPs with concentrations of 6 and 9 $\mu\text{g}/\text{ml}$, respectively, as compared to the corresponding reference indicator. This points to the necessity of taking into account the specific biochemical changes inherent to each process of differentiation when assessing the nature of the change in Amide vibrations as an apoptotic marker [25].

The ratios between the signals in the $2853\text{--}2291 \text{ cm}^{-1}$ region (absorption of CH_2 groups) and in the $2945\text{--}2980 \text{ cm}^{-1}$ region (absorption of CH_3 groups) were analyzed. An increase of the CH_2/CH_3 ratio is observed during the cells growth in one type of cell culture. The results presented in [29] showed that changes were observed in the ratio of CH_2/CH_3 in the process of cell growth and are not the only characteristic of apoptosis.

The IR spectrum presented on Figure 4 and in Table 5 shows the ratio of asymmetric stretching modes of CH_2/CH_3 hydrocarbon functional groups as markers of apoptosis in cells with directed adipogenic differentiation. In this case, the ratio of CH_2/CH_3 asymmetric modes increases with the rise

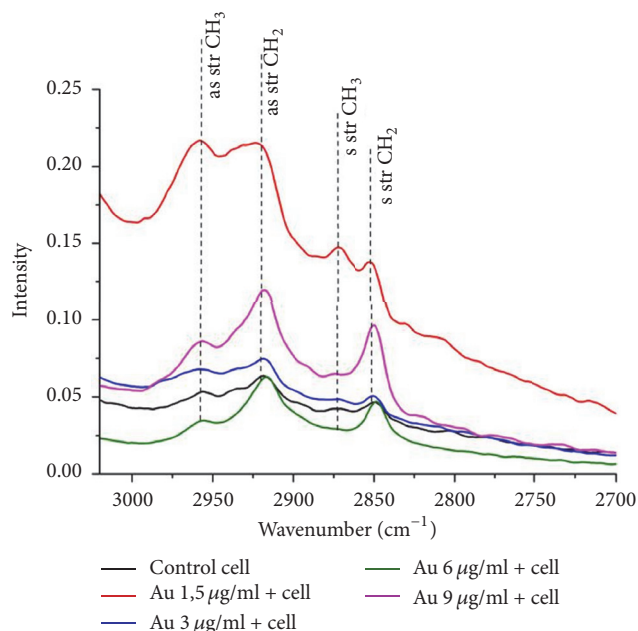


FIGURE 4: FTIR spectra of pristine MSCs (labeled as control cell, black) and of MSCs incubated with AuNPs in concentrations of 1.5 (red), 3 (blue), 6 (green), and 9 (magenta) $\mu\text{g}/\text{ml}$ for 21 days of adipogenic differentiations enlarged in the region of CH vibrations. Resolution 2 cm^{-1} ; 232 scans are collected. The spectra background are subtracted.

of the AuNPs concentration and most sufficient growth is observed at concentration of 9 $\mu\text{g}/\text{ml}$.

The experimental data obtained regarding the change in the CH_2/CH_3 ratio are not fully understood and, therefore, cannot be considered as characteristic of apoptosis. On the contrary, they may be associated with an increase in the number of lipids in the secondary messenger that regulates cell growth. Another explanation is the possible reduction of the cell volume and, hence, of the actual number of molecules with CH_2/CH_3 during the cell growth and are not the only characteristic features of apoptosis [30].

It is important to note that IR spectroscopy does not damage the cells and provides both qualitative and quantitative information related to proteins, lipids, and nucleic acids of living, necrotic, or apoptotic cells within one experimental point without manipulation or staining of the sample.

The molecular mechanism behind the increase in the CH_2/CH_3 ratio is still unclear, but this may be due to an

TABLE 5: Ratio of intensities of asymmetric bands CH₂/CH₃ in MSCs under conditions of adipogenic differentiation.

| Sample | IR band for CH ₂ (as) | | IR band for CH ₃ (as) | | Ratio of CH ₂ /CH ₃ | Standard deviation |
|--------------------|----------------------------------|-----------------|----------------------------------|-----------------|---|--------------------|
| | Position, cm ⁻¹ | Intensity, a.u. | Position, cm ⁻¹ | Intensity, a.u. | | |
| Control (no AuNPs) | 2921 | 0.123 | 2956 | 0.082 | 1.502 | ±0.0006 |
| Au_NPs_1.5 μg/ml | 2921 | 0.087 | 2960 | 0.076 | 1.513 | ±0.0006 |
| Au_NPs_3 μg/ml | 2917 | 0.058 | 2956 | 0.043 | 1.531 | ±0.0006 |
| Au_NPs_6 μg/ml | 2921 | 0.044 | 2956 | 0.040 | 1.547 | ±0.0006 |
| Au_NPs_9 μg/ml | 2921 | 0.037 | 2957 | 0.032 | 1.762 | ±0.0006 |

increase in the number of lipids in the secondary messenger that regulates cell growth or a slight decrease in cell volume after the cells have grown. Indeed, the decrease in the volume of cells corresponds to a relative increase in surface area. This can lead to an increase in the proportion of phospholipids in biomass and, respectively, a major increase in CH₂ in relation to CH₃ groups.

Thus, based on the IR spectroscopy data, it has been established that the AuNPs at concentrations of 1.5–6 μg/ml do not affect the structure of the MSC of the bone marrow. It is shown that the addition of the AuNPs at concentrations of 9 μg/ml under conditions of adipogenic differentiation to MSCs of the bone marrow leads to the formation of the Amide I shoulder in the region of 1617–1630 cm⁻¹ [31, 32], increasing lipid content; appearance of intensive peak at 1740 cm⁻¹, which is usually associated with the non-hydrogen-bonded ester carbonyl C=O stretching mode within phospholipids; and increasing the shoulder at ~1725 cm⁻¹ which is associated with hydrogen-bonded C=O groups. An increase in a peak at ~1725 cm⁻¹ was seen by [33] for investigated cells that had experienced necrosis and was visually changed morphologically because of a loss of cell membrane integrity. The results are likely to indicate the destruction processes in the studied cells. The fact that the ~1740 cm⁻¹ peak in Figure 3 is significantly more intense than the ~1725 cm⁻¹ peak implies that the C=O ester carbonyl groups of lipids in the cell are becoming predominantly non-hydrogen-bonded, which would be in agreement with oxidative damage having occurred. Apoptosis is associated with, among other factors, increased oxidative damage [34, 35]. Therefore, the cells with the AuNPs at concentrations of 9 μg/ml that we measured may have been in the early stages of apoptosis and not a lysosomal type of death whereas cells visually observed to have lost membrane integrity were most likely lysosomal and had different IR spectral characteristics.

4. Conclusions

It was shown that the use of AuNPs in concentration of 1.5–9 μg/ml did not lead to significant changes in the level of expression of CD 45, CD 90, and CD 73. It should be noted that AuNPs in concentrations of 6 and 9 μg/ml led to a decrease in CD 44 cells by 6% and 9%, respectively. The content of CD 105 cells was reduced by 5% when AuNPs were applied at a concentration of 9 μg/ml. It was found that AuNPs in concentration of 1.5–6 μg/ml are safe for MSCs, while increase up to 9 μg/ml has a toxic effect,

manifested by the reduction of synthesis collagen type I, adipogenic differentiation ability, and apparent apoptosis. IR spectroscopy data have shown that the AuNPs at concentrations of 1.5–6 μg/ml do not affect the structure of proteins, lipids, and nucleic acids of the MSC of the bone marrow. The addition of the AuNPs at concentrations of 9 μg/ml under conditions of adipogenic differentiation to MSCs leads to the destruction processes in the cells. The obtained results are related to the field of applied nanotechnology, which extends to regenerative medicine, especially in development of bioimplantology.

Conflicts of Interest

The authors declare that they have no conflicts of interest.

Authors' Contributions

Anatolij Goltsev and Nataliia Volkova contributed to study design; Nataliia Volkova and Olena Pavlovich performed the experiments of cultivation and differentiation of MSCs, analyzed the data, and wrote the manuscript; Olena Fesenko performed analysis of results of IR study of MSCs and participated in writing the manuscript; Oksana Budnyk and Serhii Kovalchuk measured IR spectra of MSCs and analysis of resulting IR spectra.

Acknowledgments

The work was carried out within the research project of Marie Curie ILSES FP7, Projects 612620 and N70/17-H National Academy of Sciences of Ukraine.

References

- [1] Y. Teow, P. V. Asharani, M. P. Hande, and S. Valiyaveetil, "Health impact and safety of engineered nanomaterials," *Chemical Communications*, vol. 47, no. 25, pp. 7025–7038, 2011.
- [2] A. M. Alkilany and C. J. Murphy, "Toxicity and cellular uptake of gold nanoparticles: what we have learned so far?" *Journal of Nanoparticle Research*, vol. 12, no. 7, pp. 2313–2333, 2010.
- [3] E. Söderstjerna, F. Johansson, B. Klefbohm, and U. Englund Johansson, "Gold- and silver nanoparticles affect the growth characteristics of human embryonic neural precursor cells," *PLoS ONE*, vol. 8, no. 3, Article ID e58211, 2013.
- [4] N. Khlebtsov and L. Dykman, "Biodistribution and toxicity of engineered gold nanoparticles: a review of in vitro and in vivo

- studies," *Chemical Society Reviews*, vol. 40, no. 3, pp. 1647–1671, 2011.
- [5] G. V. Lowry, K. B. Gregory, S. C. Apte, and J. R. Lead, "Transformations of nanomaterials in the environment," *Environmental Science & Technology*, vol. 46, no. 13, pp. 6893–6899, 2012.
- [6] A. Bour, F. Mouchet, J. Silvestre, L. Gauthier, and E. Pinelli, "Environmentally relevant approaches to assess nanoparticles ecotoxicity: A review," *Journal of Hazardous Materials*, vol. 283, pp. 764–777, 2015.
- [7] N. G. Khlebtsov, A. G. Melnikov, L. A. Dykman, and V. A. Bogatyrev, "Optical properties and biomedical applications of nanostructures based on gold and silver bioconjugates, photopolarimetry in remote sensing," *Photopolarimetry in Remote Sensing*, pp. 265–308, 2004.
- [8] J. G. Leu, S. A. Chen, H. M. Chen et al., "The effects of gold nanoparticles in wound healing with antioxidant epigallocatechin gallate and alpha-lipoic acid," *Nanomedicine: Nanotechnology, Biology and Medicine*, vol. 8, no. 5, pp. 767–775, 2012.
- [9] N. Volkova, M. Yukhta, O. Pavlovich, and A. Goltsev, "Application of cryopreserved fibroblast culture with au nanoparticles to treat burns," *Nanoscale Research Letters*, vol. 11, no. 1, article no. 22, pp. 1–6, 2016.
- [10] R. Cao-Milán and L. M. Liz-Marzán, "Gold nanoparticle conjugates: recent advances toward clinical applications," *Expert Opinion on Drug Delivery*, vol. 11, no. 5, pp. 741–752, 2014.
- [11] R. Arvizo, R. Bhattacharya, and P. Mukherjee, "Gold nanoparticles: opportunities and challenges in nanomedicine," *Expert Opinion on Drug Delivery*, vol. 7, no. 6, pp. 753–763, 2010.
- [12] J. P. M. Almeida, A. L. Chen, A. Foster, and R. Drezek, "In vivo biodistribution of nanoparticles," *Nanomedicine*, vol. 6, no. 5, pp. 815–835, 2011.
- [13] Y. Pan, S. Neuss, A. Leifert et al., "Size-dependent cytotoxicity of gold nanoparticles," *Small*, vol. 3, no. 11, pp. 1941–1949, 2007.
- [14] M. Dominici, K. Le Blanc, I. Mueller et al., "Minimal criteria for defining multipotent mesenchymal stromal cells. the international society for cellular therapy position statement," *Cytotherapy*, vol. 8, no. 4, pp. 315–317, 2006.
- [15] H. Busser, M. Najar, G. Raicevic et al., "Isolation and characterization of human mesenchymal stromal cell subpopulations: comparison of bone marrow and adipose tissue," *Stem Cells and Development*, vol. 24, no. 18, pp. 2142–2157, 2015.
- [16] S. J. Soenen, B. Manshian, J. M. Montenegro et al., "Cytotoxic effects of gold nanoparticles: A multiparametric study," *ACS Nano*, vol. 6, no. 7, pp. 5767–5783, 2012.
- [17] Y. Kohl, E. Gorjup, A. Katsen-Globa, C. Büchel, H. Von Briesen, and H. Thielecke, "Effect of gold nanoparticles on adipogenic differentiation of human mesenchymal stem cells," *Journal of Nanoparticle Research*, vol. 13, no. 12, pp. 6789–6803, 2011.
- [18] K. Ataka and J. Heberle, "Functional vibrational spectroscopy of a cytochrome c monolayer: SEIDAS probes the interaction with different surface-modified electrodes," *Journal of the American Chemical Society*, vol. 126, no. 30, pp. 9445–9457, 2004.
- [19] M. Li, J. Xu, M. Romero-Gonzalez, S. A. Banwart, and W. E. Huang, "Single cell Raman spectroscopy for cell sorting and imaging," *Current Opinion in Biotechnology*, vol. 23, no. 1, pp. 56–63, 2012.
- [20] A. D. McFarland, C. L. Haynes, C. A. Mirkin, R. P. Van Duyne, and H. A. Godwin, "Color my nanoworld," *Journal of Chemical Education*, vol. 81, no. 4, p. 544A, 2004.
- [21] D. Baksh, R. Yao, and R. S. Tuan, "Comparison of proliferative and multilineage differentiation potential of human mesenchymal stem cells derived from umbilical cord and bone marrow," *Stem Cells*, vol. 25, no. 6, pp. 1384–1392, 2007.
- [22] J. P. Rodríguez, L. Montecinos, S. Ríos, P. Reyes, and J. Martínez, "Mesenchymal stem cells from osteoporotic patients produce a type I collagen-deficient extracellular matrix favoring adipogenic differentiation," *Journal of cellular biochemistry*, vol. 79, no. 4, pp. 557–565.
- [23] N. Volkova, O. Pavlovich, O. Fesenko, O. Budnyk, and A. Goltsev, "Influence of gold nanoparticles on morphological and functional characteristics of bone marrow mesenchymal stem cells: MTT assays and spectroscopic data," *Nano Studies*, vol. 14, pp. 151–160, 2016.
- [24] E. V. Pavlovich and N. A. Volkova, "Influence of gold nanoparticles on human fibroblast before and after cryopreservation," in *Nanoplasmonics, Nano-Optics, Nanocomposites, and Surface Studies*, vol. 167 of *Springer Proceedings in Physics*, pp. 413–420, Springer International Publishing, Basel, Switzerland, 2015.
- [25] C. Yi, D. Liu, C.-C. Fong, J. Zhang, and M. Yang, "Gold nanoparticles promote osteogenic differentiation of mesenchymal stem cells through p38 MAPK pathway," *ACS Nano*, vol. 4, no. 11, pp. 6439–6448, 2010.
- [26] J. H. Fan, W. I. Hung, and J. M. Yeh, "Biocompatibility study of gold nanoparticles to human cells," *ICBME Proceedings*, 2009.
- [27] J. Fan, W. Li, W. Hung, C. Chen, and J. Yeh, "Cytotoxicity and differentiation effects of gold nanoparticles to human bone marrow mesenchymal stem cells," *Biomedical Engineering : Applications, Basis, and Communications*, vol. 23, no. 02, pp. 141–152, 2011.
- [28] L. M. Ricles, S. Y. Nam, K. Sokolov, S. Y. Emelianov, and L. J. Suggs, "Function of mesenchymal stem cells following loading of gold nanotracers," *International Journal of Nanomedicine*, vol. 6, pp. 407–416, 2011.
- [29] X. Zhang, "Gold nanoparticles: recent advances in the biomedical applications," *Cell Biochemistry and Biophysics*, vol. 72, no. 3, pp. 771–775, 2015.
- [30] W. Zhou, X. Gao, D. Liu, and X. Chen, "Gold Nanoparticles for in vitro diagnostics," *Chemical Reviews*, vol. 115, no. 19, pp. 10575–10636, 2015.
- [31] Y. Gao, X. Huo, L. Dong et al., "Fourier transform infrared microspectroscopy monitoring of 5-fluorouracil-induced apoptosis in SW620 colon cancer cells," *Molecular Medicine Reports*, vol. 11, no. 4, pp. 2585–2591, 2015.
- [32] H. Y. Holman, M. C. Martin, E. A. Blakely, K. Bjornstad, and W. R. McKinney, "IR spectroscopic characteristics of cell cycle and cell death probed by synchrotron radiation based Fourier transform IR spectromicroscopy," *Biopolymers*, vol. 57, no. 6, pp. 329–335.
- [33] N. Jamin, P. Dumas, J. Moncuit et al., "Highly resolved chemical imaging of living cells by using synchrotron infrared microspectrometry," *Proceedings of the National Academy of Sciences of the United States of America*, vol. 95, no. 9, pp. 4837–4840, 1998.
- [34] R. Mittler and A. Y. Cheung, *When Cells Die II: A Comprehensive Evaluation of Apoptosis and Programmed Cell Death*, Wiley, New York, NY, USA, 2004.
- [35] R. Birge, *When Cells Die II: A Comprehensive Evaluation of Apoptosis and Programmed Cell Death*, John Wiley and Sons, Inc., New York, NY, USA, 2003.

Research Article

Bacterial Stress and Osteoblast Responses on Graphene Oxide-Hydroxyapatite Electrodeposited on Titanium Dioxide Nanotube Arrays

Yardnapar Parcharoen,¹ Preecha Termsuksawad,² and Sirinrath Sirivisoot³

¹Chulabhorn International College of Medicine, Thammasat University, Pathum Thani 12120, Thailand

²Division of Materials Technology, School of Energy, Environment and Materials,
King Mongkut's University of Technology Thonburi, Bangkok 10140, Thailand

³Biological Engineering Program, Faculty of Engineering, King Mongkut's University of Technology Thonburi, Bangkok 10140, Thailand

Correspondence should be addressed to Sirinrath Sirivisoot; sirinrath.sir@kmutt.ac.th

Received 27 April 2017; Accepted 25 July 2017; Published 30 August 2017

Academic Editor: Faheem Ahmed

Copyright © 2017 Yardnapar Parcharoen et al. This is an open access article distributed under the Creative Commons Attribution License, which permits unrestricted use, distribution, and reproduction in any medium, provided the original work is properly cited.

To develop bone implant material with excellent antibacterial and biocompatible properties, nanotubular titanium surface was coated with hydroxyapatite (HA) and graphene oxide (GO). Layer-by-layer deposition was achieved by coating HA on an anodic-grown titanium dioxide nanotube array (ATi) with electrolytic deposition, followed by coating with GO using anodic-electrophoretic deposition. The antibacterial activity against both Gram-negative (*Escherichia coli*) and Gram-positive (*Staphylococcus aureus*) bacteria was determined based on the percentage of surviving bacteria and the amount of ribonucleic acid (RNA) leakage and correlated with membrane disruption. The oxidative stress induced in both strains of bacteria by GO was determined by cyclic voltammetry and is discussed. Importantly, the antibacterial GO coatings on HA-ATi were not cytotoxic to preosteoblasts and promoted osteoblast proliferation after 5 days and calcium deposition after 21 days in standard cell culture conditions.

1. Introduction

Hydroxyapatite (HA, $\text{Ca}_{10}(\text{PO}_4)_6(\text{OH})_2$) is a mineralogic component of natural bone with a molar calcium to phosphate ratio of 1.67 [1]. Several methods for coating HA onto biomaterial surfaces include plasma spray, microarc oxidation, and electrodeposition. Electrodeposition is an easy method that allows for adjustment of the thickness and porosity of the HA coating, increased corrosion protection, and reduced release of metal ions by changing systemic parameters. HA may be electrodeposited on an anodic-grown titanium dioxide (TiO_2) nanotube array on titanium (Ti), which is widely used in orthopedic implants to form a direct bone-to-metal interface, referred to as osseointegration [2, 3]. TiO_2 nanotubes fabricated by anodization are highly ordered and highly adhesive to the substrate due to the intrinsic chemical bonds between the nanotubes and Ti.

Bioactive HA has been widely used as a coating material for dental and orthopedic implants for many years, but by itself, it does not prevent bacterial infection after implantation. Infections associated with surgical implants are generally difficult to be suppressed and may require a longer period of antibiotic therapy and repeated surgical procedures [4]. Antibacterial property of HA coating could be improved by adding other nanomaterials such as graphene oxide.

Graphene oxide (GO) has antibacterial activity that can reduce the risk of bacterial infection. GO nanosheets inhibit bacterial growth [5, 6]. GO coatings also promote osteoblast function and the antibacterial properties of implant materials [3, 6–8]. A hydrothermal synthesized nanocomposite of HA nanorods on GO sheets showed faster adsorption of bovine serum albumin in adsorption-desorption process on its surface [9]. Such nanocomposite was suitable for drug delivery due to its biocompatibility, high drug loading efficiency,

and biodegradability. The nanocomposite of HA on reduced GO was also used as enzymatic electrochemical glucose biosensors which exhibited a superior detection limit and higher sensitivity [10]. Graphene cytotoxicity in neural cells is due to the production of reactive oxygen species (ROS) in a concentration- and time-dependent manner [11, 12]. The antibacterial mechanism of another carbon-based nanomaterial, carbon nanotubes (CNTs), is induced by oxidizing a cellular structure or component of bacteria with CNTs [13]. For example, the increased cytotoxicity of single-walled CNTs might be due to an increase of in cellular oxidative stress and a loss of cell membrane integrity [14]. It remains unclear, however, whether intracellular ROS are most likely induced by external ROS produced by GO outside of the bacteria or whether intracellular ROS are directly produced by the GO surface.

Oxidative stress (or ROS formation) generated from other carbon nanomaterials, such as graphene [12], fullerene [15], and CNTs [16], is a key antibacterial mechanism. Many studies have measured oxidative stress and its relationship to disease, such as in acute pancreatitis and hemorrhagic shock syndrome [17, 18]. In the present study, electrochemical method was used to indirectly detect ROS in bacteria on the electrodeposited GO coatings. Once ROS react with an electron-acceptor protein at the cell membrane, an electrical signal is detected from the bacteria-seeded electrode in an electrochemical cell. Here, oxidative stress in both Gram-positive (*Staphylococcus aureus*) and Gram-negative (*Escherichia coli*) bacteria was studied after they colonized on GO coatings after 24 h. In addition, preosteoblast (MC3T3-E1) cell proliferation and calcium deposition under standard cell culture condition were examined to determine the early osteoblast response to electrodeposited GO coatings *in vitro*.

2. Experimental Materials and Methods

2.1. Anodic-Electrophoretic Deposition of Graphene. GO solutions were prepared by dispersing GO in isopropyl alcohol (Ajax Finechem, New Zealand) at concentrations of 50, 100, 150, and 200 $\mu\text{g ml}^{-1}$, named GO1, GO2, GO3, and GO4, respectively. GO was deposited by anodic-electrophoretic deposition on HA-ATi samples prepared as described previously [3, 19]. A direct current of 10 V was applied at room temperature for 10 min during anodic-electrophoretic deposition. HA-ATi layers without GO (GO0) were used as a control.

2.2. Physical and Chemical Characterizations. The surface morphology of the coatings was characterized by scanning electron microscopy (SEM, CamScanMX2600, UK) with a 10 keV electron beam. The amount of GO was indirectly analyzed using image analysis software (ImageJ version 1.32, Montgomery, National Institutes of Health, Maryland). The crystal structures of the coating were examined using an X-ray diffractometer with $\text{CuK}\alpha 1$ radiation (Shimadzu Model: XRD 6000, Japan) at a scanning rate of $1^\circ/\text{min}$.

2.3. Bacterial Responses. All samples were tested against *S. aureus* and *E. coli* bacteria as Gram-positive and Gram-negative models, respectively. The bacteria were cultured in

Mueller-Hinton broth (Thailand Science Park, Thailand) at 37°C for 24 h with shaking at 200 rpm. The bacteria were then centrifuged at 5000 rpm for 5 min. The bacteria pellet was added to 10 ml sterilized saline solution to reach a concentration of bacteria of 10^6 colony forming units (CFU) per milliliter.

2.3.1. Antibacterial Drop Test. Each sample was placed into a sterilized 24-well plate. Then, 100 μl of diluted bacterial suspension was spread on the surface of the sample. After sonication of the sample at 37°C for 60 min, the bacteria were washed from the surface of the sample with 1.5 ml sterilized phosphate-buffered saline (PBS) in the sterilized 24-well plate. Then, 50 μl of each bacterial suspension was added to Mueller-Hinton broth and incubated at 37°C for 24 h to measure bacterial absorbance using a spectrophotometer, and percent of relative bacterial cell survival was calculated (1). The reported data are the mean value of three independent experiments.

$$\begin{aligned} & \% \text{ Relative cell survival} \\ & = \frac{\text{Absorbance of sample} \times 100\%}{\text{Absorbance of control}}. \end{aligned} \quad (1)$$

2.3.2. Measurement of Ribonucleic Acid (RNA) Efflux. First, the media remaining from oxidative stress measurement of each sample were centrifuged at 13,000 rpm for 2 min. The supernatant of the solution was then used to measure the RNA efflux of the bacteria. RNA was separated using a RNA purification kit (RBC Bioscience, Taiwan) in which single-stranded RNA and double-stranded RNA of more than 200 to 1000 of base pairs in length were efficiently purified. Elution solutions of RNA were measured to determine the RNA concentration with a microplate reader (Infinite® 200 PRO NanoQuant, Switzerland).

2.3.3. Determination of Bacterial Oxidative Stress Using the Electrochemical Method

(1) Preparation of Samples for Electrochemical Measurements. Oxidative stress was studied electrochemically using cyclic voltammetry (CV) technique. CV analysis was selected as a reliable and effective method to measure oxidative stress without pretreating the sample surface or using any specific chemical before analysis. Effects of various GO concentrations and initial-seeding cell concentrations on oxidative stress in bacterial cells were studied. The oxidation measurement area, 0.25 cm^2 , was controlled by coating with corrosion-protective paint (Jotun, Thailand), as shown in Figure 1. Prior to testing with bacteria, sterilized samples were exposed to $30,000 \mu\text{WS cm}^{-2}$ of 254 nm UV energy (JKL, USA) for 4 h on each side.

(2) Culture of Bacterial Cells for Electrochemical Measurements. The samples (Figure 1) were placed in a sterilized 24-well plate. Then, 1 ml of the diluted bacterial suspension (10^6 CFU ml^{-1}) was spread onto the sample surface. The bacteria were cultured in Mueller-Hinton broth at 37°C for 24 h at

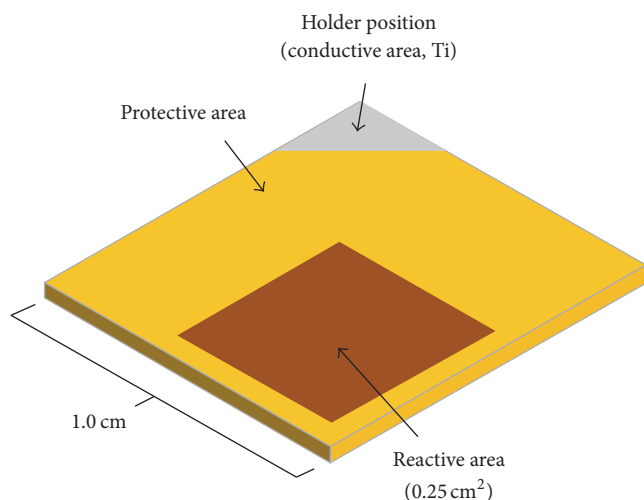


FIGURE 1: Scheme of sample preparation for electrochemical measurements.

an angular velocity of 200 rpm. The samples were placed in a three-electrode electrochemical system to measure oxidative stress. Bacteria absorbance in the medium of each sample was measured using a microplate reader (Infinite® 200 PRO NanoQuant, Switzerland). Relative bacterial cell survival was calculated using (2). The mean percent of relative cell survival was determined from three independent experiments.

$$\text{Relative cell survival (\%)} = \frac{\text{Absorbance of sample} \times 100\%}{\text{Absorbance of control (polystyrene plate)}} \quad (2)$$

(3) *Cyclic Voltammetry.* A three-electrode electrochemical system was used in this study. Samples with living bacteria were used as the working electrodes. A silver/silver chloride (Ag/AgCl, 6.0726.107, Metrohm Autolab B.V., Switzerland) and a platinum coil (Alfa Aesar) were used as reference and counter electrodes, respectively. The changes in the electrical current through working electrodes were recorded with a potentiostat PGSTAT 302N (Metrohm Autolab B.V.) with the NOVA program (version 1.9.16, Metrohm Autolab B.V.). Prior to measurement, all electrodes were cleaned

with deionized water. All electrodes were connected to an electrochemical workstation and immersed in electrolyte solution, a 1x PBS (Gibco) solution. CV was also performed in 1.0 mM $\text{K}_3[\text{Fe}(\text{CN})_6]$ (Ajax Finechem, New Zealand) dissolved in 0.1 M $\text{NaH}_2\text{PO}_4/\text{Na}_2\text{HPO}_4$ (Ajax Finechem, New Zealand) buffer to test for a direct electron transfer at electrodes without living bacteria. The scan rate for CV was 100 mV s^{-1} , whereas the potential step was 0.00244 V with a start potential of -1.0 V . The upper vertex potential, the lower vertex potential, and the stop potential were +1, -1 , and -1 V , respectively. Three independent samples were tested for each condition.

2.4. Osteoblast Responses

2.4.1. *Cell Culture.* Preosteoblasts (MC3T3-E, passage number = 11, Mahidol University, Thailand), were cultured in alpha-modified minimal essential medium (alpha-MEM; Invitrogen Corporation, Paisley, UK) supplemented with 10 vol% fetal calf serum (Dominique Dutcher, Brumath, France) and 1 vol% penicillin/streptomycin (Invitrogen Corporation). Cells were cultured at 37°C in a humidified atmosphere of 5% CO_2 in air and media were replaced every 3 days.

2.4.2. *Cell Viability.* Cells were subcultured through trypsinization (0.25% trypsin and 0.53 M EDTA; Invitrogen Corporation) and then seeded onto plastic polystyrene (control) at a density of $4 \times 10^4 \text{ cells cm}^{-2}$ in 24-well culture plates. Cell viability was tested using a commercial MTT assay (Sigma-Aldrich, Thailand). The 10 vol% solution of MTT in 1x phosphate buffer saline was mixed with alpha-MEM without phenol red to form a yellowish solution before being added to the cell-seeded samples at day 5 of the culture. Mitochondrial dehydrogenases of viable cells cleave the tetrazolium ring, yielding purple formazan crystals on cell-seeded samples after incubation for 1 h. The blue formazan crystals trapped in the cells were dissolved in sterile DMSO ($100 \mu\text{l}$) by incubating at 37°C for 30 min. Absorbance of the purple solution was measured at 550 nm using a spectrophotometer (Synergy Mx Multi-Mode Reader, US). A concomitant change in the amount of formazan formed correlates to the change in the number of viable cells in the samples. Therefore, the percentages of viable cells in the samples are calculated as shown in

$$\text{Cell viability (\%)} = \frac{\text{Absorbance of colored solution incubated with samples} \times 100\%}{\text{Absorbance of colored solution incubated with control (polystyrene plate)}} \quad (3)$$

2.4.3. Calcium Deposition Assay

(1) *Induction of Osteogenic Differentiation.* Preosteoblasts or bone-forming cells were used in this study. The cells were cultured in alpha-MEM (Invitrogen Corporation) supplemented with 10 vol% fetal calf serum (Dominique Dutcher, Brumath, France), 1 vol% penicillin/streptomycin (Invitrogen Corporation), 5 mM β -glycerophosphate (Sigma-Aldrich), $50 \mu\text{g ml}^{-1}$

ascorbic acid (Sigma-Aldrich), and 100 nM dexamethasone (Sigma-Aldrich) [20]. The initial cell seeding density was $4 \times 10^4 \text{ cells cm}^{-2}$ at 37°C in a humidified atmosphere of 5% CO_2 in air. The cell culture media were replaced every 3 d. The calcium content was monitored at 21 d of culture.

(2) *Cell Lysis and Calcium Content Analysis.* After removing the culture media and washing the samples with PBS, $200 \mu\text{l}$

SDS lysis buffer was added to each sample. The samples were shaken using an orbital shaker at an angular velocity of 200 rpm for 5 min and then incubated in a CO₂ incubator at 37°C for 1 h. Incubated samples were placed into a mixture of 5 N HCl solution (Ajax Finechem, New Zealand) and the cell lysate, with a fixed ratio as 250 μ l of 5 N HCl per 1 ml of cell lysate. The solution was mixed with the samples using an orbital shaker at 200 rpm for 5 min. The samples were then incubated at 4°C for 4 h.

Calcium quantification was performed after cell lysates were incubated more than 4 h. The cell lysates were then mixed with ethanolamine buffer as 10 μ l per 1000 μ l in autoclaved microcentrifuge tubes, and 100 μ l ortho-cresolphthal-ein (0.63 mM; Sigma-Aldrich) was added to the ethanolamine and cell lysate solution in microcentrifuge tubes to obtain a purplish red color of solution. The light absorbance of calcium in the supernatant was measured using a microplate reader at a wavelength of 570 nm. The calcium concentration was calculated according to a standard curve generated from a serial dilution of standard calcium solutions. Calcium content was reported as micrograms of calcium per square centimeter of the sample area (μ g cm⁻²). Nine samples in each group were tested at culture day 21. The experiment was repeated three times.

2.5. Statistical Analysis. Analysis of variance (ANOVA) and independent-samples *t*-test were used with Minitab® 16 (Minitab Inc., USA). A probability of 0.05 was considered statistically significant.

3. Results and Discussion

3.1. Anodic-Electrophoretic Deposition of a Graphene Oxide and Hydroxyapatite Coating. SEM images of GO coatings on HA-ATi by anodic-electrophoretic deposition are shown in Figures 2(a)–2(e). The SEM images show thin layers of GO coatings on top of HA layers. Our previous study confirmed the presence of the carbon content of the GO on the coatings after electrodeposition by energy-dispersive X-ray and Fourier transform infrared spectroscopy [10]. In the present study, quantitative analysis of the carbon content was conducted by indirectly measuring HA intensity using ImageJ. The results in Figure 2 suggest that the HA content decreases when the electrodeposited GO content increases, and the highest GO content was found on the GO4 sample (200 μ g ml⁻¹) compared to the other coatings. This implies that a thick GO coating is obtained when using a high concentration of GO in the electrolyte during the electrophoretic deposition process. The crystal structures of the samples in the present study were analyzed using XRD, as shown in Figure 3. The results of XRD spectra confirmed that the layers of HA (Ca₁₀(PO₄)₆(OH)₂) and TiO₂ (anatase phase) existed on all surfaces; however, the intensity of their peaks was lower on the GO-coated samples. In our previous work, XRD spectrum of GO powder (before electrodeposition) showed a peak at two Theta = 10.16° [21]. However, the XRD patterns of GO1, GO2, GO3, and GO4 samples (Figure 3) did not show the peaks at two Theta range of 10–12°. The previous study reported that the absence of the peak at two Theta

approximately to 10–12° was found in reduced GO [22]. It is possible that reduced GO coating is formed after the electrophoretic deposition in the present study. In addition, if GO content in coating is less than 5 wt%, its peak would not show due to limitation of the technique. Although the GO peaks did not appear, it may be implied from XRD patterns that GO existed on the surface due to reduction of apatite and anatase peaks with an increase of GO content used in the anodic-electrophoretic deposition. The reduction of the peaks may be resulted from an increase of GO concentration on the coatings.

3.2. Bacterial Responses

3.2.1. Measurements of Bacterial Survival and RNA Leakage. GO0 samples had weak antibacterial activity. The GO-coated samples, however, exhibited considerable antibacterial activity. Specifically, after 1 h of culture, 98% (GO1), 49% (GO2), 34% (GO3), and 37% (GO4) of the *E. coli* survived on the surface of the GO-coated samples. Figure 4 shows similar results for *S. aureus*. Similar to *E. coli*, the GO was toxic to *S. aureus*. The GO exhibited stronger antibacterial activities against *S. aureus* than against *E. coli*. In fact, only 86% (GO1), 57% (GO2), 23% (GO3), and 26% (GO4) of the *S. aureus* survived on the GO surface after 1 h of culture. Although electrodeposited GO on HA-ATi was toxic to both types of bacteria, it was more toxic to the Gram-positive (*S. aureus*) bacteria.

The results confirmed that the GO-coated samples reduced bacterial survival. The mechanisms to kill the bacteria were likely oxidation and membrane disruption. Therefore, the toxicity of the samples to bacteria through membrane damage can be investigated by measuring intracellular materials such as RNA in the supernatant surrounding the bacteria exposed to the GO-coated samples [9]. Thus, the efflux of the cytoplasmic materials of the bacteria was examined by measuring the concentration of RNA in the solution (Figure 4). The RNA concentrations in the solutions of bacteria exposed to GO-coated samples at each concentration were significantly higher than that of the control samples (GO0), except that for GO1 against *E. coli* bacteria. This is due to direct contact between GO and bacteria causing RNA leakage. Because GO has extremely sharp edges, it could damage the bacterial membrane [23]. In the present study, when the GO concentrations increased, RNA leakage also increased.

The RNA effluxes from *S. aureus* exposed to GO were significantly higher than those of *E. coli* under the same culture conditions. This may be due to the greater resistance of *E. coli* in direct contact with the edge of the GO compared with *S. aureus*. Although *S. aureus* is a Gram-positive bacteria whose peptidoglycan layer provides additional strength to the cell wall, which is also thicker (20–80 nm) than that of *E. coli* (Gram-negative) bacteria (7–8 nm) [9, 24, 25], the *S. aureus* was less resistant than *E. coli*. Gram-negative *E. coli* has a much thinner layer of peptidoglycan, but it also has a layer of lipopolysaccharides that might protect the cell. A previous report indicated that *E. coli* exhibited more resistance to direct contact interaction induced by

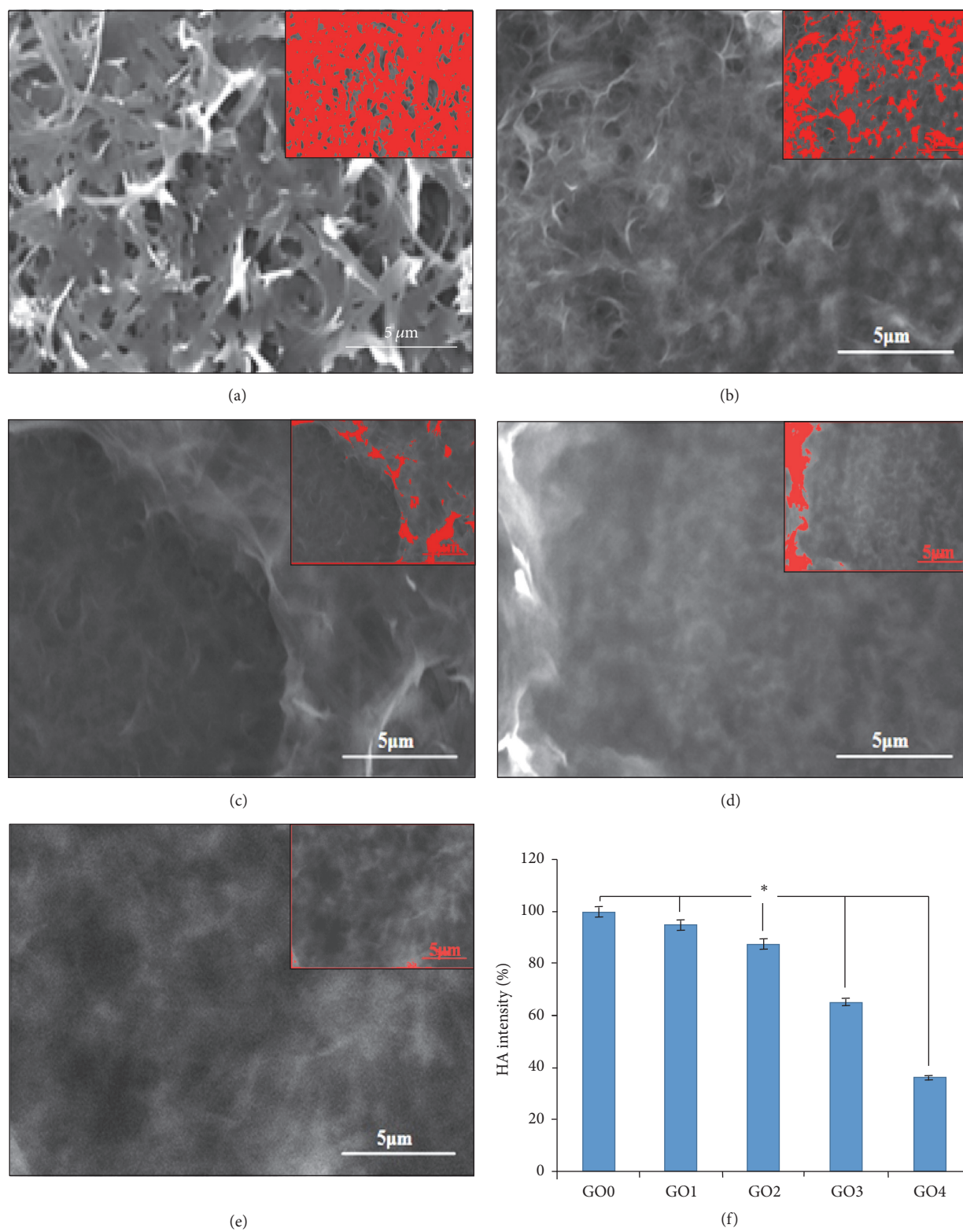


FIGURE 2: SEM micrographs of GO coated on HA-ATi in a layer-by-layer deposition method on (a) HA-ATi or GO0 and HA-ATi coated with various GO concentrations. (b) GO1; (c) GO2; (d) GO3; (e) GO4. Inset micrographs show ImageJ analysis of the figures; (f) a comparison of HA intensity, derived from ImageJ analysis. The p value was calculated using one-way ANOVA; $N = 3$, $*p < 0.05$. Scale bars are $5 \mu\text{m}$.

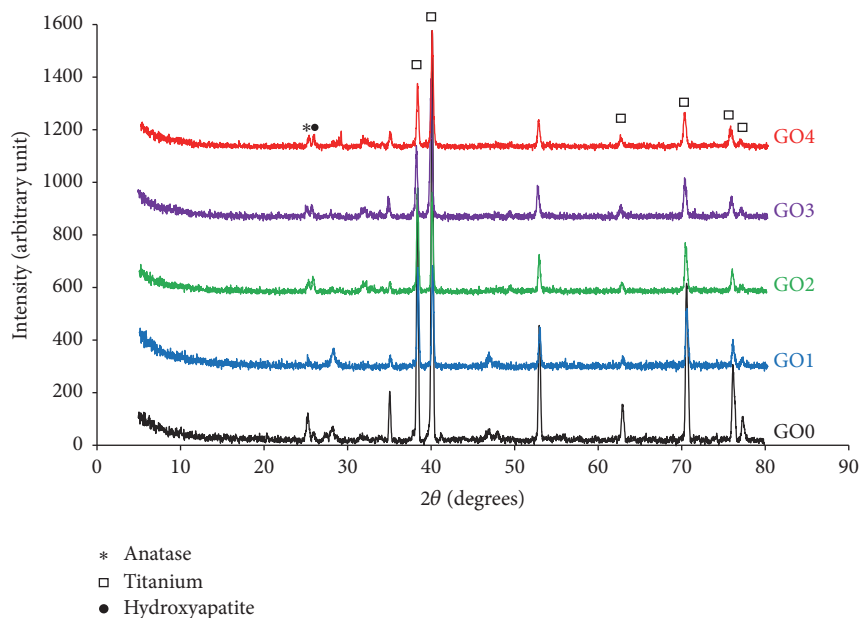


FIGURE 3: XRD spectra of GO0, GO1, GO2, GO3, and GO4.

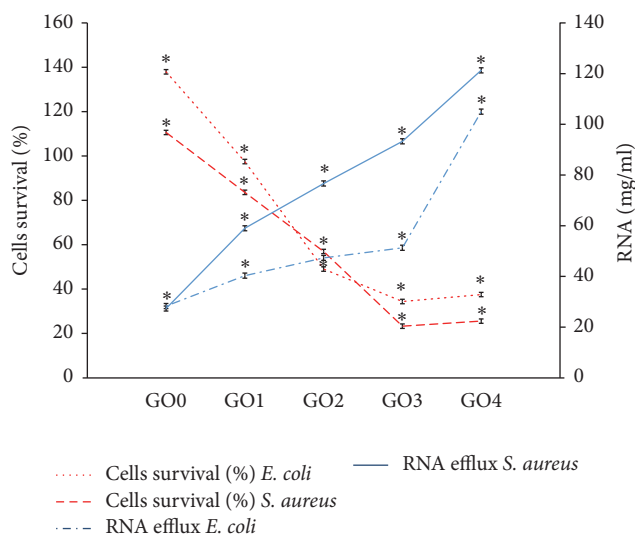


FIGURE 4: Bacterial survival and RNA efflux in PBS after bacteria were cultured on the GO coatings with an antibacterial drop test. The p value was calculated using one-way ANOVA; * $p < 0.05$ when compared with other coating conditions.

an atomic force microscopy tip than *S. aureus* due to the outer membrane of the Gram-negative *E. coli* bacteria [26]. Moreover, comparison between the stiffness of Gram-positive and Gram-negative bacterial cells suggested that, for these particular strains of bacteria, the stiffness of *S. aureus* (95 MPa) was lower than that of the *E. coli* (220 MPa) [27]. Therefore, *E. coli* should be more resistant to membrane damage than *S. aureus*.

3.2.2. Determination of Bacterial Oxidative Stress Using the Electrochemical Method. Bacterial survival percentages of

S. aureus and *E. coli* were presented in Figure 5(a). GO samples exhibited weak antibacterial activity for both bacteria strains. In contrast, GO-coated samples exhibited considerable antibacterial activity based on a toxicity test. The number of both bacterial species was significantly reduced with an increase in the GO concentration. Relative survival of bacteria on the GO3 sample, however, did not differ significantly from that on the GO4 sample ($p > 0.05$). Antibacterial activities against *S. aureus* of the GO-coated samples were stronger than those against *E. coli*. Importantly, GO on HA-ATi samples was more toxic to Gram-positive *S. aureus* than Gram-negative *E. coli*. The exact mechanism of damage to the bacteria remains unclear. There are other models, however, suggesting that bacterial adhesion is influenced by some force factors such as electrostatic forces, van der Waals forces, hydrophobic forces, hydrogen bonding, and covalent bonding of bacterial cells and substrates [28, 29]. Mafu et al. reported that the first and the most important such force was the electrostatic force of charges between the surface substrate and bacterial membrane [29]. They show that GO being negatively charged due to the presence of carboxyl, hydroxyl, and epoxy groups is less repulsive to Gram-positive bacteria than Gram-negative bacteria [25].

CV is fundamental electrochemical method, applied for many electrochemical characterizations. This technique can be used to analyze oxidation/reduction behaviors or antioxidants without requiring any pretreatment, catalysts, or use of specific reagents [30]. CV was used in this study to demonstrate the oxidation signals of both *S. aureus* and *E. coli* after treatment with different GO concentrations on HA-ATi (Figures 5(b)-5(c)). One of the most widely used redox systems utilizes the redox couples of $\text{Fe}(\text{CN})_6^{4-/3-}$ (Figure 6(a)). The redox couple potentials of $\text{Fe}(\text{CN})_6^{4-/3-}$ were at $-0.27/-0.40 \text{ V}_{\text{Ag}/\text{AgCl}}$ for GO-HA-ATi samples. The oxidation peaks at $-0.95 \text{ V}_{\text{Ag}/\text{AgCl}}$ were usually redox couple

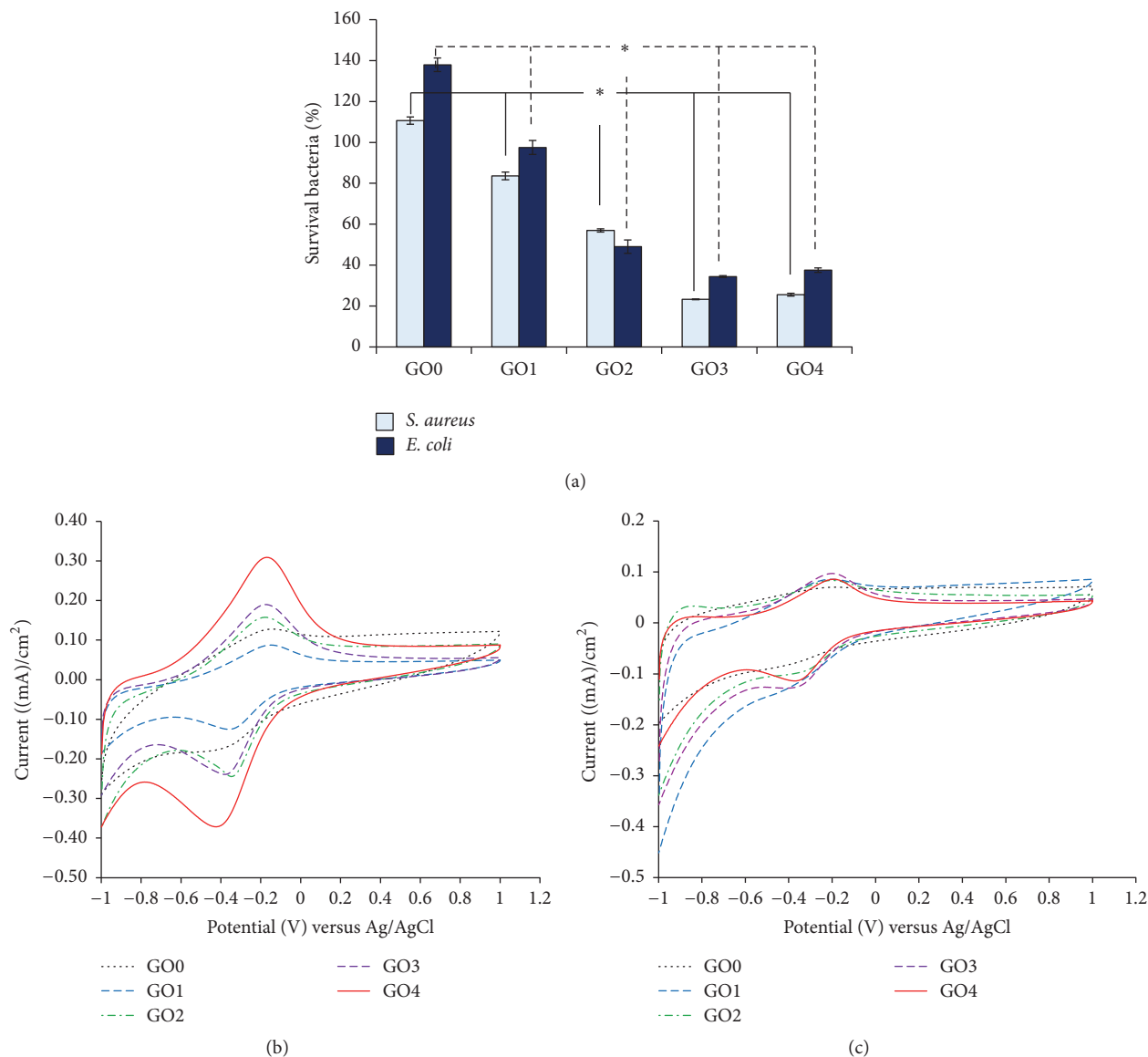


FIGURE 5: (a) Cytotoxicity of GO coating on HA-ATi to *E. coli* and *S. aureus* exposed to various concentrations of GO coating on HA-ATi samples, for 24 h. The p value was calculated using one-way ANOVA; $N = 3$; * $p < 0.05$. Cyclic voltammograms of detected (b) *S. aureus* and (c) *E. coli* ROS. The bacteria were incubated on GO-HA-ATi and CV was measured in PBS electrolyte at room temperature after 24 h.

potentials of O_2/H_2O [31]. The other controls were samples without an oxidation reaction in PBS solution. There was no oxidation peak but there was a reduction peak, which may be due to the reduction of some of the C-C bonds of GO detected in PBS (Figure 6(b)). Such behavior was previously reported by Kamyabi and Shafiee [32].

The cyclic voltammograms, Figure 5(b), showed the electron exchange of *S. aureus* with the GO coating on HA-ATi samples. The redox peak was observed in samples with GO coatings. The cyclic voltammograms of GO0, GO1, GO2, GO3, and GO4 in Figure 5(c) showed two pairs of well-defined redox peaks. The oxidation/reduction peaks were at $-0.14/-0.36$ (GO0), $-0.15/-0.32$ (GO1), $-0.18/-0.33$ (GO2),

$-0.18/-0.36$ (GO3), and $-0.17/-0.40$ V_{Ag/AgCl} (GO4). The cyclic voltammograms shown in Figure 5(c) demonstrated the electron exchange of *E. coli* with GO coatings on HA-ATi samples. A redox peak was observed for all GO coatings except GO0. The cyclic voltammograms of GO1, GO2, GO3, and GO4 in Figure 5(c) showed two pairs of well-defined redox peaks. The oxidation/reduction peaks were at $-0.21/-0.35$ (GO1), $-0.20/-0.30$ (GO2), $-0.20/-0.34$ (GO3), and $-0.19/-0.33$ V_{Ag/AgCl} (GO4). The redox peaks demonstrated a shift of the potential for samples incubated with *S. aureus* with various GO concentrations on HA-ATi samples. Qiao et al. reported that the redox peaks resulted from the electron transfer from inside to outside through the cell

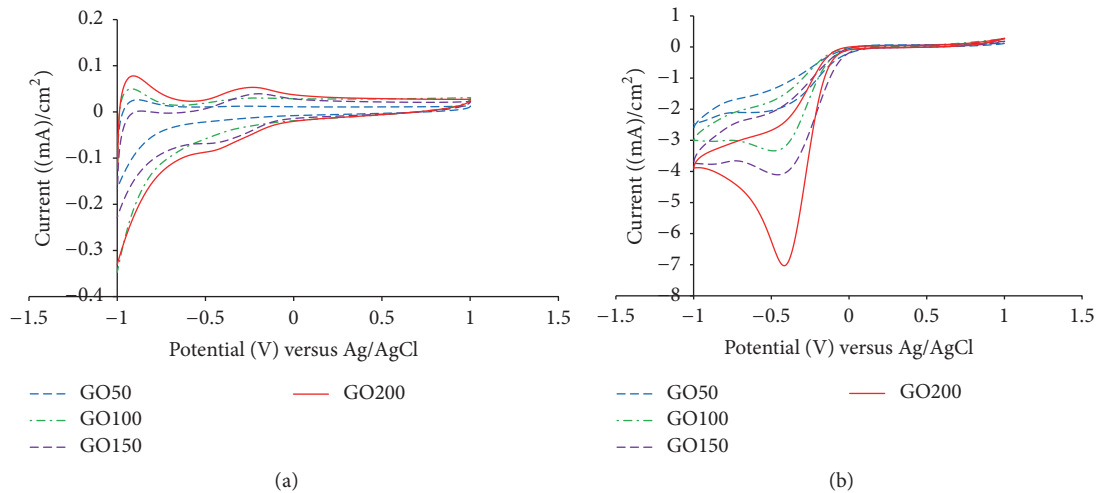


FIGURE 6: (a) Cyclic voltammograms of the $\text{Fe}(\text{CN})_6^{4-/3-}$ redox system were used as a positive control and (b) samples without adhered cells in PBS solution were used as a negative control.

membrane using a mediator (outer membrane cytochromes and/or conductive pili) at a voltage of -0.14 to -0.40 V_{Ag/AgCl} [33].

Furthermore, a shift in the higher oxidation current with an increase in GO concentration was observed (Figures 5(b)-5(c)). For a better understanding of the induced oxidative stress, voltammograms were replotted to compare peak currents, which are representatives of the oxidative power of the materials on each bacterial species, with the GO concentrations (Figure 7). An increase in the GO concentration increased the oxidative current peaks in *S. aureus*, which can be explained in two ways. First, it is possible that a high GO concentration causes high oxidative stress, resulting in high oxidation peak [8]. Second, the increase of GO concentration increased an electrical conduction between bacteria and electrode when GO was used as the mediator of the sensor system [34]. The effect of GO concentration on peak current for *E. coli*, however, was much lower. As discussed previously, the cell membrane of each bacterium affects adhesion to the substrate. For *S. aureus*, there was a higher potential to adhere on the surface, as shown in the cyclic voltammograms (Figure 7).

To better understand the oxidative stress mechanism, more studies of this bacterial process are needed. Moreover, these GO-coated samples show the potential to be used as sensors to detect biological matter [12]. In situ diagnosis using this GO-coated material will be a new trend for an implantable label-free sensor. Biocompatibility testing will be required to develop this new potential use of this novel material.

3.3. Osteoblast Responses

3.3.1. Preosteoblast Proliferation (MTT Assay). To evaluate the biological responses to biomaterials, the osteoblast cell density of 4×10^4 cells cm^{-2} was seeded on samples in each well. An MTT test was performed to evaluate cell viability. Cell viability was higher in GO3 than in the other samples

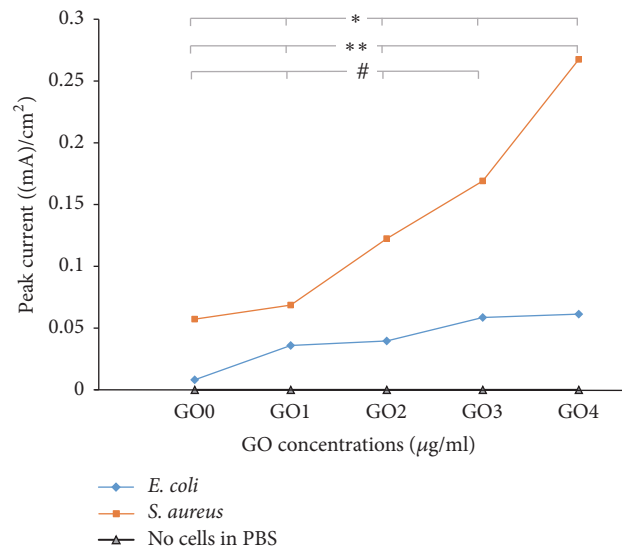


FIGURE 7: Plot of the samples with anodic peak current analysis. A p value was calculated using one-way ANOVA; $N = 3$; * $p < 0.05$ when compared with coating incubated with *S. aureus*. ** $p < 0.05$ when compared with coating incubated with *E. coli*.

(Figure 8). Although MTT activity on HA-ATi (GO0) was high, it was still lower than those on the other GO-coated samples. Thus, the GO did not exert any cytotoxic effects on the cells and actually promoted osteoblast cell attachment and proliferation. Several previous reports focused primarily on the biocompatibility of GO films [14, 35, 36]. The results of the previous studies are generally consistent with those of the present study with regard to the finding that GO film enhances mammalian cell proliferation. Taken together, these findings indicate that GO supports osteoblast growth and proliferation. GO effects on cellular inhibition are dose-dependent, as reported by Chang et al. [14]. They found that the GO did not enter A549 (adenocarcinoma human alveolar

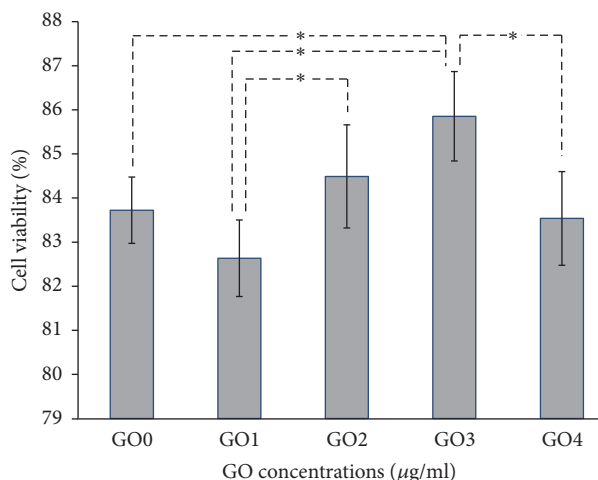


FIGURE 8: MTT test on osteoblast cultures 5 d after cell seeding. Percentages of cell viability were analyzed using absorbance at 550 nm. The p value was calculated using an independent-samples t -test; $n = 3$; $N = 3$; $*p < 0.05$.

basal epithelial cells) and had no obvious cytotoxicity. GO causes dose-dependent oxidative stress in the cell and high concentrations of GO induce a slight loss of cell viability. Moreover, Wojtoniszak et al. reported that GO at concentrations ranging from 3.125 to $25 \mu\text{g ml}^{-1}$ exhibited the best biocompatibility with mouse L929 fibroblast cells [37].

The osteoblast cell membrane has the same negative charge as bacterial cell membranes. The negative charge is due to phosphate groups on the bilayers. The charge of the membrane protein does differ, however, from that of the extracellular matrix. To adhere onto negatively charged surfaces, Gongadze et al. reported that the mechanism was established in two steps [38]. The osteoblast cell membrane first makes nonspecific contact caused by electrostatic forces. Positively charged proteins then attach to the negatively charged surface, followed by specific binding involving an integrin assembly [39]. A number of questions arise regarding the protective mechanism that preosteoblast cells use to protect themselves from GO. Almeida reported that, to prevent oxidative stress, cells utilized diverse mechanisms involving both enzymatic reactions and altered gene transcription [40]. These mechanisms are superior to those of bacteria with respect to stability and high reducing power. In another study, glutathione reductases from *Saccharomyces cerevisiae* and *E. coli* were rapidly inactivated following aerobic incubation with NADPH, NADH, and several reductants in a time- and temperature-dependent manner [41]. Therefore, to eliminate the effect of ROS inside the cells, ROS reduction in mammalian cells must be easier than that in bacteria. The toxicity of GO nanomaterials, however, is concentration dependent for both bacterial and mammalian cells.

3.3.2. Preosteoblast Differentiation (Calcium Deposition). Proliferation of osteoblasts on material surfaces alone, however, is not sufficient to achieve long-term osseointegration for orthopedic implants. For this reason, long-term (in the

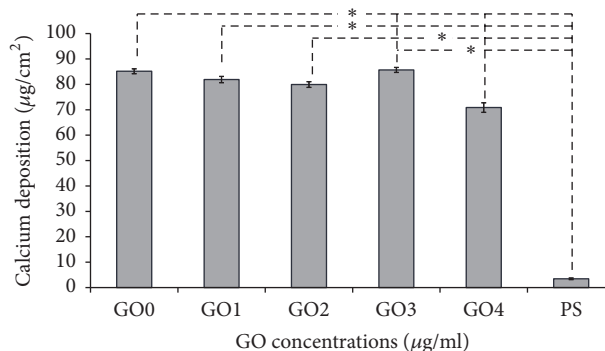


FIGURE 9: Calcium deposition after 21 d of preosteoblast cultures on the GO coating on HA-ATi and polystyrene surface (PS). The p value was calculated using independent-samples t -test; $n = 3$; $N = 3$; $*p < 0.05$.

order of days to weeks) functions of osteoblasts on the GO-coated HA-ATi materials were investigated using a calcium deposition assay. The mineralization process of preosteoblasts in *in vitro* culture was used as a model to test the effects of biomaterial surfaces on bone cell differentiation and bone formation. Calcium deposition is an indicator of successful *in vitro* bone formation and can be measured specifically by calcium deposition assay [1].

A calcium deposition assay was performed to evaluate different GO-coated HA-ATi surfaces. For any test period, there were barely detectable amounts of calcium deposited on the polystyrene substrates (Figure 9). The calcium content in the extracellular matrix in all samples in this study was significantly ($p < 0.05$) greater than that on polystyrene substrate formulations after 21 d of culture. The GO3 surface had the highest ability to support the mineralization of preosteoblast cells after 21 d. Moreover, compared with GO0, the calcium content in the extracellular matrix for GO3 was significantly ($p < 0.05$) greater after culture for 21 d.

The findings of the present study supported previous cell proliferation studies indicating that GO3 exhibited the highest potential to support cell growth compared with the other concentrations of GO. Proliferation and differentiation showed similar trends. At the beginning, cell-biomaterial interactions during the first period (such as cell adhesion and proliferation) could affect long-term cell function, such as synthesis of extracellular matrix proteins or calcium deposition [42, 43].

The effect of GO-coated HA-ATi on bacterial behavior and the response of preosteoblast cells are summarized in Table 1. The cytotoxic effects of the materials on cell survival were classified as medium if cell survival was lower than 70% according to the ISO 10993-5 standard [44]. In the cases of GO0 and GO1, there was no sign for toxicity toward MC3T3-E1, *S. aureus*, and *E. coli*. High GO concentrations (GO2, GO3, and GO4) exhibited slightly toxic effects on both types of bacteria (*S. aureus* and *E. coli*), but not for MC3T3-E1. These findings indicated that biomaterials coated with GO2, GO3, and GO4 had antibacterial properties. Moreover, they were cytocompatible with preosteoblast cells

TABLE 1: Toxicity of GO-coated sample on MC3T3-E1, *S. aureus*, and *E. coli*. (+) indicates cytotoxicity and (–) indicates no harmful effects to the cells.

| GO concentration on HA-ATi | Organism | Toxicity (+, –) |
|----------------------------|------------------|-----------------|
| 0 $\mu\text{g/ml}$ | MC3T3-E1 | – |
| | <i>S. aureus</i> | – |
| | <i>E. coli</i> | – |
| 50 $\mu\text{g/ml}$ | MC3T3-E1 | – |
| | <i>S. aureus</i> | – |
| | <i>E. coli</i> | – |
| 100 $\mu\text{g/ml}$ | MC3T3-E1 | – |
| | <i>S. aureus</i> | + |
| | <i>E. coli</i> | + |
| 150 $\mu\text{g/ml}$ | MC3T3-E1 | – |
| | <i>S. aureus</i> | + |
| | <i>E. coli</i> | + |
| 200 $\mu\text{g/ml}$ | MC3T3-E1 | – |
| | <i>S. aureus</i> | + |
| | <i>E. coli</i> | + |

and promoted cell proliferation and calcium deposition. Importantly, the highest cell viability and calcium deposition were observed for GO3. Thus, this novel material has the potential to promote osseointegration of surrounding bone cells. The results of the *in vitro* study revealed that GO-coated HA-ATi enhanced long-term functions (specifically, concentration of calcium deposition) of preosteoblasts when the GO concentration in electrolyte was 150 $\mu\text{g ml}^{-1}$. More studies of long-term osteoblast cultures are needed to ensure differentiation on GO-HA-ATi.

The cytotoxicity of GO is expected to differ significantly from that of widely studied three-dimensional CNTs [45]. The two materials have a similar crystalline structure, however, but a different shape (flat atomic sheets for GO and tubular for nanotubes). Zhang et al. studied GO interactions with neuron-like cells (PC12) *in vitro* and found that GO cytotoxicity in PC12 cells was relatively low compared with CNT; both GO and CNT induced concentration- and shape-dependent cytotoxic effects [11]. Zhang et al. [11] also suggested that fibroblast adhesion and proliferation should be studied in addition to preosteoblasts to examine the integration between implants with the surrounding soft tissues. Moreover, the solubility of GO composite in stimulated body fluid solution should be tested to confirm the stability of this composite material in the host [46].

4. Conclusions

The antibacterial properties and osteoblast response (proliferation and calcium deposition) of GO on HA-ATi samples were studied. The GO coatings on HA-ATi were prepared using anodic-electrophoretic deposition. Various GO concentrations in electrolytes were used to deposit GO nanowalls on HA-ATi. Based on the antibacterial drop test, GO reduced the growth of bacteria in both strain models: *S. aureus* and *E. coli*. The results of RNA leakage tests revealed that direct

contact of the bacteria with GO causes membrane stress, leading to irreversible damage. The RNA efflux indicated greater damage to the cell membrane of *S. aureus* compared with the cell membrane of *E. coli*. The higher resistance of *E. coli* against interaction with the nanowalls compared with *S. aureus* might be due to the greater stiffness of *E. coli*. The increased current density of oxidative peaks in the CV tests in this study positively correlated with the number of surviving bacteria, suggesting that the increase in cytotoxicity was due to an increase in cellular oxidative stress (similar to the result of membrane stress causing RNA leakage). Therefore, the findings of the present study indicated that survival of bacteria, oxidative stress, and membrane stress were GO-concentration-dependent mechanisms. The results also suggested that GO-HA composite coatings decreased susceptibility to both *S. aureus* and *E. coli* and thus could be applied as effective antibacterial agents to suppress bacterial invasion in orthopedic implants. Moreover, the osteoblast responses demonstrated that the GO-HA composite coatings increased osteoblast proliferation after 5 d of cultures. The results from the calcium deposition assay after culture for 21 d confirmed that GO-HA composite coatings supported an early stage of osteoblast differentiation. Electrodeposited GO at concentrations of 150 $\mu\text{g ml}^{-1}$ and 200 $\mu\text{g ml}^{-1}$ was found to be optimal in this study because GO coatings at these concentrations induced cell death in both strains of bacteria but promoted high proliferation and calcium deposition of preosteoblasts. Therefore, GO electrodeposited on HA-ATi are very promising not only for antibacterial applications, but also for orthopedic applications. Further *in vitro* studies and *in vivo* studies are needed to examine long-term osteoblast differentiation, protein, and gene expression of osteoblasts.

Conflicts of Interest

The authors declare that there are no conflicts of interest regarding the publication of this article.

Acknowledgments

The authors would like to acknowledge the Research Strengthening Project of the Faculty of Engineering, King Mongkut's University of Technology Thonburi, Bangkok, Thailand, for funding.

References

- [1] M. S.-A. Johnsson and G. H. Nancollas, "The role of Brushite and octacalcium phosphate in apatite formation," *Critical Reviews in Oral Biology and Medicine*, vol. 3, no. 1-2, pp. 61–82, 1992.
- [2] K. S. Brammer, S. Oh, C. J. Cobb, L. M. Bjursten, H. van der Heyde, and S. Jin, "Improved bone-forming functionality on diameter-controlled TiO₂ nanotube surface," *Acta Biomaterialia*, vol. 5, no. 8, pp. 3215–3223, 2009.
- [3] Y. Parcharoen, P. Kajitvichyanukul, S. Sirivisoot, and P. Termsuksawad, "Hydroxyapatite electrodeposition on anodized titanium nanotubes for orthopedic applications," *Applied Surface Science*, vol. 311, pp. 54–61, 2014.

- [4] J. D. Whitehouse, N. Deborah Friedman, K. B. Kirkland, W. J. Richardson, and D. J. Sexton, "The impact of surgical-site infections following orthopedic surgery at a community hospital and a university hospital: adverse quality of life, excess length of stay, and extra cost," *Infection Control and Hospital Epidemiology*, vol. 23, no. 4, pp. 183–189, 2002.
- [5] K. Krishnamoorthy, U. Navaneethaiyer, R. Mohan, J. Lee, and S. Kim, "Graphene oxide nanostructures modified multifunctional cotton fabrics," *Applied Nanoscience*, vol. 2, no. 2, pp. 119–126, 2012.
- [6] S. Liu, T. H. Zeng, M. Hofmann et al., "Antibacterial activity of graphite, graphite oxide, graphene oxide, and reduced graphene oxide: membrane and oxidative stress," *ACS Nano*, vol. 5, no. 9, pp. 6971–6980, 2011.
- [7] O. Akhavan and E. Ghaderi, "Toxicity of graphene and graphene oxide nanowalls against bacteria," *ACS Nano*, vol. 4, no. 10, pp. 5731–5736, 2010.
- [8] Y. Parcharoen, P. Termsuksawad, and S. Sirivisoot, "Electrochemical deposition of novel graphene oxide-hydroxyapatite composite onto titanium dioxide nanotubes for orthopaedic applications," in *International Conference on Advances in Science and Technology (ICAST)*, pp. 201–208, Science Publication, Pattaya, Thailand, 2014.
- [9] G. Bharath, B. S. Latha, E. H. Alsharaeh, P. Prakash, and N. Ponpandian, "Enhanced hydroxyapatite nanorods formation on graphene oxide nanocomposite as a potential candidate for protein adsorption, pH controlled release and an effective drug delivery platform for cancer therapy," *Analytical Methods*, vol. 9, no. 2, pp. 240–252, 2017.
- [10] G. Bharath, R. Madhu, S.-M. Chen et al., "Enzymatic electrochemical glucose biosensors by mesoporous 1D hydroxyapatite-on-2D reduced graphene oxide," *Journal of Materials Chemistry B*, vol. 3, no. 7, pp. 1360–1370, 2015.
- [11] Y. Zhang, S. F. Ali, E. Dervishi et al., "Cytotoxicity effects of graphene and single-wall carbon nanotubes in neural pheochromocytoma-derived pc12 cells," *ACS Nano*, vol. 4, no. 6, pp. 3181–3186, 2010.
- [12] J. Li, L. Zheng, L. Zeng, Y. Zhang, L. Jiang, and J. Song, "RGD Peptide-Grafted Graphene Oxide as a New Biomimetic Nanointerface for Impedance-Monitoring Cell Behaviors," *Journal of Nanomaterials*, vol. 2016, Article ID 2828512, 2016.
- [13] C. D. Vecitis, K. R. Zodrow, S. Kang, and M. Elimelech, "Electronic-structure-dependent bacterial cytotoxicity of single-walled carbon nanotubes," *ACS Nano*, vol. 4, no. 9, pp. 5471–5479, 2010.
- [14] Y. Chang, S. T. Yang, J. H. Liu et al., "In vitro toxicity evaluation of graphene oxide on A549 cells," *Toxicology Letters*, vol. 200, pp. 201–210, 2011.
- [15] D. Y. Lyon, L. Brunet, G. W. Hinkal, M. R. Wiesner, and P. J. J. Alvarez, "Antibacterial activity of fullerene water suspensions (nC 60) is not due to ROS-mediated damage," *Nano Letters*, vol. 8, no. 5, pp. 1539–1543, 2008.
- [16] S. Kang, M. Herzberg, D. F. Rodrigues, and M. Elimelech, "Antibacterial effects of carbon nanotubes: size does matter!," *Langmuir*, vol. 24, no. 13, pp. 6409–6413, 2008.
- [17] A. Mittal, R. J. Flint, M. Fanous et al., "Redox status of acute pancreatitis as measured by cyclic voltammetry: Initial rodent studies to assess disease severity," *Critical Care Medicine*, vol. 36, no. 3, pp. 866–872, 2008.
- [18] A. Mittal, F. Göke, R. Flint et al., "The redox status of experimental hemorrhagic shock as measured by cyclic voltammetry," *Shock*, vol. 33, no. 5, pp. 460–466, 2010.
- [19] A. Mohammed Ali Al-Sammarraie and M. Hasan Raheema, "Electrodeposited Reduced Graphene Oxide Films on Stainless Steel, Copper, and Aluminum for Corrosion Protection Enhancement," *International Journal of Corrosion*, vol. 2017, pp. 1–8, 2017.
- [20] P. Arpornmaeklong, S. E. Brown, Z. Wang, and P. H. Krebsbach, "Phenotypic characterization, osteoblastic differentiation, and bone regeneration capacity of human embryonic stem cell-derived mesenchymal stem cells," *Stem Cells and Development*, vol. 18, no. 7, pp. 955–968, 2009.
- [21] P. Tanurat and S. Sirivisoot, "Osteoblast proliferation on graphene oxide electrodeposited on anodized titanium," in *Proceedings of the 8th Biomedical Engineering International Conference, BMEiCON 2015*, tha, November 2015.
- [22] K. Satheesh and R. Jayavel, "Synthesis and electrochemical properties of reduced graphene oxide via chemical reduction using thiourea as a reducing agent," *Materials Letters*, vol. 113, pp. 5–8, 2013.
- [23] X. Guo and N. Mei, "Assessment of the toxic potential of graphene family nanomaterials," *Journal of Food and Drug Analysis*, vol. 22, no. 1, pp. 105–115, 2014.
- [24] M. T. Cabeen and C. Jacobs-Wagner, "Bacterial cell shape," *Nature Reviews Microbiology*, vol. 3, no. 8, pp. 601–610, 2005.
- [25] B. Gottenbos, D. W. Grijpma, H. C. Van Der Mei, J. Feijen, and H. J. Busscher, "Antimicrobial effects of positively charged surfaces on adhering Gram-positive and Gram-negative bacteria," *Journal of Antimicrobial Chemotherapy*, vol. 48, no. 1, pp. 7–13, 2001.
- [26] Y. F. Dufrene, "Refining our perception of bacterial surfaces with the atomic force microscope," *Journal of Bacteriology*, vol. 186, no. 11, pp. 3283–3285, 2004.
- [27] P. Eaton, J. C. Fernandes, E. Pereira, M. E. Pintado, and F. Xavier Malcata, "Atomic force microscopy study of the antibacterial effects of chitosans on *Escherichia coli* and *Staphylococcus aureus*," *Ultramicroscopy*, vol. 108, no. 10, pp. 1128–1134, 2008.
- [28] J. Li and L. A. McLandsborough, "The effects of the surface charge and hydrophobicity of *Escherichia coli* on its adhesion to beef muscle," *International Journal of Food Microbiology*, vol. 53, no. 2-3, pp. 185–193, 1999.
- [29] A. A. Mafu, C. Plumety, L. Deschênes, and J. Goulet, "Adhesion of pathogenic bacteria to food contact surfaces: Influence of pH of culture," *International Journal of Microbiology*, Article ID 972494, 2011.
- [30] J. F. Arteaga, M. Ruiz-Montoya, A. Palma, G. Alonso-Garrido, S. Pintado, and J. M. Rodriguez-Mellad, "Comparison of the simple cyclic voltammetry (CV) and DPPH assays for the determination of antioxidant capacity of active principles," *Molecules*, vol. 17, no. 5, pp. 5126–5138, 2012.
- [31] G. Tratnyek Paul, in *Aquatic Redox Chemistry*, Grundle Timothy and B. Haderlein Stefan, Eds., American Chemical Society, 2011.
- [32] M. A. Kamyabi and M. A. Shafiee, "Electrocatalytic oxidation of dopamine, ascorbic acid and uric acid at poly-2,6-diaminopyridine on the surface of carbon nanotubes/GC electrodes," *Journal of the Brazilian Chemical Society*, vol. 23, no. 4, pp. 593–601, 2012.
- [33] Y. Qiao, C. M. Li, S.-J. Bao, Z. Lu, and Y. Hong, "Direct electrochemistry and electrocatalytic mechanism of evolved *Escherichia coli* cells in microbial fuel cells," *Chemical Communications*, no. 11, pp. 1290–1292, 2008.
- [34] F. Liu, K. S. Choi, T. J. Park, S. Y. Lee, and T. S. Seo, "Graphene-based electrochemical biosensor for pathogenic virus detection," *Biochip Journal*, vol. 5, no. 2, pp. 123–128, 2011.

- [35] H. Chen, M. B. Müller, K. J. Gilmore, G. G. Wallace, and D. Li, "Mechanically strong, electrically conductive, and biocompatible graphene paper," *Advanced Materials*, vol. 20, no. 18, pp. 3557–3561, 2008.
- [36] S. Park, N. Mohanty, J. W. Suk et al., "Biocompatible, robust free-standing paper composed of a TWEEN/graphene composite," *Advanced Materials*, vol. 22, no. 15, pp. 1736–1740, 2010.
- [37] M. Wojtoniszak, X. Chen, R. J. Kalenczuk et al., "Synthesis, dispersion, and cytocompatibility of graphene oxide and reduced graphene oxide," *Colloids and Surfaces B: Biointerfaces*, vol. 89, no. 1, pp. 79–85, 2012.
- [38] E. Gongadze, D. Kabaso, S. Bauer, J. Park, P. Schmuki, and A. Igljić, "Adhesion of osteoblasts to a vertically aligned TiO₂ nanotube surface," *Mini-Reviews in Medicinal Chemistry*, vol. 13, no. 2, pp. 194–200, 2013.
- [39] G. Ekaterina, K. Doron, B. Sebastian et al., "Adhesion of osteoblasts to a nanorough titanium implant surface," *International Journal of Nanomedicine*, vol. 6, 1816 pages, 2011.
- [40] M. Almeida, "Aging mechanisms in bone," *BoneKEy Reports*, vol. 1, no. 7, 2012.
- [41] M. C. Pinto, A. M. Mata, and J. Lopez-barea, "Reversible inactivation of *Saccharomyces cerevisiae* glutathione reductase under reducing conditions," *Archives of Biochemistry and Biophysics*, vol. 228, no. 1, pp. 1–12, 1984.
- [42] J. Y. Martin, Z. Schwartz, T. W. Hummert et al., "Effect of titanium surface roughness on proliferation, differentiation, and protein synthesis of human osteoblast-like cells (MG63)," *Journal of Biomedical Materials Research*, vol. 29, no. 3, pp. 389–401, 1995.
- [43] B. Groessner-Schreiber and R. S. Tuan, "Enhanced extracellular matrix production and mineralization by osteoblasts cultured on titanium surfaces in vitro," *Journal of Cell Science*, vol. 101, no. 1, pp. 209–217, 1992.
- [44] J. C. Hornez, A. Lefèvre, D. Joly, and H. F. Hildebrand, "Multiple parameter cytotoxicity index on dental alloys and pure metals," *Biomolecular Engineering*, vol. 19, no. 2-6, pp. 103–117, 2002.
- [45] V. L. Colvin, "The potential environmental impact of engineered nanomaterials," *Nature Biotechnology*, vol. 21, no. 10, pp. 1166–1170, 2003.
- [46] C. Zhao, X. Lu, C. Zanden, and J. Liu, "The promising application of graphene oxide as coating materials in orthopedic implants: Preparation, characterization and cell behavior," *Biomedical Materials (Bristol)*, vol. 10, no. 1, Article ID 015019, 2015.